



University of HUDDERSFIELD

University of Huddersfield Repository

Furness, Thomas Richard

INTERNAL FEATURE MEASUREMENT UTILISING INFRARED THERMOGRAPHY

Original Citation

Furness, Thomas Richard (2021) INTERNAL FEATURE MEASUREMENT UTILISING INFRARED THERMOGRAPHY. Doctoral thesis, University of Huddersfield.

This version is available at <http://eprints.hud.ac.uk/id/eprint/35681/>

The University Repository is a digital collection of the research output of the University, available on Open Access. Copyright and Moral Rights for the items on this site are retained by the individual author and/or other copyright owners. Users may access full items free of charge; copies of full text items generally can be reproduced, displayed or performed and given to third parties in any format or medium for personal research or study, educational or not-for-profit purposes without prior permission or charge, provided:

- The authors, title and full bibliographic details is credited in any copy;
- A hyperlink and/or URL is included for the original metadata page; and
- The content is not changed in any way.

For more information, including our policy and submission procedure, please contact the Repository Team at: E.mailbox@hud.ac.uk.

<http://eprints.hud.ac.uk/>

THE UNIVERSITY OF HUDDERSFIELD

INTERNAL FEATURE MEASUREMENT
UTILISING INFRARED THERMOGRAPHY

By

THOMAS RICHARD FURNESS

A thesis submitted in partial fulfilment for the
Degree of Doctor of Philosophy

In the
School of Computing and Engineering
Centre for Precision Technologies

SEPT 2021

Copyright Statement

- The author of this thesis (including any appendices and/or schedules to this thesis) owns any copyright in it (the “Copyright”) and s/he has given The University of Huddersfield the right to use such copyright for any administrative, promotional, educational and/or teaching purposes.
- Copies of the thesis, in either full or in extracts, may be made only in accordance with the regulations of the University Library. Details of the regulations may be obtained from the Librarian. This page must form part of any such copies made.
- The ownership of any patents, designs, trademarks and any and all other intellectual property rights except for the Copyright (the “Intellectual Property Rights”) and any reproductions of copyright work, for example graphs and tables (“Re-productions”), which may be described in this thesis, may not be owned by the author, and may be owned by third parties. Such Intellectual Property Rights and Reproductions cannot and must not be made available for use without the prior written permission of the owner(s) of the Intellectual property Rights and/or Reproductions.

Acknowledgements

Whilst performing this investigation has been both interesting and for the most part enjoyable, it has been extremely challenging to try to finish this thesis on a part time basis. Work commitments and other engagements meant that this study often had to be pushed down the list of priorities. Without the understanding and constant support, both technical and otherwise, of my supervisory team this thesis would not have reached fruition.

First, I would like to give a huge thank you to my primary supervisor Dr Simon Fletcher. His constant support, technical prowess and guidance have proved invaluable during this project. Without his knowledge and supportiveness this work would be infinitely more difficult to complete.

I would also like to thank Dr Andrew Longstaff. His guidance and support have often helped me to find the right path during this period.

Thank you also to research office for their constant understanding of the difficulties of doing a part time PhD.

Finally, to my family, especially my wife Charlotte, for your encouragement and belief (and for proofreading this document numerous times). Thank you all for your constant love and support.

Abstract

Whilst Part inspection and dimensional validation (PIDV) is a well-established practice for external and accessible features, the capture and analysis of internal features and the dimensions associated with them has always been an issue. As parts designed for additive manufacture become more widely used, this issue is compounded, since internal features and hollows can be easily introduced. For parts manufactured through additive manufacture or by traditionally cast methods, if the internal structure requires PIDV or an in-line validation check, the internal structure will need to be revealed so that a measurement can take place. Presently, the only available solutions to this issue are destructive measurement, or X-ray computed tomography (XCT) scanning. Neither of these solutions are universally practical, and in the latter case not readily available.

This thesis introduces an alternative method for measuring internal features. The method requires an intentionally induced temperature differential between the internal and external features. The resultant temperature distribution is measured on the surface using a thermographic camera.

Using this technique, in combination with standard multi-view projection, this method of data recovery can discern an object's internal structure and provide inferred measurements for that structure. This result, combined with any industry-standard method for the measurement of the external features, can provide a complete 3D digital recreation of the object in question. This technique has the benefits of being non-destructive, not requiring extensive training or knowledge to operate, and being more affordable and more portable than XCT.

The aim of this investigation was to devise and evaluate the feasibility of this approach. This process began with a series of FEA simulations to prove that internal geometric measurements could be extracted from forcibly induced surface temperature profiles and that the spatial and temperature resolution required for this extraction were sufficient. For low conductive materials, with forcible induced internal temperatures or around 100°C, internal edge extraction was possible to within 1.5mm. From this initial validation, a series of physical experiments using 3D printed, and machined artefacts were performed to validate the computer simulations and understand the limitations when using a real thermographic camera, rather than picking ideal data from a simulation.

The experimental results showed that through the thermal manipulation of an object's internal structure, geometric dimensions could be resolved to within +/-1.8mm with a repeatably of 0.6mm. When combined with external surface data from industry-standard capture techniques, this novel approach successfully resolved a complete Computer Aided Design (CAD) "solid model" encapsulating a holistic set of geometric measurements.

In addition to findings relating to spatial accuracy, and material limitation, this research has highlighted how this capture technique can discern differing internal structures based on temporally gathered temperature data. When the temperature data from the test artifacts is gathered temporally, the resultant data shows differing results for curved, angled, and straight internal faces respectively. This, going forward, would allow for the automatic categorisation and recognition of internal features based upon the recovered thermal response.

Contents

Copyright Statement	i
Acknowledgements.....	ii
Abstract.....	iii
List of Figures	ix
List of Tables	xvi
Abbreviations.....	xvii
Symbols.....	xix
Chapter 1. Introduction	1
1.1. Overview.....	1
1.2. Thesis Structure	8
Chapter 2. Literature Review	11
2.1. Introduction to part inspection and dimensional validation.....	11
2.2. Internal Part measurement	15
2.3. Uses and Limitations of IRT.....	25
2.3.1. Definition of Thermography	25
2.3.2. Emissivity and Absorptivity	28
2.4. IRT uses in PIDV.....	31
2.4.1. Thermal Overlay	33
2.4.2. Thermographic vision systems	36
2.4.3. Geometric Shape Reconstruction Using Thermal Imagery	38
2.5. Chapter Summary	39
Chapter 3. Motivation, Aim, Research Objectives, Scope and Methodology	44
3.1. Motivation.....	44
3.2. Aim	45
3.3. Research questions.....	45
3.4. Research objectives.....	46
3.5. Scope.....	47
3.6. Methodology and hypothesis	48
3.6.1. Hypothesis.....	48
3.6.2. Methodology	49
Chapter 4. Preliminary FEA Modelling and Results	56
4.1. Introduction to Thermal FEA Simulations	56
4.2. Preliminary geometry for simulation of surface temperature profiles.....	57

4.2. Heating inside the Cavity.....	59
4.2.1. Mesh.....	59
4.2.2. Boundary conditions	60
4.2.3. Initial simulation	61
4.2.4. Change of cavity depth.	66
4.2.5. Change in width.	72
4.2.6. Change in thermal conductivity	76
4.3. Edge drift vs Edge Curvature/Angle.....	78
4.4. Adjusting Internal Temperature.	83
4.5. External Heating	84
4.6. Experimental Artefact Simulation	94
4.7. Effects of Thermal Expansion	103
4.8. Chapter Summary	106
Chapter 5. Thermographical Analysis	109
5.1. Artefact Generation.....	109
5.2. Artifact calibration	111
5.3. Scanning.....	113
5.3.1. 3D External Scanning	113
5.3.2. Effects of Emissivity.....	114
5.3.3. 3D Internal Scanning	117
5.3.4. First Face Feature Extraction	122
5.3.5. Second Face Feature Extraction.....	134
5.3.6. 3D Internal Reconstruction	136
5.4. Aluminium Version and external heating	140
5.5. Second Artefact - Cuboid.....	152
5.6. Third Artefact – L-shape.....	155
5.7. Accuracy, and repeatability	160
5.7.1. Accuracy and repeatability using a lower resolution camera	162
5.8. Potential Error Sources	165
5.9. Chapter Summary	169
Chapter 6. Temporal Thermal Imagery (TTI).....	171
6.1. Introduction to TTI	171
6.2. TTI Software.....	172
6.2.1. TTI Planar cavity example.....	176
6.2.2. Circular Internal Face Example	181

6.2.3. Angled (diamond) Cavity Example	185
6.3. Chapter Summary	187
Chapter 7. Conclusions and Future Work	189
7.1. Summary of Investigation/Research question	189
7.2. Summary of achieved objectives	191
7.2.1. Objective i.....	191
7.2.2. Objective ii.....	191
7.2.3. Objective iii.....	193
7.2.4. Objective iv	193
7.2.5. Objective v	194
7.2.6. Objective vi.....	195
7.3. Conclusions and Contributions to Knowledge	196
7.3.1. Conclusions.....	196
7.3.2. Contributions to Knowledge	197
7.4. Closing Statement	200
7.5. Future Work.....	200
7.5.1. Thermal conductivity, edge position relationship.....	201
7.5.2. Edge position response curves characterisation.....	201
7.5.3. Heating methods	202
7.5.4. Large scale scanning	202
7.5.5. Uncertainty analysis.....	204
7.5.6. Enhanced small scale scanning	204
References.....	206
Appendix A. Mesh modification.....	215
Appendix B. Initial simulation dimensions	217
Appendix C. FEA results	218
a. Change in cavity depth.....	218
i. Aluminium depth – 2mm.....	218
ii. Aluminium Depth – 8mm.....	219
iii. Aluminium Depth – 16mm.....	220
iv. PLA Depth – 2mm.....	221
v. PLA Depth – 8mm	222
vi. PLA Depth – 16mm.....	223
b. Change in width results.....	224
i. Width - 10mm.....	224

ii. Width – 30mm	225
iii. Width – 60mm	226
c. Change in material results	227
i. Aluminium	227
ii. Copper.....	228
iii. Ceramic.....	229
iv. Nylon	230
v. PLA.....	231
vi. Steel	232
d. Edge position differences for difference profiles.....	233
e. External heating results	238
i. 20mm cavity width	238
ii. 25mm cavity width	239
iii. 30mm cavity width	240
iv. 35mm cavity width	241
v. 40mm cavity width	242
vi. 45mm cavity width	243
vii. 50mm cavity width	244
viii. 55mm cavity width	245
ix. 60mm cavity width	246
x. PLA t=1200s	247
xi. PLA t=2400s.....	248
xii. PLA t=4800s.....	250
xiii. PLA t=9600s.....	251
f. Experimental artefact result.....	253
Appendix D. 3D external scanning.....	254
a. Digitisation.....	254
b. CPD Editing	256
c. Mesh creation.....	259
Appendix E. Artifact Calibration Results	263
a. Square Artifact	263
b. Rectangular Artifact.....	264
c. Cylinder Artifact	265
d. Angled Artifact	266
e. L-shaped Artifact	267

f. Aluminium Square Artifact.....	268
Appendix F. Feature Extraction with traditional Edge Detection Algorithms	269
Appendix G. Internal/External Reconstruing	275
Appendix H. Matlab Code	281
a. <i>LoadSW</i> – Single Solidworks temperature extraction program	281
b. <i>feapeaks</i> – FEA peak extraction code	287
c. <i>manySW</i> – Loading multiple solidworks file program.....	288
d. <i>Extract</i> - Feature extraction code	295
e. <i>Peakdet</i> - Peak detection Code.....	298
f. <i>Squareass</i> - Assembly Code	299
Appendix I. REVETTI results	301
a. Curved feature line fitting results.....	301
b. Angled feature line fitting results	302
Appendix J. Thermograms used in accuracy and repeatability tests – square artifact	304
a. Run 1	304
b. Run 2.....	304
c. Run 3	305
d. Run 4.....	305
e. Run 5	306
Appendix K. Thermograms used in accuracy and repeatability tests – L-shaped artifact.....	307
a. Run 1	307
b. Run 2.....	307
c. Run 3	307
d. Run 4.....	308
e. Run 4.....	308
Appendix L. Thermograms used in accuracy and repeatability tests – square artifact with A35	309
a. Run 1	309
b. Run 2.....	309
c. Run 3	309
d. Run 4.....	310
e. Run 5	310

List of Figures

Figure 1-1: CMM unable to reach target Dimension.....	3
Figure 1-2: CMM unable to reach internal feature	3
Figure 1-3: Generalized View of an Active Optical System	4
Figure 1-4: Cross section of a turbo charger showing cast internal structures.	5
Figure 1-5: Example of Orthographic Projection	8
Figure 2-1: Data acquisition methods	13
Figure 2-2: A typical MRI machine.....	24
Figure 2-3: Electromagnetic spectrum.....	26
Figure 2-4: Typical thermal image of a human	27
Figure 2-5: Faulty electrical connection.	27
Figure 2-6: Thermographic capture scenario [39]	28
Figure 2-7: Vollmer et al's [43] Leslie Cube	29
Figure 2-8: Vollmer et al [42] cube results.....	30
Figure 2-9: Example of a 3D thermography, showing 3D heat loss map on a building. Curtsey of Gonzalez-Aguilera et al [48]	33
Figure 4-1: Simple block with cavity and edges for profile extraction	59
Figure 4-2: Resultant meshed model (note the denser mesh around the example edge on the top face).....	60
Figure 4-3 (L) The initial geometric factors used in this simulation, (R) thermal distribution after simulation	61
Figure 4-4: Spatial temperature distribution across probe edge PE2 at T=40s.....	62
Figure 4-5: Temporal temperature due to time at all nodes along probe edge PE2.....	62
Figure 4-6: Differentiated data. MAX (blue) and MIN (red) marked as the detected peaks...	63
Figure 4-7: Depiction of laminar boundary regions, courtesy of Convection Heat transfer by A. Bejan [67].....	64
Figure 4-8: MAX/MIN edge positions over time	64
Figure 4-9: Differentiated temperature data at T=31s (L), with a replication of Figure 4-6 (R) for comparison, at T=2s	65
Figure 4-10: Adjusted depth dimension.....	66
Figure 4-11: Compiled edge position for all eight-depth simulation. Refer to Figure 4-12 for edge convention	67
Figure 4-13: Cavity width deduced from edge position	67
Figure 4-14: Percentage accuracy of cavity width with aluminium	68
Figure 4-15: Compiled edge position for all eight simulations with PLA.....	69
Figure 4-16: Cavity width deduced from edge position for PLA	70
Figure 4-17: Percentage accuracy of cavity width with PLA	70
Figure 4-18: Cavity width for aluminium for 2s.....	71
Figure 4-19: X marks the dimension (width) that will be changed	72
Figure 4-20: Edge positions and difference for all simulations.....	73
Figure 4-21: Cavity width over time.....	73
Figure 4-22: The actual and nominal results for changes in cavity width.....	74
Figure 4-23: Cavity width over time for 316	75
Figure 4-24: Error between nominal start points and actual.....	75

Figure 4-25: Edge positions due to varying material thermal properties.....	77
Figure 4-26: Edge position over time for PLA over 600s	78
Figure 4-27: Square, circle, and angled geometry	79
Figure 4-28: Square profile edge position results	80
Figure 4-29: Internal profile edges position results	81
Figure 4-30: Best fit comparison between edge separation differences	82
Figure 4-31: Surface temperature profile for all simulations at t=5s.....	84
Figure 4-32: Simulation set up for side heating	85
Figure 4-33: Thermal distribution across model at t=15s.....	86
Figure 4-34: Thermal distribution along probe edge at t=15s	86
Figure 4-35: Nodal temperatures for each time step.....	87
Figure 4-36: Edge position over time for side heating simulation.....	87
Figure 4-37: Average temperature profiles over time for cavity heating and side heating on aluminium block	88
Figure 4-38: X showing the dimension to be changed in this series of simulations.....	89
Figure 4-39: Resultant dimensional data for width change from side heating simulations.....	90
Figure 4-40: Percentage error comparison between internal heating simulations and side heating simulations	91
Figure 4-41: Side heating results with PLA: L: thermal distribution across object, R: extracted temperature from probe line on the top surface	91
Figure 4-42: Side heating results with PLA T=600s: L: thermal distribution across object, R: extracted temperature from probe line on the top surface	92
Figure 4-43: L- Nodal temperatures over time, R- differentiated temperature for t=600s	93
Figure 4-44: Section view of test artefact 1	94
Figure 4-45: Boundary condition for the artefact simulation	96
Figure 4-46: Thermal distribution of 320s simulation at T=320s.....	96
Figure 4-47: Nodal temperature distribution over time from vertical probe edge for 320s simulation.....	97
Figure 4-48: Random selected nodes from the vertical probe edge.....	97
Figure 4-49: Zoomed section of the model showing node position on the vertical probe edge	98
Figure 4-50: Edge position from vertical probe edge over time	99
Figure 4-51: Nodal temperature distribution over time from horizontal probe edge for 320s simulation.....	99
Figure 4-52: Random selected nodes from the horizontal probe edge	100
Figure 4-53: Edge position from horizontal probe edge over time.....	100
Figure 4-54: Zoomed section of the model showing node position on the Horizontal probe edge	101
Figure 4-55: Visualisation of recovered edge positions with the nominal and external edge positions	102
Figure 4-56: Thermal distribution.....	104
Figure 4-57: Thermal deformation at t=320s.....	105
Figure 4-58: Average surface temperature vs average thermal deformation.....	105
Figure 5-1: 3D printed test artefacts	111
Figure 5-2: Example artifact in the CT scanner	111
Figure 5-3: PCD of square artifact from XCT, and corresponding dimensions	112

Figure 5-4 (R): External scanning of artefact, (L): Final sharpened TTM	113
Figure 5-5: Setup of emissivity test	115
Figure 5-6: Emissivity test thermogram	115
Figure 5-7: Temperature over time due to emissivity.....	116
Figure 5-8: Standard deviation of object face, with and without heat source.....	117
Figure 5-9: Internal Thermal Capture Set Up	118
Figure 5-10: Thermal Capture of set up before heating.....	120
Figure 5-11: Adding of the heating medium. The funnel is highlighted at the top of the image	120
Figure 5-12: Front view of the artefact showing thermal conduction distribution.....	121
Figure 5-13: Temperature profiles corresponding to Figure 5-12	121
Figure 5-14: Thermogram to be used in geometry reconstruction.	122
Figure 5-15: Flow diagram of the feature extraction algorithm	123
Figure 5-16: Monotone image of the thermogram shown in Figure 5-14	124
Figure 5-17: Thermogram after edge detection has been performed.....	125
Figure 5-18: L: the cropped RGB image, R: visual representation of the cropped temperature data.....	125
Figure 5-19: Temperature data before filtering	126
Figure 5-20: Temperature data after filtering	126
Figure 5-21: FEX operational flow chart.....	127
Figure 5-22: Temperature profile in X from a random point in Y.....	128
Figure 5-23: Differentiated data. Orange x marked the detected peaks	129
Figure 5-24: Compiled differentiated data for every pixel line in Y in the cropped image ..	129
Figure 5-25: Original Thermogram showing max and min coordinates outlining edges in the Y direction	130
Figure 5-26: Temperature profile in the X direction (blue), and the Differentiated Data in the X direction showing Max/Min position (orange)	131
Figure 5-27: Compiled differentiated data for every pixel line in X in the cropped image ..	131
Figure 5-28: Cropped thermogram with overlaid X/Y MAX/MIN coordinates.....	132
Figure 5-29: First face X/Y geometric positions	133
Figure 5-30: First view sign convention	134
Figure 5-31: L - 2nd face thermogram, R - 2nd face X/Y coordinates.....	135
Figure 5-32: Second view sign convention.....	136
Figure 5-33: Example of projection courtesy of Engineering Graphics – Solving the intricacies of orthographic projection by A.M. Chandra [69].....	137
Figure 5-34: Visual representation of the projection of the internal structure.....	138
Figure 5-35: Points from the projection planes and their corresponding points in 3D.....	138
Figure 5-36: Squareass.m Process flow diagram	139
Figure 5-37: Complete 3D set compiled from two orthographic projections.....	140
Figure 5-38: Aluminium test artifact	141
Figure 5-39: L - Aluminium artifact at t=55.2s, R - PLA artifact at t=55.2s.....	142
Figure 5-40: Surface temperature profiles from "line 1" in Figure 5-39 at t=55.2s for PLA and aluminium	142
Figure 5-41: Example thermograms from the aluminium heating cycle. Potential edge positions imposed over the top.....	143
Figure 5-42: Surface temperature profile with differentiated temperature data	144

Figure 5-43: CAD model of aluminium artifact showing heating patch and probe edge.....	145
Figure 5-44: L - Resultant thermal model of aluminium artifact at t=40s, R - corresponding surface temperature profile	146
Figure 5-45: Resultant internal edge positions from simulation.....	146
Figure 5-46: External heating set up (artefact moved so heater is visible).....	147
Figure 5-47: Actual surface temperature profiles for T=15,20,25,30s	148
Figure 5-48: Simulated Surface temperature profiles for T=15,20,25,30s	148
Figure 5-49: Differentiated temperature data from Figure 5-47	149
Figure 5-50: Thermogram using external heating at t=30s.....	150
Figure 5-51: Surface temperature profiles from external heating (heater fixed).....	151
Figure 5-52: Differentiated temperature data from.....	151
Figure 5-53: Cuboid artefact.....	152
Figure 5-54: L- Front face, R- Side face.....	153
Figure 5-55: Resultant CPD.....	153
Figure 5-56: Dimension sign convention.....	154
Figure 5-57: Third artefact - Cuboid with L-shaped hollow.....	155
Figure 5-58: Four-perpendicular thermogram representing the four vertical sides.....	155
Figure 5-59: Face 1 feature extraction results.....	156
Figure 5-60: Face 2 feature extraction results.....	156
Figure 5-61: Face 3 feature extraction results.....	157
Figure 5-62: Face 4 feature extraction results.....	157
Figure 5-63: L-shape artefact sign convention for faces 1 and 2.....	158
Figure 5-64: L-shape artefact sign convention for faces 3 and 4.....	158
Figure 5-65: L-Shaped artefact final CPD	160
Figure 5-66: CT scan of L shaped artifact with sign convention.....	161
Figure 5-67: 3 images showing the effect of the coma as the subject is moved around the A35's FOV.....	164
Figure 6-1: TTI front panel.....	174
Figure 6-2: TTI operational flow chart	175
Figure 6-3: TTI after image/data loading and image preparation.....	176
Figure 6-4: Example of an initial frame for the loaded sequence. Images like this will return a NaN value.	177
Figure 6-5: Edge position over time	178
Figure 6-6: Showing the locations of the MAX/MIN location the data set.....	179
Figure 6-7: L- Average surface temperature for frame 400, R- average surface temperature for frame 600	180
Figure 6-8: Circular Test Artefact.....	181
Figure 6-9: Thermogram showing the change in intensity and edge position over time.....	181
Figure 6-10: Results from TTI edge detection for curved artefact showing best fit curved comparison.....	182
Figure 6-11: Addition of exponential curve to peak 1(X1) best fit	183
Figure 6-12: Addition of exponential curve to peak 2 (X2) best fit	183
Figure 6-13: Actual dimensions of circular artifact.....	184
Figure 6-14: Angled planar internal features	185
Figure 6-15: Edge position for angled planar object	186
Figure 6-16: Comparison between circular best fit and angled best fit	187

Figure 7-1: Example of large component edge recovery. All dimensions are in metres.....	203
Figure 7-2: Edge position of large part.....	204
Figure 7-3: Concept of small object thermal scanner.....	205
Figure A-1: Examples of mesh density. LH - 2mm, RH-0.25mm.....	215
Figure A-2: Edge position by varying mesh density.....	215
Figure B-1: Drawing of initial test part.....	217
Figure C-1: Thermal distribution at X=2mm.....	218
Figure C-2: Nodal temperature over time for X=2mm.....	218
Figure C-3: Thermal distribution at X=8mm.....	219
Figure C-4: Nodal temperature over time for X=6mm.....	219
Figure C-5: Thermal distribution at X=14mm.....	220
Figure C-6: Nodal temperature over time for X=16mm.....	220
Figure C-7: Thermal distribution at X=2mm with PLA.....	221
Figure C-8: Nodal temperature over time for X=2mm with PLA.....	221
Figure C-9: Thermal distribution at X=8mm with PLA.....	222
Figure C-10: Nodal temperature over time for X=8mm with PLA.....	222
Figure C-11: Thermal distribution at X=16mm with PLA.....	223
Figure C-12: Nodal temperature over time for X=16mm with PLA.....	223
Figure C-13: Thermal distribution at X=10mm.....	224
Figure C-14: Nodal temperature over time for X=10mm.....	224
Figure C-15: Thermal distribution at X=30mm.....	225
Figure C-16: Nodal temperature over time for X=30mm.....	225
Figure C-17: Thermal distribution at X=60mm.....	226
Figure C-18: Nodal temperature over time for X=60mm.....	226
Figure C-19: Thermal distribution of aluminium.....	227
Figure C-20: Nodal temperature of aluminium over time.....	227
Figure C-21: Thermal distribution of copper.....	228
Figure C-22: Nodal temperature of copper over time.....	228
Figure C-23: Thermal distribution of ceramic.....	229
Figure C-24: Nodal temperature of ceramic over time.....	229
Figure C-25: Thermal distribution of nylon.....	230
Figure C-26: Nodal temperature of nylon over time.....	230
Figure C-27: Thermal distribution of PLA.....	231
Figure C-28: Nodal temperature of PLA over time.....	231
Figure C-29: Thermal distribution of steel.....	232
Figure C-30: Nodal temperature of steel over time.....	232
Figure C-31: Parallel planar - difference between peaks.....	233
Figure C-32: Circular - difference between peaks.....	233
Figure C-33: Angled planar - difference between peaks.....	234
Figure C-34: Side heating thermal distribution 20mm cavity width.....	238
Figure C-35: 20mm internal edge position results.....	238
Figure C-36: Side heating thermal distribution 25mm cavity width.....	239
Figure C-37: 25mm internal edge position results.....	239
Figure C-38: Side heating thermal distribution 30mm cavity width.....	240
Figure C-39: 30mm internal edge position results.....	240
Figure C-40: Side heating thermal distribution 35mm cavity width.....	241

Figure C-41: 35mm internal edge position results.....	241
Figure C-42: Side heating thermal distribution 40mm cavity width	242
Figure C-43: 40mm internal edge position results.....	242
Figure C-44: Side heating thermal distribution 45mm cavity width	243
Figure C-45: 45mm internal edge position results.....	243
Figure C-46: Side heating thermal distribution 50mm cavity width	244
Figure C-47: 50mm internal edge position results.....	244
Figure C-48: Side heating thermal distribution 55mm cavity width	245
Figure C-49: 55mm internal edge position results.....	245
Figure C-50: Side heating thermal distribution 60mm cavity width	246
Figure C-51: 60mm internal edge position results.....	246
Figure C-52: Thermal distribution, external heating, PLA, t=1200s.....	247
Figure C-53: Temperature profile from probe edge t=1200s.....	247
Figure C-54: (L) nodal temperature over time, (R) differentiated temperature data at t=1200s	248
Figure C-55: Thermal distribution, external heating, PLA, t=2400s.....	248
Figure C-56: Temperature profile from probe edge t=2400s.....	249
Figure C-57: (L) nodal temperature over time, (R) differentiated temperature data at t=2400s	249
Figure C-58: Thermal distribution, external heating, PLA, t=4800s.....	250
Figure C-59: Temperature profile from probe edge t=4800s.....	250
Figure C-60: (L) nodal temperature over time, (R) differentiated temperature data at t=4800s	251
Figure C-61: Thermal distribution, external heating, PLA, t=9600s.....	251
Figure C-62: Temperature profile from probe edge t=9600s.....	252
Figure C-63: (L) nodal temperature over time, (R) differentiated temperature data at t=9600s	252
Figure C-64: 160s artefact simulation - nodal temperature	253
Figure C-65: 160s artefact simulation - edge position.....	253
Figure D-1: Romer Absolute 7525 Arm with RS3 laser line scanner	254
Figure D-2: External scanning of artefact.....	255
Figure D-3: Captured external CPD of artefact	256
Figure D-4: Out-liars separated from the main bulk of the primary.....	257
Figure D-5: Final Sampled CPD - The red areas indicate additional out-liars that require deletion.....	258
Figure D-6: Initial TTM after wrapping	259
Figure D-7: Region subdivision of the TTM	261
Figure D-8: Placement curve lines and their extensions.....	262
Figure D-9: Final sharpened TTM.....	262
Figure E-1: PCD of Square artifact.....	263
Figure E-2: PCD of rectangular artifact.....	264
Figure E-3: PCD of Cylinder artifact.....	265
Figure E-4: PCD of Angled artifact	266
Figure E-5: PCD of L-shaped artifact.....	267
Figure E-6: Sign convention of aluminium artifact	268
Figure F-1: Cropped Monotone Thermogram	269

Figure F-2: Results from applied edge detection algorithm. From left to right: Canny, Sobel, Prewitt, Roberts.....	270
Figure F-3: L-R Canny method at 0.01, 0.5, 0.99, sensitivity threshold values	271
Figure F-4: L-R Sobel method at 0.01, 0.5, 0.99, sensitivity threshold values	271
Figure F-5: L-R Prewitt method at 0.01, 0.5, 0.99, sensitivity threshold values	271
Figure F-6: L-R Roberts method at 0.01, 0.5, 0.99, sensitivity threshold values	272
Figure F-7: Canny method with 0.49 threshold	272
Figure F-8: Canny method with 0.6 threshold	273
Figure F-9: Positional results from Canny method with 0.6 threshold.....	273
Figure G-1: Imported internal CPD	275
Figure G-2: Assigning planes to individual faces.....	276
Figure G-3: Planes representing inside mesh after tessellation.	276
Figure G-4: L - Internal TTM after cropping, R - Section view of the new merged TTM ...	277
Figure G-5: TTM broken down into separate boundary regions	278
Figure G-6: L - Deviation colour map for fitted surfaces	279
Figure G-7: Section view of the stitched model	280
Figure I-1: Curve fitting for peak 1 of circulate profile.....	301
Figure I-2: Curve fitting for peak 2 of circulate profile.....	301
Figure I-3: Curve fitting for peak 1 of angled profile.....	302
Figure I-4: Curve fitting for peak 1 of angled profile.....	302
Figure I-5: Exponential curve extension from best-fit curve from peak 1	303
Figure I-6: Exponential curve extension from best-fit curve from peak 2	303
Figure J-1: L - Horizontal edges, R - vertical edges for run 1	304
Figure J-2: L - Horizontal edges, R - vertical edges for run 2	304
Figure J-3: L - Horizontal edges, R - vertical edges for run 3	305
Figure J-4: L - Horizontal edges, R - vertical edges for run 4	305
Figure J-5: L - Horizontal edges, R - vertical edges for run 5	306
Figure K-1: L - Vertical edges 1, C - Vertical edges 2, R - Horizontal edges for run 1	307
Figure K-2: Vertical edges 1, C - Vertical edges 2, R - Horizontal edges for run 2.....	307
Figure K-3: Vertical edges 1, C - Vertical edges 2, R - Horizontal edges for run 3.....	307
Figure K-4: Vertical edges 1, C - Vertical edges 2, R - Horizontal edges for run 4.....	308
Figure K-5: Vertical edges 1, C - Vertical edges 2, R - Horizontal edges for run 5.....	308
Figure L-1: Horizontal edges, R - vertical edges for run 1	309
Figure L-2: Horizontal edges, R - vertical edges for run 2	309
Figure L-3: Horizontal edges, R - vertical edges for run 3.....	309
Figure L-4: Horizontal edges, R - vertical edges for run 4.....	310
Figure L-5: Horizontal edges, R - vertical edges for run 5.....	310

List of Tables

Table 2-1: Summery of XCT literature review	40
Table 2-2: Summery of IRT/PIDV literary review	42
Table 3-1: Components of FEA sim design.....	50
Table 3-2: Components for physical validation.....	53
Table 4-1: Initial boundary conditions.....	60
Table 4-2: Thermal properties of PLA.....	69
Table 4-3: Materials and their thermal properties.....	76
Table 4-4: Standard deviation of temporal results	81
Table 4-5: Table showing comparative results from side heat simulations with change in width	90
Table 4-6: PLA Material properties and dimensions	94
Table 4-7: Boundary conditions for thermomechanical simulation	103
Table 4-8: Additional mechanical properties for PLA	103
Table 5-1: Test artefact material properties and dimensions	110
Table 5-2: Dimensional results for square artifact PCD as seen in Figure 5-3.....	112
Table 5-3: FLIR A655SC with 25° FOV 24.6mm Specifications	119
Table 5-4: First view geometric results	134
Table 5-5: Second view geometric results	136
Table 5-6: Recovered results from aluminium artifact with false positive error	143
Table 5-7: Recovered results from aluminium artifact without false positive error	144
Table 5-8: Cuboid artifact geometric results	154
Table 5-9: Geometric results for L shaped artifact	159
Table 5-10: Accuracy and repeatability results from square artifact	160
Table 5-11: Accuracy and repeatability results from the L shaped artifact	162
Table 5-12: A35 Specifications (Specifications for A255SC for comparison)	163
Table 5-13: Accuracy and repeatability results from using the A35	164
Table 6-1: MAX/MIN/MEAN Results for square artefact	178
Table 6-2: Circular artifact geometric results	184
Table C-1: Numerical results for cavity comparison	234
Table D-1: Romer arm and RS3 specifications	255
Table E-1: Square Artifact result	263
Table E-2: Rectangular Artifact result	264
Table E-3: Cylinder Artifact result	265
Table E-4: Angled Artifact result	266
Table E-5: L-shaped Artifact result	267
Table E-6: Aluminium artifact results	268

Abbreviations

- 3D – 3 Dimensional
- AM – Additive manufacture
- AV – Average
- CAD - Computer Aided Design
- CPD – Cloud Point Data
- CT – Computerised Tomography
- Err - Error
- FEA – Finite Element Analysis
- FEX – Feature Extraction Algorithm
- FOV – Field of View
- Gr – Grey
- IRT – Infrared Thermography
- MRI – Magnetic Resonance Imaging.
- NURBS - Non-Uniform Rational B-Spline
- OP – Orthographic Projections
- PLA – Polylactic Acid
- POP - Plane of Projection
- RE - Reverse Engineering
- RGB – Red green Blue
- SLS – Structured Light Scanning
- Stdev – Standard Deviation
- TOF – Time-of-Flight
- TTM – Tessellated Triangular Mesh

- TTI – Timer thermal imagery

Symbols

°C - Degree centigrade

Gr – Grey

j – Joules

k – Kelvin

Kg – Kilogram

m - Meter

Pi – Pixel

s – Second

T – temperature

t – time

W - Watt

α – Absorptivity

ε – Emissivity

Chapter 1. Introduction

In this chapter, the focus of this investigation is introduced, and a general overview is presented. Also, outlined in this chapter is the thesis structure, detailing the contents of all additional chapters.

1.1. Overview

Inspection and dimensional validation (PIDV) of manufactured engineering components or products is an important stage of the manufacturing process. In manufacturing, such a component, part or product is referred to as the workpiece [1] and the inspection of which ensures conformity to the customer requirements, and traceability as part of the manufacturing process.

The concept of part inspection is as old as the manufacturing process itself, as the state of the final product has always needed to be known.

Whether measuring a part as part of an in-line inspection cycle, or when performing the final part inspection, the process and objective is the same; to capture dimensional information. Today, there are multitudes of different metrology devices available for the measurement of objects, from simple callipers and micrometres to high accuracy coordinated measure machines (CMM) and optical scanners. The choice of measurement device usually depends on the complexity of the part under scrutiny and accuracy requirements. Simple geometric shapes can have their dimensions recovered easily using simple tactile means. More complex geometric shapes, or parts with large dimensions may require the use of a CMM for ease of capture. Parts whose geometry is comprised of free-form surfaces can be captured using the same techniques

however, it is considerably more complex and time consuming. These Parts generally have their dimensions recovered by non-contact optical techniques.

One main challenge that persists in PIDV regardless of capture technique is the recovery of internal feature geometry. This issue has now been further highlighted by the advent of new additive manufacturing technologies.

For a designed component undergoing traditional subtractive manufacturing processes, internal PIDV should not be an issue as during the design phase it will be considered whether the internal structure needs to be inspected and allowances made if necessary. However, additive manufacture now offers designers new versatilities in part design that until now were physically impossible to produce, especially in the areas of internal structure. Parts with internal structures and complex voids, that would otherwise be impossible to machine in subtractive terms can now be easily produced.

However, these new manufacturing techniques present a new problem with respect to the PIDV of these potential complex internal structures. This problem is mainly due to the limitations of the metrology equipment currently available to most manufactures.

Currently using CMM's to capture internal data is a possibility but the CMM probe may not have the length to reach all the features (see Figure 1-1). Another common problem is a feature with larger dimensions may only be accessible through a connecting feature with a smaller set of dimensions. This will block the probe from contacting the larger features, shown in Figure 1-2.

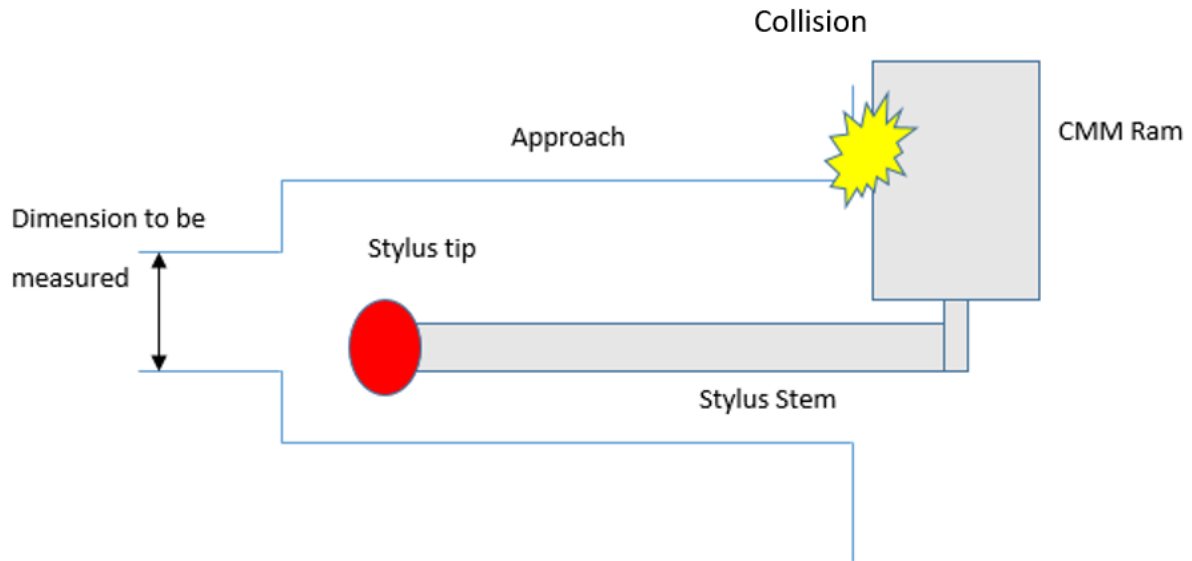


Figure 1-1: CMM unable to reach target Dimension

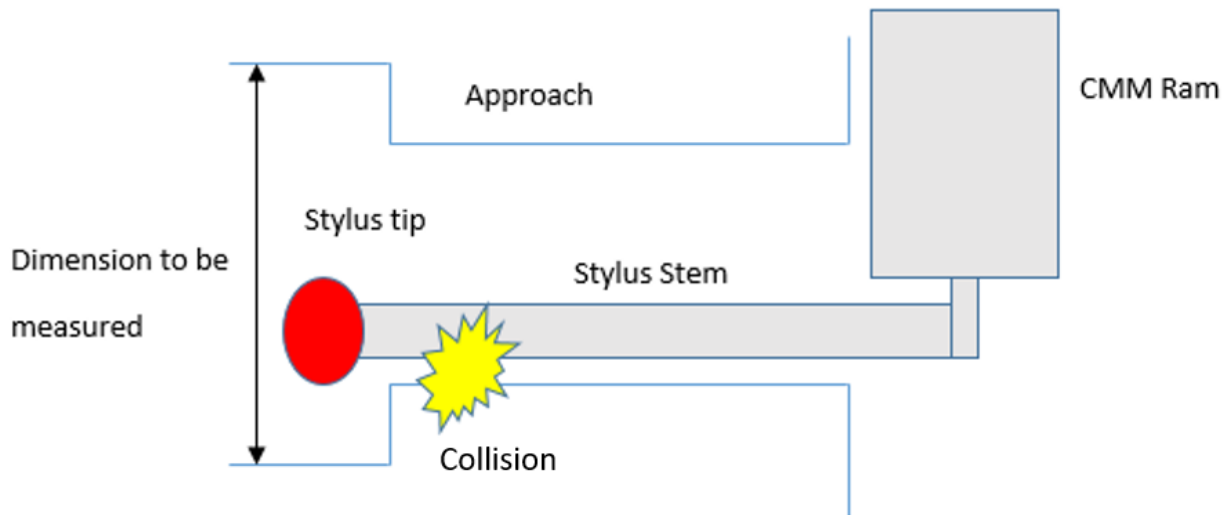


Figure 1-2: CMM unable to reach internal feature

Optical systems suffer from a similar potential issue. Active optical systems generally work on the principle of emitting light, which interacts with the object under scrutiny. The light emitted at a specific angle with respect to the object. The light hits the object and is reflected back to a receiver at the same angle it was emitted. This is shown in Figure 1-3.

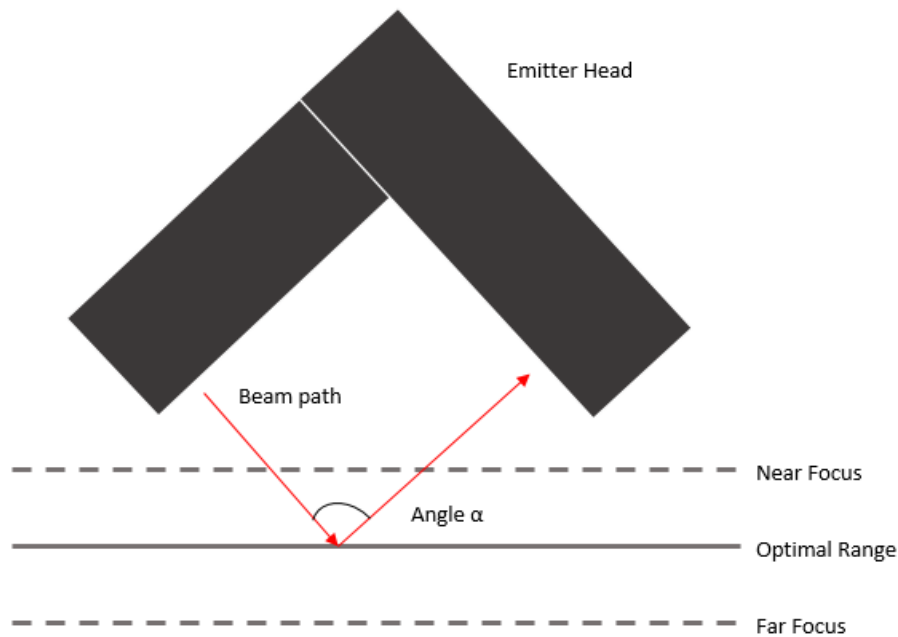


Figure 1-3: Generalized View of an Active Optical System

However, problems with this kind of system start to occur when attempting to capture internal features, such as bores, or features with sharp concave corners. This occurs because the geometry of features may consist of angles that are smaller than the emitter/receiver angle, shown in Figure 1-3 as α . If a feature has a smaller angle than α , the beam cannot complete its path from emitter to feature to receiver. This can lead to incomplete data recovery, sometimes called missing data error, which is a common issue with parts that have complex geometry or have been subjected to an imperfect scanning procedure [2]. With concave edges, this problem can be overcome by re-orientating the scanner head with respect to the feature in question in order to change the viewing angle. However, this approach would not be applicable when trying to capture bores, deep recesses, and internal geometry. When using a laser scanner to capture bores or deep recesses, one might find the same problem when scanning edges, yet this cannot be overcome by any amount of re-orientation of the scanner head. The bore might be too deep for the optimal range of the scanner, or the diameter may be too small, stopping the emitted beam from returning.

Whether or not a tactile probe or optical scanner can capture data from shallow bores or relatively sharp corners is academic if the object in question has a structure consisting of closed off or sealed internal features because there is no physical access.

This is a common problem with respect to traditional cast parts, and this same problem will potentially be present with additively manufactured parts.

Cast parts such as engine blocks or turbo charger casings, shown in Figure 1-4, can have complex internal geometries. By design, these internal structures may not need to be inspected so do not need to be reached by inspection tools. From the initial design and manufacture point of view this might be acceptable, however if dimensional validation is required at a later stage, for example, if the part is not operating optimally, problem will arise. In addition to dimensional validation, there is also the potential need to validate the internal structure visually. As said additive manufacture allows designs to incorporate new design aspects in manufactured parts. This may include internal webbing and supports that whilst do not need to be dimensionally validated, may be critical to load distribution etc. Therefore, it may be necessary to ascertain that these features have survived the printing process and have not collapsed or deformed.

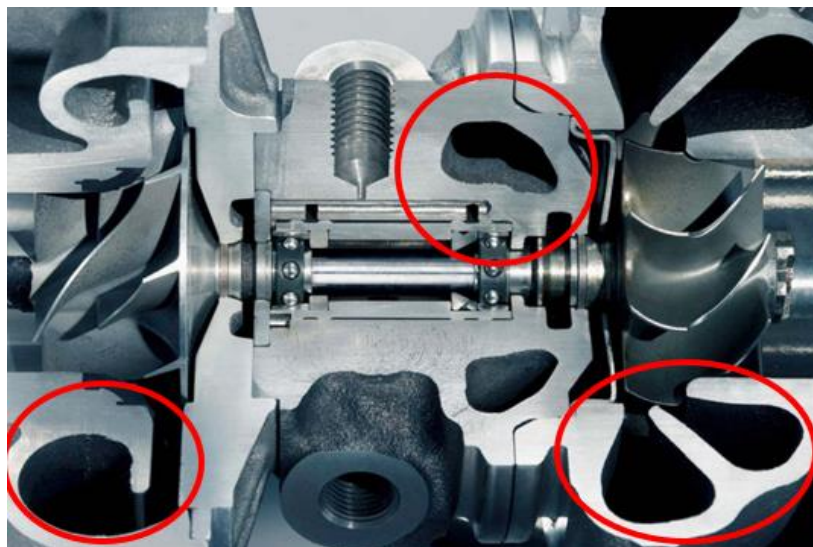


Figure 1-4: Cross section of a turbo charger showing cast internal structures.

At this stage, there are two potential ways to preform PIVD or internal visual inspections on objects of this nature; the first would be to incorporate the use of a more complex recovery system, for example, a Magnetic Resonance Imaging (MRI) scanner, or X-ray Computed Tomography (CT) scanning. The second would be to employ destructive techniques, such as bisecting the part in question, to access the internal features so that they can be measured by means that are more traditional. However, if the exercise is to inspect the component, then have it resume its operation, destroying it to measure it would not be the best approach. Destructive techniques might be a potential option in batch production where one component can be sacrificed for inspection purposes, but if destructive techniques are indeed not suitable, the only existing options for recovering the geometric data from internal features is the use of one of the more complex techniques previously mentioned, such as CT scanning.

Magnetic, X-ray, and acoustic techniques in the form of MRI scanners, CT scanners, and Ultrasound scanners have the ability to “look into” an object and are discussed in further detail in Chapter 2. Whilst these devices can recover the internal geometry of an object, this ability comes at a price that may preclude their use in some scenarios. Again, the positives and negatives of these devices are illustrated in detail in Chapter 2; but they can be very expensive to acquire and operate, can be limited in scope in terms of material and size of object they can measure, and can have complex operational requirements with respect to power and training requirements.

Therefore, given the limitations of traditional tactile and optical data capture methods, and the requirements and scope of the current possible alternatives, this investigation focuses on a new method for obtaining information about complex internal geometry.

This new idea investigates using a combination of infrared thermography (IRT) and a form of parallel projection to deduce the geometry of an internal structure. In principle, any object

hotter than absolute zero will emit radiation. The intensity and spectral composition of the emitted radiation is determined by the temperature and thermal properties of the radiating material. This radiated emission can be remotely sensed and captured to determine the radiant temperature of an object [3]. This practice is generally called thermography. Determined by the laws of conduction heat will also flow from hot to cold, so in theory heated internal features that have temperatures that are higher than the surrounding surfaces will see a conduction of heat towards those cooler surfaces. Once the heat flow reaches the surface of a part, the change in temperature will cause the objects emitted radiation to change, which in turn can be captured by an IR camera. Due to the temperature differential between the hotter internal features and the cooler material between them, the captured data will show the shape of the internal structure in a single 2D plane. However, this practice alone would not be enough to recreate the internal structure of an object spatially.

As with CT scanning, where multiple X-ray measurements are taken from different angles, this system will also require an indexable rotation of the part to acquire multiple thermograms to ensure a complete 3D rendition of an object internal geometry. By using a form of projection, a second and possibly third set of data taken from two separate perpendicular views will be needed to complete the data set and show all 3D spatial data of the internal geometry.

Parallel projection is a style of graphical projection mainly used in mechanical design and is a way of representing a 3D object through the projection of several 2D views (shown in Figure 1-5 is orthographic projection, a dependant projection form of parallel projection). Whilst this is the most common way of using parallel projection, the technique discussed here will use it in reverse to generate 3D objects from several 2D views. In addition to this, traditional parallel, and in particular orthographic projection, utilises three separate views (as shown below). This proposed technique for internal data capture may not use all three separate views, but for the purposes of this thesis will still be referred to as parallel projection.

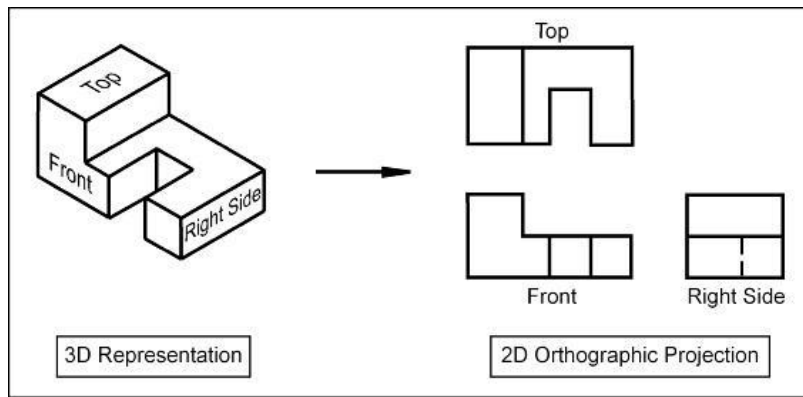


Figure 1-5: Example of Orthographic Projection

This principle of taking several views of an object to create one 3D entity can be combined with the proposed principles of thermographic capture. If one takes several thermograms of an object that has been subjected to internal heat generation, combines them together through the principles of parallel projection, the result will show the complete internal structure of an object from which geometric information can be deduced.

1.2. Thesis Structure

- Chapter 1: Introduction

Chapter 1 of thesis outlines the rationale behind this thesis. This chapter details the need for PIDV of internal structures and current limitations that exist in acquiring them.

- Chapter 2: Literature review

The literature review is split into two main areas. The first details the context of PIDV and focuses on the current solutions available for the PIDV of internal structures, chief amongst which is XCT. The use of XCT for internal measurement is discussed here, including several of the issues currently associated with using XCT in the manner. The second part of this literature review will look at areas in which thermography and metrology have been previously combined. This will ensure the novelty of this work but also help identify areas that can be built upon to further this research.

- Chapter 3: Motivation, aim, objectives, scope, and methodology

Chapter 3 details the motivation behind this research based upon the findings from the literature review. It goes on to then outline the aim, objectives, and the scope of this project. Finally, the main methodology detailing how this work will be performed is then presented.

- Chapter 4: Preliminary FEA analysis and results

Chapter 4 provides the details, results, and discussion of preliminary Finite Element Analysis (FEA) simulations used to confirm the feasibility of the proposed approach. The FEA is used to ensure that heat conduction from an internal cavity to the surrounding external surfaces can be observed, and that temperature profiles from which geometric features can be deduced are observable. Chapter 4 also details how internal edge position is affected by different boundary conditions, such as, thermal conductivity, depth and geometry of cavity, and heating techniques.

- Chapter 5: Experimental Investigation

The main investigative part of this thesis is presented in chapter 5. In this chapter, the following is discussed:

- The techniques used to capture and digitise the external features of an object.
- The algorithm used to detect and extrapolate the internal geometry of the same object in 2D, as well as filtering and edge detection techniques.
- The capture of internal dimensions of artifacts with differing internal structures and materials.
- The accuracy and repeatability of this proof-of-concept system
- The use of projection to discern and observe the internal geometry in 3D

- The amalgamation of both the internal and external data sets into a single usable 3D object.

This chapter also discusses several differing examples using the afore mentioned techniques.

- Chapter 6: TTI - Timed thermal imagery

Chapter 6 explains the evolution of the software developed in chapter 5 into a system that can track the drift of an edge position results, detected through a series of thermal images. It explains how temporally tracking edge position results can be used to better estimate the geometry of an objects internal structure. Curved and angled edge recovery is assessed as a case study for using this enhanced extraction software.

- Chapter 7: Conclusions and future work

This chapter provides a summary of the research and how the aim and objectives set forth in Chapter 3 have been met. It then goes on to draw the main conclusions from the work and states the contributions to knowledge that this research has provided. Several areas requiring further study that has arisen from this work are also presented here.

Chapter 2. Literature Review

In this chapter a literature review of the current methods available for the inspection of workpiece internal features is presented. This review also highlights the issues connected with these current methods, and how those issues present a problem for modern industrial metrology.

In addition, this review also assesses previous work that has been performed in the combined area of metrology and thermal imagery, and to verify if these two subject areas have been used in conjunction before with respect to internal feature PIDV.

This chapter is split into five main sections. The first introduces the area of part inspection and dimensional validation. The second section of this review will look at the current solutions to internal feature PIDV, and their limitations. Section three is added because infrared thermography or ‘thermal imaging’ is not normally associated with PIDV therefore this section starts by introducing the subject area of infrared thermography, thermal imagery, and its applications before reviewing how thermography and metrology are currently used in conjunction. The fourth section of this review discusses areas of interest where thermal imagery and metrology have been combined, to either resolve geometric dimensions or use thermal imagery as a form of thermal overlay on 3D models. The fifth section will then summarise the findings from the previous four sections.

2.1. Introduction to part inspection and dimensional validation

This first section will briefly introduce inspection and dimensional validation, the need behind it and some of the data acquisition methods currently available to perform part inspection.

Part inspection and dimensional validation (PIDV) is a critical part of the manufacturing process, ensuring design verification and conformity, quality control and traceability

throughout the manufacturing process. In manufacturing, maintaining a robust inspection system can ensure the quality of the end product and can have an effect on production costs as the impact of rework is potentially reduced.

Typically speaking, the act of PIDV involves the taking of measurements from a manufactured article and comparing those measurements to a known set of nominal dimensions, as set out by the designer.

Today, depending on the part complexity and the accuracy of the required inspection there are a multitude of inspection data acquisition techniques available to perform dimensional validation. Figure 2-1 shows a collection of tactile and non-contact data acquisition techniques currently available for performing dimensional validation.

The data acquisition methods shown in Figure 2-1, between them can deal with most industry inspection requirements. This can in part be attributed to designers' attitude towards the manufacturing process and the subsequent required inspection. Today the majority of manufacture is still performed by subtractive means, meaning that designers need to understand the practicalities and limitations when designing parts for these production methods. Features on components produced by subtractive methods, quite often can be easily inspected as the physical approach and direction used in manufacturing them can be utilised during inspection.

Even for subtractive manufactured components with internal features, inspection should still be possible as if a cutting tool can make the internal feature, an inspection system should be able to reach the same feature. In addition, designers can also make allowances in the component design to allow for inspection if necessary.

However, problems arise when trying to use the same inspection techniques and data acquisition methods on parts produced by additive means.

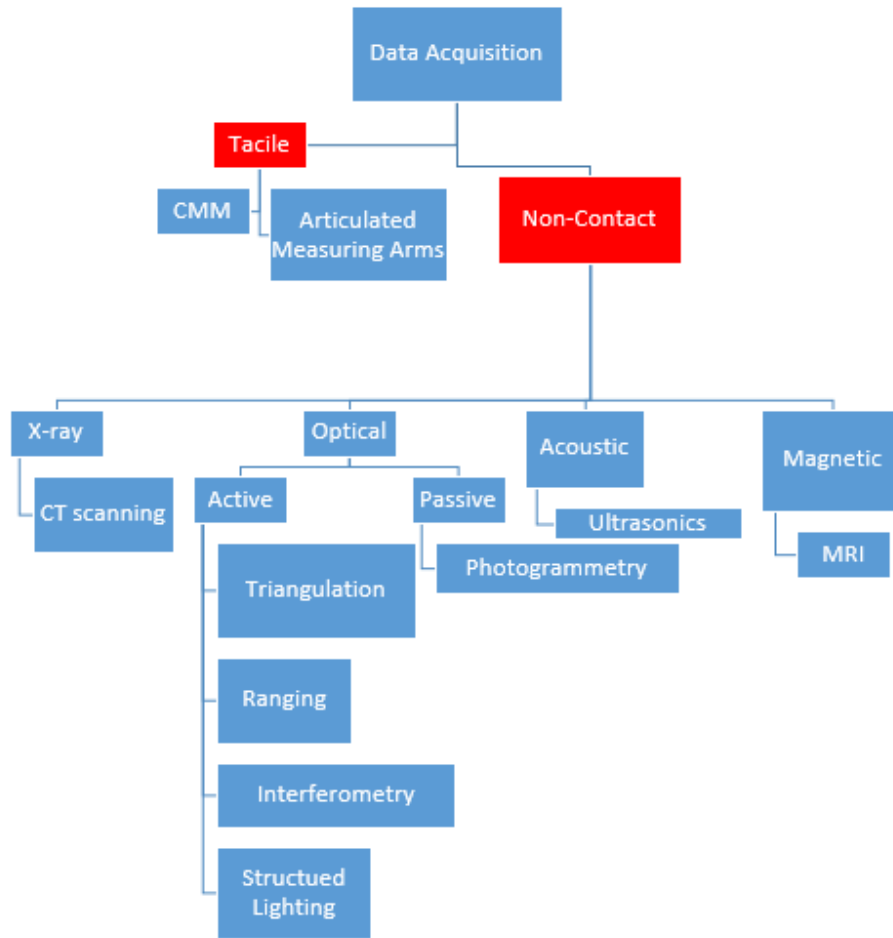


Figure 2-1: Data acquisition methods

Over the last two decades additive manufacture (AM) has become more and more integrated in terms of it being a mainstream manufacturing method. Initially considered as an esoteric tool limited to specific applications and industries [4], the advent of more affordable machines and a drive within manufacturing to utilise this technology has seen it become a more prominent fixture within the manufacturing sector.

Unlike traditional subtractive manufacturing, which involves the removal of material from stock or a billet, AM, as the name suggests, “builds” up the component layer by layer. This can be performed by several different methods, fused deposition modelling (FDM), selective laser sintering (SLS), and stereolithography (SLA), to name a few [5].

In contrast to subtractive methods, which can require, fixturing and tooling, thus constraining the design process, AM, with this layer-by-layer approach can in theory create any complex shape or topology [6]. This approach to design is further enhanced by the ease of which internal features can be incorporated into component design. At this point internal features can be broken down into two separate categories: 1, specific internal features with a direct purpose, such as internal conduits and cavities, and 2, infill lattices for support.

Looking at the first category: specific internal features, AM allows for a much more optimal placement of internal features, without the need to consider external tooling or tooling reach etc. The second category: infill lattices, is a procedure that has come about with the advent of AM. Infill lattices or other internal cellular structures, allow for production of lightweight parts without reducing the parts nominal mechanical properties. That said, these internal structures can also be optimised to ensure a specific part stiffness or directional strength [7].

However, this advancement in design and manufacturing versatility, comes at the cost of ways to perform typical quality assurance, especially with respect to internal features. Typical tactile and optical techniques do not have the reach or the field of view to perform PIDV on these potentially complex or sealed internal features. Whilst there are methods and techniques to provide quality assurance, which will be covered in detail in the next section, *Everton et al* [8] state that this lack in established quality assurance, especially in the area of in-situ metrology is possibly the biggest technological barrier in allowing AM to become a more mainstream practice in manufacturing.

PIDV is essential in any manufacturing quality control process, and AM parts are not exempt from this. Arguably PIDV is even more critical in AM parts, as not only is dimensional data required to validate the design. If the design is utilising a cellular structure to provide internal

support or stiffness, additional validation may be needed to ascertain that this structure is correct and has not failed during the manufacturing process.

2.2. Internal Part measurement

As previously mentioned, there are other techniques utilised by PIDV that are more suitable for the extraction of internal data. X-ray Computerised tomography (CT), ultrasonic scanning, and magnetic resonance imaging (MRI) are three of the more specialised forms of data acquisition. One advantage these methods have over optical and tactile alternatives is the ability to penetrate an object to reveal and measure internal features and cavities. Whilst they may have the ability to penetrate the solid outer shell of an object to reveal the internal structure, these systems are not without issue. The following literary review section will look at the three above mentioned data capture techniques, reviewing their data capture methods, limitations, and suitability when used with respect to PIDV of internal features of additively manufactured parts.

2.2.1. X-ray Computerised Tomography (CT) Scanning

X-ray Computerized Tomography, more commonly referred to as CT scanning, is a scanning technique that employs the use of high energy X-rays. In industrial CT scanners, the system consists of an X-ray tube and an in-line detector, located in either side of the object under investigation. The object is then rotated allowing for the capture of multi-directional radiograms [9]. This layout is slightly different in medical grade CT scanners where the X-ray tube and detector rotate around the subject [10]. Each radiogram or projection is the same as a single X-ray; with rotation, enabling the object to be viewed from any point in a minimum of a 180° field of view. Each projection consists of hundreds of line integrals that, depending on the intensity of the exposure, determine the depth of the projection. This builds up a complete representation of the object in three dimensions at multiple depths. The number of projection

and line integrals the object is subjected to, and the exposure time dictates image clarity and therefore accuracy. Modern clinical CT scanners will now take around a thousand projections, each consisting of several hundred-line integrals, through a full 360° field of view, to maximise the clarity of the resultant radiogram [11]. Even though the main area of usage for CT scanning has been in the medical world, it does have a growing presence in other disciplines, particularly for inspection purposes in manufacturing which has benefitted from increased performance in the machines as well as ongoing research into performance evaluation and industrial metrology. Industrial CT scanning differs from typical CT scanning found in hospitals due to the objects being scanned. Medical CT scanners can scan medium to large objects, such as humans and large animals, because organic matter can be thought of as having a low attenuation coefficient. The attenuation coefficient of a material is related to how X-rays propagate through said material in terms of absorption and scattering. Metallic materials generally have high attenuation coefficients and as such require higher photon energy leading to higher drive voltages than their medical counterparts. Medical CT scanners normally operate in the range of 120-130KV, whilst their industrial counterparts start at 225KV [12]. This higher attenuation coefficient in metallic objects also limits the size of the object an industrial CT scanner is able to accept. If an objects size is increased but the power level of the scanner remains the same, the X-ray photons will not be able to penetrate through the object before photoelectric absorption occurs, which in turn leads to electron scattering. If a response is recorded in the detector, these additional electrons, ejected by proton impacts, will be observed as noise leading to inaccurate results [13]. To overcome this problem the photon energy would have to be increased. However, this would lead to higher electrical requirements and higher levels in ionizing radiation. As a result, industrial CT scanners are normally suited to small to medium sized objects so that drive voltages can be kept relatively low. CT scanners are currently the only technology presently available to measure the internal geometry of an object without

destroying it. As a metrology tool, CT scanners can provide a comprehensive 3D representation of an entire object. *Kruth et al* [14] provides an in-depth review of the use of CT scanners in dimensional metrology. In this, they highlight some of the distinctive issues that must be understood in order to obtain accurate results from CT scanning. As mentioned, a complete 3D CT scan consists of multiple 2D radiograms taken in a rotational pattern. The accuracy of the full 3D scan can be broken down into two main areas: the accuracy of the 2D radiogram, and the accuracy of the reconstructed 3D model. 2D radiograms can be affected by, but not limited to, photon energy, X-ray flux, beam hardening, and as mentioned above, attenuation and scatter. Errors in the 3D reconstruction process can be related to the accuracy of the CT's kinematics, magnitude of rotational increments, and the reconstruction algorithm itself, to name a few.

Whilst a number of factors, many of which are unique to CT scanning, can affect accuracy *Hiller et al* [15], with the use of a calibrated ball-bar reference length have obtained 3D generated models with a measurement uncertainty between $6.9\mu\text{m} - 1\mu\text{m}$.

Whilst it can be stated that CT scanners, within the environment of industrial metrology, can be a versatile tool, capable of recovering geometric dimensions from both internal and external features to within a high level of accuracy, there are some significant considerations that may preclude their use for many applications and users. The initial outlay for a typical XCT scanner used for small to medium cast parts can be in the order of £500,000 (at the time of writing this thesis), with higher prices for larger measurement volume or higher power. The type of material an object is made from can also dictate what type of CT scanner has to be used. Denser materials will require higher energy levels to penetrate the object all the way through. This in turn will normally lead to industrial electrical requirements that can then be an added expense for installation. This requirement also leads to CT scanners having small scan volumes, as large volumes would require additional energy requirements. For example, Carl Zeiss Volumax

F1500, can scan objects unhindered to a maximum height (H) and diameter (D) of 430 by 800mm. These values can be increase to 1100mm for height and 700mm for dimeter at the loss of certain measurement capabilities and axis travel restrictions [16]. That said the values mentioned above offer insight into the volumetric size of the measurement chamber. The actual measurement range is much less for a complete 3D scan of an object. The Volumax's nominal measurement range is only 260mm (H) and 305 (D).

However, with the introduction of additive manufacture, XCT in metrology is becoming a more attractive method concerning inspection. *Moroni et al* [17], describe how the introduction of additive manufacture has led to the increase in the production of more geometrically complex parts. As a result, inspection of such parts has become more challenging. They place XCT as the most viable solution for the inspection and the geometric verification of such complex parts, also stating that as a volumetric scanning system it can also take into account the internal structure. They also define some considerations that designers should consider to reduce errors in XCT geometric results. Sharp edges should be avoided as they can increase the amount of X-ray scatter, causing a loss in resolution. Different materials in a single part should be avoided, as different materials have different X-ray absorption rates. This can lead to poor results through bad propagation for a denser material, if the XCT scanner is set to scan less dense materials; and if the XCT scanner is set to scan a dense material with will cause beam hardening on the less dense material. This makes finding a balance that works for both materials more difficult. They also discuss the issue of XCT penetration depth, and that wherever possible designers should reduce part thickness. They show that for steel, even a 225KV scanner can only penetrate a depth of up to a maximum of 40mm.

Aloisi et al [18] also detail how a component's surface finish can increase the uncertainty on recovered CT dimensional measurements. In their work they compare the dimensional results of three steel SLS printed tubes, with a specified surface finish value of 125 μ m. The CT

measurements were compared to reference measurements taken using a tactile CMM. Their work shows external diameters measured by the CT were always smaller than the same external diameters measured by the CMM. Conversely internal diameters measured by the CT were always larger than the measured values from the CMM. In both cases the difference in values from the and CT and the CMM were always approximate to the surface finish value over two. They determine that this difference in systematic error between the CT result and the calibrated CMM result is due to the different measuring principles in which the CT and the CMM rely on, and how dimensional results are established from the recovered data when uncertainties such as surface finish are taken into account within the two systems.

Landis et al [19] offer a comprehensive review of X-ray microtomography, describing it as a versatile non-destructive tool, capable of micron level spatial resolution. However, they summarise that as a metrology tool this system is not without its own specific limitations. These limitations encompass, X-ray penetration with respect to material density and sample size, X-ray absorption for materials with different phases, leading to poor contrast in the recovered result, and the free availability of such facilities. These findings are in keeping with the conclusions of *Moroni et al* [17].

The work by *Thompson et al* [20] show how XCT tomography has evolved to be well placed for the PIDV of AM parts. They show how today XCT is used in a variety of differing fields including reverse engineering for the AM of historic cultural artifacts, as well as density and porosity measurements. They also highlight that for dimensional validation against nominal CAD models, XCT is fast becoming the dimensional metrology tool of choice with regards to AM parts, due to the impracticality of traditional methods, and at the time of publication, XCT was the sole industrially viable method for gaining internal data without destroying the part. However, they do highlight the same issues as before with using XCT for dimensional measurement. They state that X-ray penetration variation with respect to part aspect ratio is a

difficult scenario for XCT metrology. Higher powered x rays are needed to penetrate the parts long axis, whilst for the short axis the x ray intensity will needed to avoid scatter and reduce overexposure in the recovered image. They also state that beam hardening can have an effect of surface determination and location. This beam hardening effect can create an artificial offset on the internal surface edges, with respect to the external edges. This presents a huge issue with regards to the examination of internal surfaces.

Previously mentioned, beam hardening is related to the non-linearity of the X-ray attenuation as the beam propagates though the part under scrutiny. Low energy X-rays attenuate much faster than high energy ones. This leads to the number of photons striking the detector to also be non-linear. However, most of the reconstruction algorithms used in XCT assume linear attenuation, leading to false assumptions that the part “skin” is made from a denser material than it actually should be. This in turn can lead to poor image quality, critical for accurate edge detection, and thus dimensional metrology. To counter this effect numerous beam hardening correction algorithms have been presented. These algorithms have been examined by *Dewulf et al* [21]. Their work shows that the inclusion of these corrective algorithms can indeed increase image and quality and the absolute accuracy of an XCT machine. However, for multi-feature parts these corrective algorithms can have a detrimental effect. They observed, when using these corrective algorithms, sudden shifts in the dimensional results when the external geometry of the part changed. Whilst stating this is not a complete comprehensive understanding of this phenomena, for dimensional metrology this issue is a huge drawback for XCT.

Work by *De Chiffre et al* [22] gives an overview of the industrial applications of XCT, and how the technology is slowly advancing within the industry. As with other work reviewed, they highlight the benefits of this technology; non-destructive, internal feature data extraction, and the holistic gathering of all artifact information. However, they also highlight the complex

issues and in-depth user understanding (already mention in this section) that is necessary to perform meaningful dimensional measurement with an XCT machine. They also highlight some of the more mundane, yet critical aspects of the use of XCT in the industrial area. One that is a probable concern for industrial applications is the takes to perform a complete inspection of a part. Their work shows that XCT can take nearly four times longer than a traditional CMM to perform a complete part inspection. That said, if the part does have internal features that require inspection XCT might be the only option. This work also provides a brief introduction to X-ray dosage with respect to industrial XCT, which in this work, up to this point has been difficult to quantify outside of medical applications. They state that with adequate shielding, exposure to CT operators, is extremely small if not negatable. However, high energy X-rays can have detrimental effects on the compositions of certain polymers, such as PLA, PVC, and PAN. It has been found that prolonged exposure (>15 mins) to high intensity X-rays, can affect the polymers material properties, for example, causing brittleness and that these decomposition effects can influence the recovered data, and therefore need to be taken into account during part analysis [23] [24].

It has also been found that in addition to the detrimental effect that X-rays can have on polymers, some consider the use of XCT for the analysis of polymers unsuitable. As polymers are made from light atomic elements, the X-ray absorption is comparatively small with respect to metallic or ceramic items. This in turn can lead to a lower contrast in the reconstructed XCT image [25]. *Nishikawa et al* [26] overcome this issue by tuning the XCT machine so they can produce high contrast images from low density materials. By calculating the X-ray absorption of the material, they can predict the recovered pixel contrast value at any given photon energy. By keeping the photon energy low, they can maintain a high level of contrast ratio in the recovered image. Their practical work validates this by being able to achieve a spatial resolution of 3 μ m for the polymer case they presented.

Whilst this work does debunk the idea that XCT is not suitable metrology tool for polymers, it does highlight the need for a comprehensive understanding of the relationship between the XCT operating parameters, and the material, size, shape etc, of the part under scrutiny.

2.2.2. Ultrasonic Scanning

Acoustic distance measurement has been employed in various forms for several decades [27], with the most common example being sonar used on submarines. Ultrasonic echo scanning works on the same principle as time-of-flight wave propagation. In ultrasonic echo scanning a piezoelectric transducer generates a wave field in the component under scrutiny. These waves propagate through the structure and are reflected when they encounter acoustic interfaces such as faults or internal boundaries. Additional secondary transducers then in turn receive the reflected waves. By observing the time elapsed from wave emission to recovery, the depth of the reflector can be established [28]. Today, ultrasonic echo scanning is a common practice in several engineering fields and most prominently used in metallic weld fault detection. As a fault or observation tool ultrasonic is well established today in several industries, both medical and industrial. However, as a metrology device it is constrained by several factors. Firstly, the part under scrutiny and the ultrasonic scanner must have an extremely clean physical contact, free of all foreign matter and have a good surface finish [29]. This makes it difficult to scan objects that are rough, small or have an irregular shape.

Ultrasonic scanning also only shows features in its perpendicular orthographic view and does not provide volumetric information. For a full representation of an internal feature, a collection of 2D ultrasonic scans would need the addition of a 1D mechanical armature positional data (or a freehand alternative), plus a system of registration would be required to organise and register each ultrasonic scan in turn. *Neshat et al* [30], propose a system that tracks individual 2D ultrasonic scans, through mechanical means. By attaching an ultrasonic transducer onto a

mechanical scanning mechanism, and then dictating the scanning pitch and origination, the 2D scans are acquired and in turn reconstituted in a registered 3D domain. This system also does the 3D generation of an object comprising of different internal geometries. However, designed for clinical applications, the object of interest here cannot be considered hollow, but comprised of varying densities. The system they provide has a mean geometric accuracy between 0.6 and 1mm for X and Y positions, and an accuracy of between 2.3mm and 3.2mm depending on scan depth, for the Z position. This does lead to large volumetric errors, but as this system has been designed for clinical applications, it is deemed acceptable.

Ultrasonic thickness or depth measurement is used in a number of metallurgy practices with accuracies up to 0.05mm [31] [32]. The advent of 3D ultrasonic scanning in clinical applications has led to increased research in this area in an effect to reduce errors and increase accuracy. For the 3D geometrical characterization of engineering artefacts using ultrasonic scanning systems, some examples in have been found in literature.

Marcio et al [33] performed a comparative study involving the digitisation of surface profiles of large diameter pipes, using pulse-echo ultrasonics, and laser triangulation scanning. This study showed that for surface measurement pulse-echo ultrasonics the error uncertainty was 0.2mm lower than the results recovered by the laser triangulation scanner. Whilst this showed that their ultrasonic system maintained a higher accuracy, capture time was excessively slow, taking eight hours to capture a sample 170mm long with an internal radius of 76mm. This compared to the laser scanning system that took only ten minutes. Furthermore, whilst this system was designed for the inspection of pipes, the pipe sample used in their investigation was cut open so that the measurement could be performed.

2.2.3. Magnetic Resonance Imaging (MRI)

Magnetic resonance imaging or MRI (shown in Figure 2-2) is another capture technique that has a main usage in the medical industry. Unlike CT scanning, which uses X-rays, MRI scanning utilises strong magnetic fields and radio waves to generate imagery from inside an object. Simply put, when placed in an external magnetic field, certain nuclei are able to emit and absorb radio frequencies. The most often used nuclei are hydrogen atoms, due to their abundance in biological entities. When a sample is placed into the MRI scanner the samples nuclei realign to the direction of the magnetic field. Pulsed radio frequencies are then applied which alter the magnetic alignment of the nuclei relative to the magnetic field.



Figure 2-2: A typical MRI machine

To bring the atoms back into equilibrium the nuclei are subjected to a rotating motion that induces a magnetic flux from the nuclei. This magnetic flux in turn yields a voltage change which can be recorded by a receiver coil. Changing the intensity of the magnetic field or the frequency of the radio pulses can alter the response recovered [34]. In medical fields, MRI scanning is preferable to CT scanning because MRIs do not utilise ionizing radiation. This is further compounded in medical research as using CT scanning for research purposes can be deemed unethical as individuals are exposed to unnecessary levels of radiation [35]. For industrial purposes, MRI scanning has one overriding issue. Due to the magnetic field

generated by the scanner, this system cannot be used to scan ferrous metals such as steel and other alloys of iron.

2.3. Uses and Limitations of IRT

As previously stated in Chapter 1 this work intend to create and validate a novel vision system based around thermography capable of extracting dimensional data from internal features. Therefore, the next two sections of this literature review discuss the role of thermography in modern metrology, including its limitations and applications; and areas in which thermography and metrology currently overlap, with regards to thermal information providing second order data.

2.3.1. Definition of Thermography

Infrared thermography (IRT), also known as thermal imaging (TI), is the ability to observe the infrared part of the electromagnetic spectrum. All objects with a temperature above 0K (-273°C) emit radiation in the infrared region of the electromagnetic spectrum [36]. Infrared radiation is in the region outside of the visible part of the electromagnetic spectrum, shown in Figure 2-3, typically with a wavelength between 0.75 μm -1000 μm . As it is outside the visible part of the spectrum, special equipment is necessary to be able to view it, namely a thermal camera.

Thermal cameras can be assimilated to normal visible light cameras, in that they record thermal information in the same way a visible light camera would recreate a scene as observed by the naked eye. The main difference being the information that is supplied to each camera, and how each camera interprets that information. Visible images are made up of different tonalities based upon how the incident light is reflected into the camera. The object in the scene can be thought of as a reflector, reflecting the light into the camera. If there is no light source the object becomes unobservable. In comparison, ignoring the issues with reflected thermal

radiation that will be covered later in section 2.3.2; objects being viewed through a thermal camera are the primary energy emission source. A thermal image is a measure of the energy emitted by the viewed object [37]. By the object being the energy source, the object can be viewed using IRT even in the absence of visible light. *Gade et al*, [38] offer a comprehensive insight in the complex workings of IR cameras and their broad range of applications.

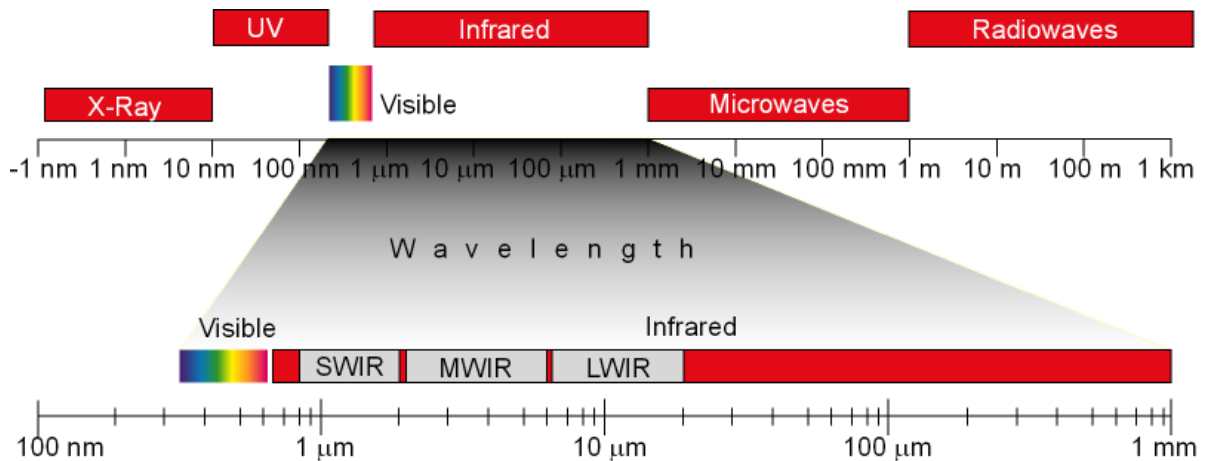


Figure 2-3: Electromagnetic spectrum

Through technological advancements, thermal imaging camera equipment has become more affordable and now IRT is used extensively in many different fields. IRT is now a common tool in condition monitoring, medical imaging, military and surveillance applications, search and rescue, building maintenance and many more.

IRT's use in the areas of surveillance is prevalent because a person can be viewed even in the absence of a light source making it an effective night vision tool. Concerning search and rescue applications, it can be used to locate injured persons quickly in either night or day as the human body emits more radiation than the surrounding area as shown in Figure 2-4. In this image, the warmer areas are shown in red, with the lower temperature background in blue. These areas of use do however have their limitations. For the subject to be visible and distinguishable there must be a suitable temperature gradient between the subject and the ambient background temperature.



Figure 2-4: Typical thermal image of a human

IRT is also one of the main tools in condition monitoring, especially in the areas of electrical engineering when fault finding in electrical circuitry. Faulty electrical connections or areas of unexpectedly high resistance will generate heat that can then be quickly located using a thermal camera, allowing them to be resolved before any serious issues arise. Figure 2-5 shows three circuit breakers, with middle one showing a higher temperature indicating a potential fault.



Figure 2-5: Faulty electrical connection.

As a visualisation tool, IRT is extremely simple to use, and the results are easy to interpret. However, as a temperature measurement tool several factors must be considered, as they will influence the recorded result. Using IRT, the measured value for a temperature measurand consists of several components and can be influenced by other external factors before the value is captured by the thermal camera.

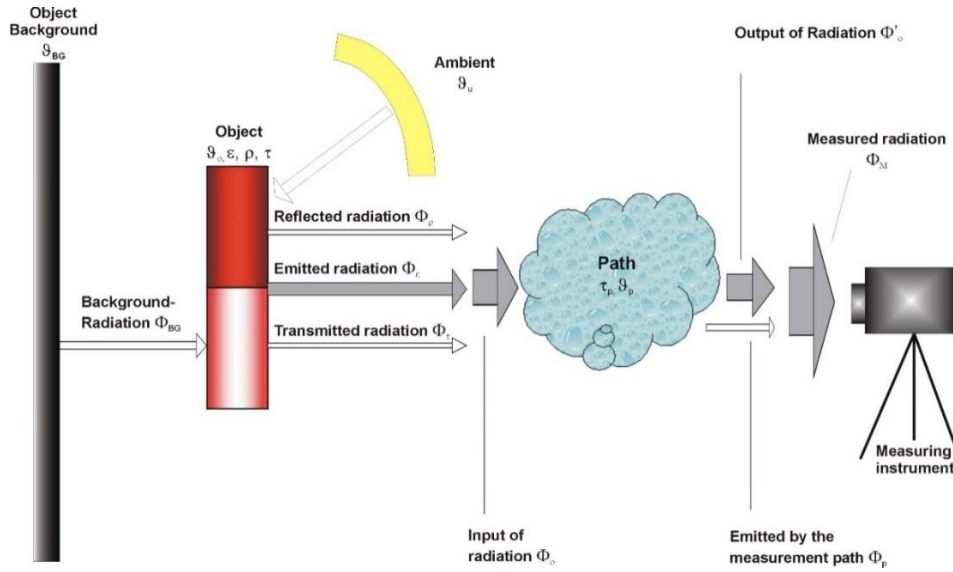


Figure 2-6: Thermographic capture scenario [39]

As can be seen in Figure 2-6, the measured radiation consists of three separate components emitted from the object: the objects own emitted radiation, transmitted radiation from other external sources, and reflected radiation. These components are then affected by the temperature and humidity of the environment. The relationship between the value for the measured radiation and its component parts can be summarised below in equation 2, with reference to Figure 2-6.

$$\Phi_m = \tau_p * (\epsilon * \Phi(\vartheta_o) + (1 - \epsilon) * \Phi(\vartheta_U)) + (1 - \tau_p) * \Phi(\vartheta_p) \quad (1)$$

[39]

2.3.2. Emissivity and Absorptivity

When using ITF as a temperature measurement tool, the influences of external additional factors must be considered in order to understand the recorded measurement. Chief amongst these factors is emissivity and absorptivity.

Emissivity and absorptivity are two factors in IRT that are intrinsically linked when measuring the temperature of an object's surface. The emissivity (ϵ) of an object is its ability to radiate

electromagnetic radiation when compared with that of a black body at the same temperature [40], (in heat transfer, a black body is a theoretical object that has a ϵ and α value of 1). Absorptivity (α) is the ratio of the radiant absorbed by a body to the radiant that falls on it. A surface's emissivity is always equal to its absorptivity [41]. Both are arbitrary values with a range of 0 to 1. For example, for a black body that has both α and ϵ values of 1, all radiation that falls on the surface is absorbed and in turn emitted perfectly regardless of angle of incidence. Conversely, an object that has values of 0 would reflect all radiation and emit none. However, both of these objects are hypothetical. In the real world, all surfaces would have an emissivity and absorptivity between 0 and 1 but never reach each extreme. For example, at room temperature polished brass has an emissivity value of 0.04, whilst coal soot would have a value of 0.95 [42]. This is best demonstrated with the use of a Leslie Cube (Figure 2-7). A Leslie cube is a hollow metallic cube where the four-vertical sides of the cube have different surface properties, being either painted or coated in different surface textures.

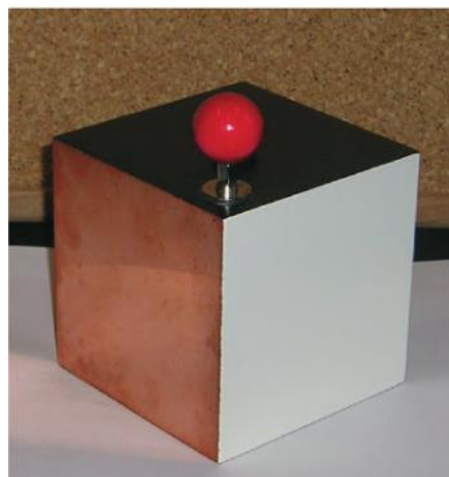


Figure 2-7: Vollmer et al's [43] Leslie Cube

Vollmer et al [43], use the above cube to demonstrate how a surface emissivity value can affect the temperature reading of an IR camera. Their copper cube consisted of two of the sides being painted, one black and one white. The third being polished copper and the fourth; rough copper. Using temperature probes it indicated that all four sides of the cube were at the same

temperature, they then observed the cube through IR camera with an ϵ value for the camera at 0.96. The results shown in Figure 2-8, show that the painted side (LH side of cube) of the cube showed the highest temperature at 84.3°C and the polished side (RH side of cube) was much lower 22.6°C. This demonstrates that even at the same temperature emissivity can vastly affect the results when observed through an IR camera.

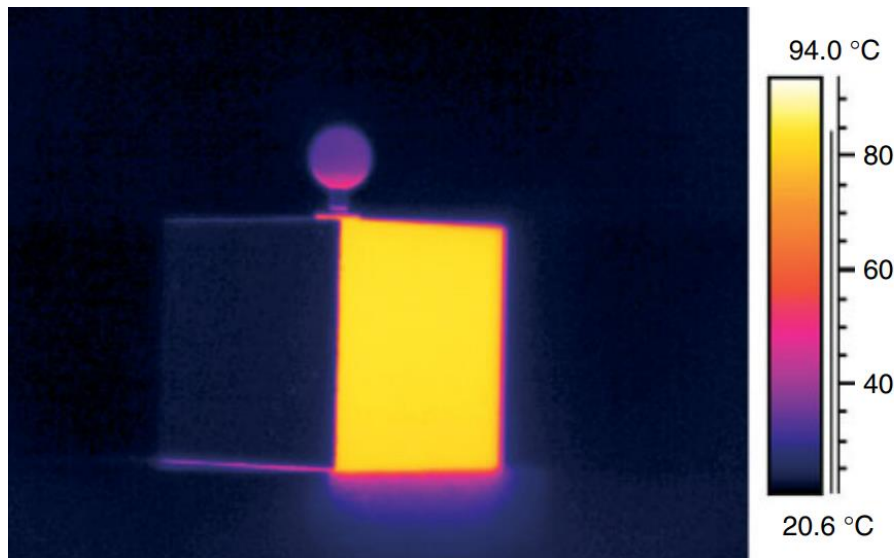


Figure 2-8: Vollmer et al [42] cube results

In most modern IR cameras, the emissivity value can be adjusted to be in-line with the emissivity value of the surface under observation so that more readings that are accurate can be collected. However, if an object is comprised of multiple surfaces each with different textures or coatings, the ϵ value will be constantly changing. One way to ensure a consistent emissivity value across a range of surfaces is to apply a coating or use a cover material with a known emissivity value. Masking tape is a good example of the latter. The tape is sufficiently thin to behave as a perfect conductor, but by covering the object under observation in tape the objects emissivity value is constant across all surfaces regardless of the type of surface underneath. The emissivity of masking tape is 0.92 [44].

2.4. IRT uses in PIDV

Increasingly the fields of PIDV and IRT are starting to overlap. Infrared radiation has shown to be a possible alternative to visible light in the 3D digitisation of objects, where the objects have optical properties that are not conducive to visible light scanning. *O. Aubreton et al* [45] describe a system that uses IRT to digitise the surfaces of highly reflective metallic surfaces, in a technique they call “scanning from heating”. They start by outlining the issues with scanning specular surfaces that are glossy or transparent. Surface reconstruction of specular surfaces is more complicated than the reconstruction of diffused surfaces due to several prominent issues [46]:

- The observing light from the source can be reflected away from the light source.
- The observing light can be diffracted by the material.
- The observing light can fully transport through the material, as can be the case with materials such as glass
- When changing the point of view features can appear to move on the surface due to laws of reflection.

To alleviate these issues *O. Aubreton et al* [45] attempt to use the measurement of the emitted infrared radiation instead of the reflected visible light. To do this they use a 50W Ytterbium fibre pumped diode focused to a 0.44mm beam spot, geometrically linked through a specific angle to an IR camera. The laser held at a set distance from the object, is then pulsed for a specific time based on the thermal properties of the object’s material. A thermal image is then taken of the area where the laser intercepts the object. A mechanical stage then moves the laser/thermal camera rig a set distance in either X or Y, and the process is repeated until the object has been covered in its entirety. Through a pre-defined geometric calibration of the

system, the 3D coordinates of each point are extracted from each thermal image and are reconstructed to form a complete digitised point cloud set of the object.

When comparing their system to a standard visible light scanner across several samples, the average error between the two systems is comparable, with the average error of the scanning by heating method being only 20 μ m lower. However, the standard deviation across all the entire samples was much lower using this novel method, compared to that obtained by the standard method. Whilst their novel approach to the scanning of specular surfaces has yielded promising results, their system is not without issue. This system does require the use of a high-powered laser, which aside from the cost implications does imply several health and safety concerns. In addition, the use of such a high-powered laser means that an in-depth knowledge about the material of the object under investigation is needed. They themselves state that to avoid melting or damaging the material the pulse time of the laser needs to be carefully calculated, employing the use of FEA to ascertain accurate pulse timings. Finally, the acquisition rate of capture for this system is comparably slow, at only three points per second. In addition, the laser needs to be shut down between points to avoid thermal patterning (heating the material between pulse locations) on the recovered image. This also adds extra time onto the overall data capture.

Whilst this work is not particularly conducive to the PIDV of internal features, it does offer an insight into the techniques used in accurately defining points taken from a thermal image. One example of this is Coma effect. The Coma effect or comatic aberration [47] is optical distortion caused by the curve in the camera lens and the angle of incident between the rays entering the lens and the optical axis of that lens. This can result in a geometrical aberration, effectively elongating features. They propose two solutions for this issue. One, using optical filters to limit the spectral domain (however this results in a reduction in sensitivity), and two, to ensure that

the area of interest is centred on the middle of the image. This decreases the angle of incidence reducing the effect.

2.4.1. Thermal Overlay

Another area where metrology and IRT are used in combination is thermal overlay or 3D thermography. Adding the thermographic data to a 3D digitised model incorporates an additional level of information on top of the geometric and visual data. This idea of 3D thermography is prevalent in several fields ranging from medical applications such as tumour location, to structural engineering and heat loss maps of buildings. An example of a heat loss map rendered to a 3D scan of a building is shown in Figure 2-9.



*Figure 2-9: Example of a 3D thermography, showing 3D heat loss map on a building.
Curtsey of Gonzalez-Aguilera et al [48]*

In medical applications, it is convenient due to its non-contact, non-invasive attributes. *Kreffer et al* [49] demonstrate this with their method for generating 3D thermal models. Their technique encompasses typical 3D digitisation and combines it with a type of photogrammetry they describe as “structure from motion”.

To start, they capture the 3D data using standard structured light techniques. This is done because low-resolution thermal images generally describe little in the way of geometric information, which leaves points of interest ambiguous. Then a technique similar to photogrammetry is used to capture the thermal data by acquiring multiple thermal images all around the subject. However, issues arise when attempting to stitch the thermal images together.

Photogrammetry relies on matching similar features in separate images. Thermal images by their nature are generally homogeneous with sharp or outstanding features being blended into surrounding areas. This limits the effectiveness of being able to stitch together two concurrent images. To circumnavigate this issue *krefer et al* [49] add in an additional level of pre-processing that creates artificial contrasts between the differing intensity levels in the thermal image. This contrast helps emphasise image variations that may have otherwise been too subtle to detect. This method thus generates significantly more areas of interest allowing concurrent images to be stitched together.

The thermal images are then projected onto the 3D mesh, through a common global alignment. The result is a fully encapsulated 3D thermal model.

Whilst their work is focused on the external overlay of an object and is aimed more at medical applications, where geometric tolerances are not a primary concern (max errors in their system can be as high as 3.7mm), their technique's in creating artificial contrasts is worth consideration for this investigation. As will be demonstrated, feature resolution, whilst already low due to the nature of thermal images, is further decreased when trying to view internal features. Their techniques in contrast manipulation could reduce ambiguity in identifying that the internal feature regions.

This use of thermal overlay is further demonstrated in a more industrial setting by *Gonzalez-Aguilera et al* [48]. Their work in efficiency evaluation combines large scale scanning with IRT to form comprehensive 3D textured models. The texturing in this case comes in the form of 2D thermograms that are registered to the 3D point cloud set. The aim of this is to allow the location and quantifiability of heat losses and thermal defects in buildings.

Their technique first utilises a time-of-flight laser scanning system to generate the 3D point cloud representation of the building in question. Separately, 2D thermographic images are

captured by a FLIR[®] camera. Several thermograms and point cloud sets are captured and overlaid to increase spatial resolution. In addition to the thermograms, corresponding visible light images are captured. These are used to align the thermograms to the point cloud data set by matching points of interest in the visible image to the corresponding points in the point cloud data. Feature extraction is performed by utilising a Harris operator, applied to the entire compressed image. A Harris operator is used due to its invariance to potential image rotations and scaling factors. Once these points have been identified, they are matched with the corresponding points in the point cloud set. This allows the visible light images that are matched to the thermograms to be overlaid on the point cloud data. The visible light images are then removed leaving a fully thermally rendered 3D model. Geometric tolerances for the point cloud scanning are given to be 1.4mm, which is dictated by the accuracy of the laser. No positional accuracy is given for the registration of the overlaid images. Whilst these techniques are interesting and potentially useful to one of the objectives in their study, namely the thermal image registration, they do extrapolate on how thermal imagery can be used to deduce geometric features.

This idea of combining IRT and 3D scanning is further explained in the works of *Lagueta et al* [50]. Their work is similar to that described in [48], in that they use this idea of IRT/RE combination for the visualisation of energy efficiencies in the form of 3D textured models. Both use traditional 3D digitisation systems to recover geometric data, and both use thermographic cameras to record the thermal overlay. Both also go into detail about the importance of considering radial lens distortion within the recovered thermograms. However, one main difference between the two is how the thermal information is portrayed on the 3D model. As previously said *Gonzalez-Aguilera et al* [48] take multiple thermal images and corresponding visible light images from multiple overlapping angles and orientations, using the visible light images to register the thermal images to the point cloud through common areas

of interest. This technique combined with the high number of images they have captured, allows them to wrap the visible images, and therefore the thermal images, to the point cloud data. This results in a complete 3D thermal model that can be viewed from any orientation whilst showing the information relevant to that orientation. The *Lagueta et al* [50] capture technique differs somewhat to this in that they do not take corresponding visible light images and the thermal images they capture are only taken perpendicular to the immediate facade of the building in question. They then register the thermal images to the point cloud through common areas of interest taken from the thermal images. They state that doing this leads to a low registration error. However, the error that they quote is given in pixels, and they do not offer a conversion factor that would allow the calculation of a true geometric error. Therefore, their error value is ambiguous in the context of this work. Furthermore, the technique they have adopted to capture the thermal data, i.e., perpendicular to the façade, means that the thermal information can only be viewed in its entirety from a single orthographic projection plane. If this thermal model were viewed from any other orientation, it would appear to have missing data.

2.4.2. Thermographic vision systems

This technique of adding thermal overlay as an additional level of information to a reverse engineered model is extrapolated further by *Yu et al* [51]. Whilst the other areas involved with this idea of thermal overlay have focused on using it as a tool for energy efficiencies in buildings, they provide an all-in-one system that can capture 3D-textural and thermal information simultaneously. Using a visible light camera and a projector, in a typical structured light setup, they then add a thermal camera to provide thermal information. To ensure that all three parts of the system (visible camera, projector, and thermal camera) use the same global correspondence system *Yu et al* employ a three-view-geometry system to encode the three parts together. To begin with, they use standard structured light calibration techniques (*Zhang et al*

[52] and *Hartley et al* [53]) to qualify known 2D geometries to the recovered 3D information. To register the thermal camera, the checkerboard used in the visual registration is modified with holes, and a heat source is placed behind it. The checkerboards differentiation in colour allows for visible registration with the receiving camera, and the holes in the board that allow heat transfer can be detected by the thermal camera. The result is a trifocal tensor between the three separate parts of the system. Given this registration, corresponding points between the projector and visible camera can be determined and expressed in a 3D model. As the thermal camera is registered in the same domain, the corresponding point in the thermal data can be extracted, through point transfer and added to the same 3D model. This results in a complete 3D thermal facial recognition. Whilst this system does allow the capture of thermal facial 3D models, it is not designed or intended for geometric reconstruction. As such, whilst the accuracy of this system was determined by the authors the results are given in pixels and can be considered ambiguous in the context of this investigation. It does however offer insight into the thermal/visual registration required for IRT in PIDV, which will be helpful to the first objective of this investigation.

Vidas et al [54] take this idea of an all-in-one 3D thermography system even further with their handheld system, *Heatwave*. *Heatwave* is portable system that allows the capture of 3D thermographical surfaces for energy auditing. As with [64] it consists of a thermal camera and structured light project system for 3D reconstruction. This work focuses on the thermographical reconstruction of mechanical objects, unlike *Yu et al*, which looked at facial reconstruction. As such, the authors go into extensive detail regarding the geometric and radiometric calibration of the system. The geometric calibration is broken down into intrinsic and extrinsic calibration. The intrinsic calibration defines the relationship between the object under investigation and the sensors capturing that data. Intrinsic properties include optical features such as focal length, optical centre, sensor size, etc. The extrinsic calibration designates the geometrical relationship

between each of the sensors within the system. Finally, radiometric calibration is used to define the relationship between the pixels in the IRT image and the corresponding temperature of the object that a given pixel represents.

Whilst the authors give a detailed account of the calibration procedure required to capture accurate models, no results regarding the actual geometric accuracy of the system are given.

2.4.3. Geometric Shape Reconstruction Using Thermal Imagery

Away from using IRT as an additional layer of information within 3D reconstruction, there have been several studies into geometric shape reconstruction using thermal imagery. The work performed by *Barker et al* [55], looks at the extraction of a single orthographic profile of an object from a single thermal image. This is performed by using radiative heating pulsed in the direction of the surface of interest. The external profile is recovered by recording the evolution of the temperature as the heat moves across the part's surface. This process relies heavily on understanding not only the thermal mechanics of the object but also the introduced heating aspects and the relationship between the two. The surface area of the object, object emissivity and specific heat, thermal diffusivity, and the power the object receives are all required before the profile extraction can begin. Knowing these factors is imperative for the mathematical discernment of power distribution across the objects surface. Once this is known and following a correct calibration procedure, the profiles spatial orientation and position can be deduced from captured thermal images.

Each pixel line of the captured thermogram is then analysed and divided into linear and non-linear segments. This allows them to mathematically extract the objects profile based upon temperature variations due to changes in shape or curvature. Linear sections show little variation in the resultant IR camera output, however non-linear sections show up as temperature-rise variations due to the change in distance from the IR camera.

This technique shows that basic geometric primitives can be extracted from a single thermogram, with no other equipment required. However, this work only shows results for a single 2D slice of a complete 3D object. It is not stated but assumed that for a full 3D reconstruction their process would need to be repeated for every pixel line in a given thermogram to give a full and comprehensive reconstruction. Furthermore, their work does not offer any insight into the geometric accuracy of their system. Lastly, this system, as with many others that have been researched, is based upon the reconstruction of the external profiles of objects using IRT, not internal geometry.

2.5. Chapter Summary

This chapter has introduced the field of PIDV, and the inherent issues when trying to perform PIDV on internal geometry. Furthermore, it has highlighted the upcoming increased requirement of PIDV on internal geometry as additive manufacture opens new design possibilities within the manufacturing sector. As has been found, the current main barrier to the more extensive use of additive manufacture in industry is the lack of viable and available PIDV solutions for additively manufactured parts.

As has been seen many times throughout this literature review, the only currently available system for the extraction of the internal geometry data is XCT. However, whilst being an extremely versatile option, XCT is not a universal solution.

In addition to the more mundane factors regarding the use of XCT, such as large capital investment, and large power requirements adding additional expense, which may be barriers in themselves to XCT use, Table 2-1 summarises the technical gap for the sustained use of XCT with respect to parts with internal geometry.

Table 2-1: Summery of XCT literature review

<i>Du Plessis et al</i> [12]	This paper highlights the higher energy requirement necessary for industrial XCT machine, due to the higher attenuation coefficient of metallics.
<i>Kruth et al</i> [13] [14]	This paper discusses the need for higher XCT drive voltages, so that X-ray photons can fully penetrate an object. If they cannot then photoelectric absorption will occur, which can lead to observed noise and inaccurate results. This paper also introduces the issue of beam hardening and the relevance it has on recovered results, as well as potential error sources from the XCT kinematics and the relationship that has with the reconstructed results
<i>Hiller et al</i> [15]	Despite the potential issues concerned with XCT for dimensional metrology, the work by <i>Hiller et al</i> show that the measurement uncertainty is quite low, between 6.9 μ m -1 μ m.
<i>Moroni et al</i> [17]	<i>Moroni et al</i> do show that currently for internal dimensional metrology XCT is currently the most viable option. However, they highlight some of the design considerations that must be considered to ensure accurate results. Sharp corners, composite materials and dense materials can all have an impact on the final geometric reconstruction. This work also highlights the issue of penetrative depth a XCT can achieve with denser materials, such as metallics.
<i>Aloisi et al</i> [18]	<i>Aloisi et al</i> highlight how other mechanical properties can affect XCT results. They concentrate on surface finish and show that when compared to a reference CMM, the two comparable measured dimensions differ, with respect to that objects surface finish.
<i>Landis et al</i> [19]	The work by <i>Landis et al</i> echoes that of <i>Moroni et al</i> [17], in that XCT is an extremely versatile tool, but with regards to dimensional metrology, the interaction between the X-rays and the measured part can lead to inaccuracies in the final result
<i>Thompson et al</i> [20]	The issues of using XCT for dimensional metrology are further discuss by <i>Thompson et al</i> , in accordance with [17] and [19]. However, from a design point of view, they show how parts with large aspect ratios is a potential pitfall for XCTs' as the X-ray intensity will need to be altered in accordance with the aspect ratio to ensure consistent results. They also highlight the issue with beam hardening and if overlooked how this can add artificial offsets between internal and external edges.
<i>Dewulf et al</i> [21]	In this work the issues of beam hardening are acknowledged and <i>Dewulf et al</i> explain how numerus algorithms have been produced to correct the numerical offsets created by beam hardening. However, their work shows how these corrective algorithms can have their own detrimental effects on resultant dimensional data, especially with regards to multi-featured parts.
<i>De Chiffre et al</i> [22]	<i>De Chiffre et al</i> present an overview of industrial XCT, and like other works reviewed here, they state that for internal dimensional metrology it is currently the most viable solution. However, in concurrence with other works found in this review they list shortcoming of the technology as a barrier to industry. Aside from the huge increase in longevity of a XCT measurement plan,

	compared to a traditional CMM one, they highlight how high-powered X-rays can have detrimental effects of polymer components.
<i>Nishikawa et al</i> [25]	<i>Nishikawa et al</i> further review the use of XCT with polymer components, considering it tentatively unsuitable, given the low density of polymers compared to metals and ceramics, stating that this lower density can lead to low contrast images in the reconstructed data.
<i>Nishikawa et al</i> [26]	<i>Nishikawa et al</i> follow up the above work, by tuning their XCT machine so it can produce high contrast images from low density materials. However, their process requires a comprehensive understanding of how the parts material properties, such as size, shape etc, relate to the XCT being used.

In addition to XCT, which as this review has shown is the currently the most viable solution to the PIDV for internal geometry, other technologies also with the ability to penetrate an objects external face to detect internal surfaces, features, etc, have also been reviewed.

MRIs cannot be used in conjunction with objects containing ferrous metals, which severely limits their industrial application potential. Added to that, there is negligible research attributed to MRIs in such industrial measurements.

Ultrasonic thickness measurement is also well established in industry. Used mainly in an inspection capacity for fault identification, ultrasonic thickness measurement systems can have accuracies as high as 0.05mm. Whilst these systems do have a high degree of accuracy and are fit for purpose for distance and defect measurement, they are not used in the area of 3D dimensional metrology, other than in certain medical practices where accuracy is a secondary concern, with abnormality identification the primary goal.

From the currently available technology, and given the defined problem at hand, this review has shown that the only viable solution for the dimensional measurement of internal features is industrial XCT. That said, whilst this review has shown this it extremely versatile, XCT is not a universal solution for dimensional metrology. It has been found that aside from being a costly capital expense, size of part limitations, and the added longevity in measuring time, there

are several more intrinsic factors that placate XCT from being the industry standard for internal dimensional metrology. The need for a comprehensive understanding of a parts material, density, shape, composition etc, and how these features can affect the interaction with X-rays is critical so that accurate results can be gathered. Even then accurate results are not guaranteed as designers design parts for a purpose, not to satisfy the particulars of XCT so that accurate results can be obtained.

Given the potential need for internal PIDV, and the reviewed limitations of the currently available technology, as said in Chapter 1 the purpose of this work is to investigate a viable alternative measurement system utilising inferred thermography (IRT).

This chapter has also reviewed the application of IRT as a temperature measurement tool, in several different fields. This investigation thus far has shown that in terms of geometric metrology, there are a few cases where IRT and PIDV are being used in conjunction. What has been reviewed has mainly been shown to be in the area of energy auditing, where a 3D model can be textured with thermal information culminating in a complete 3D thermal model. However, this is mainly being used as a visual tool, rather than an intrinsic measurement application. Table 2-2 summaries the reviewed work in the IRT/PIDV area.

Table 2-2: Summery of IRT/PIDV literary review

<p><i>Krefer et al</i> [49] <i>Gonzalez-Aguilera et al</i> [48] <i>Lagueta et al</i> [50]</p>	<p>The work by <i>Krefer et al</i> shows a combination of structured light digitisation, and thermal imagery photogrammetry. By layering the stitched photogrammetric images onto the 3D mesh the authors can generate a fully thermally textured 3D model. However, this technique may not be applicable for dimension metrology due to the resultant large spatial errors.</p> <p>This idea of thermal overlay is further investigated by <i>Gonzalez-Aguilera et al</i> and <i>Lagueta et al</i>, both who utilise this technology for energy auditing purposes of buildings.</p> <p>Neither are conducive for the PIDV of internal structures, but they do offer insight into the particulars of using thermal cameras as metrology tools, such as lens distortions and the homogeneous natural of thermograms.</p>
<p><i>Yu et al</i> [51]</p>	<p><i>Yu et al</i> take this idea of thermal overlay, and encompass it into an all-in-one reverse engineering tool, that can digitise an object and</p>

<i>Vidas et al</i> [54]	thermally texture it in a single pass, with the use of a structured light, thermal camera hybrid solution. This hybrid system is further investigated by <i>Vidas et al</i> , who use this technology to create a portable hand-held device that can scan an object/environment and simultaneously thermally map it.
<i>Barker et al</i> [55]	The work by <i>Barker et al</i> is one of the few examples found in this review of geometrical data being extracted from a thermal image. In this work the authors extract single orthographic profile from the part by reviewing the evolution of the heat path as it propagates through the object. However, this work only focuses on external geometries.

In conclusion, from the literature that has been reviewed it has been found that the use of IRT in a metrology environment is not unique. Many fields involve IRT for their temperature acquisition, and it is apparent that more and more IRT is being used in conjunction with techniques that could be classified in a metrological sense. Most of the work reviewed shows IRT being adapted to form an additional level of information on top of that which is traditional gathered. However, this additional information is, as expected, temperature data applied over geometric data gathered by industry standard techniques, where the novelty is in the fusion of the two data sources, not how the data is extracted. Concerning geometric feature extraction from thermal images, the reviewed research has found examples that focuses solely on the external feature extraction. At this point, no literature is currently available concerning the use of IRT for internal geometric measurement, which would lead to the complete inspection of an object consisting of internal features.

Chapter 3. Motivation, Aim, Research Objectives, Scope and Methodology

This chapter provides an overview of the research aim, the motivation behind this aim based on the introduced problem and findings of the literature review, the research objectives, the overall scope of the research, and the proposed research methodology.

3.1. Motivation

Whilst standards for the inspection and dimensional validation of external geometry are well-established and performed throughout industry, very few solutions exist in the way of a process for the validation of internal features. As AM becomes a more available method to produce parts, the prevalence will increase for the inspection of designed functional internal features that cannot be accessed once made. This issue of internal dimensional validation, and internal quality assurance therefore becomes more prominent [56]. Currently for the PIDV of internal features only two suitable methods are available. The first would be to destructively measure the object by cutting it open and measuring the features with standard techniques for the now-exposed features. This may be acceptable in large production runs where sampling of a batch is performed on one or more “sacrificial” parts. However, it does lead to waste and in all other manufacturing scenarios this approach is likely to be prohibitively expensive. The second option would be to use XCT scanning. However, as described in section 2.2, XCT scanning is not a universal solution, with several aspects of their operation potentially limiting its use dimensional metrology.

Therefore, the main motivation for this thesis is to investigate and develop a novel system, based around IFT, capable of extracting geometric data from internal features as a viable

alternative to XCT and destructive testing. This system has the benefits of being cost effective, portable, non-destructive, and has the potential to be unaffected by design factors that can be draw backs for XCT. Given the current technology readiness level (TRL) of this proposal, it is expected that that the overall performance, in terms of dimensional accuracy, will not be currently as high as the present alternatives, however, the benefits of being able to sample non-destructively are considered to be reasonable grounds to pursue this line of research.

3.2. Aim

The aim of this investigation is to initiate, design and evaluate a novel proof-of-concept thermography-based vision system, capable of performing internal dimensional validation, as well as internal quality assurance. This work will introduce a low cost, versatile solution capable of discerning geometric data from thermal information. It will utilise readily available instrumentation, with the design aim to be less cumbersome, and more user accessible than XCT.

3.3. Research questions

From the performed literature review which has generated the motivation and aim, the following questions have arisen:

- RQ1. Can internal dimensional data be extracted from a thermographic image of an object's surface if the object is subjected to a series of controlled temperature perturbations?
- RQ2. If the answer to the above RQ is yes, can the system differentiate changes in geometrical and mechanical states from the captured results?
- RQ3. To what extent does analysis of the transient behaviour provide additional useful information for the measurement task?

RQ4. To what level of accuracy can measurement results be obtained from such a system.

Referring to the literature review, only the first question has been partially answered by *Barker et al* [55], who showed that external geometric information could be extracted from a thermogram. However internal dimensions are far more challenging due to the far more subtle change in surface temperature gradients. Whether internal dimensional information can be extracted from a thermogram still remains unanswered, as do the subsequent detailed questions relating to this work. Therefore, it is expected that the below objectives will help answer these and satisfy the aim.

3.4. Research objectives

To answer the above questions the following objectives will need to be completed:

- i. Verify computationally that changes in surface temperature are detectable to the extent that internal geometry profiles can be extracted in the resultant surface temperature profile. Performing this will validate whether geometric information can indeed be extracted from thermal data from the very basic first instance.
- ii. Verify that changes in internal geometry, such as shape, depth from surface, size, and material properties, such as thermal conductivity, still allow for internal geometry profile extraction. Building upon the information gained from objective one, changing a multitude of factors will indicate the limitation of system, and offer insight into the where this system will yield best results, and where potential pitfalls may exist.
- iii. Design, simulate, and manufacture test artefacts that can be validated experimentally, based upon the information gathered in objectives one and two. These artifacts will need to be calibrated before any experimental validated to determine their actual internal dimensions.

- iv. Design an experiment around the manufactured artefacts that will validate the finding of objective one and two. Emphasis will need to be made upon the thermal data capture technique, and the technique used in manipulating the object internal temperature relative its external temperature.
- v. Investigate ways in which the recovered data can be used and manipulated into deduced geometric data sets of the internal geometry, which if needs be, can be combined with other external data sets to form complete 3D renditions of the object in question. This will show how versatile the system is, and its practical imitations; can it be used for single 2D stills or can it produce complex 3D models that can be combined with third party information.
- vi. Determine the accuracy and repeatability of the system. As this is a critical part of any metrology tool, if the experiment from objective four is successful, it will need to be repeated several times to ascertain its accuracy and repeatability.

3.5. Scope

The main scope of this work is to devise and primarily evaluate a vision system that can determine the internal geometry dimensional data of an object using IR thermography. Due to the novelty of this proof-of-concept project, only objects consisting of primitive shapes will be within the scope of this investigation and will be designed and manufactured to allow the primary validation of PIDV through infrared thermography. These artefacts will differ in size, material, and internal shape, including changes in depth, angle, geometry, curvature etc, to offer insight into any limitations. The practical work is limited to six artefacts with two different materials. While many more artefacts could have been included, this number is considered to provide sufficient evidence of the applicability of the approach to provide a case for extending to further artefacts in a future project.

The thermal camera (FLIR A655SC) readily available for this work has technical limitations but proved sufficient for the practical validation part of this investigation. Whilst an additional camera is tested to determine the effects of lower resolution verses accuracy, testing different thermographic cameras for comparative performance is out of scope for this thesis.

Captured results from the new system are compared against current industry-standard measurement techniques to determine this system's viability, as well as accuracy and repeatability. As each of the possible reference techniques has its own limitation, XCT has been chosen as the benchmark measurement for this thesis.

3.6. Methodology and hypothesis

3.6.1. Hypothesis

During thermal conduction, heat will spontaneously flow from hotter areas to cooler parts of the body. The rate of flow is governed by the property of the material. This interaction will continue until thermal equilibrium is reached. Non-solid objects that comprise internally connected features and voids will therefore display non-uniform transfer of heat. The primary hypothesis is that:

Given a prescribed thermal excitation, the internal geometry of an object can be deduced by measuring the thermal response on the object's surface.

This transfer of energy, and detection by thermography, forms the basis of this proposed measurement system.

If an object incorporating internal geometry, at a uniform temperature, has the temperature of these internal features forcibly increased, then it will create a negative temperature gradient between the internal structure and the external faces. This temperature gradient, in keeping with Fourier's law of heat conduction, will cause the higher internal heat to flow to the cooler

external surfaces. This in turn will generate a surface temperature profile, which is it anticipated will highlight the underlying internal structure. The focus of this work is to prove that these surface temperature profiles contain the necessary information that can be extracted, and by image processing mean be converted into dimensional information relating the internal structure.

Furthermore, with photogrammetry techniques, multiple two-dimensional (2D) images of the same object can be combined to produce a three-dimensional (3D) representation. Therefore, the second hypothesis is that:

Given that 2D thermography can detect internal geometry from the conduction in the material from one view, multiple views can be combined to perform a 3D reconstruction.

3.6.2. Methodology

From the literature review it has been shown that IRT, and therefore the main aim of this work, has not been used in this way before: i.e., to provide a platform from which internal dimensional geometric data can be extracted.

Given the novelty of this idea, and the uncertainty in the initial instance as to whether dimensional data can be gathered in this way, to validate the above hypothesis the first steps of this investigation should be carried out in a computational manner.

Finite Element Analysis (FEA) is a useful tool in this regard, as one can easily set up a simulation, and repeat it varying the constraints. FEA allows the freedom to run simulations with numerous different materials, shapes, heating constraints etc. However, these simulations require assumptions regarding material properties and boundary conditions. Therefore, they will have to be validated physically, so it is important to design these simulations in a way that they can be recreated in a laboratory-based environment. Therefore, using the Design of Experiment (DoE) analogy, the computational factors will need to be based on what physical

factors can be attained in the laboratory. Table 3-1 shows the factors, levels, and desired responses of the initial FEA simulations.

Table 3-1: Components of FEA sim design

Factors	Levels	Responses
Material Properties (thermal Conductivity)	Internal temperature	Surface temperature profiles leading to dimensional data extraction.
Cavity width	External temperature	
Cavity depth (from Surface)	Mesh settings	
Cavity shape	Simulation time	

Looking at the “Factors” column in Table 3-1, material properties will be based upon materials that are physically readily obtainable, with the additions of materials that have extremes in thermal conductivity to showcase what effect that might have. Dimensional factors such as width, and depth will need to be adjusted incrementally to ascertain what separate effect they have on the response. The final factor, shape, will be defined from primitive shapes, in line with the scope of this project. Primitive features, such as flat, curved or angled (relative to the viewed external face), are to be simulated. As most complex shapes are constructed from planer primitives, curved, or planer primitives with angles, these three areas are the most critical in defining whether this system can correctly identify the difference and the preform the accurate extraction of dimensional information.

However, one design constraint necessary for the physical validation is that these artifacts are sealed at one end to allow for the addition of some form of heating medium. The only other design constraint is to ensure that the designs used in the FEA work can be easily physically replicated.

To forceably adjust the internal temperature two separate methods will be looked at. The first will involve simulating filling the internal area with a heated liquid that will then conduct the heat to outer surfaces. It is expected that this conduction, with associated thermal boundary regions between a liquid/solid interface, will generate a surface temperature profile from which the dimensional information can be extracted. The optimum internal temperature at this point is unknown. However, the internal temperature must be high enough that a suitable surface temperature profile is produced before homogeneity occurs across the viewed surface as the body approaches thermal equilibrium. A range of internal temperatures will be simulated to observe the effect and determine the most suitable temperature, or range of temperatures.

The second heating option is external heating, where a heating element will be placed on the opposite side to the “viewed” surface. In this instance it is expected that the heat from the element will conduct around the internal cavity, which will act as an insulative barrier. As the surrounding material will be at a higher temperature than the internal structure, this should be visible on the resultant surface temperature profile.

For these simulations, the mesh element density will also need to be incrementally adjusted to see what effect this has on the final response.

The external temperature, which is defined as the ambient temperature, will not be nominally changing during the simulations or experiments. It will be set to reflect a typical temperature one would find in a laboratory environment. This is an assumption to simplify the simulation, since there will be some slight temperature rise near the artefact due to convective losses. During the experimental stage, the ambient temperature is monitored to avoid contamination of the results.

Finally, simulation times will need to be reviewed during the simulation evolution. The simulations need to be long enough to ensure that the continual temperature differential

between the internal and the external surfaces is visible until homogeneity occurs. It is expected that material with high thermal conductivity will require short simulation times, and conversely materials with low thermal conductivity will need longer. This will also indicate how long the physical validation experiments will require based on the material's properties.

By changing these factors and levels it is expected that each change will affect the surface temperature response, which in turn will affect the extracted dimensional data.

For the physical validation, the response in the DoE is the same, and several of the factors and levels are carried over with certain additions.

shows the components for the for the physical validation part of this investigation. Regarding the factors, as previously said the choice of material will be dictated by what materials are readily attainable and have been simulated in the FEA section of this investigation. Priority will be given to materials that have extremes in thermal conductivity as it is envisaged that this factor will have the most effect on recovered results.

Cavity shape will again consist of primitive shapes and be of the same design of those simulated analytically. To provide baseline dimensional information, all artefacts used in the physical validation will be inspected prior to thermal testing. Part emissivity is intrinsic to the material chosen, and any materials chosen that have a high emissivity will require masking before any thermal testing.

Table 3-2 shows the components for the for the physical validation part of this investigation. Regarding the factors, as previously said the choice of material will be dictated by what materials are readily attainable and have been simulated in the FEA section of this investigation. Priority will be given to materials that have extremes in thermal conductivity as it is envisaged that this factor will have the most effect on recovered results.

Cavity shape will again consist of primitive shapes and be of the same design of those simulated analytically. To provide baseline dimensional information, all artefacts used in the physical validation will be inspected prior to thermal testing. Part emissivity is intrinsic to the material chosen, and any materials chosen that have a high emissivity will require masking before any thermal testing.

Table 3-2: Components for physical validation.

Factors	Levels	Responses
Material Properties (thermal Conductivity)	Internal temperature	Surface temperature profiles leading to dimensional data extraction.
Cavity shape	External temperature	
Part Emissivity	Camera settings: <ul style="list-style-type: none"> • FOV • Resolution • Noise levels 	
	Subject distance/Rotational position	
	Monitoring time	

The levels for the practical validation will be based upon the results from the previous FEA work and factors based on the thermal camera usage.

For example, the internal temperature, heating time, and heating method will be built upon the FEA results. The external temperature will be monitored but will be defined by the ambient temperature of the lab.

Camera-specific levels such as field of view (FOV), sensitivity, focal length etc. are constants and will be set by the choice of thermal camera used in the validation. There is a specific camera

available to this research, the specifications of which are shown in Table 5-3. The levels of noise present in thermograms are dependent on the thermal contrast, and whether the subject is in focus. Therefore, proper attention will be made to ensuring the subject is in focus. However, thermal contrast will be an issue in the first instance of any thermal test, as the subject and background will be at the same ambient temperature, providing a very low contrast between the two. One option to alleviate this is place a highly emissive object next to the subject, forcing a high contrast. This can also help with ensuring the object is in focus.

The distance the subject is from the camera will need to be investigated. This will help the relationship between subject distance and resolution. The subject will be placed to fill the camera's FOV at its minimal focal distance. This will allow for the best resolution with respect to $\mu\text{m/mm}$.

Most of these levels are also potential error sources with respect to the final response. Subject distance/resolution, thermal resolution, rotational position (relative to the camera), thermal contrast, will all influence the final response. Therefore, in the experimental part of this investigation these levels and their effects will need to be investigated.

Finally, the monitoring time for validation tests will be informed by the FEA work.

Providing the final response shown in Table 3-1 is realised, given the associated factors and levels, this validation will need to be repeated a minimum of five times to ascertain the system's accuracy and repeatability.

The penultimate objective in this work is to investigate the useability of any data that recovered. Therefore, it will be necessary to export this data in a useable format that can be fused with other dimensional data recovered from other sources. One method that will be investigated is the fusion of the outputted data as point cloud file and point cloud data of the external geometry, scanned using a separate source. The rationale behind this is that from this single data set, a

solid CAD model can be extrapolated, which are the most versatile form of CAD model, with regards to further evaluation.

Chapter 4. Preliminary FEA Modelling and Results

This chapter focuses on the preliminary FEA simulations regarding the feature extraction of internal features from thermal information with the principle of detection using accessible thermal imaging systems. Several simple CAD objects have been created with internal geometries, and have been through several simulations, with changes to certain vectors such as internal cavity position, size, and material properties. This is to determine the effect on the recovered internal geometric data when alterations to these vectors are applied. This chapter also discusses alternative methods for object heating, and the preliminary validation of the experimental artefact used in the experimental chapters, 5 and 6.

4.1. Introduction to Thermal FEA Simulations

In this thesis, the purpose of using finite element analysis (FEA) here is to evaluate the new idea of exploiting heat transfer and high spatial resolution thermal imagery for the complete measurement of unknown internal features. This may be used in the internal dimensional measurement of hollow objects, or for checking internal damage or distortion that can occur in AM parts. Depending on the results, non-destructive evaluation and inspection may also be possible depending on the accuracy requirements.

At this stage, so early in the investigation, it was not yet known what the variation in sensitivity would be at the surface of some simple shapes and whether that variation is measurable and differentiable through thermal imaging using a typical camera (considering the goal of making this technique accessible). This research had access to an FLIR A655SC thermal imaging camera, which has a thermal sensitivity of 0.05 °C (50 mK) and an image resolution of 640 x 480 pixels. A detailed specification is provided in Table 5-3, in Chapter 5. This could be

considered a low to mid-range thermal imaging camera, which has a purchase price of approximately £18,000 at the time of writing this report.

These simulations will identify the relationship between the surface temperature changes and what may be detectable, given the camera image's spatial and temperature resolution. They will also show how several factors, discussed in section 3.6.2, might affect the resultant surfaces temperature profile.

In order to induce heat transfer, it is assumed that the surfaces of internal features can be heated, for example, using boiling water or another hot substance that can be injected into the internal cavities and voids. For these simulations, a temperature boundary condition was applied of 95 °C representing an average temperature of boiling water shortly after being poured into an object. For simplification of the boundary condition, the simulated temperature remains constant whereas in reality the water would cool down a little during the measurement period. Where this idea of internal heating is not possible i.e., if the workpiece involved is a sealed unit, an idea of external heating is presented in section 4.5.

For all simulations, a convective heat transfer coefficient of 6 W/m/ °C was applied to the exposed surfaces to simulate typical heat loss. This is a reasonable average for various surface angles and is based on previous experimental work [57]. It is also assumed that the object has no conduction to the surface on which it is placed, again to simplify the simulation. This would be relatively easy to replicate in practice using insulated supports for an object.

4.2. Preliminary geometry for simulation of surface temperature profiles

Within the simulation software, it is possible to probe the FEA results to extract temperature data from the surfaces of the model. One of the options is feature selection; therefore, to access

profiles across surfaces easily and repeatedly, thin features were added so that edges were created from which all nodes can be extracted.

Figure 4-1 shows a simple block with a rectangular cavity. The factors designating the internal cavity's attributes can be adjusted in the CAD software. This is partially shown in Figure 4-1 as the imposed blue sketch on the front face of the block, showing how the cavity can be changed from planner to circular.

Other factors considered with the design of these initial computational models, were based upon what would be possible practically. The models needed to be small enough so they could be physically manufactured with the manufacturing equipment available (dimensions are shown in Figure 4-3 (L)). They also needed to have small relative heat capacities so that it would not take large amounts of energy to excite surface temperature gradients, but large enough internal cores so that any heat generation would be able to excite such gradients. Computationally, smaller model will require less nodes, compared to larger ones, so the simulations can be more efficient.

Also shown in Figure 4-1 are the nodal temperature extraction probe features as mentioned above. While SolidWorks® Simulation premium and other FEA packages provide some automation solutions such as Design Studies that enable a series of changes to be run, it was found that such studies did not return the specific nodal information over the edges of interest, therefore a series of manual updates were performed to get the data in this chapter. Solidworks® was chosen due to its combination of CAD modelling and FEA suite. This was more convenient than exporting the CAD model after every design change to another simulation package.

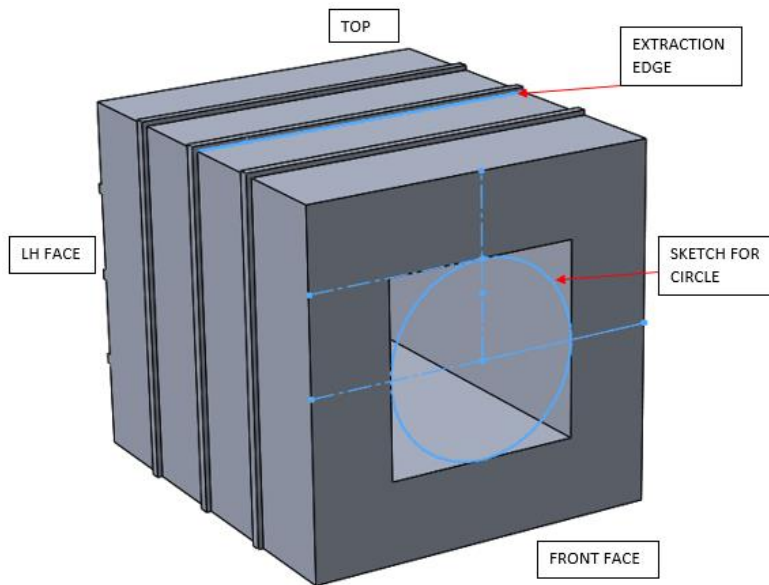


Figure 4-1: Simple block with cavity and edges for profile extraction

To begin with, the material assigned to the model was 1060 aluminium, which has a thermal conductivity of 200W/m k , and a specific heat capacity of 900J/Kg k . Aluminium was chosen as it was anticipated to be more challenging because of the speed at which homogeneity will occur and due to this, the potential for detecting gradients at the surface will reduce.

4.2. Heating inside the Cavity

4.2.1. Mesh

Before the simulations can commence the model needs to be meshed. As this is only a thermal simulation, disregarding the relatively small dynamic effects of thermal expansion, the mesh can be coarse in its generation. For the majority of the model an automated tetrahedral mesh, with an element size approximately 5mm is generated for the model. In the area around the extraction probe edge (shown in Figure 4-1), the mesh has been controlled to reduce the element size to 1mm . This will result in a data node every 0.5mm along the face of the model. Figure 4-2 shows the resultant meshed model. This mesh density level was determined by running various mesh densities and selecting the best compromise considering simulation time

and accuracy. The details of this process are included in *Appendix A*. The final mesh density is shown below (Figure 4-2)

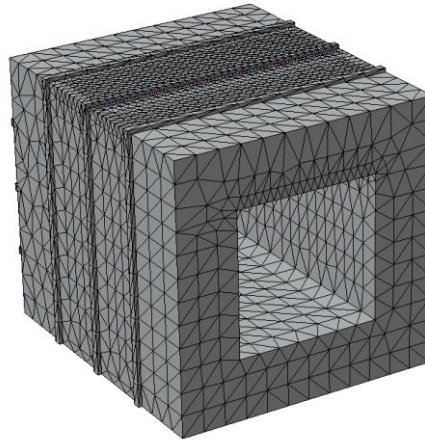


Figure 4-2: Resultant meshed model (note the denser mesh around the example edge on the top face)

4.2.2. Boundary conditions

The following is a summary of the boundary conditions that were used in most of the subsequent simulations. Later sections will use different materials, which affects the conductivity and specific heat capacity. Based on these different materials the simulation time and time step also change in later simulations

Table 4-1: Initial boundary conditions

Convective heat transfer coefficient	6 W/m/ °C
Thermal conductivity of aluminium	200W/m k
Specific heat capacity of aluminium	900J/Kg k
Initial ambient temperature	20°C
Initial surface temperature (external)	20°C
Initial core temperature	95°C
Simulation time	40s
Step time	1s

The simulation time of 40s, and time step of 1s were defined initially so that the following simulations would run efficiently, whilst maintaining a reasonable resolution. Both of these variables are adjusted in later simulations, based on different material simulation requirements.

From here, all simulations are split into two separate operations: an initial steady state simulation, to define the model's initial temperature condition, and the main 40s transient simulation. In the steady state simulation, a temperature of 20°C is applied, resulting in a homogenous temperature for the model. The main transient simulation then defines the model's initial condition from the results gained in the first simulation.

4.2.3. Initial simulation

The simulation is performed using the above-defined mesh and boundary conditions. Dimensions showing the initial geometric state are shown in Figure 4-3(L), and a mechanical drawing of the block can be found in *Appendix B*. After running the initial static simulation and importing the results into the main transient simulation, the following results were obtained: Figure 4-3 (R) shows the thermal distribution across the model, Figure 4-4 shows the spatial temperature across the top face extracted from the probe edge PE 2 (the parametric distance in the X axis is a ratio of the probe edge distance: 0-1 representing 0-70mm), and Figure 4-5 shows the temperature over time for every node along the same probe edge for the first 15s of the simulation. Whilst the simulation ran for T=40s, after T=13s the temperature had saturated the probe edge.

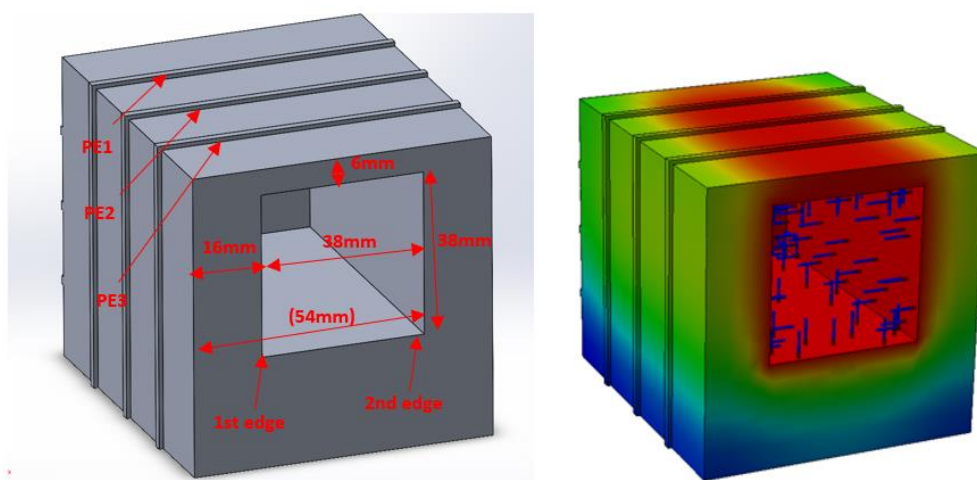


Figure 4-3 (L) The initial geometric factors used in this simulation, (R) thermal distribution after simulation

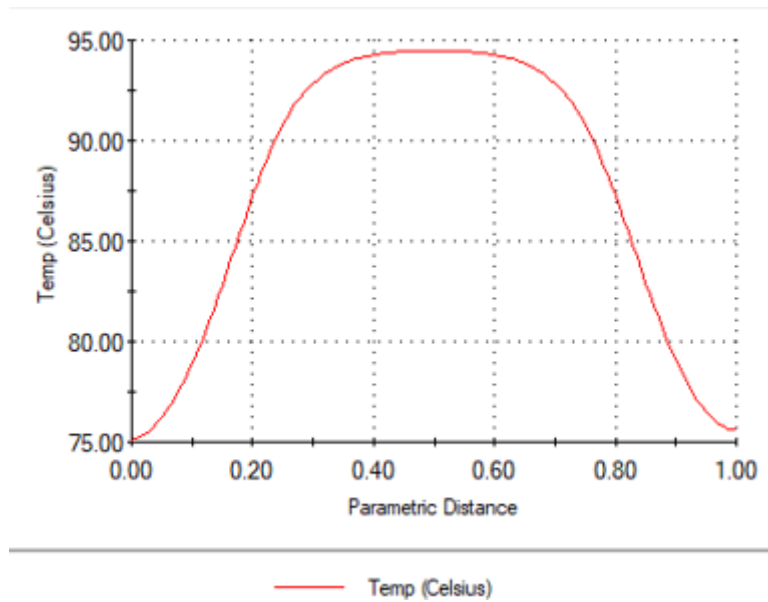


Figure 4-4: Spatial temperature distribution across probe edge PE2 at $T=40s$

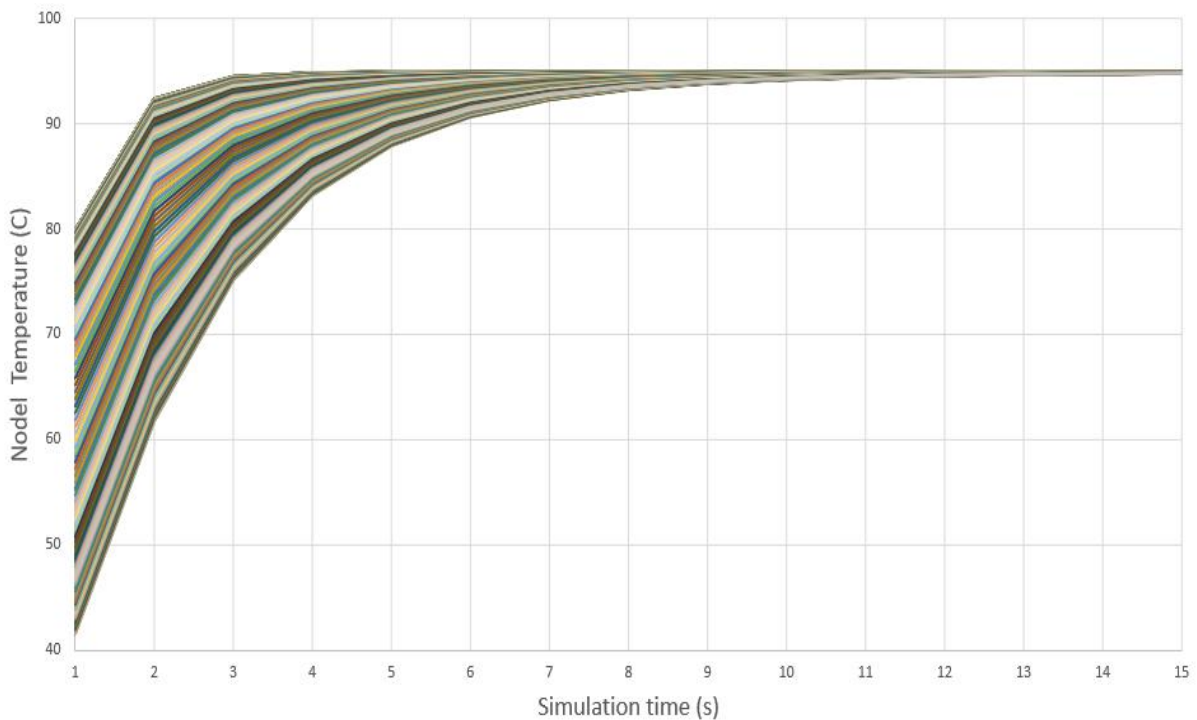


Figure 4-5: Temporal temperature due to time at all nodes along probe edge PE2

The data from Figure 4-5 is then saved and imported into a custom algorithm (*Appendix H.a - loadSW*) that can differentiate the temperature distribution for every time step. A logic diagram highlighting how *loadSW* operates can also be found in *Appendix H.a*. Temperature distribution differentiation is performed by the basic operator:

$$y' = \frac{dT}{dx} \quad (2)$$

Where T is temperature and x is the length (describe as parametric length). Figure 4-6 shows the resulting differentiated temperature data related to Figure 4-4. The largest rate of change within the distributed temperature should occur at the boundary regions, where the heat conduction transitions from the liquid to the solid wall. This is discussed below. The method for discerning the location of the largest rate of change (or peaks) within the differentiated data is a higher-than-next-neighbour peak detection function (Appendix H.b–*feapeaks*)

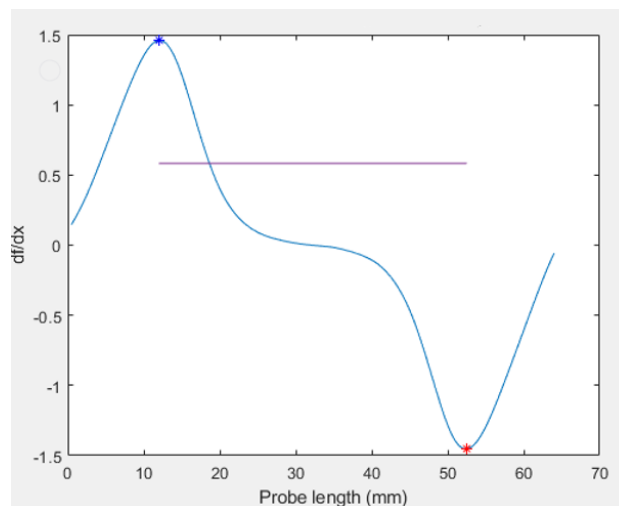


Figure 4-6: Differentiated data. MAX (blue) and MIN (red) marked as the detected peaks

The function *feapeaks* finds the maximum and minimum points within a set vector. A point is considered the maximum (or minimum) if the point preceding is lower (or higher) than a pre-defined variable.

In physical terms, maximum and minimum points in the differentiated data should be located on the boundary layer between the heating fluid and the surrounding material. The boundary layer is a region of space located “close” to a solid wall. How “close” this space is, remains the subject of much debate and will not be discussed in this thesis. The boundary layer is a distinct region, separate from the main convection domain in which both fluid velocity and temperature

changes from $u = u_0$ to $u = u_\infty$, and $T = T_0$ to $T = T_\infty$ respectively [58]. This is depicted in Figure 4-7

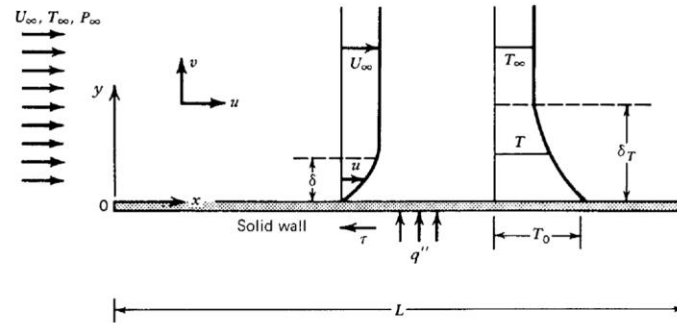


Figure 4-7: Depiction of laminar boundary regions, courtesy of Convection Heat transfer by A. Bejan [67]

This process is then repeated for every time step within the simulation. By doing this the MAX/MIN peaks position can be displayed temporally. As the object consists of planar features, it is not expected that the MAX/MIN positions will vary over time. Figure 4-8 shows the MAX/MIN positions for every time step.

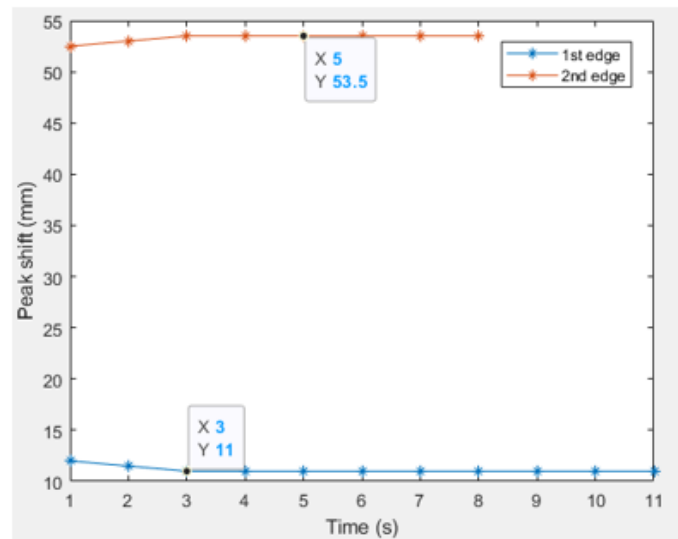


Figure 4-8: MAX/MIN edge positions over time

As can be seen in Figure 4-8 the average position for the first internal edge (nominally at 16mm) has been located at 11mm, and the average position for the second edge (nominally at

54mm) has been located at 53.5mm. Whilst this is a good result for the second edge, the position for the first edge is 5mm out of tolerance. At this stage in the investigation, it is not known what is causing this large discrepancy. This chapter will highlight multiple simulations, changing set factors to find the best solution.

Aside from the inaccuracy of the first position, it may be noted that according to Figure 4-8 there are only edge position results for the first eight time steps for peak 2 and 11 results for peak 1. This is due to the thermal conductivity of aluminium. Given the high thermal conductivity value, the model reaches homogeneity very quickly. For the first eight time steps, the results are all very similar to those shown in Figure 4-6, all with easily discernible MAX/MIN positions. As the model begins to homogenise, the location of the boundary edges becomes more difficult to detect as the difference between node temperature values becomes less. The differentiated temperature data goes from the clear results shown in Figure 4-6 to a more ambiguous result as can be seen in Figure 4-9 (L). The reduced differentiation in surface temperature is whole order of magnitude smaller due to homogenisation. This is clearly visible in the scales between the two plots in Figure 4-9. However, this is a useful observation as it shows that for objects whose material consists of a high value for thermal conductivity, the feature extraction process must be carried out almost immediately after the object has started to be heated.

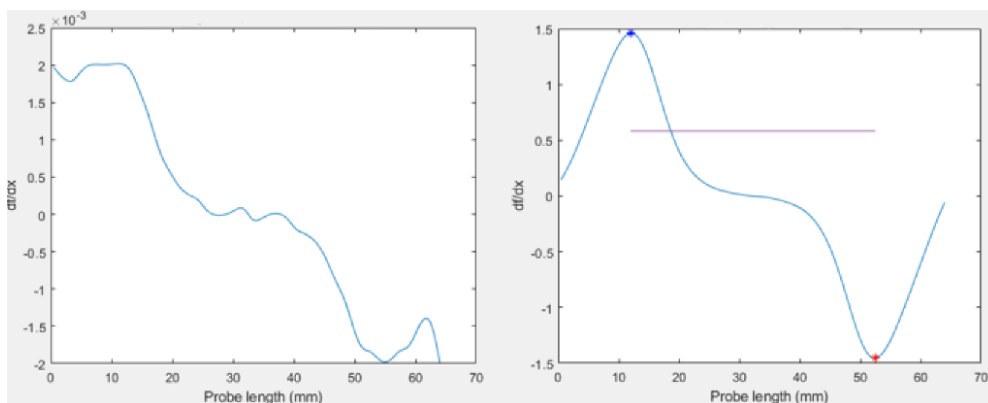


Figure 4-9: Differentiated temperature data at $T=31s$ (L), with a replication of Figure 4-6 (R) for comparison, at $T=2s$

4.2.4. Change of cavity depth.

It is clear that internal feature edges create measurable surface temperature changes. The next consideration is the relationship between this peak detection and the feature location. The CAD model was updated, the depth of the heated cavity relative to the surface where the probe edge is located. Reusing the model and setup used in the initial simulation in the depth of the cavity is adjusted through several iterations and then simulated after each one. Figure 4-10 shows the dimension that will be adjusted.

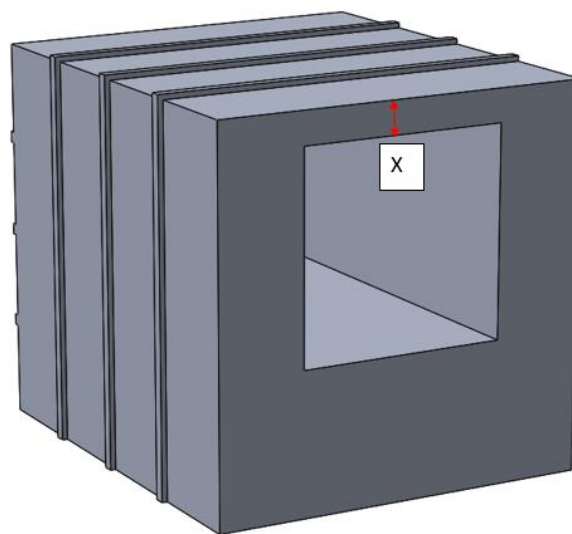


Figure 4-10: Adjusted depth dimension

In the first iteration, X is set to 2mm. For each subsequent simulation, X is increased by 2mm until the cavity is centred in the model, leading to X being 16mm. Individual temperature results and images of thermal distribution from each simulation can be found in *Appendix C.a*.

To compare the resultant sets of data from each simulation more effectively the algorithm used in section 4.2.3 has been modified to accept all data sets, which will then compile a single comparative result (*Appendix H.c – manySW*). A logic diagram for this algorithm can also be found in *Appendix H.c – manySW*.

Figure 4-11 shows the compiled edge positions for all eight data sets.

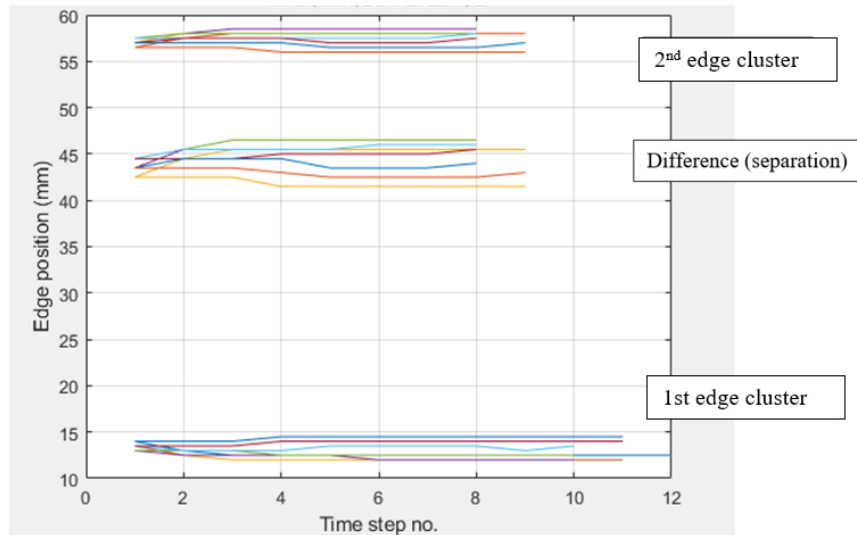


Figure 4-11: Compiled edge position for all eight-depth simulation. Refer to Figure 4-12 for edge convention

Figure 4-11 shows the 1st and 2nd edge positions, with the cluster of plots in the middle being the difference between the two. This cluster indicates the width of the cavity that is nominally 38mm. As this is difficult to visualise in Figure 4-11, this section is shown in more detail in Figure 4-13, with examples of the part geometry at the maximum and minimum depths simulated.

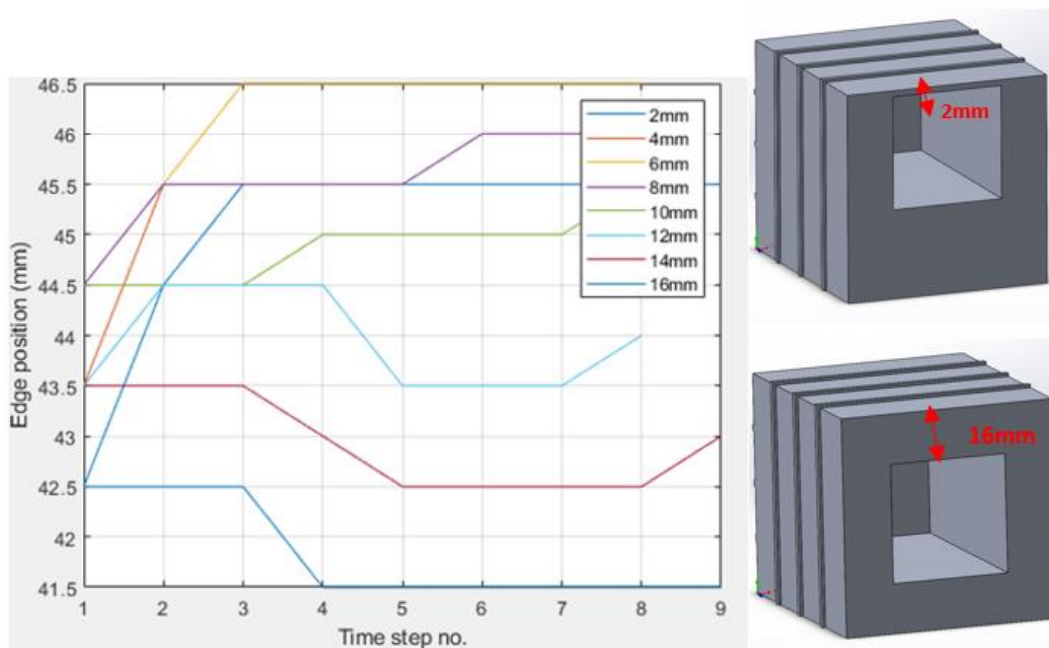


Figure 4-13: Cavity width deduced from edge position

As can be seen in Figure 4-13, by altering the depth of the cavity from 2mm to 16mm, the range in results is 5mm. By taking the average over time of each of the plots shown above and plotting them as a percentage of the nominal value, the trend of how the positional accuracy of the width of the cavity varies with depth becomes clear.

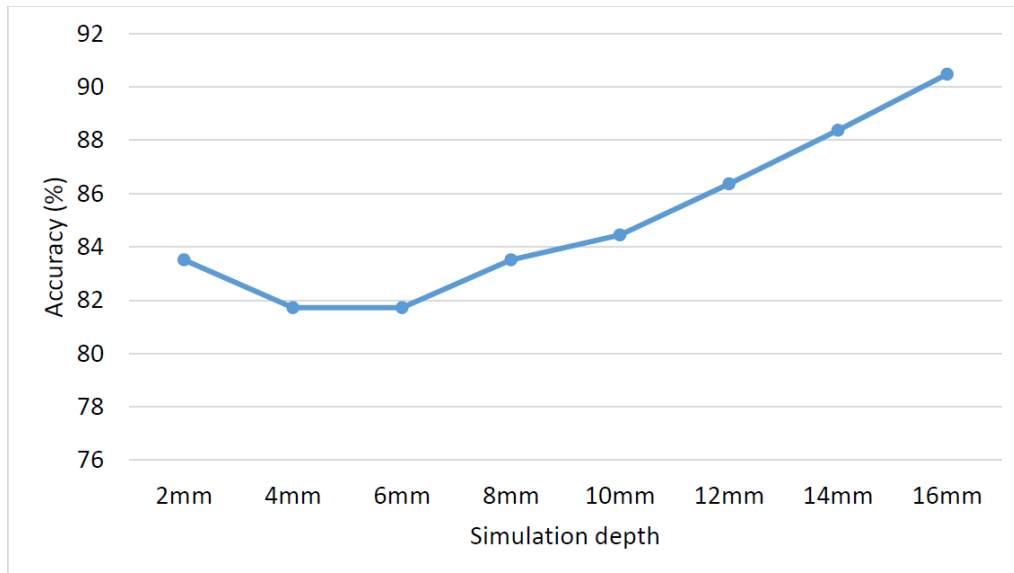


Figure 4-14: Percentage accuracy of cavity width with aluminium

As shown in Figure 4-14, the geometric accuracy of the cavity increases as the depth of the cavity from the surface is increased. This is most likely because the deeper the cavity is, the longer it takes for the surface temperature, where the probe edge is located, to saturate. At shallower depths, homogeneity occurs quickly, leading to poor results. This has shown that by increasing the depth of the cavity the uncertainty of the measurement is being reduced.

As the above results with aluminium are ambiguous, to ensure that this system can be used to determined cavity dimensions at varying depths, this set of simulations were repeated with a material of a lower thermal conductivity, in this case PLA. In addition, the simulations with aluminium are repeated over a much shorter period of 2s, with the time step frequency increased to 10Hz. Currently, the time step for the simulation is 1s or 1Hz. Increasing the

frequency will improve the simulation resolution, potentially allowing a better accuracy for these shallower scenarios at early values of t.

4.2.4.1. Depth Simulations with PLA

All eight depth simulations are repeated, starting with a depth of X=2mm, and going to X=16mm with an increment of 2mm, but with PLA used as the object material. The thermal properties used for PLA as shown in Table 4-2.

Table 4-2: Thermal properties of PLA

	Thermal Conductivity	Specific heat
PLA	0.111 W/m k (321k)	1590 J/Kg k (328k)
	0.197 W/m k (382k)	1955 J/Kg k (373k)
	0.195 W/m k(463k)	2060 J/Kg k (463k)

Simulations were first run for the same period (40s) as with the previous simulations using aluminium. However, the lower thermal conductivity of PLA meant that with deeper values of X no edge position values were recovered, as the heat transfer had yet to generate a suitable surface temperature gradient. Therefore, the period was increase to 320s for all of the PLA simulations. Figure 4-15, shows the complied edge positions for all eight simulations.

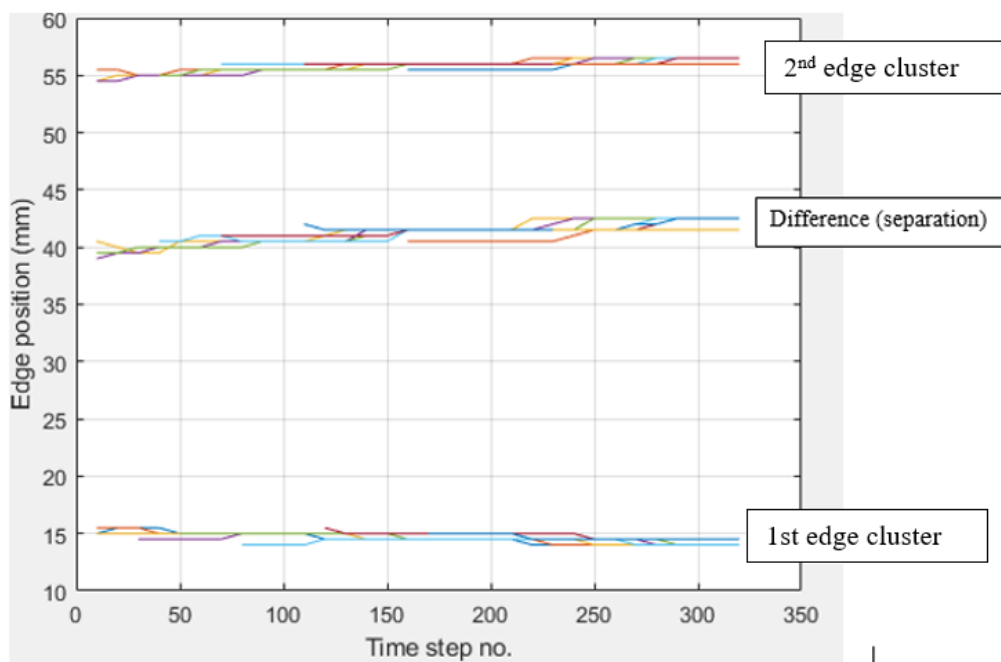


Figure 4-15: Complied edge position for all eight simulations with PLA

A selection of individual results can be found in *Appendix C.a*

As can be seen, compared to the edge positions found when the material was aluminium, shown in Figure 4-11, the results for edge position, and the separation distance are much more closely clustered together. The range of the average separation distances taken from Figure 4-16 for all eight depths is only 0.75mm, much lower than the 5mm found with aluminium. The accuracy of the average separation distance as a percentage of the nominal (38mm) is shown in Figure 4-17.

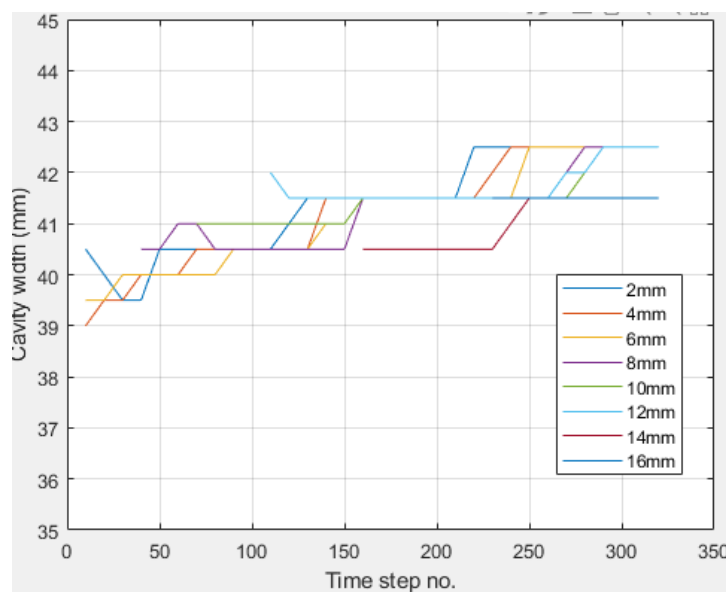


Figure 4-16: Cavity width deduced from edge position for PLA

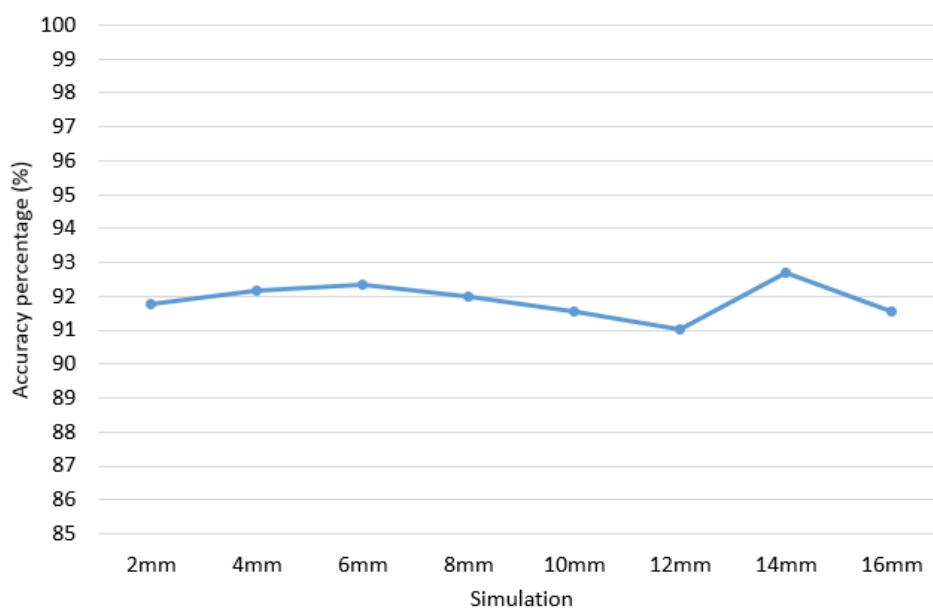


Figure 4-17: Percentage accuracy of cavity width with PLA

As can be seen in Figure 4-17, all of the average separation distances fall within 10% of the nominal, and compared to the average separation results in Figure 4-14 for aluminium, there is much less variation, an indication that the change in depth of the cavity has had little effect in this case.

This has shown that for materials with low thermal conductivity, changes in depth of the cavity will have little effect on the results recovered for internal edge position.

4.2.4.2. Smaller time step for the initial simulation period using aluminium

As previously stated, the period and time step for the aluminium simulations was adjusted to have a period of 2s and time step set to 10Hz. The 4mm depth simulation was then run with these new boundary conditions. The temporal results for cavity width are shown in Figure 4-18.

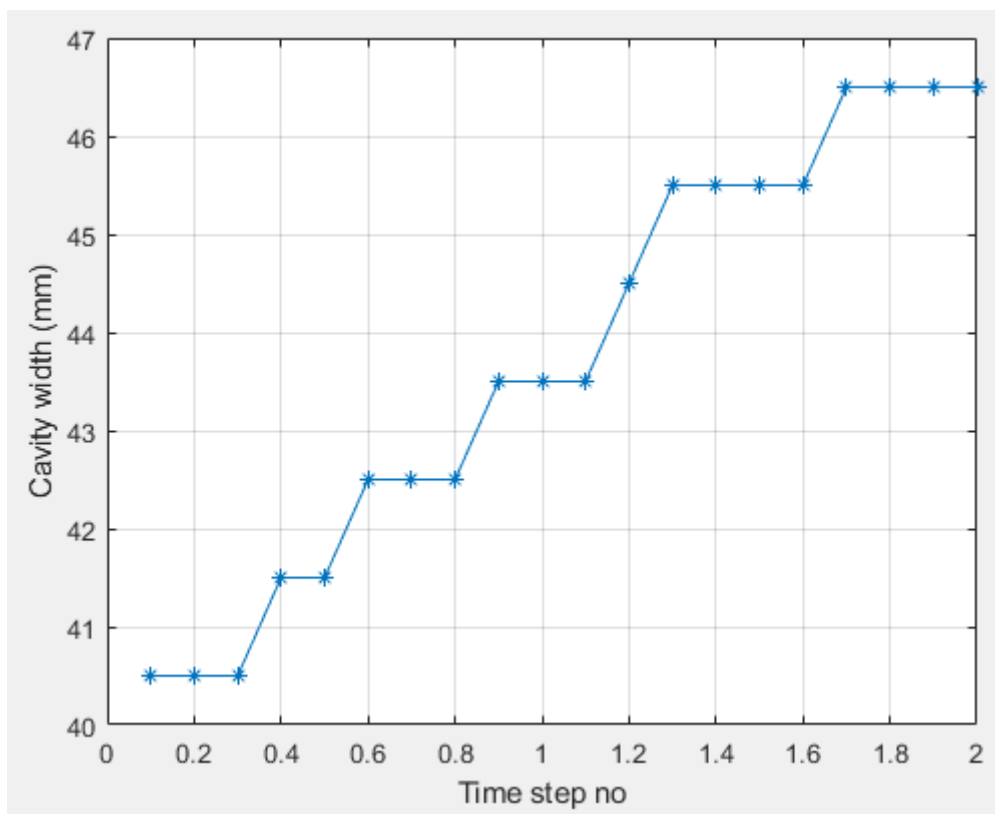


Figure 4-18: Cavity width for aluminium for 2s

As can be seen increasing the frequency has increased the resolution, however the average value for cavity width for this result is 43.75, meaning it is 86.9% of the nominal. This is a slight improvement on the 82% of nominal shown in Figure 4-14.

This result shows that high values for thermal conductivity still pose a potential issue concerning accurate edge recovery regardless of temporal resolution. However, the initial edge position at $t=0.1$ is closer to the nominal than was seen in Figure 4-13.

4.2.5. Change in width.

The next model parameter to be adjusted is the width of the cavity. The depth for this set of simulations will be set to 16mm to reduce the influence of saturation using aluminium and to focus on the width sensitivity in this preliminary work. Shown in Figure 4-19 is the dimension, Y , that is to be adjusted. Y will initially be set at 10mm, then adjusted every 5mm until $Y=60$ mm.

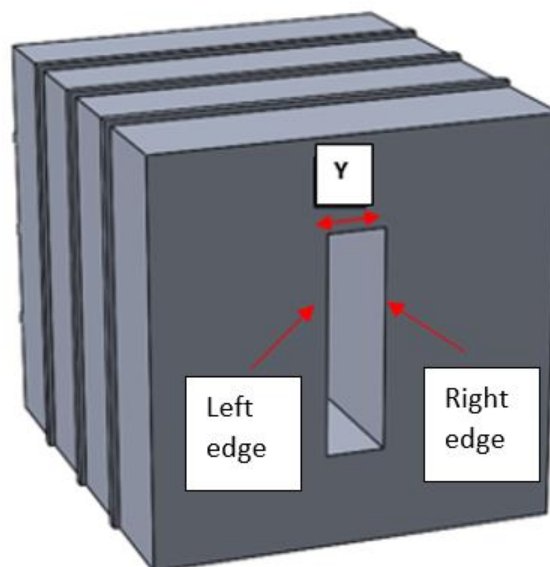


Figure 4-19: X marks the dimension (width) that will be changed

A selection of individual results can be found in *Appendix C.b*. All individual simulations are then passed through the program *manySW*. Shown in Figure 4-20 is the compiled edge positions

for all eleven-width change simulations. Figure 4-21 shows the compiled differences between edges, effectively showing the cavity width.

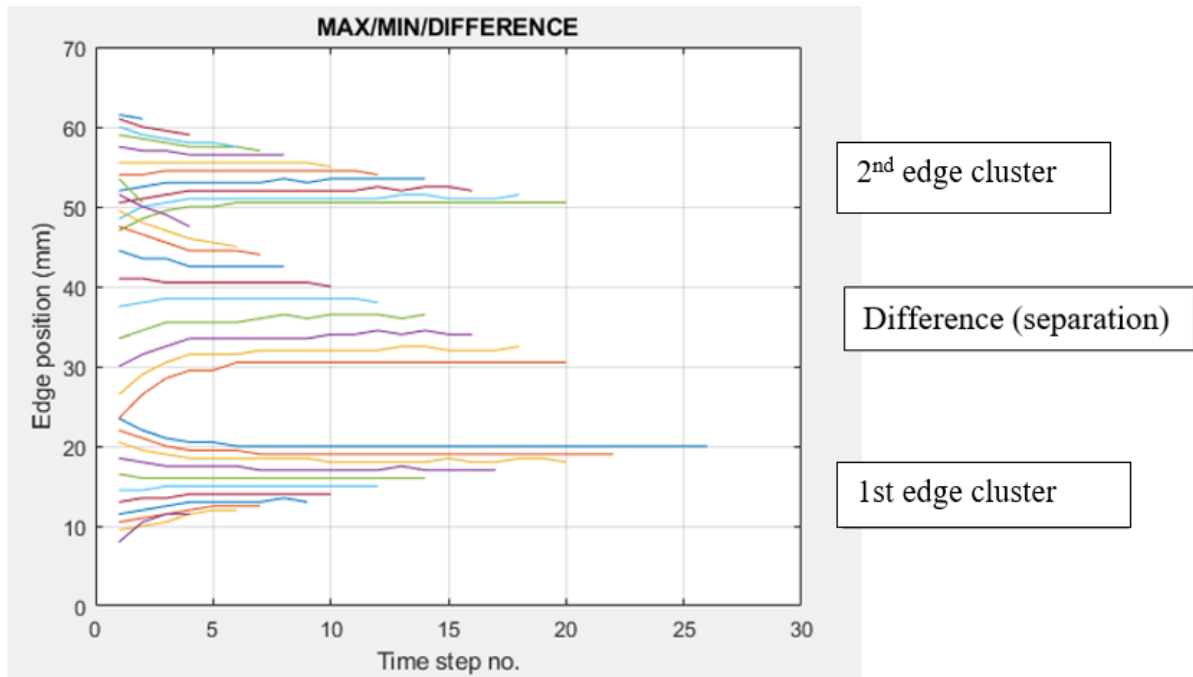


Figure 4-20: Edge positions and difference for all simulations

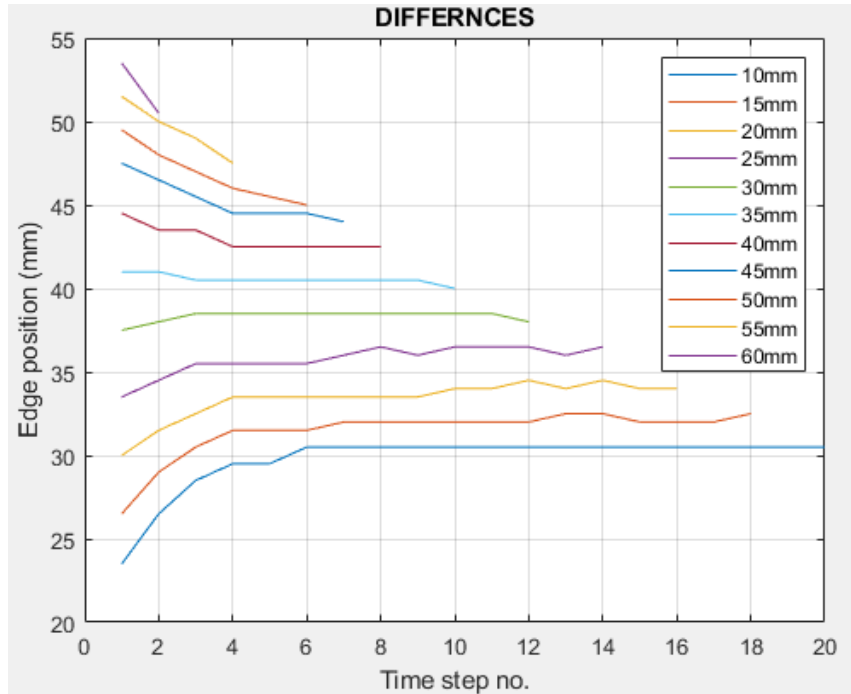


Figure 4-21: Cavity width over time

As can be seen in Figure 4-21, there is a discernible difference in the resultant geometric position of the internal edges, as the width of the cavity is increased. However, it is not

consistent with the nominal values for cavity width. This is explicitly shown for the first iteration where the cavity has a nominal value of 10mm. Here, the average result for discerned cavity width is over 30mm. The change in results is also not consistent with the change in the nominal values. Each nominal width change of 5mm is only producing an actual average width change of 2.15mm. Figure 4-22 shows the average actual width values recovered, along with the nominal values and the accuracy percentage for all eleven simulations.

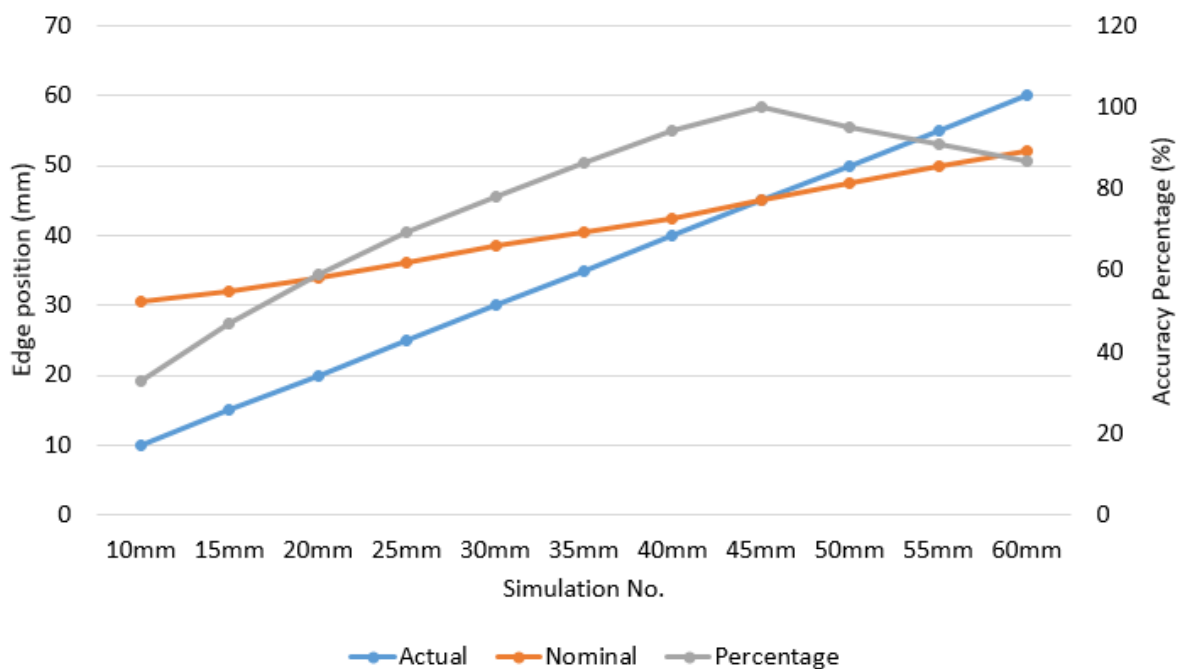


Figure 4-22: The actual and nominal results for changes in cavity width

Whilst a change in dimension has been observed here, the overall result is poor. This could be because aluminium has a very high conductivity; therefore, temperature saturation occurs very quickly. Subsequently, this round of simulations is repeated but with a different material - 316 stainless steel, another common engineering material, which has a lower thermal conductivity. Using 316 it is intended that homogeneity will take longer to occur. By doing this it is hoped that more accurate results can be recovered. 316 stainless steel has a thermal conductivity coefficient of 16.3W/m k, and a specific heat capacity of 500 j/Kg k. The simulation with this new material is rerun for cavity widths 10, 20, 30, 50, 50 and 60mm.

Figure 4-23 shows the cavity width over time.

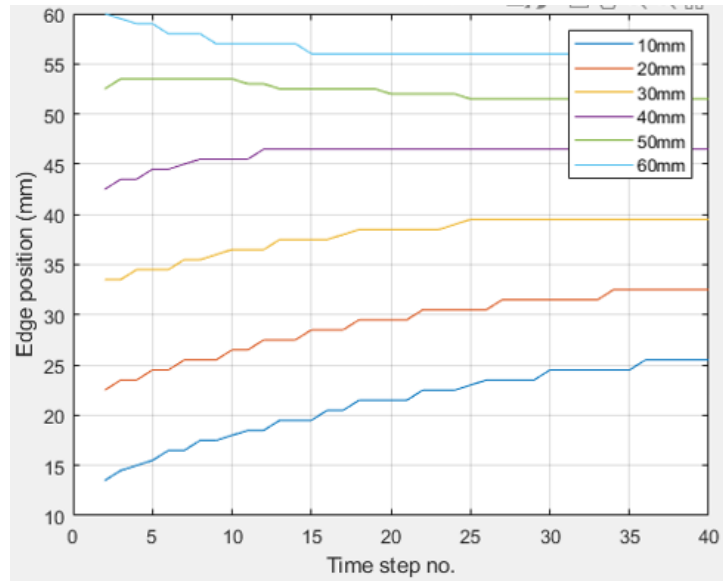


Figure 4-23: Cavity width over time for 316

As can be seen in Figure 4-23, the recovered value for cavity width does drift over time. However, the first result recovered for each simulation is approximate to each simulation's nominal value, and more correlative then when aluminium was simulated. This is shown in Figure 4-24.

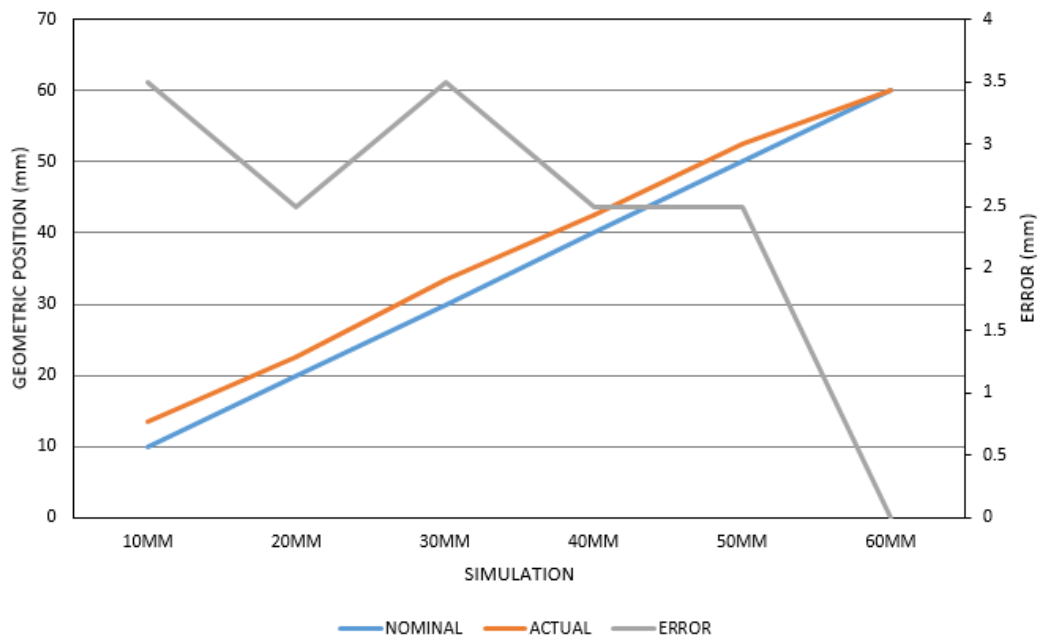


Figure 4-24: Error between nominal start points and actual

This indicates that in future physical validation, attention should be paid to the first few seconds of the test, as the best estimate for what the size of the feature is, might be found in this period.

4.2.6. Change in thermal conductivity

As has been observed in the previous two sections, thermal conductivity can have a significant effect on the geometric results obtained using this method. To evaluate in more detail the effects of thermal conductivity, the original simulation used in section 4.2.3 has been re-simulated several times, utilising several different materials with different thermal conductivities. Table 4-3 indicates the materials that were used, along with each material's thermal property variables [59] [60]. The multiple values for specific heat and thermal conductivity for PLA, is because the temperature effect on thermal conductivity differs with regards to metals and non-metals. In metallics heat conductivity is due to free electrons within the atomic structure. Unless the material is close to absolute zero, heat conductivity is relatively constant regardless of temperature. However, in non-metals heat conductivity is due to phonons, or lattice vibrations. Due to this thermal conductivity as well as specific heat capacity and vary with respect to the temperature variations [61].

Table 4-3: Materials and their thermal properties.

Material	Thermal conductivity (W/m k)	Specific heat (J/Kg k)
Copper	390	390
Aluminium	200	900
Steel	16.3	500
Nylon	0.53	1500
PLA	0.111 (321k) 0.197 (382k) 0.195 (463k)	1590 (328k) 1955 (373k) 2060 (463k)
Ceramic	1.4949	877.96

Other than the above-mentioned thermal properties, no other vectors are adjusted for these simulations. Shown in Figure 4-25 is the same cavity width over time based upon different material thermal properties (individual results can be found in *Appendix C.c*). As in certain previous simulations, the materials with high values for thermal conductivity, namely

aluminium and copper, homogenise the fastest, only producing results for the first six and eight iterations respectively. Their initial value is also much higher than the rest, as has been seen with the previous results for highly conductive materials. The results for steel indicate that whilst the object has not homogenised (as results are still being recovered); it has reached steady state equilibrium, with the energy being imputed by the core temperature, equal to that removed by convection. For ceramic, nylon and PLA, the results show that the object has not homogenised, and results with minimal drift are still being recovered

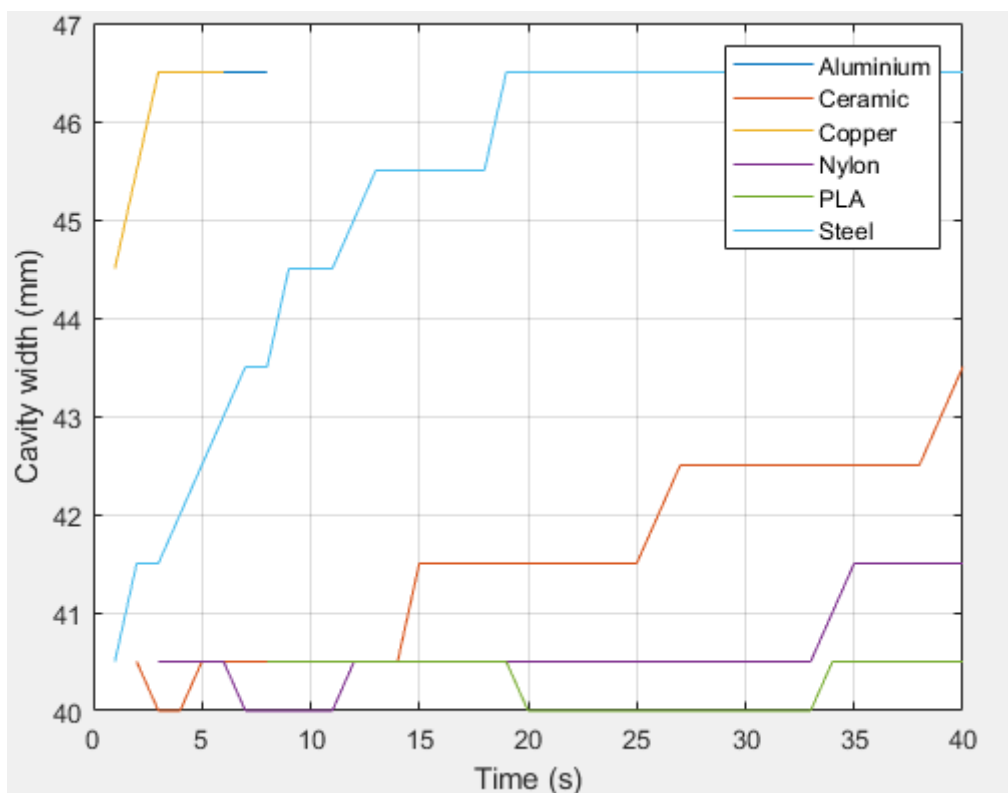


Figure 4-25: Edge positions due to varying material thermal properties

Whilst the ceramic and nylon simulations do show signs of edge shift, especially towards the end of the simulation, the edge positions from the PLA simulation only show a 0.5mm shift over the entire simulation. It is also worth noting that in the PLA simulation edge position only becomes apparent at T=7. This is because before T=7, there will be no discernible temperature change on the probe edge surface due to the low conduction coefficient.

From this round of simulations, it has been shown that at this stage in the investigation, a plastic material such as those simulated above would be the best material option to be used in a physical experiment. The low thermal conductivity allows greater time to recover more accurate edge positions. To indicate this, the simulation for PLA was re-run but for a much longer period, increasing from 40s to 600s. The time step was also increased to 10s to allow for a more efficient simulation. The position of both edges over time is shown in Figure 4-26.

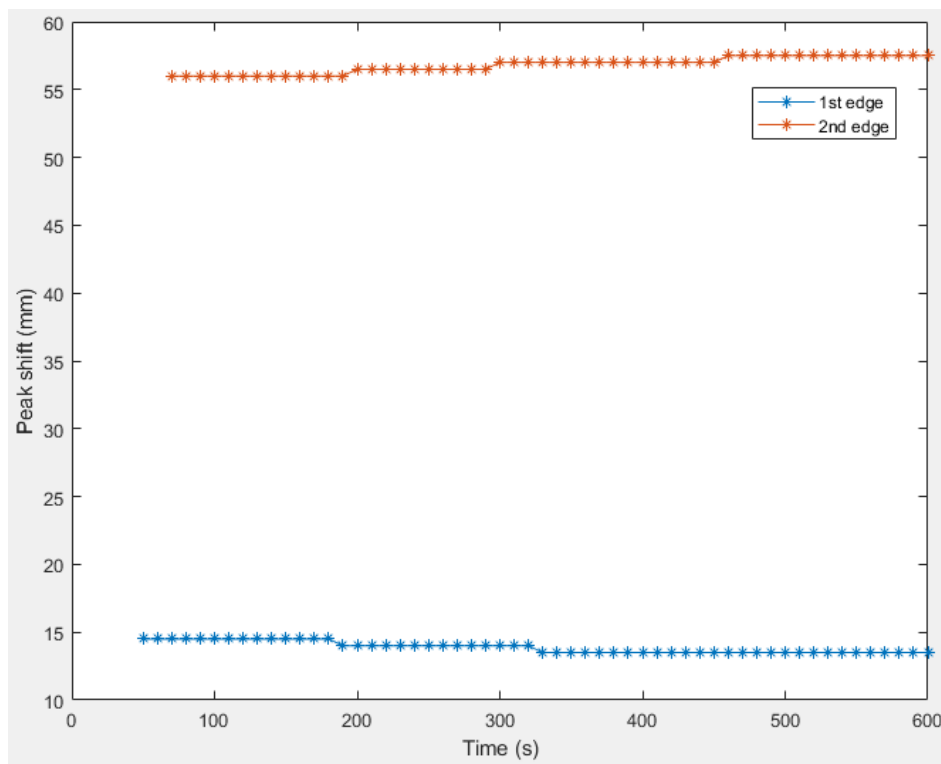


Figure 4-26: Edge position over time for PLA over 600s

As can be seen in Figure 4-26, due to the low thermal conductivity, edge position drift takes much longer to occur offering more stability results over time.

4.3. Edge drift vs Edge Curvature/Angle.

As has been observed throughout this section of the investigation, regardless of the material of the object, the recovered position of the edges shifts over time. This is due the observed edge position transitioning through the material over time due to the increase in temperature. The

speed at which this transition occurs is linked to the material thermal conductivity, as was shown in Figure 4-25. For material with high thermal conductivity, this edge shift occurs quickly and results in a steep gradient if shown over time as seen in Figure 4-25 with steel this drift was over 5mm in as little as 15s. This presents a problem when approaching the possibility of recovering curved or angled internal geometry. Until this point, the simulations that have been run have had planar internal geometry. However, if the internal geometry was curved or angled, the recovered result would be expected to shift over time as the highest temperature differential observed on the surface of the object moves across the curvature of the internal geometry.

To demonstrate this a comparison was performed between the simulation used in section 4.2.3 and remodelled versions, which consist of circular or angled internal geometry with a corresponding internal surface area. By keeping the surface area of the three models as close as possible, the cumulative heat power would be consistent.

The geometries used in these simulations are shown in Figure 4-27.

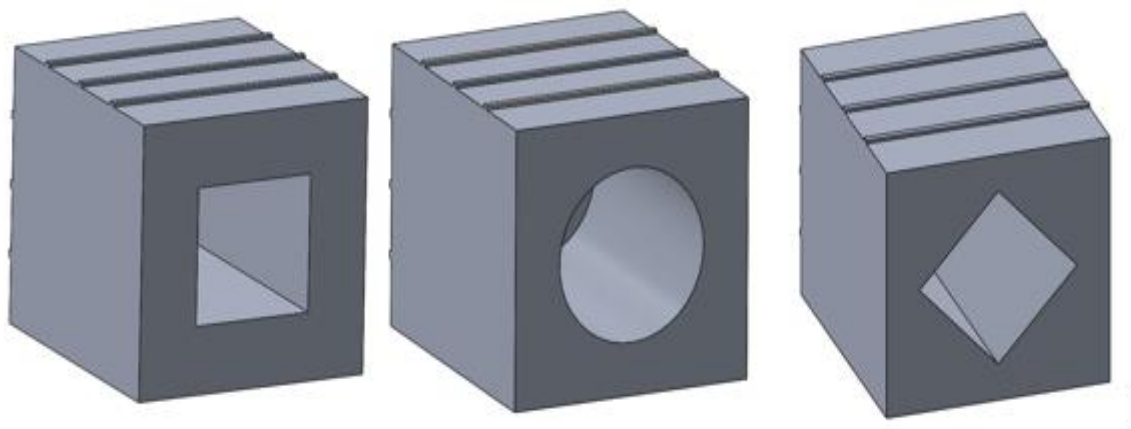


Figure 4-27: Square, circle, and angled geometry

For the cuboid feature shown in Figure 4-27 the length and width are 38mm by 38mm, with a depth of 70mm from the open face. The angled feature is the same but rotated 45°. The circular feature has a diameter of 43.5mm, with the same depth as the other two. This results in a total

internal surface area of 11025mm² and 11052mm² for the square/angled features and circle features respectively. The two values for surface area (A), along with the coefficient of thermal conductivity coefficient for PLA, 0.197W/K m (λ) and the temperature difference (t), will allow for the calculation of the absolute thermal conductivity for both models using the equation below.

$$\lambda_A = \frac{\lambda * A}{t} \quad (2)$$

For the cuboid and angled cuboid models, the absolute thermal conductivity is 2.8x10⁻⁵W/K and 2.9x10⁻⁵W/K for the cylindrical model. PLA, which has a very low coefficient of thermal conductivity, shows the smallest edge drift over time, and is therefore the best option to demonstrate this edge drift due to curvature.

Figure 4-28 shows the results for edge position from the cuboidal internal profile.

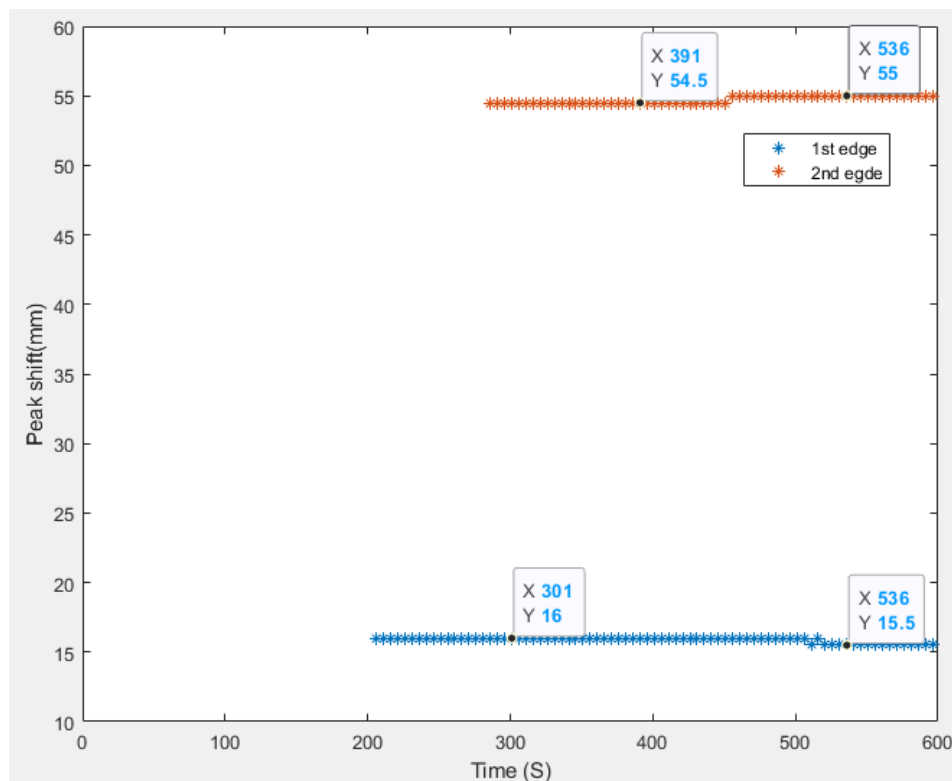


Figure 4-28: Square profile edge position results

As can be seen in Figure 4-28 the edge positions results are relatively stable with a standard deviation of 0.21mm and 0.25mm for the 1st and 2nd edges receptivity. With the same material and the same set of boundary conditions, Figure 4-29 shows the edge positional results for the cylindrical and angled internal profile.

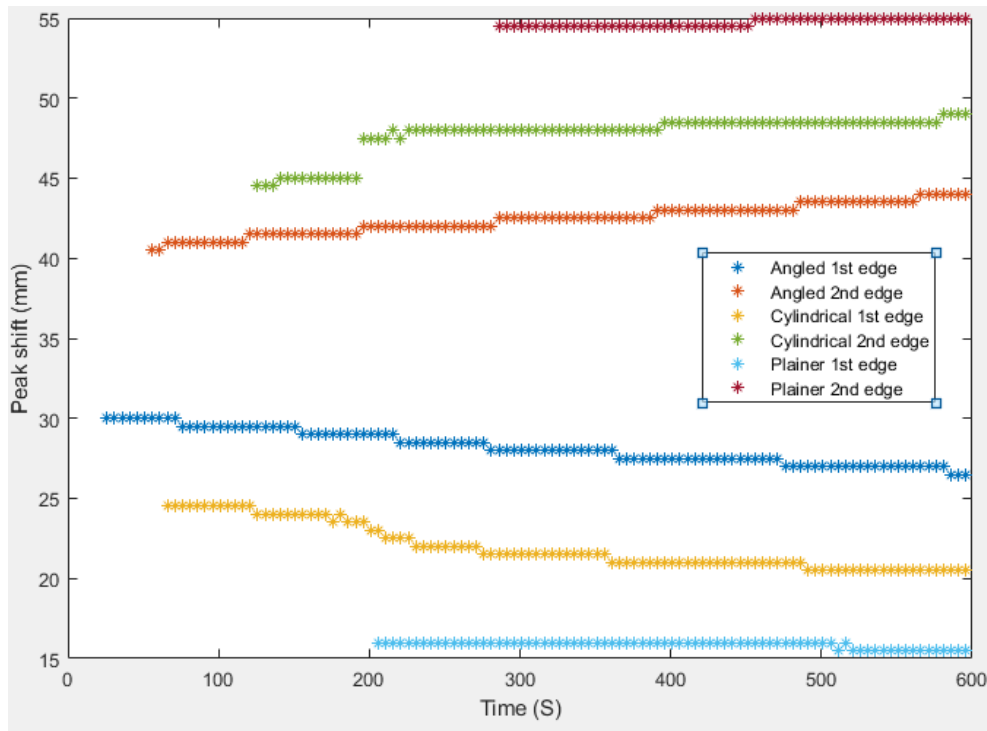


Figure 4-29: Internal profile edges position results

As can be seen in Figure 4-29, the edge positions over time for all three internal profiles differ in resolved curvature. This is partially verified by comparing the standard deviation of each result.

Table 4-4: Standard deviation of temporal results

	1 st edge	2 nd edge
Plainer	0.21mm	0.25mm
Cylindrical	1.41mm	1.24mm
Angled	1.03mm	0.90mm

As seen in Table 4-4 the standard deviation for all compared temporal results differs with each internal profile (full data can be found in Table C-1 in *Appendix C*). This would highlight a distinct change in internal geometry.

This temporal difference is better highlighted by comparing the best-fit curves taken from the difference between the 1st and 2nd edges in Figure 4-29, (graphical results can be found in *Appendix C.d*). From observation, the curvature appeared exponential in each case therefore an exponential curve fit was used and gave good results in each case. This comparison is shown in Figure 4-30.

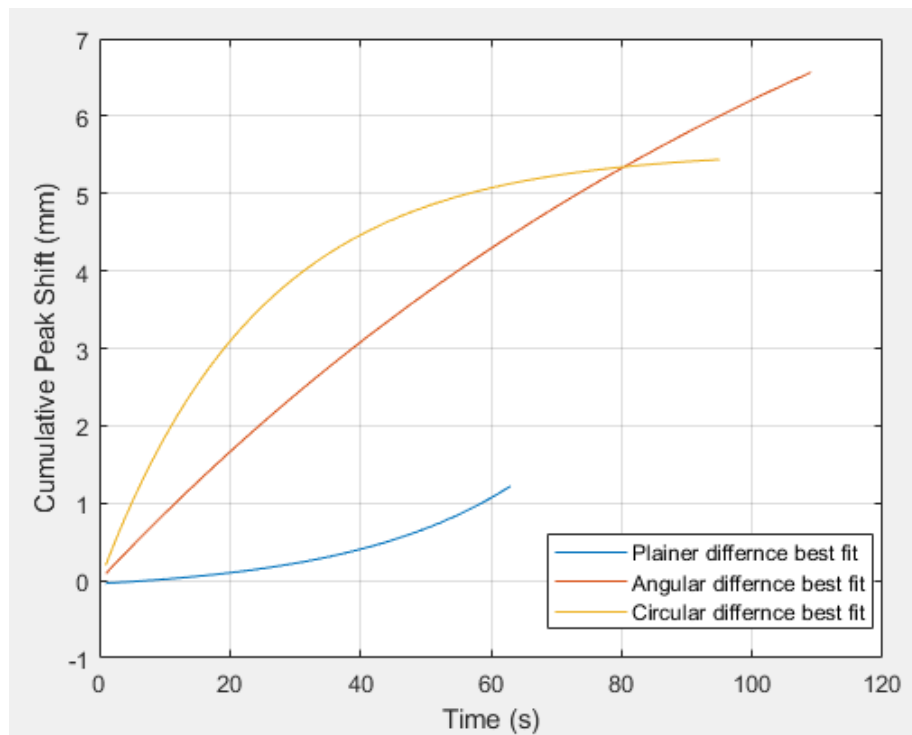


Figure 4-30: Best fit comparison between edge separation differences

Comparing the results in this way, it can be seen that even though the inputted thermal power and material properties are the same for all simulations, three different responses are recorded. With internal perpendicular planar faces, very little edge shift is recorded. For curved internal faces, a curved response with an initial steep gradient and large amount of curvature is seen. This is compared to a shallower less curved response, as seen from the angled face.

This variation in response allows the potential validation of different internal geometry based upon the shape of the time-based result that are recovered.

4.4. Adjusting Internal Temperature.

As has been seen in sections 4.2.6, materials with high values for thermal conductivity, show large values of edge position drift, and the surface temperature gradient homogenises after a very short time. The energy input being added by the simulated addition of water at 95°C is overwhelming the energy output created by the convection boundary condition. This is compounded in these simulations, as there is no simulated natural cooling of the water. These factors lead to quick homogenisation. In an attempt to increase the time it takes homogeneity to occur and reduce the edge position drift, the introduced energy was reduced by lowering the internal temperature. This was performed by repeating several iterations of the initial simulation in section 4.2.3. and incrementally lowering the values for internal temperature in each iteration. For the first simulation, the internal temperature was set to 95°C, and then reduced by 10 °C for every subsequent simulation until 25°C was reached. Figure 4-31 shows the surface temperature profile along the probe edge for all simulation iterations.

From the simulation results, reducing the internal temperature has no effect on the recovered values for peak position, with the same amount of edge position drift being observed. Concerning homogeneity, decreasing the temperature had homogeneity in the surface temperature gradient occurring faster than at higher temperatures. This was due to much less energy being required to homogenise the material at lower temperatures. This in turn led to fewer result over time for peak position, than was recovered at higher temperatures.

Concerning the physical experimentation when using artefacts of low thermal conductivity where homogeneity is less of a concern, this result shows that any significant temperature drop

in the heating medium before it is added to the artefact should not be an issue as peak positions could still be recovered even at low temperatures.

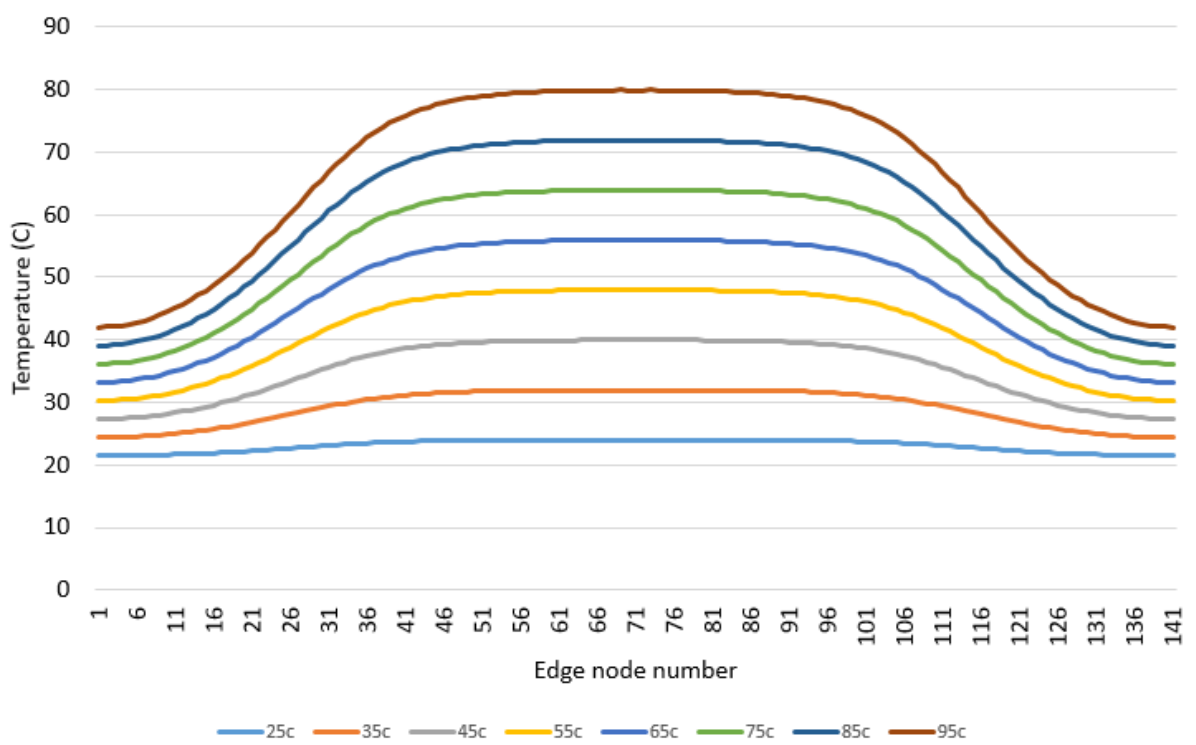


Figure 4-31: Surface temperature profile for all simulations at $t=5s$

4.5. External Heating

Currently, the simulations so far have been based upon the idea that the temperature gradient of an object can be altered by heating the internal features by means of an introduced medium such as boiling water. However, this might not always be possible. Certain engineering objects may consist of an internal structure that is sealed from the outside environment, especially with additive manufacture becoming more widely used within industry. In this section, the idea of externally heating the object is introduced. By heating one side of the object, and observing the opposite side, it is envisaged that the internal structure of the object will have pockets of insulation assuming that air has a lower conductivity than the solid, which is most often the case.

The thermal conductivity of air to be used in these simulations is assumed to be 0.025W/m k with a specific heat capacity of 100J/Kg k [62]. Disregarding radiative heat transfer, this will give a much less efficient mode of heat transfer than the surrounding walls of the cavity.

Figure 4-32 shows the boundary conditions for the side heating simulation. The CAD model in this simulation is recycled from the simulation used in section 4.2.3; however, it is not a single CAD entity but an assembly. The cavity in the object has been filled with another model representing the air. The two parts have bonded contacts with an applied heat transfer coefficient of $6\text{W/m}^2\text{°C}$ on all interacting faces.

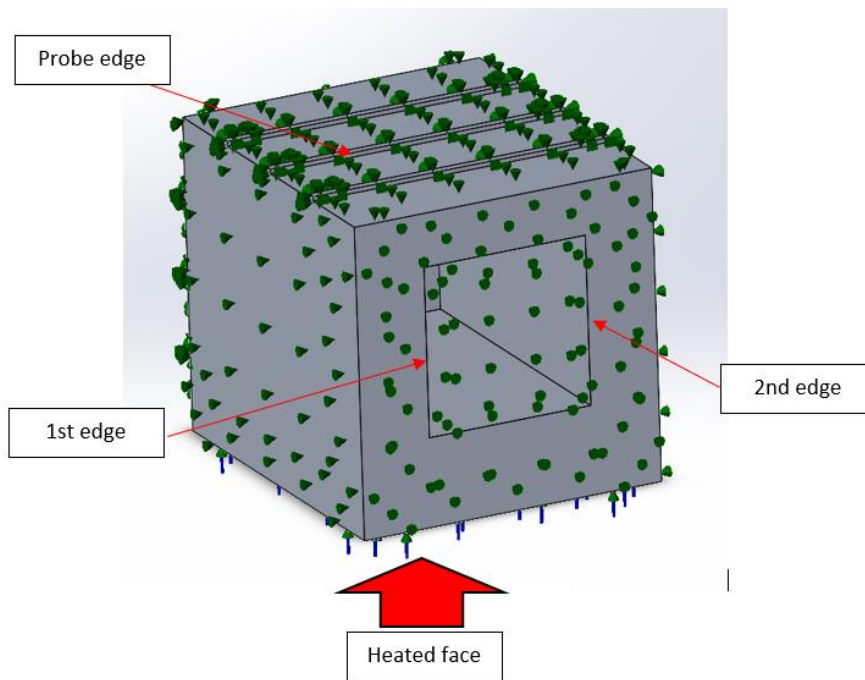


Figure 4-32: Simulation set up for side heating

In Figure 4-32, the green arrows represent convection with air with a coefficient value of $6\text{W/m}^2\text{ K}$. Again, the temperature is set to 95°C , on the underside face indicated by the red arrow. The period for this simulation was 40s with 1s time step. The material for this simulation is aluminium.

Figure 4-33 shows the thermal distribution across the object at $t=15s$, and Figure 4-34 shows the thermal distribution across the probe edge, again at $t=15s$. Finally, Figure 4-35 shows the nodal temperatures across the probe edge for every time step.

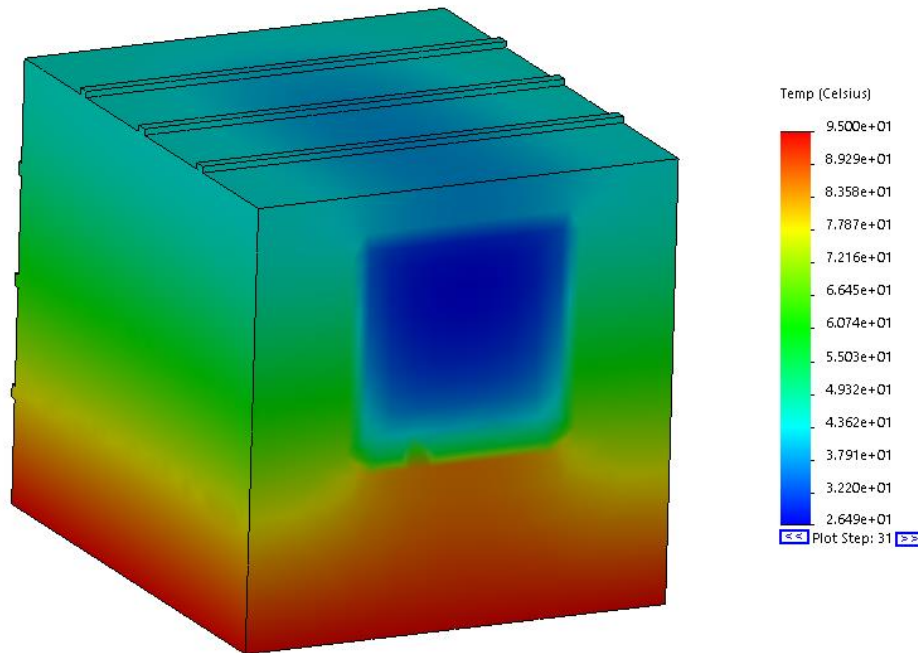


Figure 4-33: Thermal distribution across model at $t=15s$

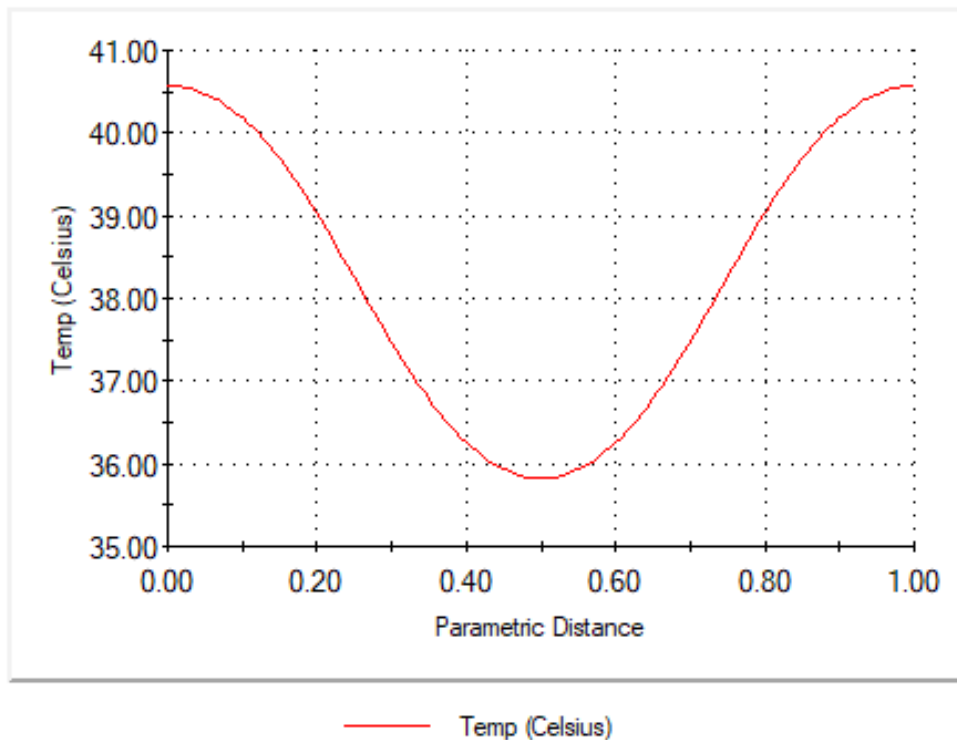


Figure 4-34: Thermal distribution along probe edge at $t=15s$

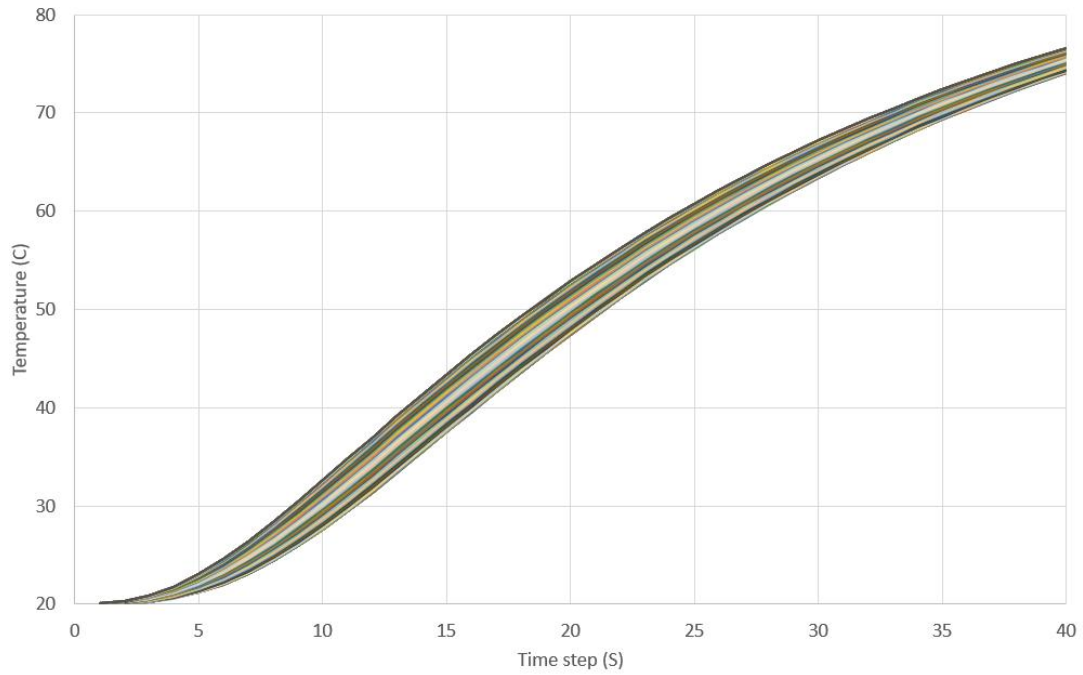


Figure 4-35: Nodal temperatures for each time step

The thermal data recovered (shown in Figure 4-35) was then entered into *loadSW*. The edge positions returned for this simulation are shown in Figure 4-36.

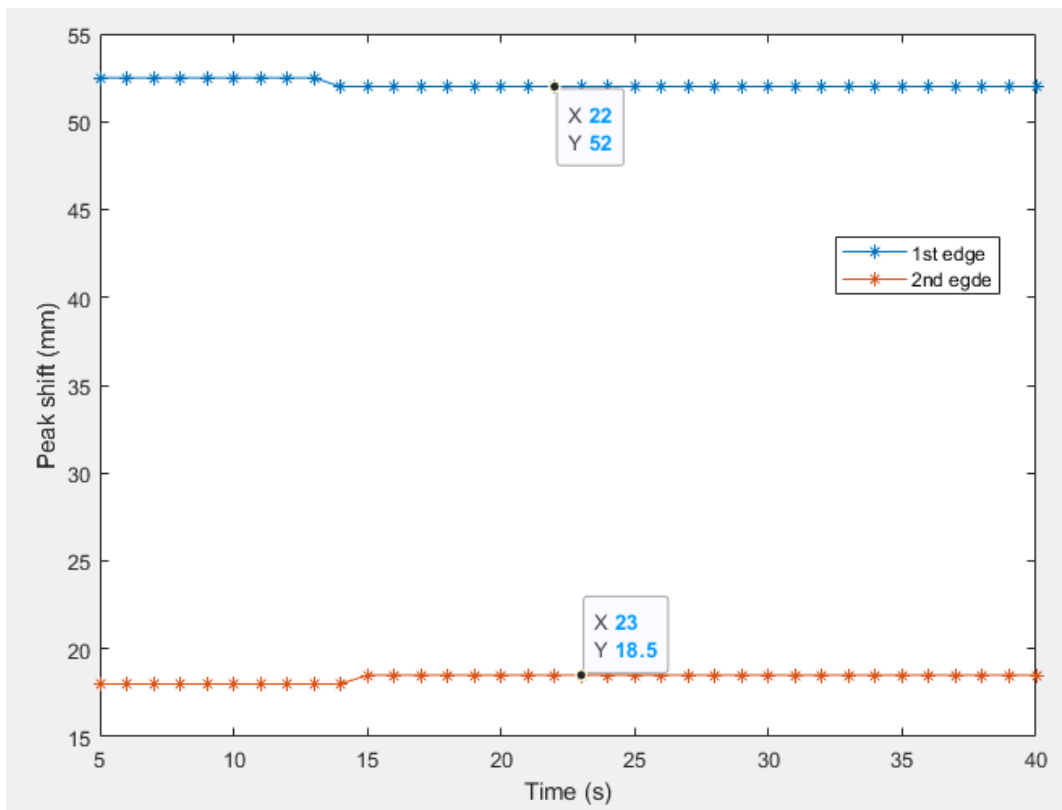


Figure 4-36: Edge position over time for side heating simulation

As can be seen in Figure 4-36, the gathered results are extremely consistent over time, and are very close to the nominal value for the internal edge position. The average edge positions shown here are 52.4mm and 18.3mm. For this object, the nominals are 54mm and 18mm respectively.

It can be seen that for this model, with this set of boundary conditions, heating the object from the side and then taking the results from a parallel side, leads to the recovery of a much more stable set of results than if the internal cavity heating method was used. This is because the induced power per surface area is less using this technique. As the power input is less, power output by convection is not being overwhelmed. This in turn means it takes longer for homogeneity to occur, allowing for a more stable temperature gradient over time from which edge position results can be more optimally gathered. This is shown in Figure 4-37, where the average surface temperature from side heating is compared against the average surface temperature from internal heating.

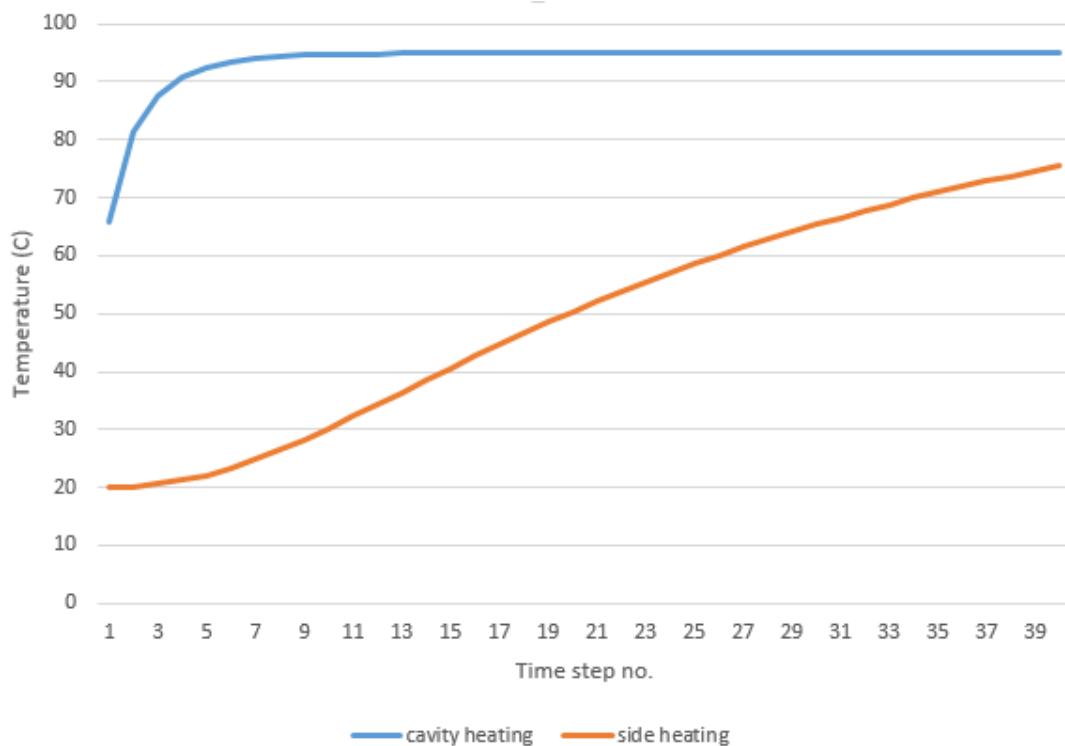


Figure 4-37: Average temperature profiles over time for cavity heating and side heating on aluminium block

With cavity heating, the temperature of the aluminium block saturated after only a few seconds leading to homogeneity. This resulted in only a few time steps producing meaningful edge position results. With side heating, the blocks temperature is still rising and in relation to Figure 4-37, has not saturated even after 40s. That has resulted in almost all time steps yielding a result for edge position.

This side heating simulation was then run again at differing widths. Figure 4-38, denoted by X, shows the dimension that is to be changed; starting at 10mm wide, and being repeated in 5mm increments up to 60mm. Figure 4-39 show the compiled results for the recovered value of X taken from the thermal data. Individual results can be found in *Appendix C.e*.

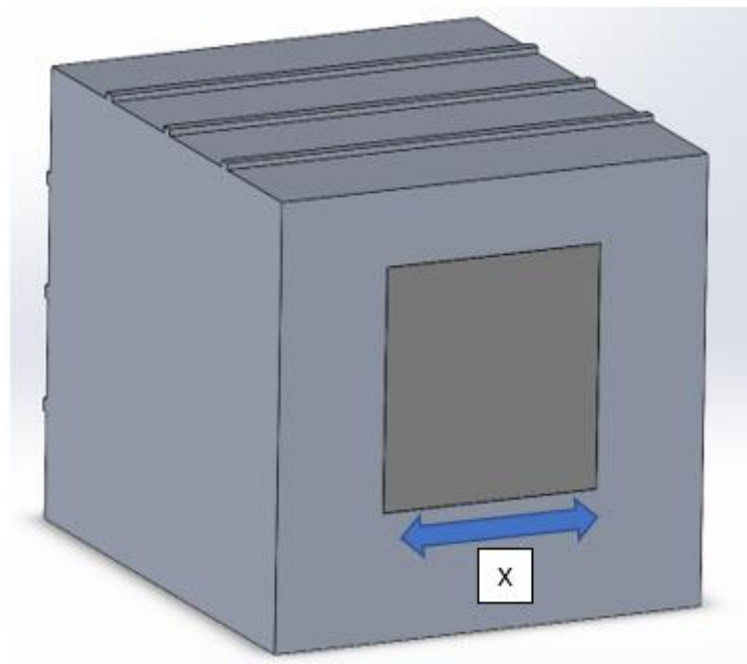


Figure 4-38: X showing the dimension to be changed in this series of simulations

Dimensional results were not obtained for the 10mm and 15mm simulations, as no suitable surface temperature variation denoting the two internal edges were distinguishable at any point of the simulation. However, edge positions leading width values for X were extractable at all steps from 20mm upwards. As can be seen in Figure 4-39, once stabilised, comparative results

(to the nominal) were obtained for each width step. Table 4-5 compares the nominal width step to recovered values for those steps.

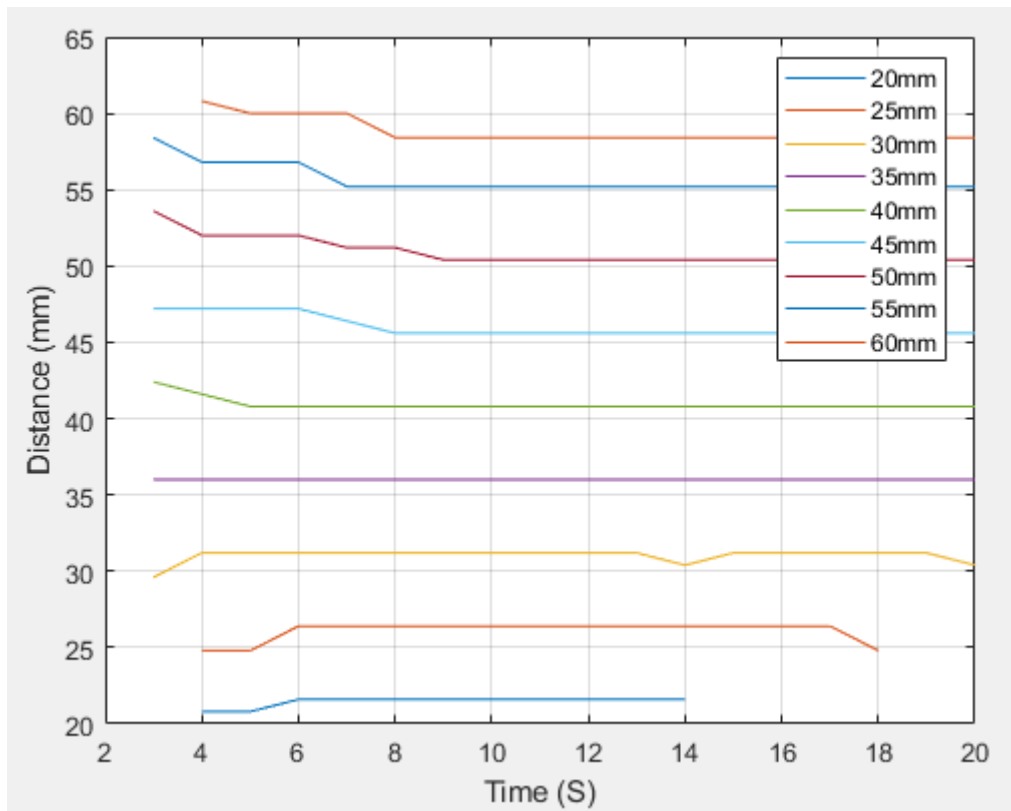


Figure 4-39: Resultant dimensional data for width change from side heating simulations

Table 4-5: Table showing comparative results from side heat simulations with change in width

Nominal step (mm)	Recovered average value (mm)	Error percentage (%)
10	NA	NA
15	NA	NA
20	21.5	93.02
25	26.1	95.79
30	31	96.77
35	36	97.22
40	40.9	97.8
45	46	97.82
50	50.9	98.23
55	55.6	98.92
60	58.8	98

When comparing this error percentage in the above table to that recorded in the width change simulations (Figure 4-22), using internal heating in section 4.2.5, the results show that side

heating with aluminium present far more comparable and constant results then with internal heating. This is shown in below in Figure 4-40.

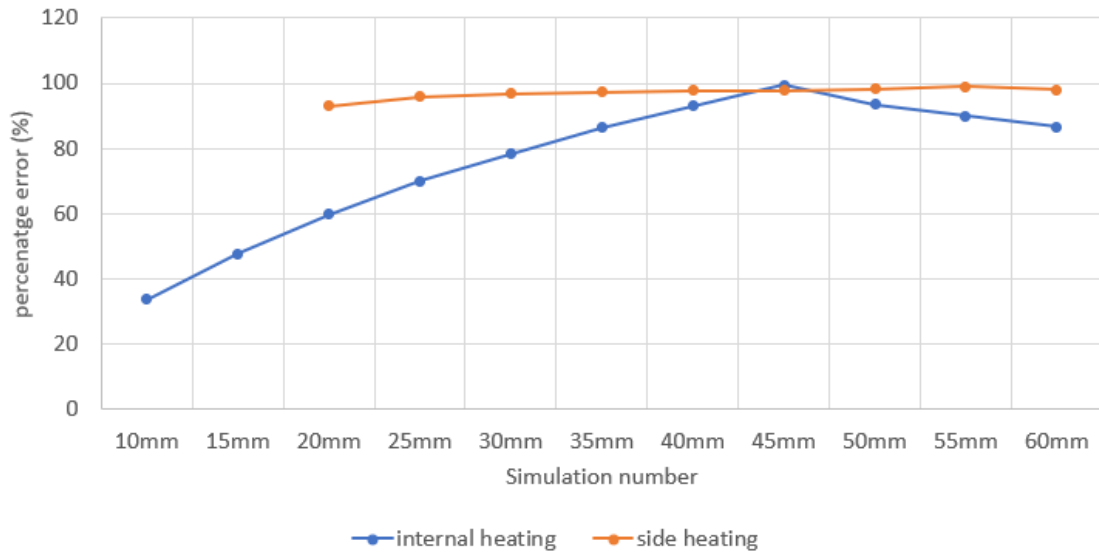


Figure 4-40: Percentage error comparison between internal heating simulations and side heating simulations

Whilst this side heating technique has shown comparable results when used on a highly conductive material, the same cannot be said when used on a less conductive materials such as PLA. The above simulation was repeated but the material was changed to PLC with the same material properties as those shown in Table 4-3.

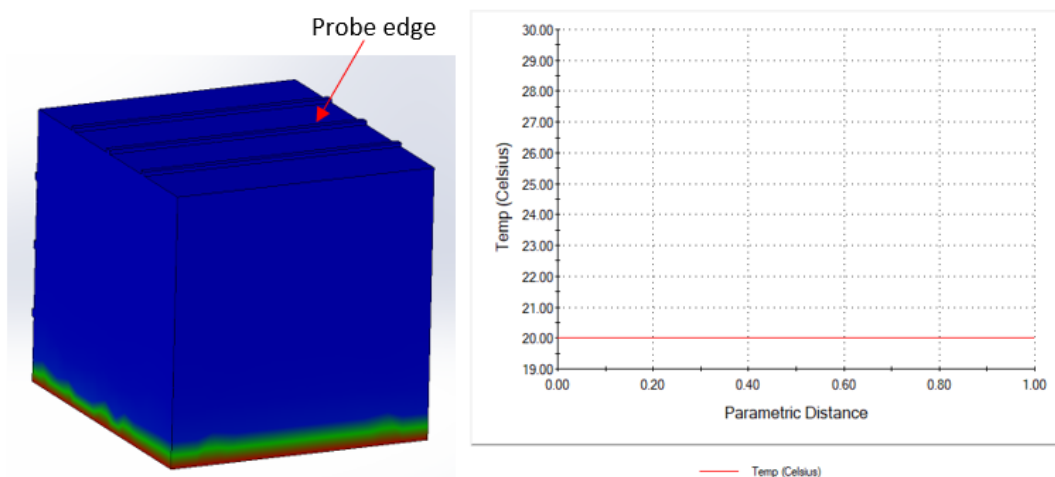


Figure 4-41: Side heating results with PLA: L: thermal distribution across object, R: extracted temperature from probe line on the top surface

As can be seen in Figure 4-41 subjecting the PLA block to the same boundary conditions as the aluminium one produced no discernible results on the opposite face where the probe edge is located. Figure 4-41 (L), shows the extent of the heat transfer and Figure 4-41 (R) shows that there was no resultant change in ΔT at the probe edge surface, with the temperature remaining at the ambient. This result was expected due to the low thermal conductive properties of PLA, and the short simulation time, with similar results seen in section 4.2.6. Therefore, this simulation was repeated with a much longer simulation time of 600s (step increment of 10s) in line with the simulation performed in section 4.2.6 for PLA. Figure 4-42 shows the results of this extended simulation.

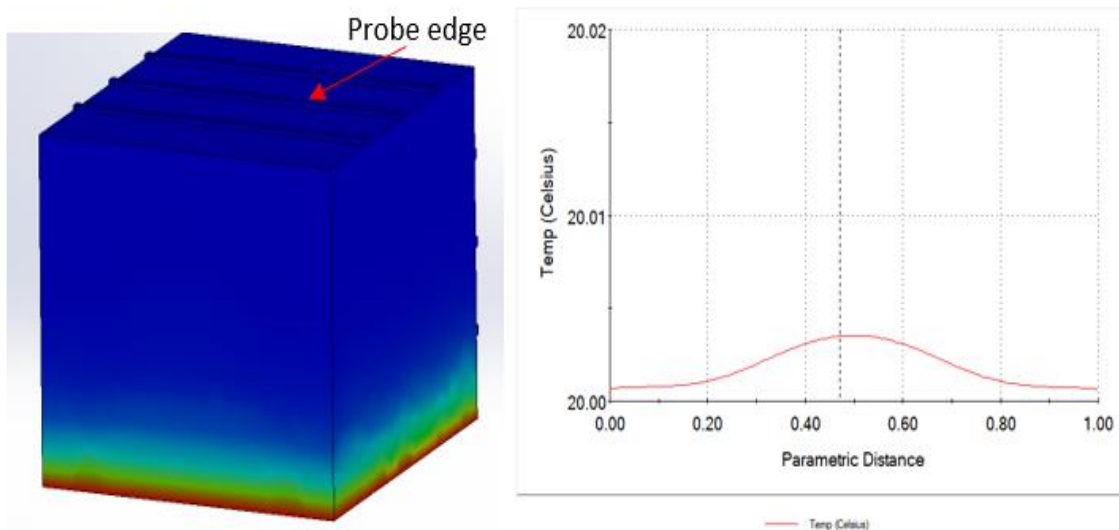


Figure 4-42: Side heating results with PLA T=600s: L: thermal distribution across object, R: extracted temperature from probe line on the top surface

As can be seen in Figure 4-42 extending the time constant by more than a factor on ten has induced a small change in ΔT at the surface, but only marginally. The max temperature difference shown in Figure 4-42 Left is only 20.004°C.

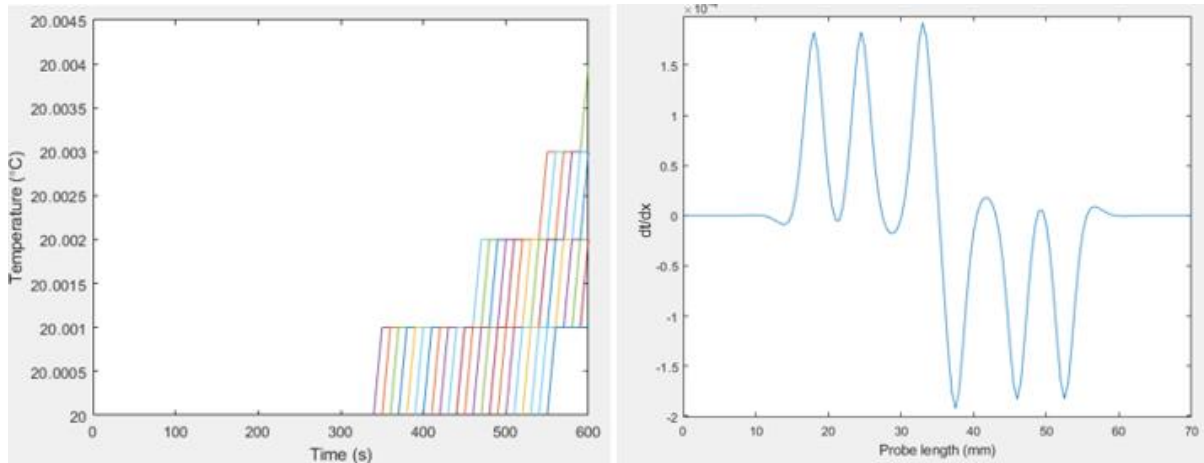


Figure 4-43: L- Nodal temperatures over time, R- differentiated temperature for $t=600s$

This small increase is not enough to be able to definitively differentiate the temperature series, thus highlighting the 1st and 2nd internal edges. Figure 4-43(L) shows the transient nodal temperatures, highlighting that the small change in temperature was situated in the last half of the simulation. Figure 4-43(R) shows the differentiated temperature data at $t=600s$. As can be seen there is no definitive location for the internal edges, given the six peaks that have been resolved and the scale of dT/dx which is in the $10e-4$ range. Both indicate that the surface temperature is not high enough to resolve the internal edge positions. This simulation was repeated with values of $t=1200, 2400, 4800s$ and $9600s$. Individual results can be found in *Appendix C.e*. In each of the simulations, even at $t=9600s$, the surface temperature gradient recovered from the probe edge did not have sufficient thermal variation allowing for the deduction of the internal geometric edge position.

This lack of temperature variation is potentially down to two issues. Firstly, the comparable values in thermal conductivity of PLA ($0.111 - 0.195W/m k$) and air ($0.025W/m K$), means the air gap and the surround PLA material will increase in temperature at a more similar rate, then was observed with aluminium which has a higher thermal conductivity ($200W/m K$). Secondly, due to the low thermal conductivity of PLA, heat loss by convection has more of an effect, leading to a more equilibrise state. This state will limit the heat conduction propagation, leading to only small changes in the surface temperature on the probe edge face.

4.6. Experimental Artefact Simulation

For the experimental validation detailed in Chapter 5, it is necessary to generate an artefact of known geometry incorporating a simple internal shape and a simple opening for the heat source. The geometry of the model used in previous simulations was modified so that the internal void was larger to provide a larger heat capacity. This would also reduce printing time when manufactured due to the thinner walls. The top face was also sealed except for a hole that would allow the heating medium to be added. The resultant hollow cuboid model is shown in Figure 4-44.

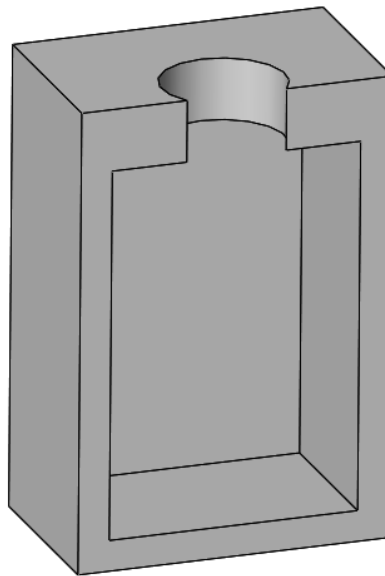


Figure 4-44: Section view of test artefact 1

The physical artefact would be manufactured from polylactic acid (PLA) due to its ability to produce good quality prints and have a high emissivity value. Therefore, PLA will be set as the material for this simulation. Dimensions and relevant material properties are shown in Table 4-6 [60] [63].

Table 4-6: PLA Material properties and dimensions

Property	Value
External Dimensions LxWxH (mm)	50x50x75
Density (g/cm³)	1.25

Specific Heat (Cp) (J/kg°C) (190°C)	2060
Specific Heat (Cp) (J/kg°C) (100°C)	1955
Specific Heat (Cp) (J/kg°C) (55°C)	1590
Emissivity	0.92
Thermal Conductivity (W/m°C) (190°C)	0.195
Thermal Conductivity (W/m°C) (109°C)	0.197
Thermal Conductivity (W/m°C) (48°C)	0.111
Internal dimensions rectangle (LxWxH) (mm)	35x35x60

For the simulation, an additional CAD model was added to the one shown in Figure 4-44, representing the heating medium that would be added to the cavity. The material that was assigned to this model was water, with a thermal conductivity coefficient of 0.61W/m C, and a specific heat capacity of 0.61J/Kg C [59]. Again, the simulation was broken down into an initial static simulation, to define the start temperature, and a transient simulation that would define the overall object temperatures over time. The initial temperature was set to 20°C in the static simulation, again with element mesh sizes of 1mm along the probe lines, and 3mm for the rest of the object.

The result from the static simulation was then imported into the transient simulation. Figure 4-45, shows the boundary conditions and probe line placement on the model for the transient simulation.

As can be seen in Figure 4-45, the green arrows represent heat convection with a coefficient of 6W/m² k, and the red dots visible inside the cavity represent the temperature on the outer faces of the water model. The temperature is set to 95°C.

This simulation was run with a period of 320s, as longer simulation times are needed, as previously seen with PLA simulations. The results for the simulation are all shown below and broken down into two parts: horizontal and vertical, with Figure 4-46 showing the thermal distribution of the model at t=320s. It also indicates which probe line is used to recover either the horizontal or vertical edge positions.

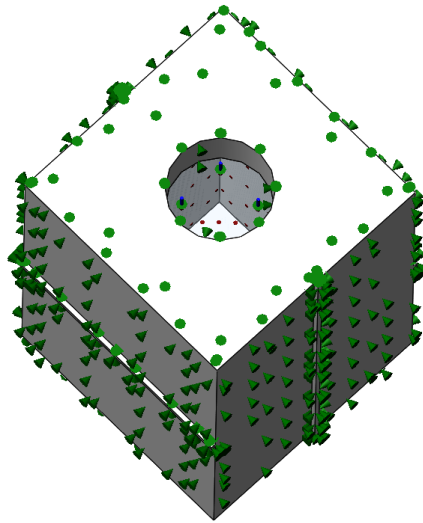


Figure 4-45: Boundary condition for the artefact simulation

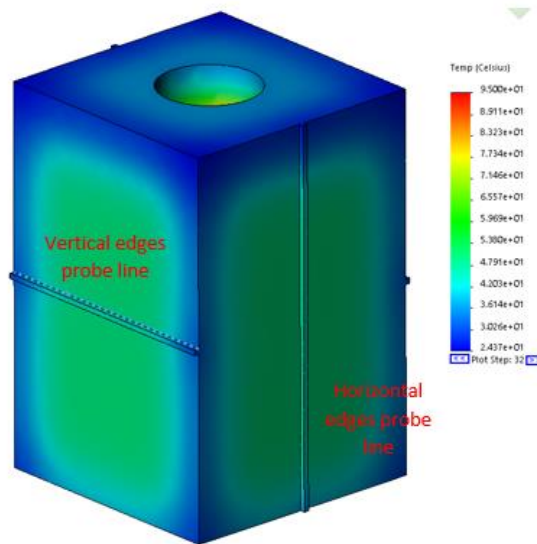


Figure 4-46: Thermal distribution of 320s simulation at $T=320s$

The first set of edge positions to be recovered using *loadSW*, are the vertical edges. Figure 4-47 shows the complete nodal temperatures over time, extracted from the vertical edge probe line. A random selection of nodes and there corresponding temperature data is shown in Figure 4-48 with Figure 4-49 showing those node locations on the probe line.

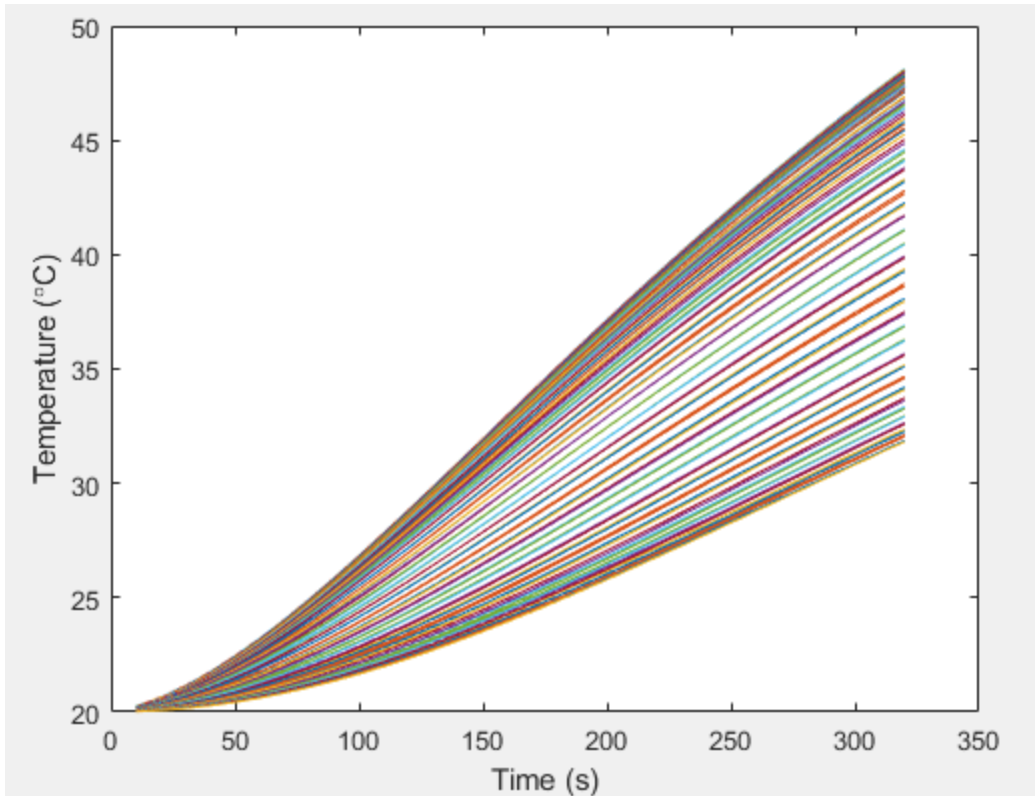


Figure 4-47: Nodal temperature distribution over time from vertical probe edge for 320s simulation

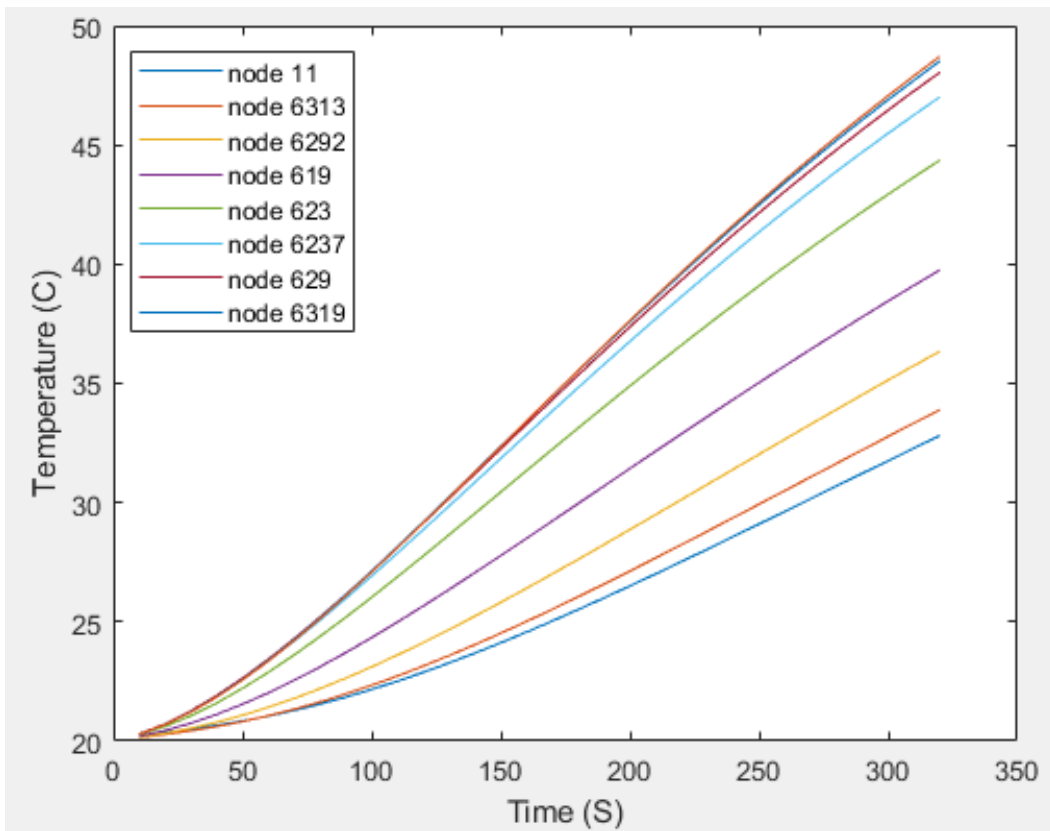


Figure 4-48: Random selected nodes from the vertical probe edge

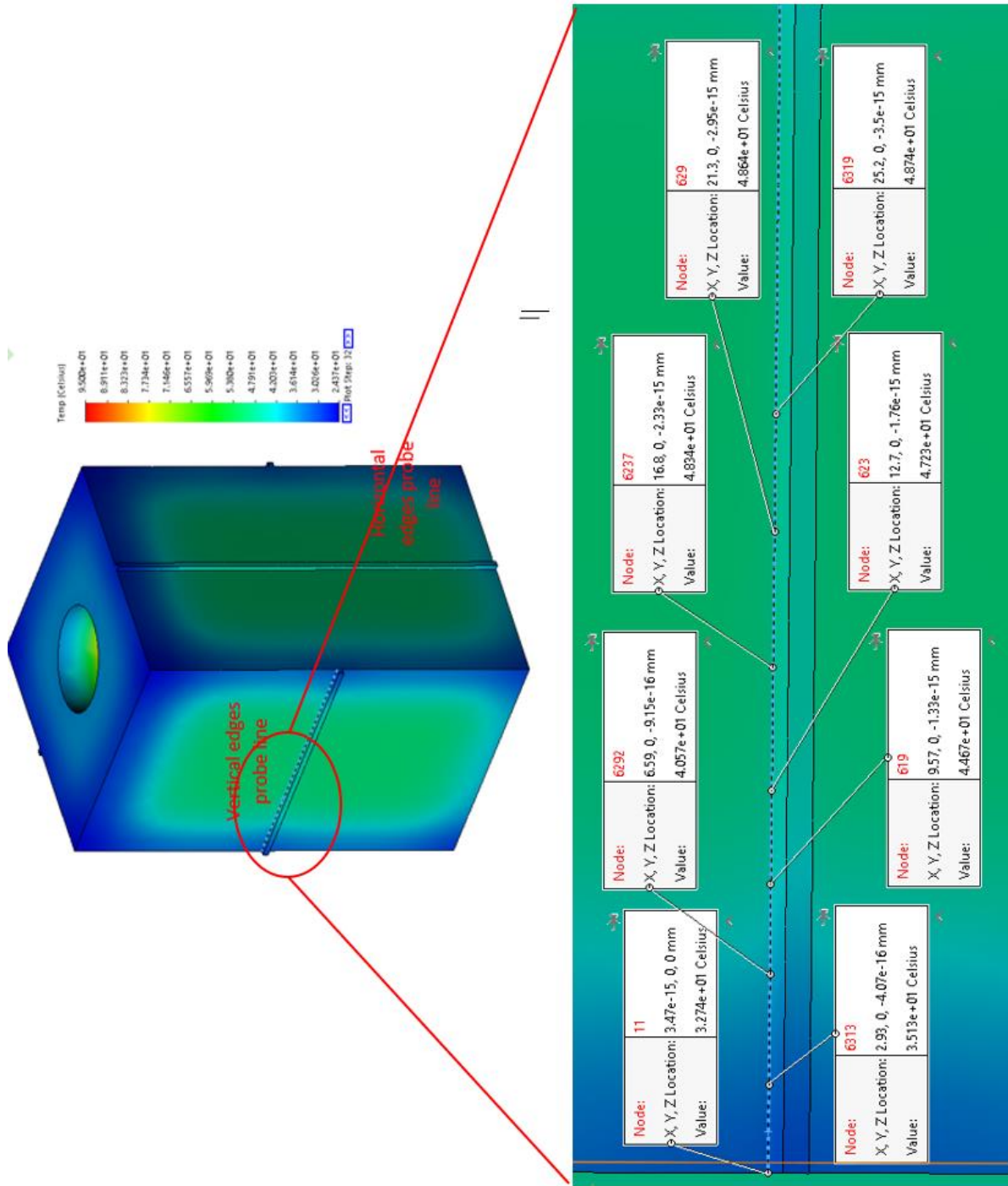


Figure 4-49: Zoomed section of the model showing node position on the vertical probe edge. The nodal temperature data was then processed by *loadSW*, with the corresponded vertical edge positions shown in Figure 4-50. As can be seen in Figure 4-50, there is very little drift in edge position over time. This is most likely due to PLA having a very low thermal conductivity. The nominal edge position values for this model should be 7.5mm for peak 1 and 42.5mm for peak

2. As can be seen in Figure 4-50 the edge position values returned are 6mm for peak 1 and 45.2mm for peak 2. This results in a cavity width of 39.2mm (nominally 35mm).

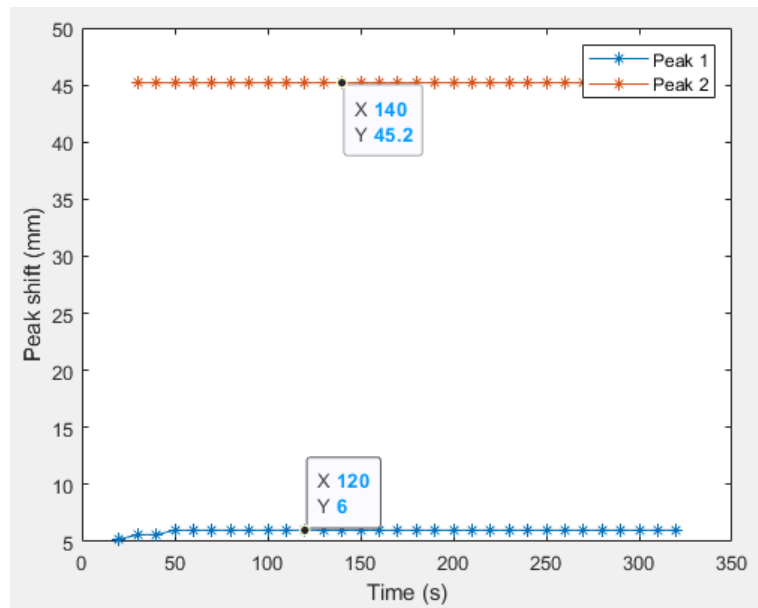


Figure 4-50: Edge position from vertical probe edge over time

This process was then repeated for the data taken from the horizontal edge probe line. The initial nodal temperature data is shown in Figure 4-51.

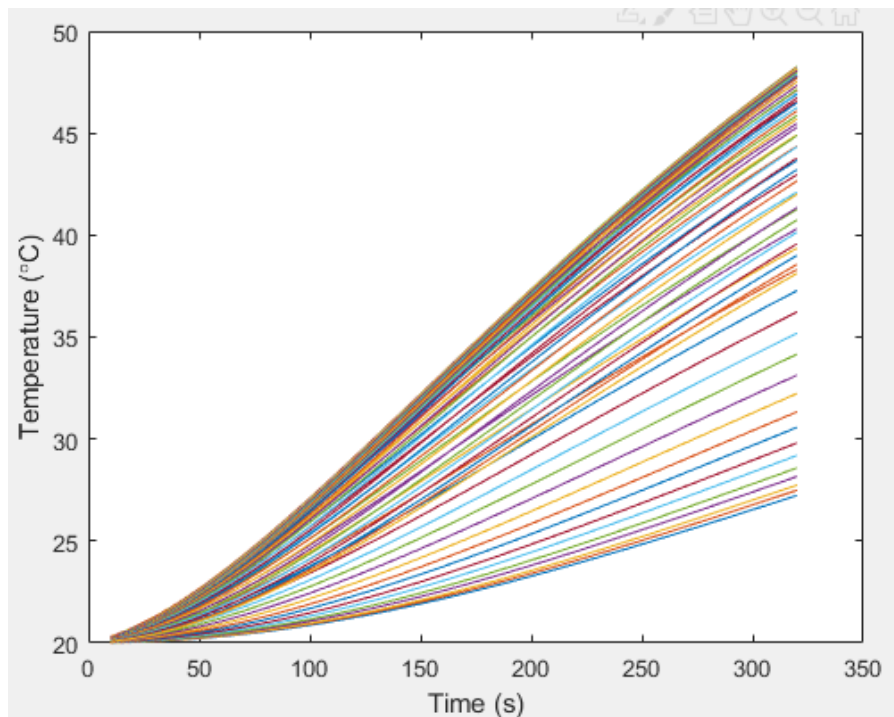


Figure 4-51: Nodal temperature distribution over time from horizontal probe edge for 320s simulation

Again, a random selection of nodes is presented in Figure 4-52 and the position of these nodes on the model in Figure 4-54.

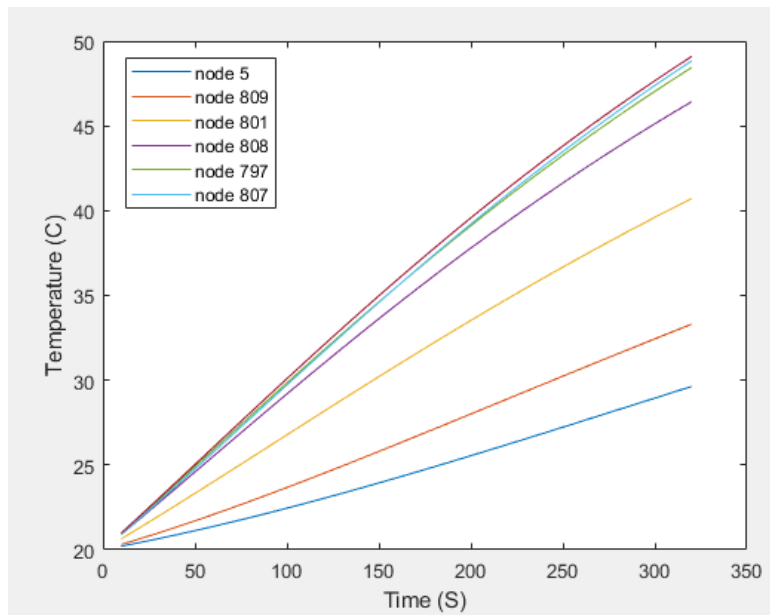


Figure 4-52: Random selected nodes from the horizontal probe edge

Again, this data from Figure 4-51 was entered into *loadSW* with the edge position results being shown in Figure 4-53.

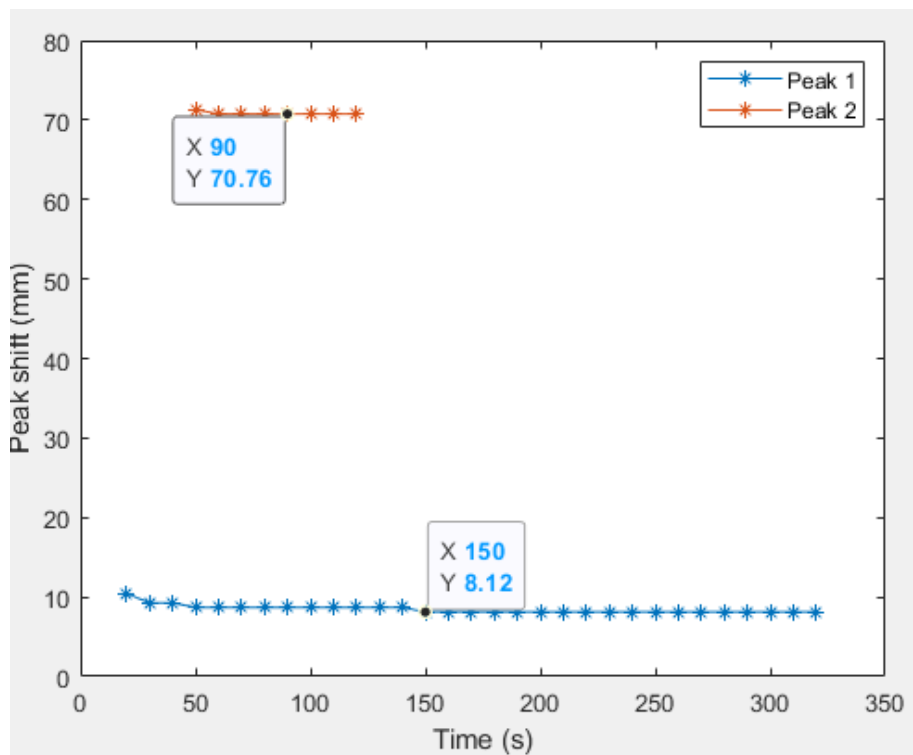


Figure 4-53: Edge position from horizontal probe edge over time

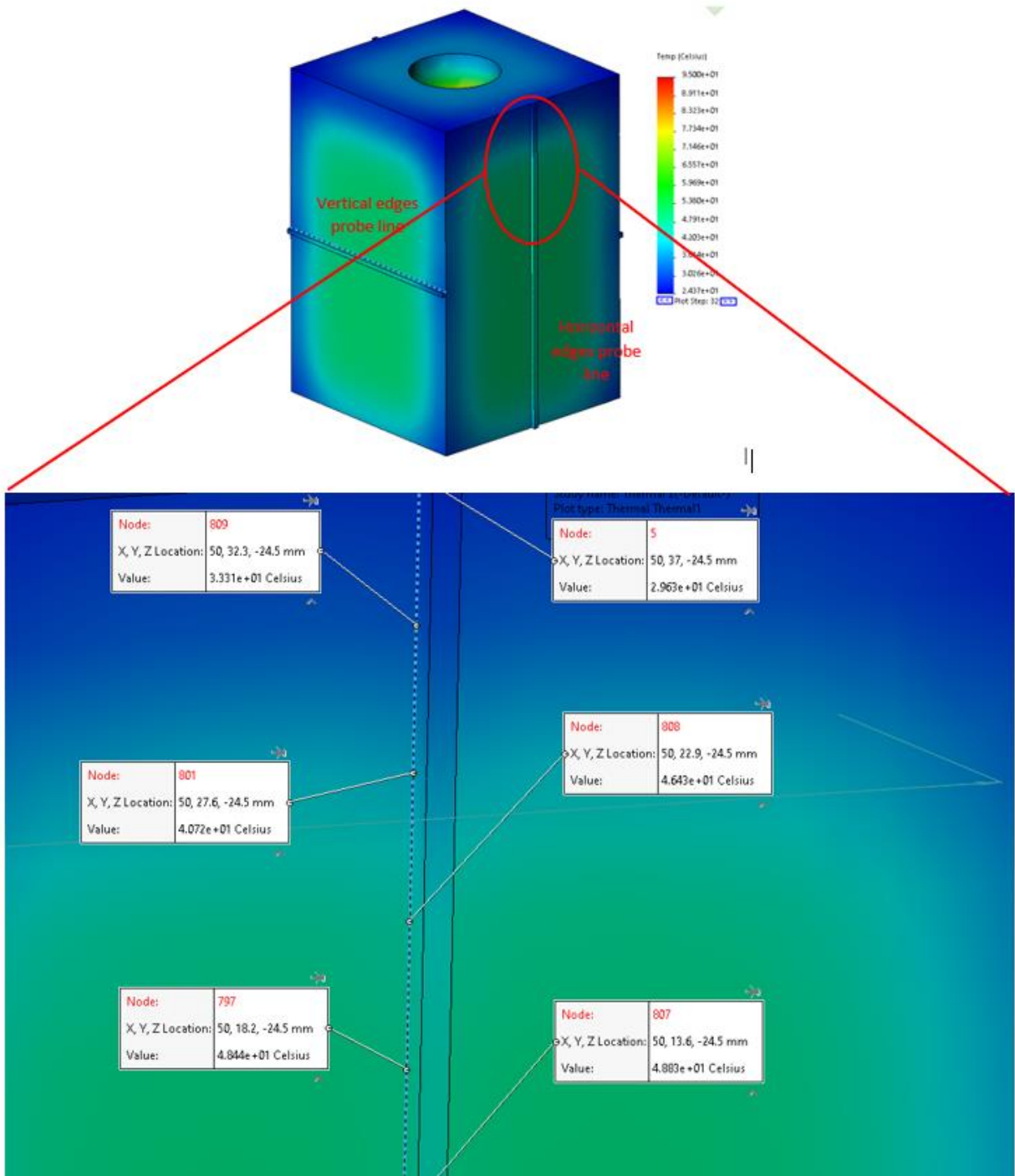


Figure 4-54: Zoomed section of the model showing node position on the Horizontal probe edge

The nominal results for the horizontal edges are 10mm and 70mm for the top and bottom respectively. The results in Figure 4-53 give an average result of 8.45 and 70.8, which represent the top and bottom positions. This would result in a height of 62.35mm.

In Figure 4-53, it is noticed that peak 2 returns much fewer values than peak 1. Peak 2 in reality is only 5mm, from the bottom edge of the object. This leads to homogeneity occurring quicker in this area than others. With no temperature gradient, the system cannot detect a peak in the differentiated data, leading to gaps in the data series.

The values for all four edges are visualised in Figure 4-55.

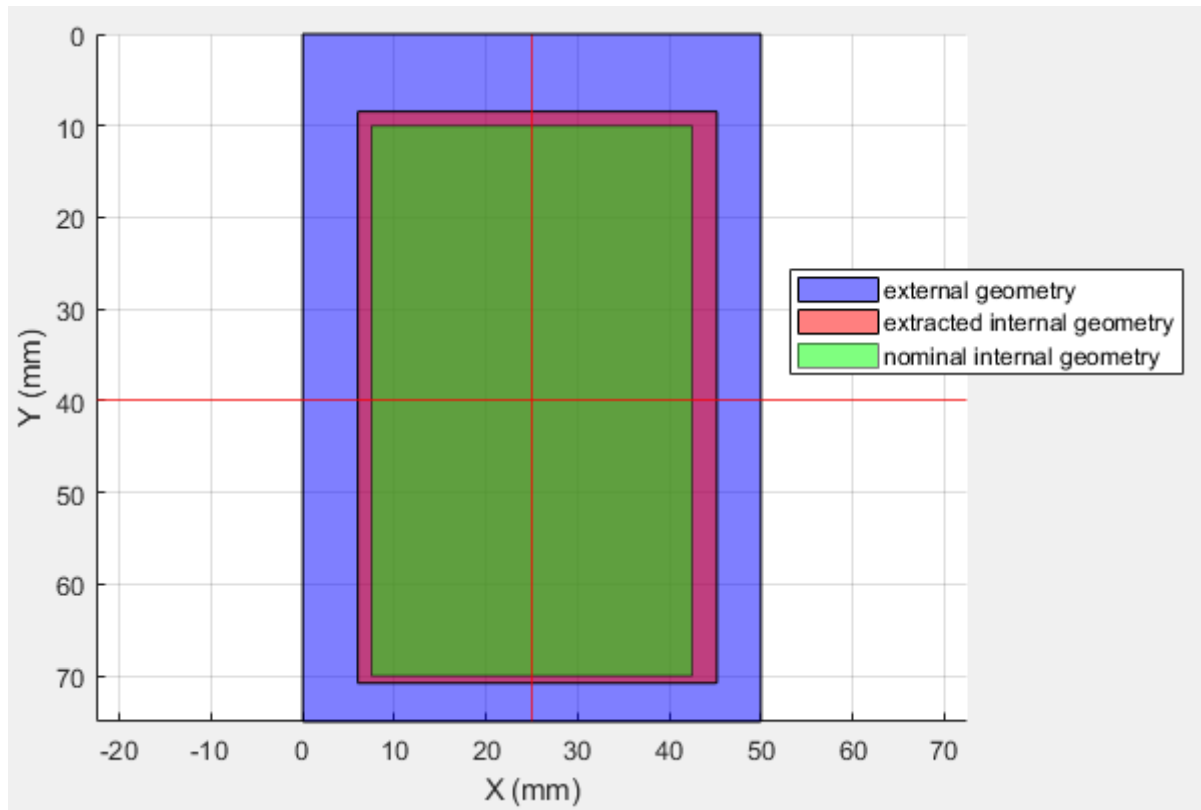


Figure 4-55: Visualisation of recovered edge positions with the nominal and external edge positions

In Figure 4-55 the blue area indicates the external surround of the object. The green area is the nominal position of the internal cavity for this projection. The purple outline is the position of the cavity drawn from the recovered coordinates. As can be seen the actual and the nominal profiles do not overlap perfectly. However, the data for this representation was taken from only one position in each direction, and X and Y. If the data from the probe edge was repeatedly taken from multiple points along both axis's, this mismatch could be reduced by averaging all the edge positions recovered along each axis. This will be discussed in Chapter 5.

4.7. Effects of Thermal Expansion¹

To understand the effects that thermal expansion has on the artefact that will be used in the thermographical analysis, a final thermo-static simulation has been performed. The simulation used to validate the artefact in section 4.6 has been reused and combined with an additional transient structural element. The initial boundary conditions from the simulation in section 4.6 are also carried over for this thermomechanical simulation. For clarity, these are shown in Table 4-7.

Table 4-7: Boundary conditions for thermomechanical simulation

Boundary Condition	Value
Initial body temperature	20°C
Internal heating temperature	95°C
Simulation time	320S
Convection Coefficient	6W/m ² C
Fixed support for static simulation	Object bottom face

In addition, the following mechanical properties for PLA, shown in Table 4-8 [60] [64], were added to allow for the structural part of the simulation.

Table 4-8: Additional mechanical properties for PLA

Mechanical property	Value
Density	1.252 g/cm ³
Young's modulus	1280 MPa
Poisson's ratio	0.36

¹ The thermal expansion simulations were run in ANSYS workbench as Solidworks simulator was unable to converge a solution due to unknown error.

Coefficient of thermal expansion	68 $\mu\text{m/m } ^\circ\text{C}$
Shear modulus	1287 MPa

The thermal part of the simulation is run, and the solution is entered into the structural part. Figure 4-56 and Figure 4-57 show the resultant temperature distribution across the artefact at $t=320\text{s}$, and the thermal expansion due to that temperature, respectively.

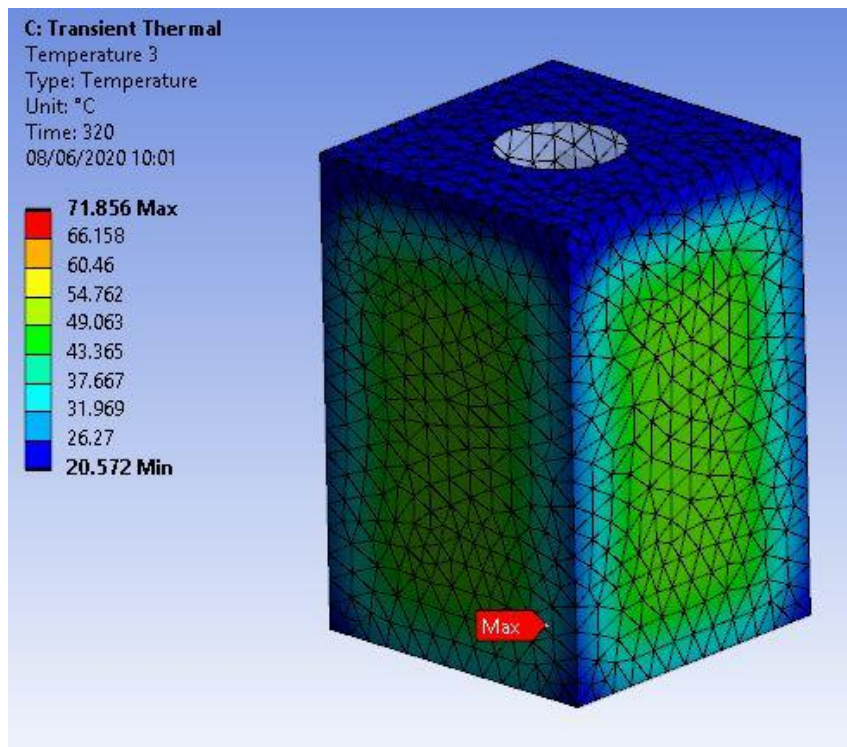


Figure 4-56: Thermal distribution

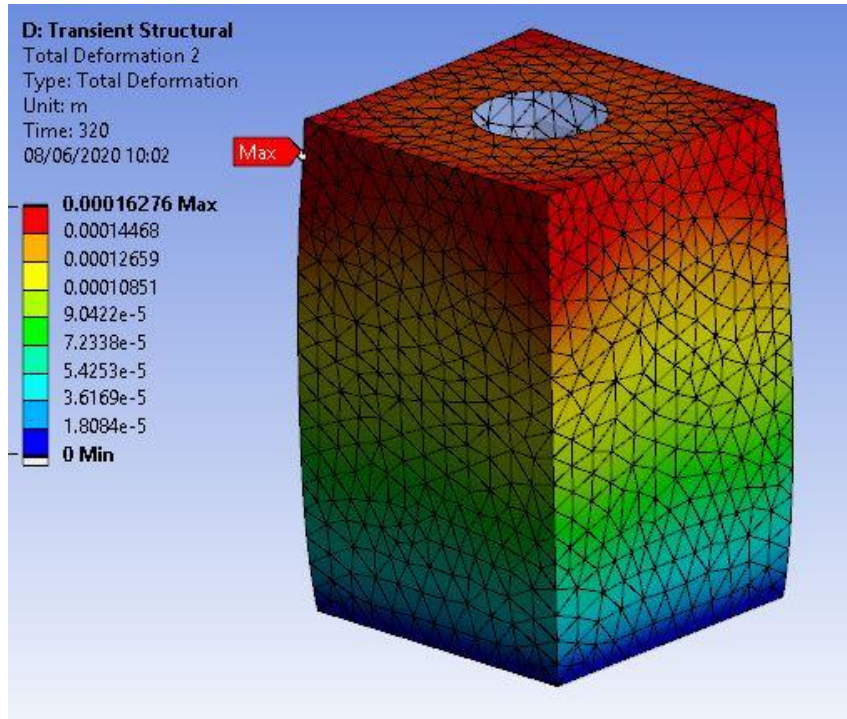


Figure 4-57: Thermal deformation at $t=320s$

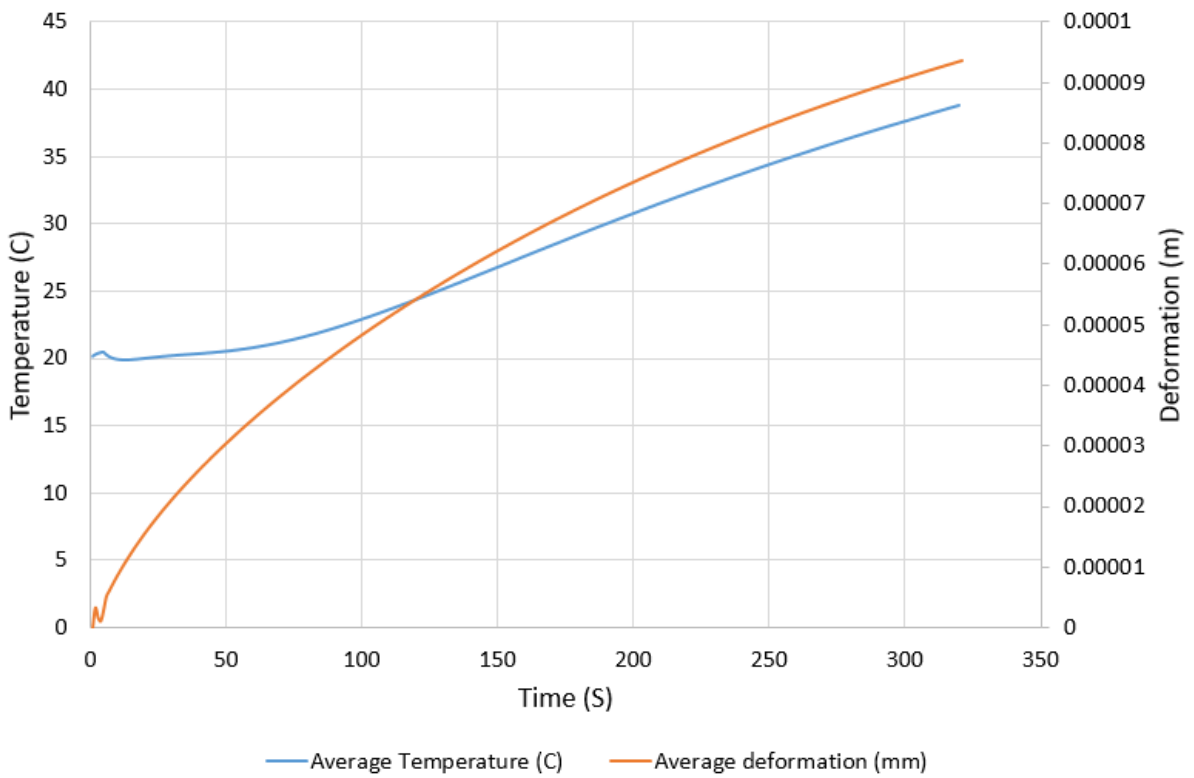


Figure 4-58: Average surface temperature vs average thermal deformation

Figure 4-58 shows the average body deformation against the average surface temperature. As can be seen after 320 seconds, due to the applied temperature, the artefact on average has deformed by nearly 0.1mm.

For this investigation, this can be deemed negligible. However, for a full uncertainty analysis of this system as a metrology tool, a systematic error such as this would have to be considered. This is further discussed in section 7.5.5.

4.8. Chapter Summary

This chapter looked at the application of infrared thermography for internal geometric data recovery, and the use of FEA to analyse heat distributions across certain CAD models. It has been shown analytically that by heating the internal space of a hollow object, an estimated position for the boundary edges of that internal space can be discerned with reference to an external origin. The simulations performed in this chapter have highlighted some of the factors that would need to be considered when this system is used in a physical experiment.

From the simulations performed here, it has been shown that by using this system a dimensional change in internal geometry can be tracked and measured to a certain degree. Whilst discrepancies in geometrical accuracy have been observed, it is admissible as the accuracy of the system at this stage is currently unquantifiable.

These simulations have shown the intrinsic relationship between edge position recovery, and thermal conductivity. As has been discussed, high conductivity materials reach homogeneity quicker than less conductive alternatives, by which time there is no longer a temperature gradient from which the edge position can be deduced. This reduces the amount of time that edge positions can be recovered in these materials. There is also the issue of edge position shift over time. As has been seen, especially with the assignment of high conductivity materials, edge position will shift over time allowing for the recovery of false positives. On smaller

features, this shift has been observed to be as high as 7mm over time. Whilst in the scope of this investigation this is not a major issue for low conductive materials, where this positional shift is much less over time allowing for a greater window where consistent results can be extracted, for high conductive materials the shift is significant. To be able to use this system with high conductive materials, a relationship between temperature, time, thermal conductivity, and edge position would need to be established.

Integrated into this would be the need for differentiating the difference between edge shift due to thermal conductivity and edge shift due to shape profile. As has been observed in this chapter the edge shift due to thermal conductivity and edge shift due to a non-planar profile produced similar results. For results given when the material has a low thermal conductivity, it can be contrived that the profile recovered is either planar or not, depending on the result. However, the same cannot be said for high conductive material where the edge shift due to shape would be lost in the edge shift due to conductivity. For this reason, going forward, this investigation will focus on test artefacts manufactured from low conductive plastics. However, future work must investigate the relationship mentioned above for this system to be fully encompassing.

In this chapter, the idea of external heating has also been investigated. Up to this point, the main solution for manipulating the temperature gradient of the object was to fill the internal cavity with a higher temperature medium (such as boiling water). In a practical environment, this technique may not be possible or agreeable given the nature of the object in question. Therefore, it is advantageous to observe that by applying heat to a single external side of the object, edge position results can still be obtained and have comparable magnitudes not only to results gathered by the internal heating technique, but also to their nominal values. This technique also reduces the amount of thermal power for a given temperature that is induced into the model. Doing this, especially for highly conductive materials, reduces the time it takes for homogeneity to occur, leading to more results being obtained over time. Conversely

however, external heating was not a conducive method when used on materials with low values for thermal conductivity. As was seen in section 4.5 only very small changes in the surface temperature profile were observed during the PLA external heating simulations. Even though small variations were recorded, these variations proved insufficient to allow to successful internal edge extraction.

Finally, this chapter looked at the preliminary FEA validation for the object that will be used in later experimental validation. From the results, it has been shown that at least for the first 320s of heating using this set of parameters, stable results, approximate to the nominal values can be obtained. It has also highlighted the potential issue with homogeneity in relation to the bottom edge of the artefact, as this thin edge yielded much fewer results than the corresponding top edge over the same period. These simulations have also shown that for the same period, a thermal expansion of around 0.1mm is to be expected. However, as previously mentioned, for this investigation this value of thermal expansion can be considered negligible.

Chapter 5. Thermographical Analysis

The main body of the experimental investigation is detailed here. In this chapter the generation of the test artefacts, the external scanning, the recovery of internal geometry using this novel thermographic techniques are all discussed here.

The process of combining the external data and internal data is also outlined in this chapter to produce a 3D model with both internal and external measurements.

This process is repeated for several test artefacts of differing internal geometric structures and materials. Comparative results against known actuals are then presented for all test artefacts.

The accuracy and repeatability of the system, as well potential error sources are also presented in this chapter.

5.1. Artefact Generation

Factors that were considered for this stage of the investigation, were internal geometry and material specification. Differing internal geometries were chosen based upon the differing geometries used in the in Chapter 4, and recreated here. Most of the artifacts used in this chapter were 3D printed in PLA. This was done for three main reasons: 1/ the ease of manufacture. Parts internal geometries could be 3D printed easily in a cost-effective manor, and 2/, as seen in Chapter 4, PLA has a very low heat transfer coefficient, and finally 3/ PLA has a very low emissivity factor. In addition to these artifacts that were made in PLA, an additional artifact was manufactured in aluminium. Aluminium was chosen as again, as seen in Chapter 4 aluminium had the largest heat transfer coefficient of any the materials simulated.

Additional factors behind the form and design of these artefacts were also considered. In addition to being able to adjust the core factors (i.e., the internal shape), the artifacts needed to

be large enough to generate a suitable heat capacity, but small enough to fill the frame of camera. By filling the FOV with the artifact, resolution levels would be maximised, and noise levels would be reduced. Having the artifacts as close as possible to the camera would also reduce atmospheric effects, such as external thermal influences. Also, sharp external edges on the artifacts would allow for easier registration in the processing stages.

These artifacts (except for the aluminium one) were then 3D printed in PLA using a BCN3D Sigma dual-head printer. This printer has a stated accuracy of $\pm 0.2\text{mm}$ [65]. From the first round of 3D print production, five artefacts were printed. 1/ consists of a cuboid with an internal cuboid with all equal faces, with internal faces parallel to the external face. This artifact was also produced in aluminium which is further detailed in section 5.4. 2/ a larger cuboid with two differing internal dimensions, but again with internal faces parallel to the external. 3/ a cuboid with an internal L-shaped void. 4/ a cuboid an internal cuboid with faces 45° to the external faces, and 5/, with an internal cylinder. The first four artefacts described above will be used and discussed in this chapter. An example of the completed artefacts from the 3D printer are shown in Figure 5-1. For reference, the material properties of these test artefacts are repeated below in Table 5-1. The other two artefacts (4-5) are for the time-based work detailed in Chapter 6. The specific dimensions and properties for these artefacts are described in Chapter 6.

Table 5-1: Test artefact material properties and dimensions

Property	Value
Density (g/cm^3)	1.25
Specific Heat (C_p) ($\text{J/kg}^\circ\text{C}$) (190°C)	2060
Specific Heat (C_p) ($\text{J/kg}^\circ\text{C}$) (100°C)	1955
Specific Heat (C_p) ($\text{J/kg}^\circ\text{C}$) (55°C)	1590
Emissivity	0.92
Thermal Conductivity ($\text{W/m}^\circ\text{C}$) (190°C)	0.195

Thermal Conductivity (W/m°C) (109°C)	0.197
Thermal Conductivity (W/m°C) (48°C)	0.111

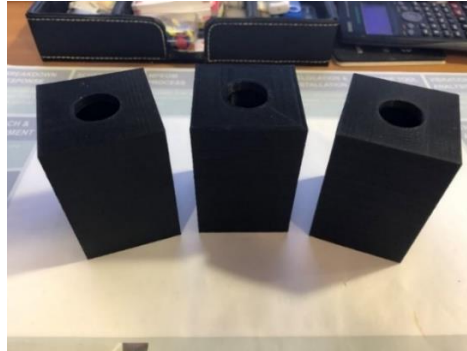


Figure 5-1: 3D printed test artefacts

5.2. Artifact calibration

As stated above the stated printer accuracy for a BNC3D Sigma is $\pm 0.2\text{mm}$. However, cumulative errors in the printer set-up and 3D printing specific error sources, such as shrinkage, and blowing, mean that to find the actual dimensions of these artifacts they will need to be calibrated before use in the thermal trials.

To calibrate the test artifacts, a X-Tek XTH 225 scanner was used. Its 225kV reflective target can generate a minimum focal spot size of $1\mu\text{m}$. Figure 5-2 shows an example of an artifact being set up inside the CT scanner.

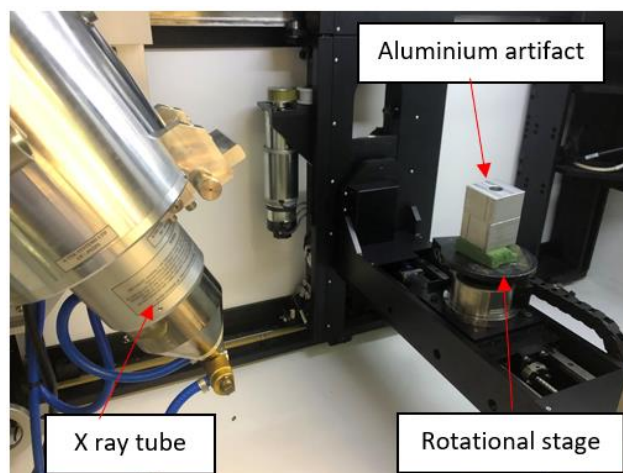


Figure 5-2: Example artifact in the CT scanner

The resultant PCDs from the CT scanning, with their corresponding extracted dimensional data can be found in *Appendix E*. However, the square artefact PCD and corresponding dimensions can be seen below (Figure 5-3 and Table 5-2) for reference.

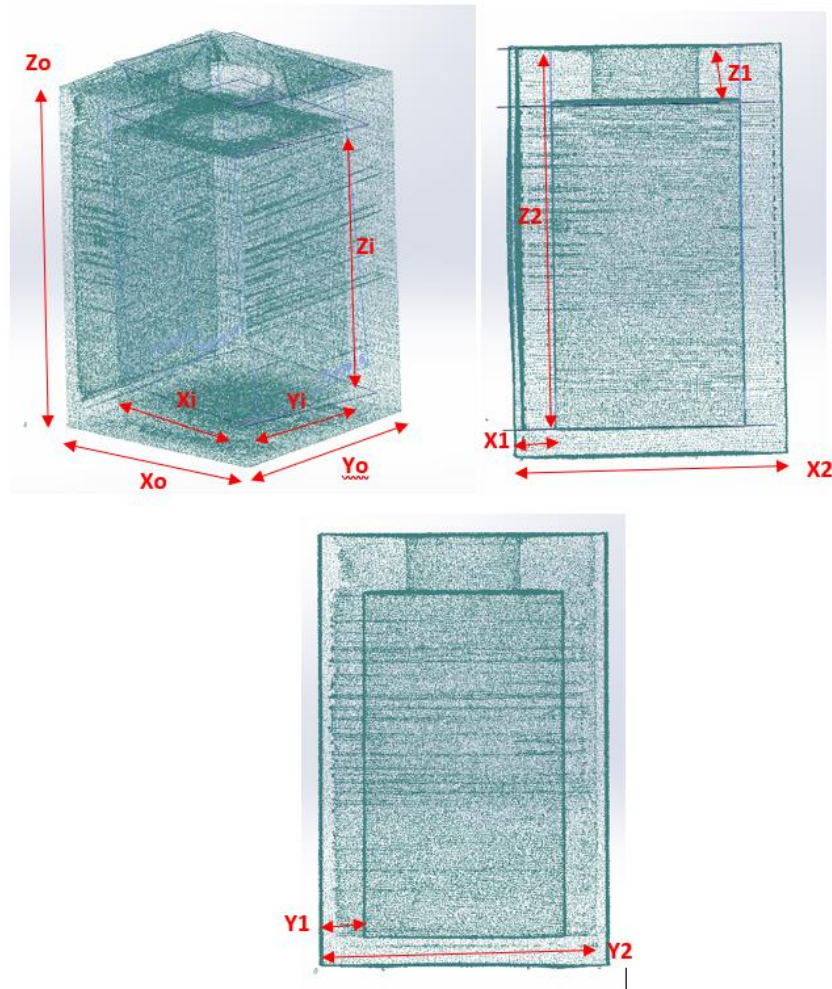


Figure 5-3: PCD of square artifact from XCT, and corresponding dimensions

Table 5-2: Dimensional results for square artifact PCD as seen in Figure 5-3.

SQUARE PLA	
Xo	49.75mm
Yo	49.7mm
Zo	74.87mm
Xi	34.77mm
Yi	34.58mm
Zi	59.43mm
X1	7.62mm
X2	42.25mm
Z1	10.62mm

Z2	69.76mm
Y1	7.52mm
Y2	42.26mm

5.3. Scanning

5.3.1. 3D External Scanning

To begin the process, external scanning was performed first due to the availability of the equipment necessary to perform the external scanning. A Romer Absolute 7525 Arm with RS3 laser line scanner was used to scan and capture the external geometry and Geomagic® Studio to digitise the CPD. The process of capturing and digitising the external geometry is not a novel process and is currently well documented in many fields. Figure 5-4 (R), shows the initial scanning of the object and Figure 5-4 (L) shows the final external tessellated triangular mesh (TTM). For this instance, the process of capturing and digitising the CPD to get to the TTM shown in Figure 5-4 is detailed in *Appendix D*.

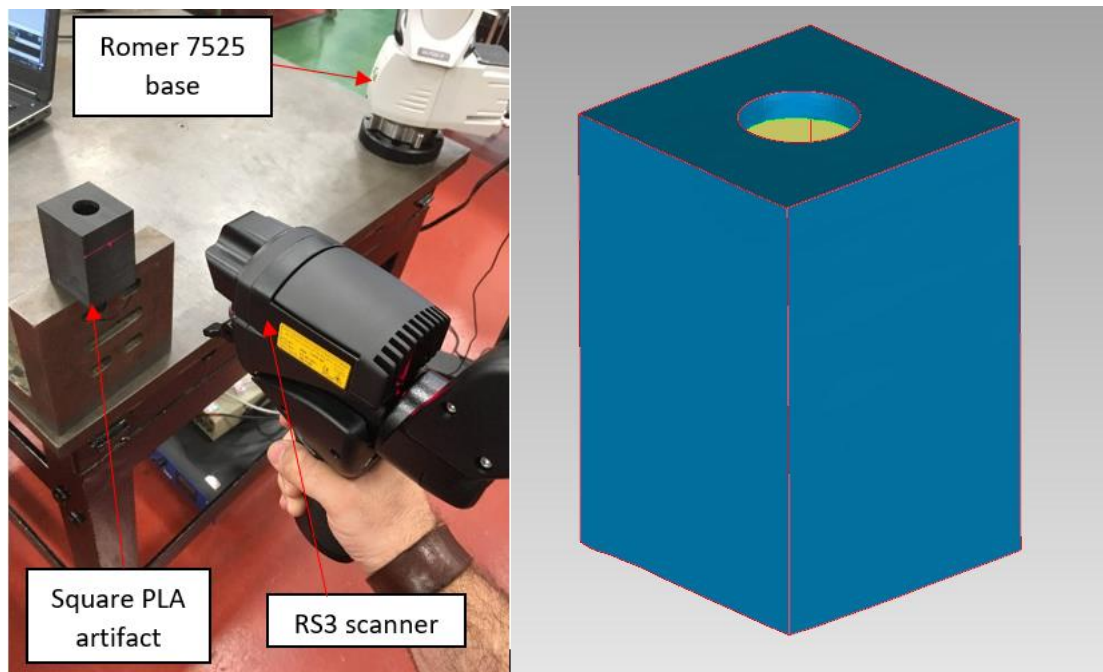


Figure 5-4 (R): External scanning of artefact, (L): Final sharpened TTM

5.3.2. Effects of Emissivity

When using thermal imaging technology to perform temperature measurements, it is important to know the emissivity of the object being investigated, and how the emissivity of the object will affect the captured results.

In this investigation, accurate recording of the absolute temperature of the object is not a primary concern, providing relative temperature, the rate of change in temperature recorded across the face of the object is consistent, and the effect of external factors is minimised.

From research [60] [63], it has been found that the objects material, PLA, has an emissivity value of 0.92. This high value will be advantageous, as surrounding heat sources will have a negligible effect on the captured results i.e., the reflectivity of the surface is very low at 0.08 so most external heat radiation will be absorbed by the object not reflected into the camera. It was not clear from the aforementioned research whether the emissivity was affected by the 3D printing process, which, depending on settings and direction of print, can create different surface finish. In order to validate the uniformity of the emissivity for the 3D printed parts a simple test was performed to ascertain the varying effects the objects emissivity may have on recorded temperature data.

The object was placed in front of a sheet of aluminium foil, in-line with the thermal camera (Figure 5-5). Aluminium foil has an emissivity of 0.04, much lower than that of the PLA object. Therefore, given the two values for each material, any external heat should be mostly absorbed by the object, and mostly reflected back into the IR camera by the foil.

With the foil and the object setup, they were left to stabilise to room temperature, which was approximately 20°C. A vessel containing two litres of boiling water was then passed from side to side directly behind the thermal camera. This motion was continued for thirty seconds. In the thermal cameras software four temperature measurement points were selected, two on the

object and two on the foil, to show the resultant temperature change. Figure 5-6, shows a randomly selected resultant thermogram.



Figure 5-5: Setup of emissivity test

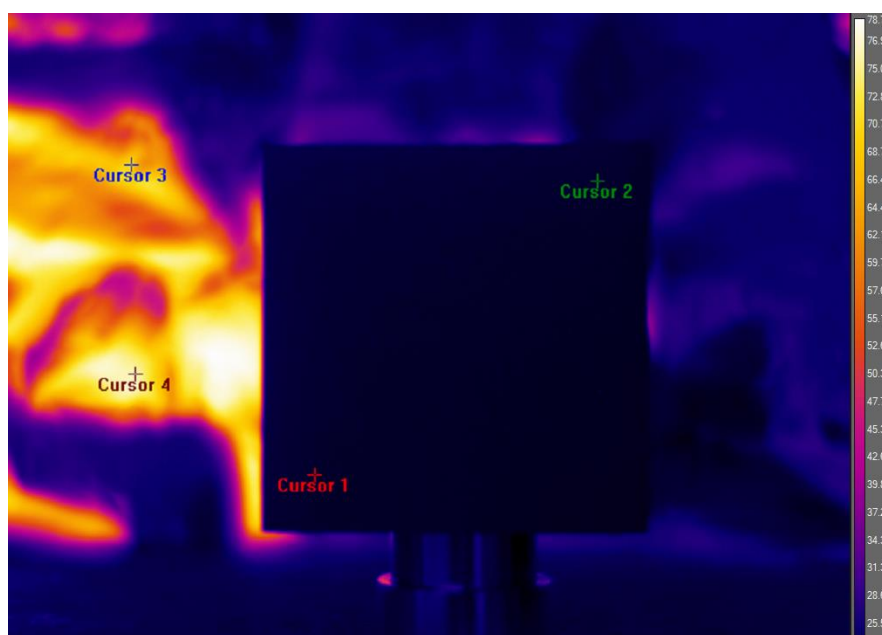


Figure 5-6: Emissivity test thermogram

The foil and the object are at the same temperature, yet as expected, the captured temperature data from the foil shows huge disparities with a surface temperature in excess of 70°C. More importantly, the object is showing a uniform surface. Figure 5-7 shows the captured resultant temperature data over an entire thirty-second period. Due to resolution of the plot in Figure 5-7, and the similarity in results, C3 and C4 are behind C1 and C2.

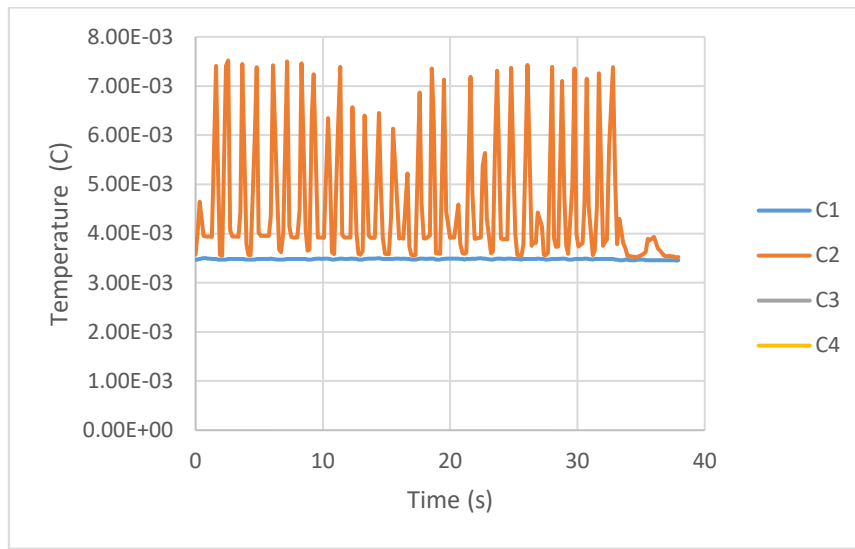


Figure 5-7: Temperature over time due to emissivity

As can be seen in Figure 5-7, C1 and C3, the measurement points on the object, do not change over time. Due to PLAs' high emissivity value most of the external convective heat is absorbed by the block and not reflected back into the camera. However, C2 and C4, the measurement points on the foil, show extremely high surface temperatures due to most of the external heat being reflected into the camera. The sinusoidal result is due to the heat source being passed from side to side.

To understand how this affects the recorded surface temperature of the object, the temperature data for the object was extracted from the thermogram, when the heat source was in front of the object, and then extracted with the heat source removed. A standard deviation was then performed on each data set, to show the maximum variation in temperature when the

object is exposed to an external heat source. The results for this standard deviation are shown in Figure 5-8.

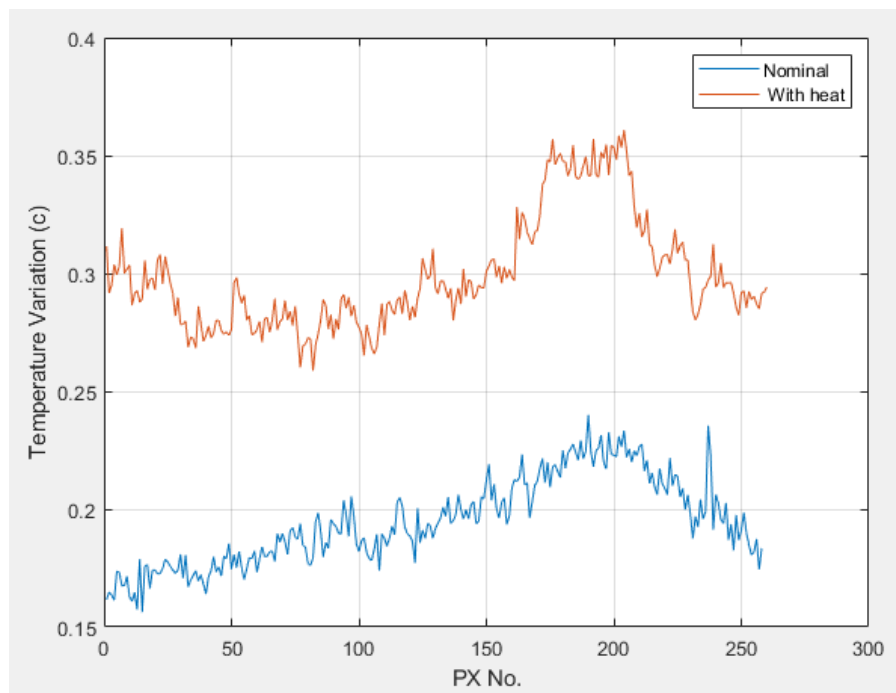


Figure 5-8: Standard deviation of object face, with and without heat source

Figure 5-8, shows that when the external heat source is in front of the object the surface temperature variation of the object rises on average by 0.1°C (average results: nominal= 0.195°C, with heat= 0.299°C). This small rise in temperature is attributed to reflected radiation from the external heat source. It should be noted that this test was an example of an extreme case where a very hot object was used. Even with such extreme conditions, the temperature variation was very small, marginally higher than the cameras thermal sensitivity of 0.03°C (see Table 5-3). During the experiments in this chapter, care will be taken to minimise radiative heat sources around the experiment therefore given the relative magnitude, the effect of external heat sources will be negligible.

5.3.3. 3D Internal Scanning

To recreate and digitise the internal geometry of this artefact a novel process is proposed. This process relies heavily on heat transfer thermodynamics and parallel plane projection. In

accordance with the second law of thermodynamics, increasing the temperature of the internal volume of the artefact will disrupt the thermal equilibrium of the object spontaneously inducing thermal conductivity. As the heat flows from the hotter internal volume to the surrounding cooler environment, the heat transfer is detectable using an IR camera. By reorienting the artefact several times through each of its plane projections, the heat transfer can be observed through the entirety of the internal structure. From each of the recovered thermograms a 2D representation of the internal geometry as viewed from that corresponding projection can be deduced. This section will highlight the steps necessary for this process. To begin the 3D internal scanning, the 2D thermographic projection must first be recovered. As shown in Figure 5-9, to perform this the artefact is mounted to a rotary stage, in the view of the IR camera.

The rotary table allows the artefact to be indexed through a precise angle. This is expedient and will be described later in this chapter. The IR camera is then positioned parallel to the artefact. The distance from the camera to the artefact is such that the artefact is approximately in the just outside the cameras minimal focal plane.

The IR camera used in this set up is a FLIR A655SC with a 25° FOV 24.6mm lens. Specifications for the A655SC and its lens are listed below in Table 5-3 [66] [67].

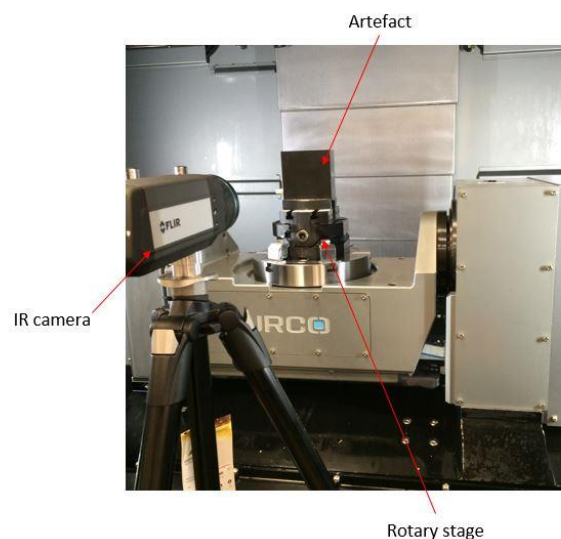


Figure 5-9: Internal Thermal Capture Set Up

Table 5-3: FLIR A655SC with 25° FOV 24.6mm Specifications

Property	Value
Thermal Sensitivity	0.03°C @30°C
Detector Type	Uncooled Microbolometer
Dynamic Range	16 bit
Spectral Range	7.5 – 14.0µm
Standard temperature range	-40°C to 150°C
Accuracy	2% of reading
f-number	f/1.0
Detector pitch	17 µm
Field of view (FOV)	25° x 19° (31° diagonal)
Frame rate	50Hz
Resolution	640x480
Minimum Focus Distance	0.25 m
Focal length	24.6mm
Spatial Resolution (IFOV)	0.69 mrad

Following the setup of the artefact/camera arrangement, using FLIR *Research IR max* software the artefact can be viewed and brought into focus (Figure 5-10). Once the image has been brought into focus, the heating medium can be added. For this initial validation of the process, the heating medium is water boiled to 100°C. The heating medium is then added to the internal void of the artefact, as shown in Figure 5-11. As the funnel used to pour the water into the void is at a higher temperature than the artefact the colour mapping of temperature changes, highlighting the funnel.

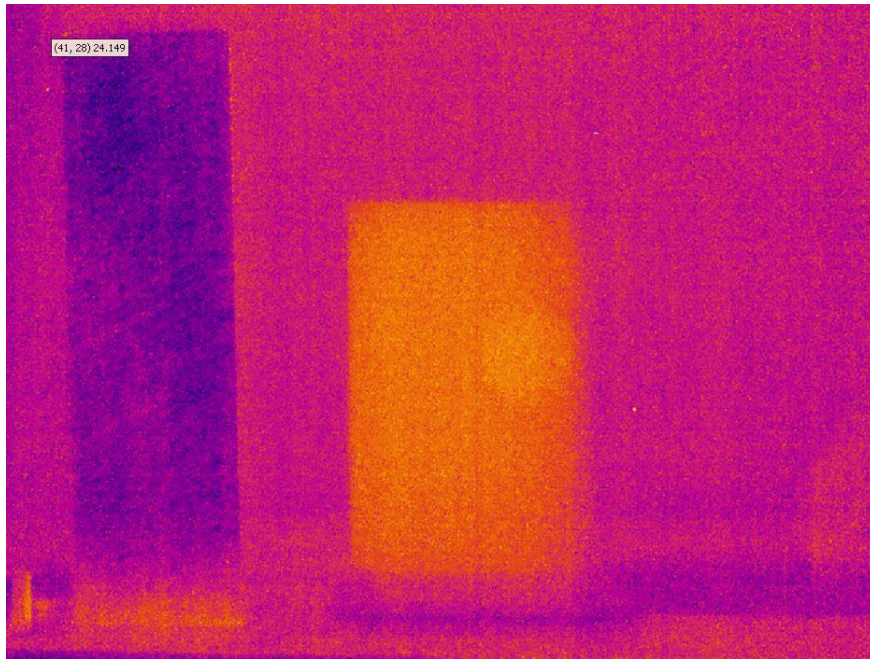


Figure 5-10: Thermal Capture of set up before heating.

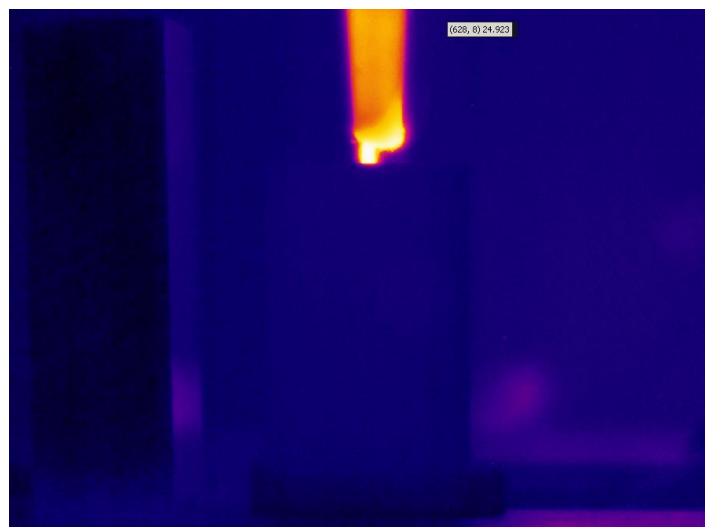


Figure 5-11: Adding of the heating medium. The funnel is highlighted at the top of the image

Following the addition of the heating medium, the thermal conduction is captured for several minutes. As was shown in Chapter 4, PLA demonstrates very little in any edge shift in the first few minutes after heating, due to its low thermal conductivity. Therefore, according to the results obtained in Chapter 4, there should be at least three hundred seconds after heating began in which data can be gathered that would produce accurate positional results. Unlike the simulations in Chapter 4, which were performed over time, this part of the investigation focuses

on results from one time step only. The decision of when to extract this single data set was based upon the temperature distribution, as shown in Figure 5-12 and Figure 5-13.

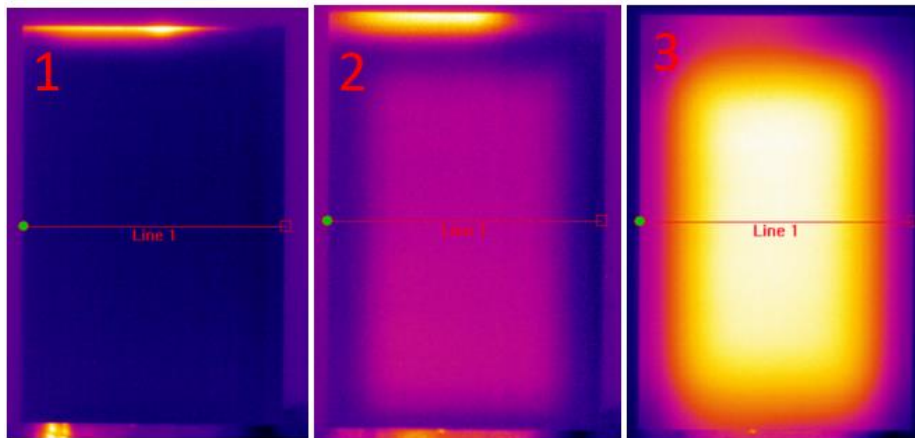


Figure 5-12: Front view of the artefact showing thermal conduction distribution.

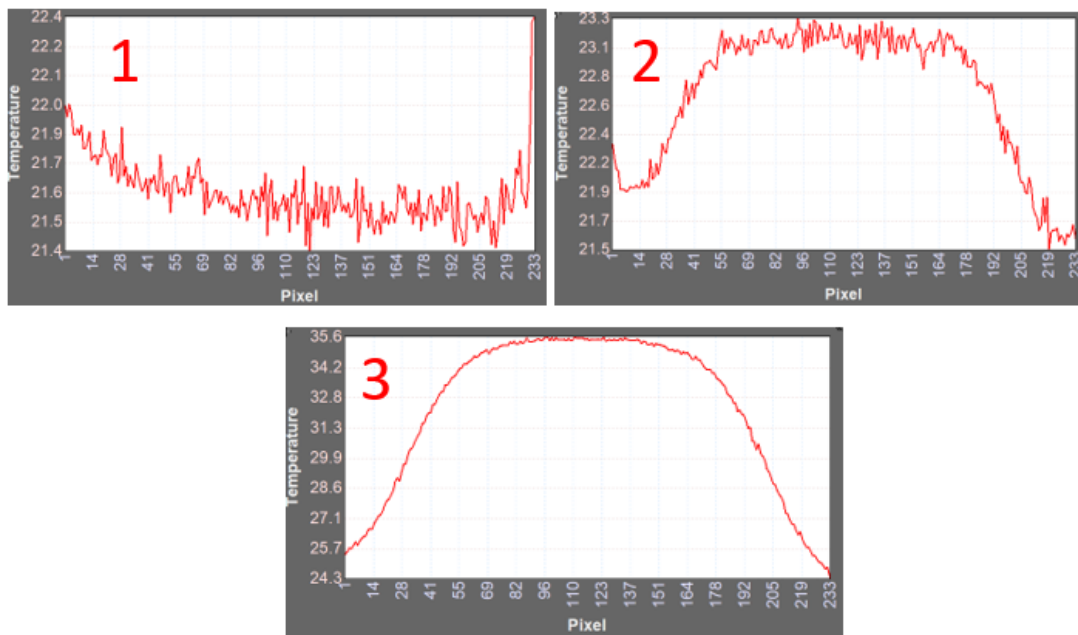


Figure 5-13: Temperature profiles corresponding to Figure 5-12

Figure 5-12 shows three thermograms taken from the intimal thermal capture. Figure 5-13 show the corresponding temperature profiles from “line-1” as seen in Figure 5-13. As can be seen the largest temperature gradient can be found in image three in Figure 5-13. This occurred 124s after the heating medium was added. At this point, the magnitude of the temperature profile did not increase any further. After several seconds, the temperature gradient began to

decrease indicating the temperature of the artefact started to saturate. It is in the window between when the temperature gradient was at its highest that the thermogram to be used in the reconstruction process was taken. This thermogram is shown in Figure 5-14.

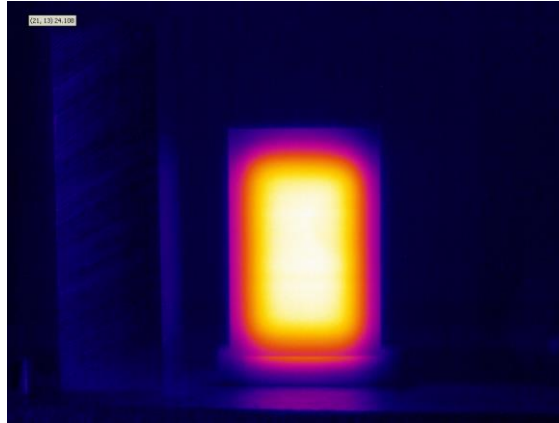


Figure 5-14: Thermogram to be used in geometry reconstruction.

5.3.4. First Face Feature Extraction

With the appropriate thermogram chosen, it is exported as both raw temperature data and as a JPEG image file. Both are now be entered into the custom written feature extraction algorithm (FEX). Figure 5-15 shows a flow diagram outlining the processes the FEX performed to extract the geometrical data from the imported thermal information.

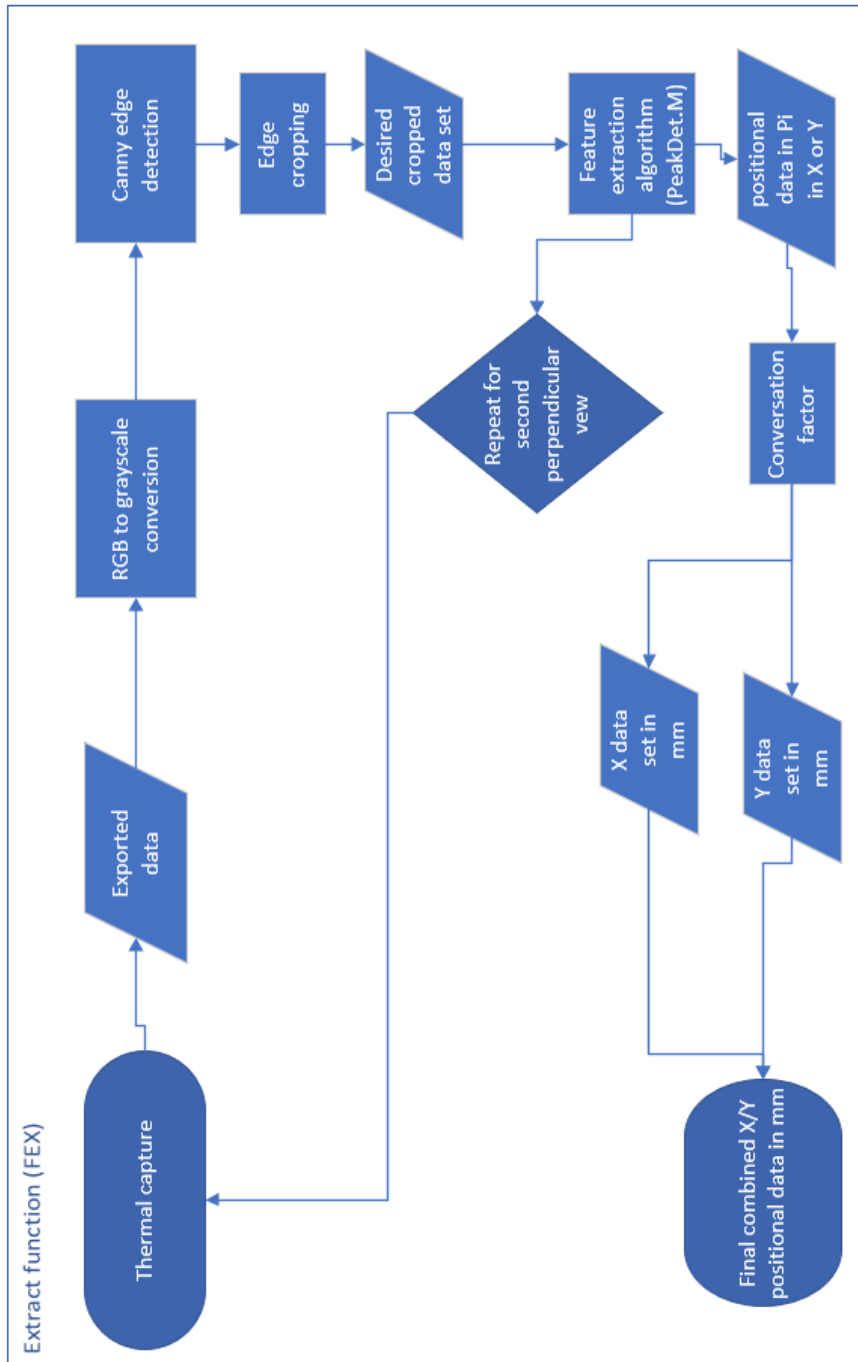


Figure 5-15: Flow diagram of the feature extraction algorithm

On initiating the FEX both the thermograms temperature data and the corresponding JPEG file are inputted. Both files are required as the actual feature extraction is extrapolated from the temperature data, but the image file is required to segment the data accurately. The code designed for the extraction of internal features can be found in *Appendix H.d- extract*.

To begin with, the image shown in Figure 5-14 is converted from a true colour Red, Green, Blue (RGB) file to grayscale. This removes the hue and saturation from the image whilst retaining the luminescence [68]. This converts the image from a multidirectional array to a simpler two-dimensional array. The monotone image can be seen in Figure 5-16.



Figure 5-16: Monotone image of the thermogram shown in Figure 5-14

This two-dimensional array can now be entered into the edge detection algorithm. The Canny detection method was used to extract the edges from the above monotone image. The Canny method is less susceptible to noise as it uses two gradient thresholds derived from a Gaussian filter. Using two gradients allows the detection of both strong and weak edges [69]. In this case, the Canny operator is more prevalent than others are, such as Sobel or Prewitt, as they can return the noise, inherent in thermograms, as false positives. The threshold for the Canny operator is manually set so that only the most pronounced edges (i.e., from the artefact) are returned. The resulting edge image is shown below (Figure 5-17)

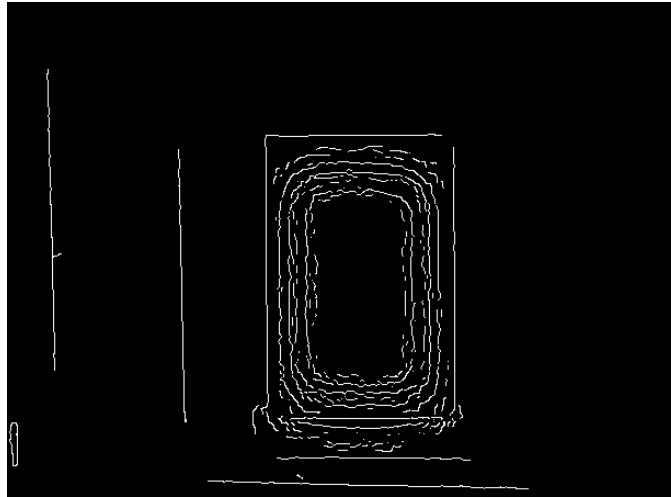


Figure 5-17: Thermogram after edge detection has been performed.

With the four edges of the block now highlighted, the area of interest in both the RGB image and the corresponding thermal data can be cropped. Choosing the four points from the edge detection image, the corners of the artefact in both X, Y, the height, and the width can be determined. The cropped RGB image and a temperature map showing the cropped thermal data are shown below (Figure 5-18).

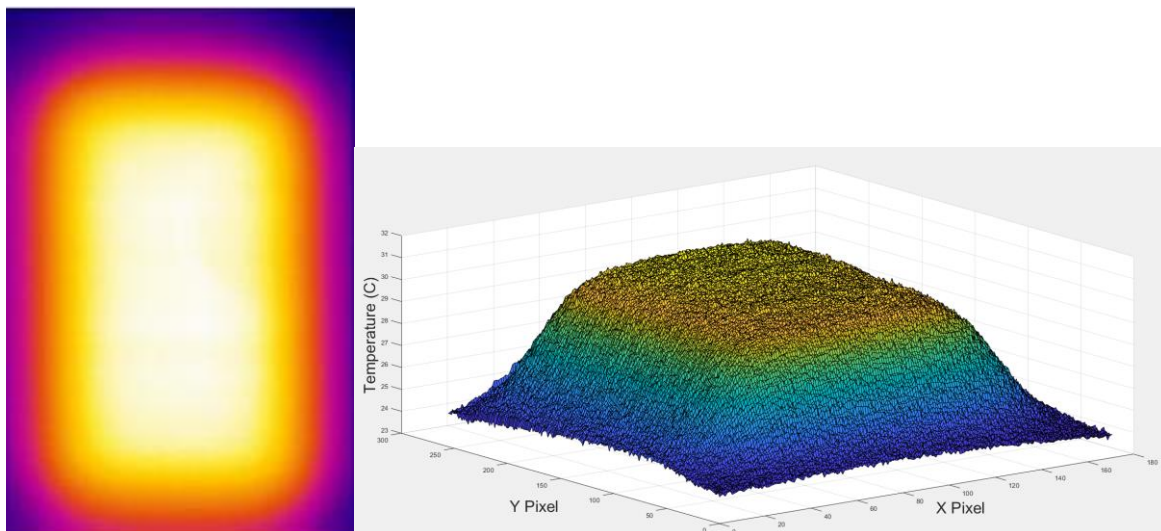


Figure 5-18: L: the cropped RGB image, R: visual representation of the cropped temperature data.

As the area of interest has now been isolated, the internal geometric profile can be determined.

To determine the geometric profile of the internal features, the designed FEX uses a combination of temperature differentiation and peak detection. To begin with, the temperature data is put through a Wiener filter. This removes a level of noise from the data, which if left can present itself as false positives when using peak detection to detect the internal geometry. The Wiener filter is an adaptive noise filtering method that uses an $M \times N$ local neighbourhood to estimate the local average around each value [70]. The lowest possible cut-off frequency is used to remove as much noise as possible before attenuation occurs. Figure 5-19 and Figure 5-20 show the data before and after it has been through the low pass filter.

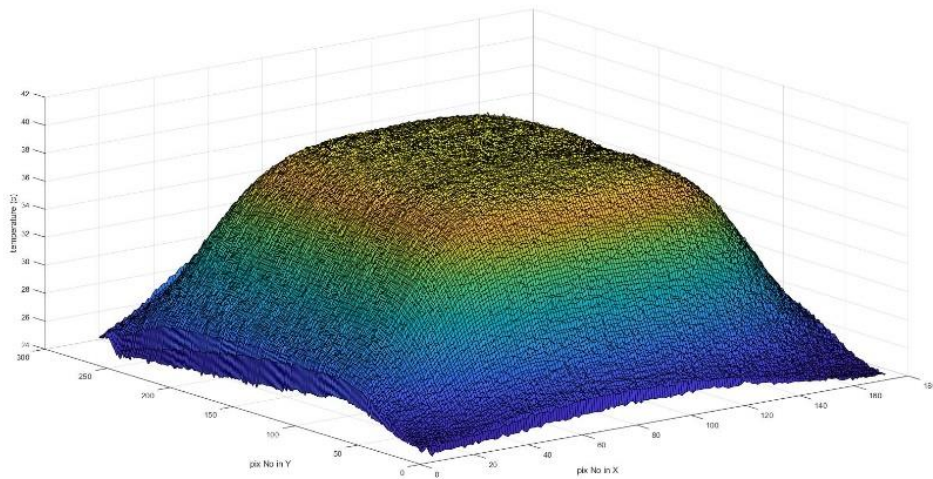


Figure 5-19: Temperature data before filtering

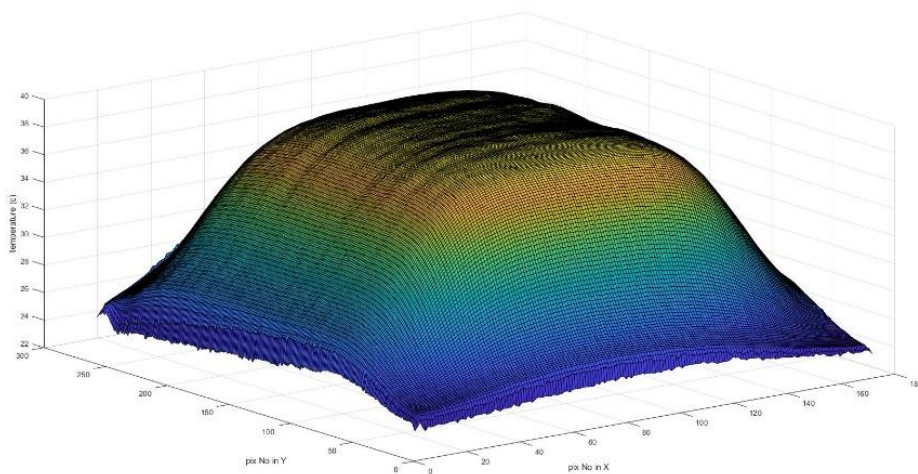


Figure 5-20: Temperature data after filtering

From this data, internal edge position can be deduced. First, traditional edge detection techniques were used in an attempt to extract the internal edge position. These trials are detailed in *Appendix F*. However, they proved not to be viable techniques. Therefore, a novel method of extracting the internal edge positions using the temperature data from the thermograms was developed. As stated above this feature extraction technique is based upon the temperature data recorded by the thermal camera, not the visual thermogram. The steps necessary to extract the geometrical edge position are detailed in this section. However, to begin with Figure 5-21, summarises this for clarity.

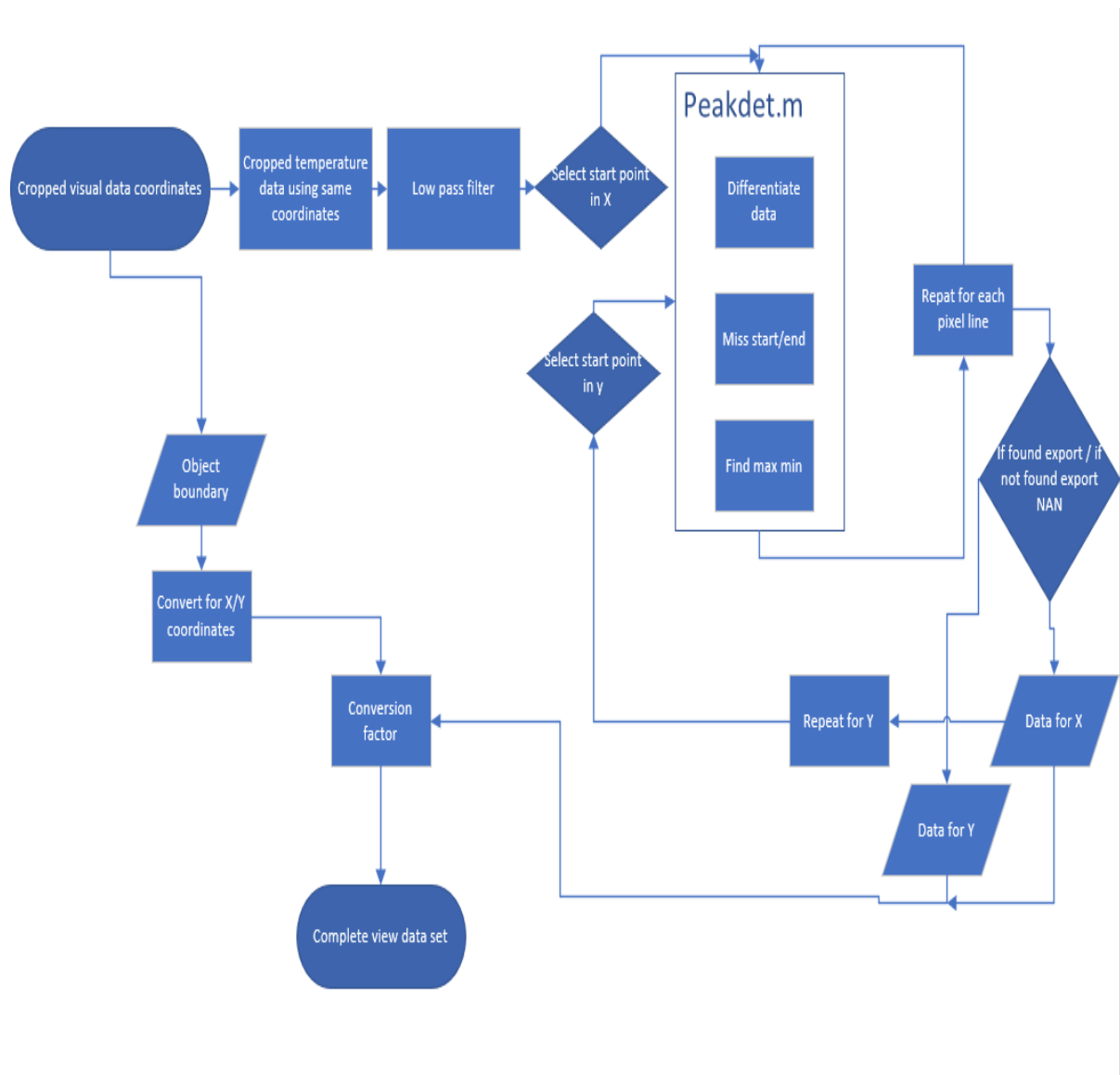


Figure 5-21: FEX operational flow chart

Once the data has been filtered, it can be differentiated. From this point, the FEX performs all operations for each line of temperature data in both the X and Y directions automatically. However, to ascertain a baseline manual user intervention is required at the start. A manually selected point in the Y direction is chosen to define the temperature profile in X. This is shown in Figure 5-22.

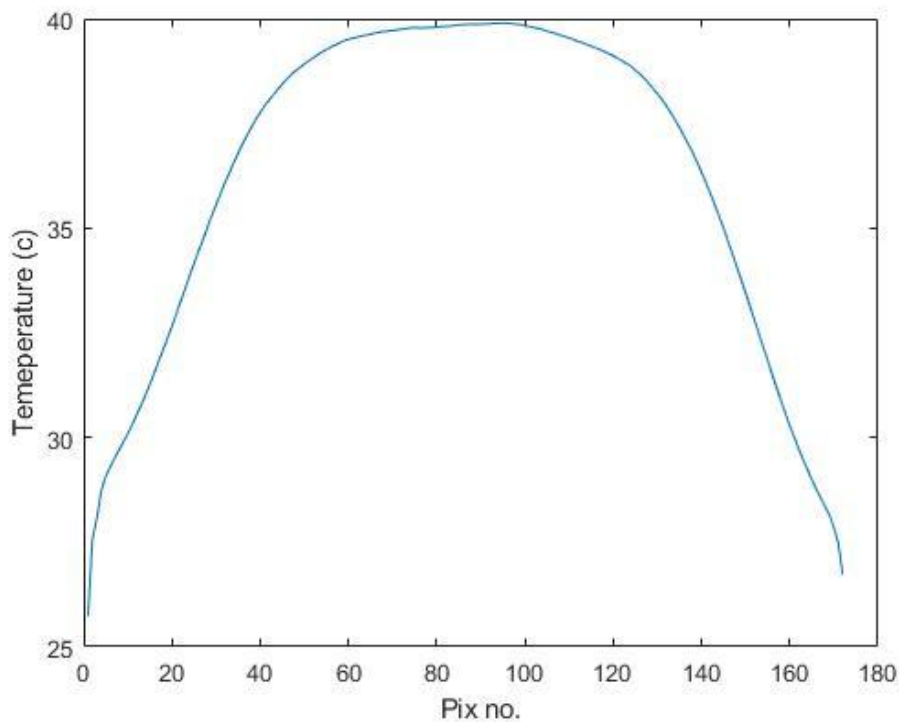


Figure 5-22: Temperature profile in X from a random point in Y

As with the FEA data in Chapter 4, the data is then differentiated using the basic operator:

$$y' = \frac{dT}{dx} \quad (2)$$

Figure 5-23 shows the resulting differentiated temperature data related to Figure 5-22. As can be seen in Figure 5-23, the highest differentiation is at the start and the end of the plot. This is effectively the external edge of the artefact and is not prevalent to finding the internal edges. Therefore, the algorithm discounts the first two highest peaks by missing the first and last five pixels in the image, thus allowing the location of the second two highest peaks. The method

for discerning the location of the peaks within the differentiated data is a higher-than-next-neighbour peak detection function (code can be found in *Appendix H.e- Peakdet*).

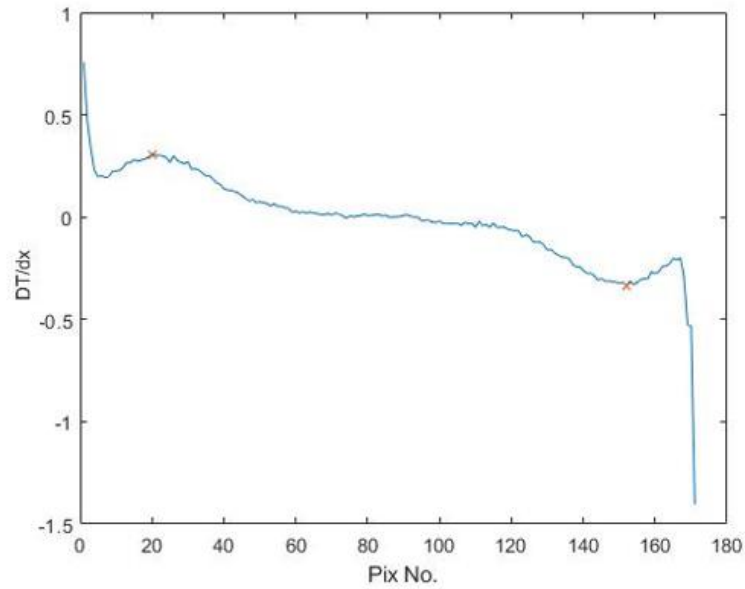


Figure 5-23: Differentiated data. Orange x marked the detected peaks

The function finds the maximum and minimum points within a set vector. A point is considered the maximum (or minimum) if the point preceding is lower than a pre-defined variable.

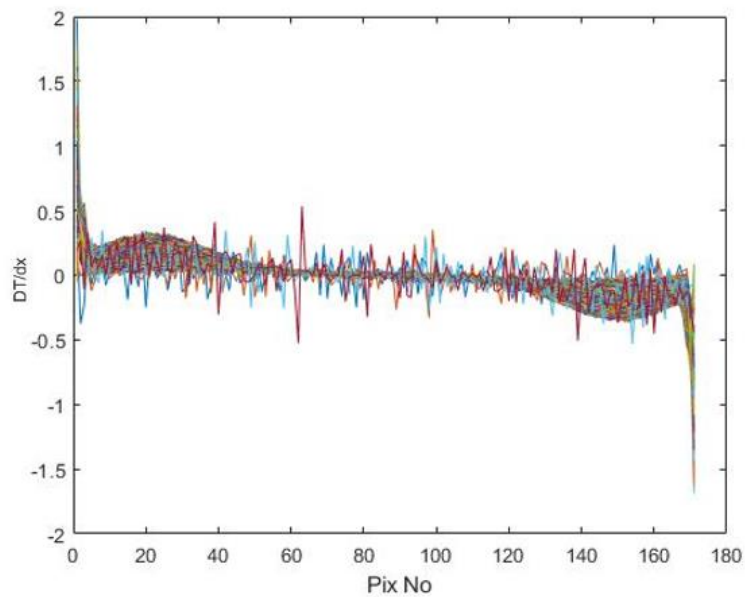


Figure 5-24: Compiled differentiated data for every pixel line in Y in the cropped image

With the boundary layer locations determined for one line of pixels, the FEX is now informed of the number of peaks that it needs to detect for each line of pixel, which in this case is two. The algorithm can now calculate the location of both peaks for each line of pixels in the Y direction of the cropped image. Figure 5-24 shows the differentiated data for every line of pixels in the Y direction.

The algorithm takes the differentiated data, again discarding the first and last five pixels, and determines the maximum and minimum points. If two points are returned, the X/Y values for those two points are stored and the algorithm moves to the next line. If less than two points are detected in the differentiated data, then that line is discarded, and the coordinates are not recorded. Figure 5-25 shows the discerned X/Y coordinates plotted on the original cropped thermogram.

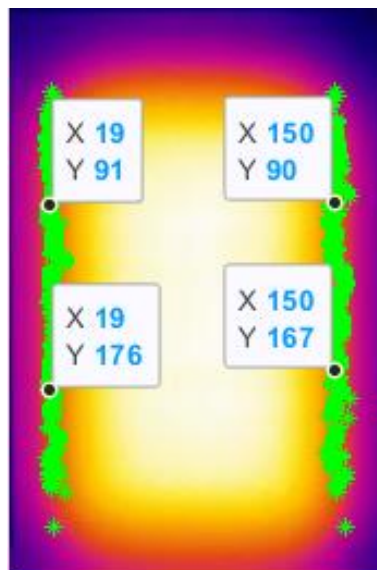


Figure 5-25: Original Thermogram showing max and min coordinates outlining edges in the Y direction

The FEX then repeats this process for the internal edges in the X direction. As with finding edges in the Y direction a random spot is selected in the X direction from which a single temperature profile in Y is selected (Figure 5-26, blue plot). This again is differentiated from

which the maximum and minimum points can be located (Figure 5-26, orange plot) using the peak detection method that was used for X. Once these points have been located and the number of max/min points is discerned, the FEX can repeat this process for every pixel line in the X direction (Figure 5-27).

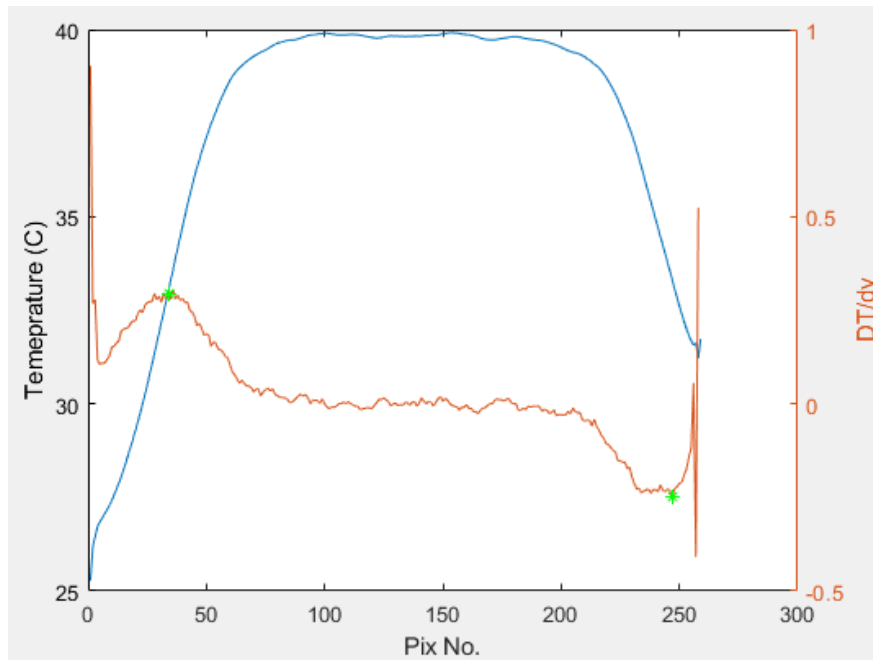


Figure 5-26: Temperature profile in the X direction (blue), and the Differentiated Data in the X direction showing Max/Min position (orange)

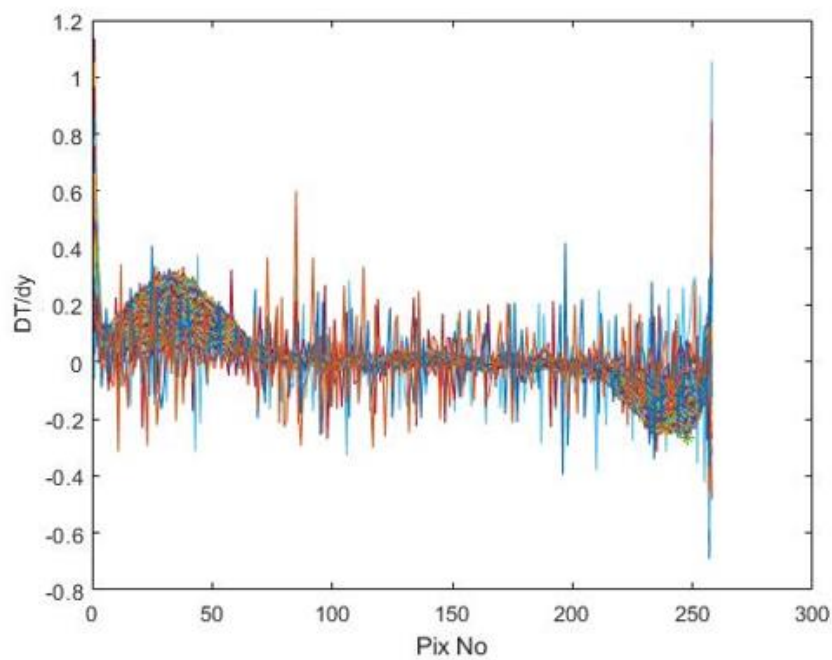


Figure 5-27: Compiled differentiated data for every pixel line in X in the cropped image

Figure 5-28 shows the max/min coordinates for all the pixel lines in the X direction in relation to the original cropped thermogram along with the corresponding coordinates for Y.

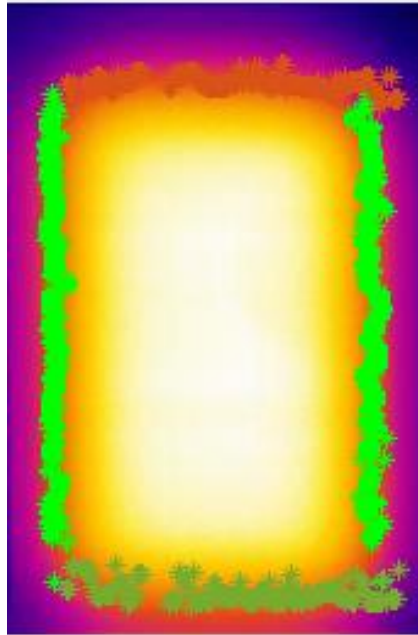


Figure 5-28: Cropped thermogram with overlaid X/Y MAX/MIN coordinates

At this point, the FEX outputs eight arrays:

1. Maxpeakxfh
2. maxpeakyfh
3. minpeakxfh
4. minpeakyfh
5. maxpeakyfv
6. maxpeakxfv
7. minpeakyfv
8. minpeakxfv

These arrays constitute all the coordinates that make up the four internal edges as shown in Figure 5-28. At this stage, they do not have a geometric position, with all X/Y positions denoted as a pixel count from (0,0), which is located in the top left corner of the cropped thermogram. To convert them into geometric distances all of the eight arrays listed above need to be the product of a geometric conversion factor. The FEX computes this conversion factor at the start of the algorithm. At the start of the algorithm, the user is requested to enter the measurement values for two of the artefact's external dimensions. The external width and height of the

artefact are 49.75mm and 74.87mm respectively. From these values and the corresponding pixel counts for the X and Y directions of the cropped image the pixel conversion factor can be deduced:

- $cl = \text{reallength} / \text{Length};$
- $ch = \text{realheight} / \text{Height};$
- $\text{conversion} = (cl + ch) / 2;$

In the above code, `Length` and `Height` are the pixel values, which for this image are given at 171px and 258px respectively. This resolves to give a conversion factor of 0.2915. With this, the X/Y pixel coordinates can be converted into geometric coordinates. Each of the eight arrays are then averaged.

Finally, the FEX reconstructs the outline of the artefact (as seen in Figure 5-29) in a new array consisting of numerous X/Y coordinates. At this stage, this outline only serves as a visual representation to highlight the external boundary of the artefact. However, when merging the internal and external point cloud sets these outline coordinates will serve as reference points. Figure 5-29 shows the final averaged geometric coordinates for all four internal edges and the external boundary.

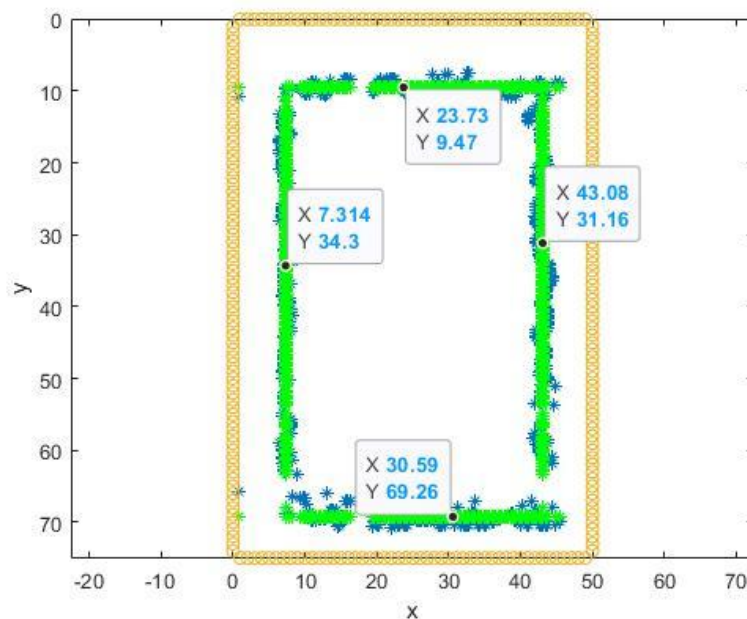


Figure 5-29: First face X/Y geometric positions

The final positions for the internal rectangle as seen in this view are shown below in Table 5-4 with the sign convention shown in Figure 5-30:

Table 5-4: First view geometric results

Dimension	Actual (mm)	Recovered (mm)	Error (mm)
X1	7.62	7.31	-0.19
X2	42.25	43.08	0.58
Z1	10.62	9.47	-0.53
Z2	69.76	69.26	-0.74

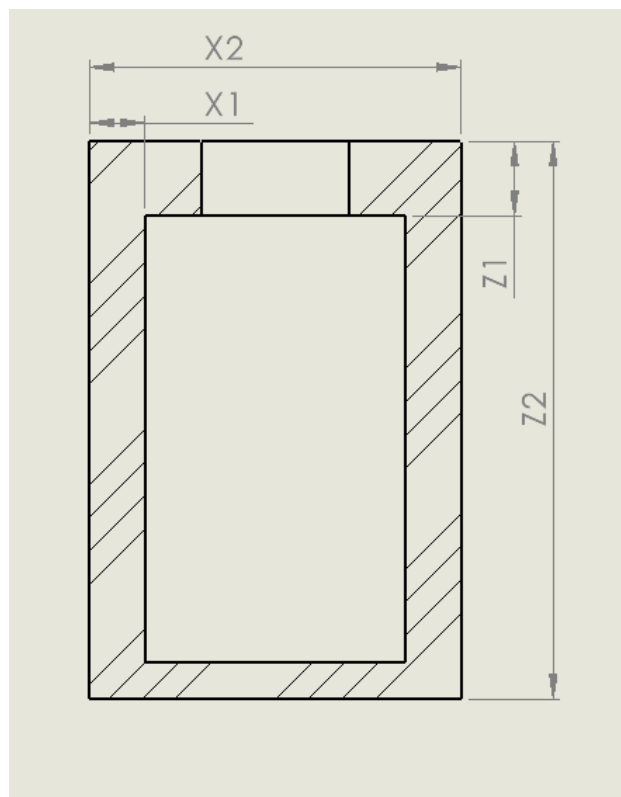


Figure 5-30: First view sign convention

As can be seen in Table 5-4 the recovered values do deviate from the actual with the max error found at Z1 being -0.74mm. The minimum error is at X1 being only -0.19mm, and the conditional average error for the whole dimensional set is 0.51mm.

5.3.5. Second Face Feature Extraction

For the reconstruction of the internal features of most shapes, a minimum of three projections are generally required. The artefact currently being reverse engineered is symmetrical in all

three axes; therefore, the reconstruction of a single face would be sufficient for a full reconstruction. However, if the artefact under investigation was a complete unknown entity, there is no way to tell if the internal geometry has changed when viewed from a different projection. Also, for this example it is beneficial to show how the next stage of the reconstruction software merges two perpendicular projections. From the feature extraction of face one the length and height of the internal structure has been ascertained. However, to determine a complete set of internal dimensions for this artefact the width is also required.

Therefore, the FEX program is run again but from a new projection. Figure 5-31 (L) shows the corresponding thermogram from the new projection.

From this point, the operation is the same as in section 5.3.4. The results of running this image through the FEX are as follows. Figure 5-31 (R) shows the acquired internal positional results for the second face, and Table 5-5 shows the comparison between the actual values and the recovered values.

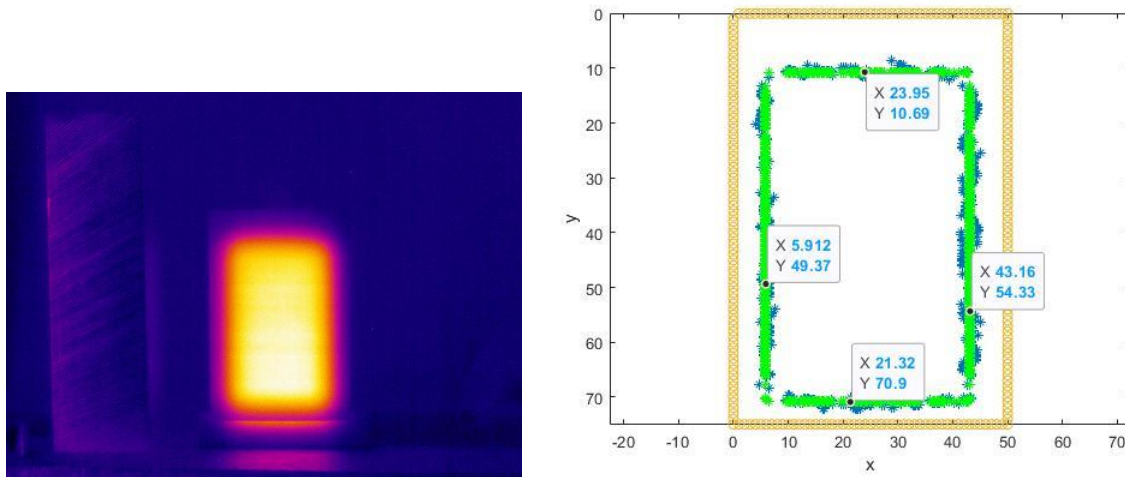


Figure 5-31: L - 2nd face thermogram, R - 2nd face X/Y coordinates

The sign convention for Table 5-5 is shown in Figure 5-32:

Table 5-5: Second view geometric results

Dimension (mm)	Actual (mm)	Recovered (mm)	Error(mm)
Y1	7.52	5.91	1.61
Y2	42.26	43.16	-0.9
Z1	10.62	10.69	-0.07
Z2	69.76	70.9	-1.14

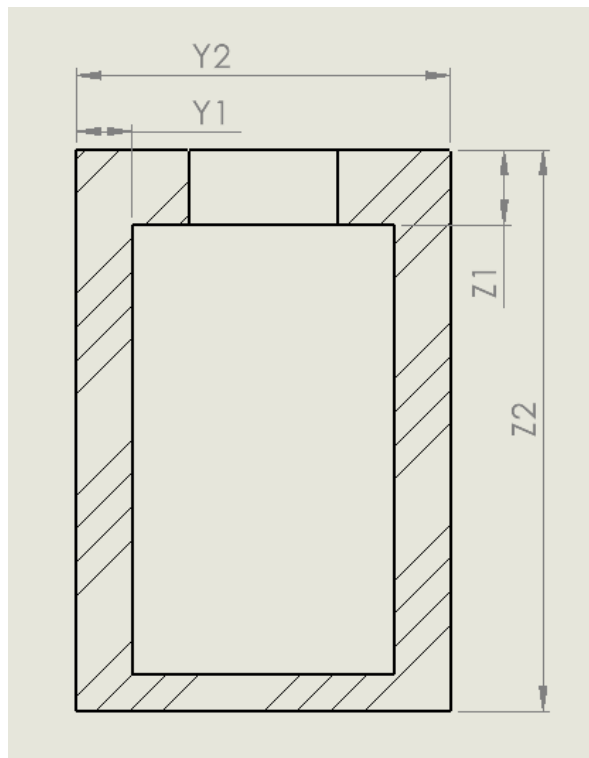


Figure 5-32: Second view sign convention

The results presented in Table 5-5 show that Y1 has the largest error (1.61mm), whilst Z1 has the smallest (-0.07mm). The conditional average error for this dimensional set is 0.93mm.

5.3.6. 3D Internal Reconstruction

Now that two perpendicular faces have been processed, the points that have been recovered can be assembled in three dimensions. The reconstruction phase is effectively reverse projection. As shown in Figure 5-33, in orthographic projection, the face of a 3D object is projected onto a 2D plane parallel (POP) to that face. Projectors or rays connect the intersection point on the 3D object to the corresponding ones on the 2D projection [71].

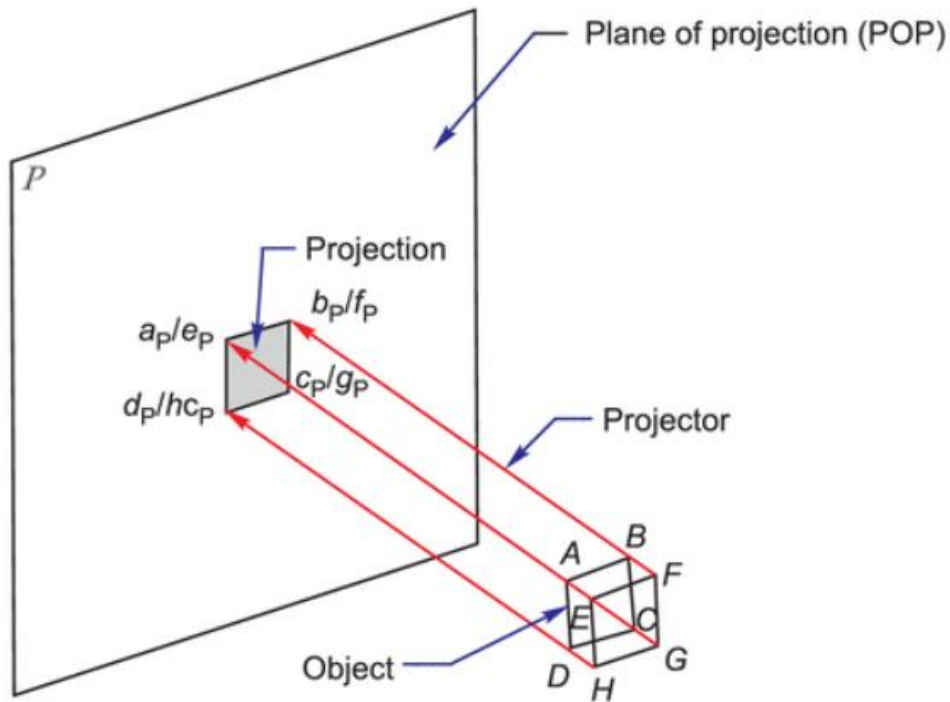


Figure 5-33: Example of projection courtesy of Engineering Graphics – Solving the intricacies of orthographic projection by A.M. Chandra [69]

In this investigation, in effect we already have the projections, the two extracted faces. From reviewing the results from the two sets of recovered face data it can be determined that the internal geometry consists of a single primitive geometric shape. This is visualised by overlaying the thermograms onto the corresponding faces of the TTM. Figure 5-34 shows this overlay and the resulting projections that such a shape would produce if it were disassembled orthographically. Figure 5-35 is a simple visual representation of the projected internal structure, however using the two sets of recovered data, geometrical distances can be added, and an accurate representation can be created. As was stated above, this procedure is effectively parallel projection in reverse as the projections have already been produced.

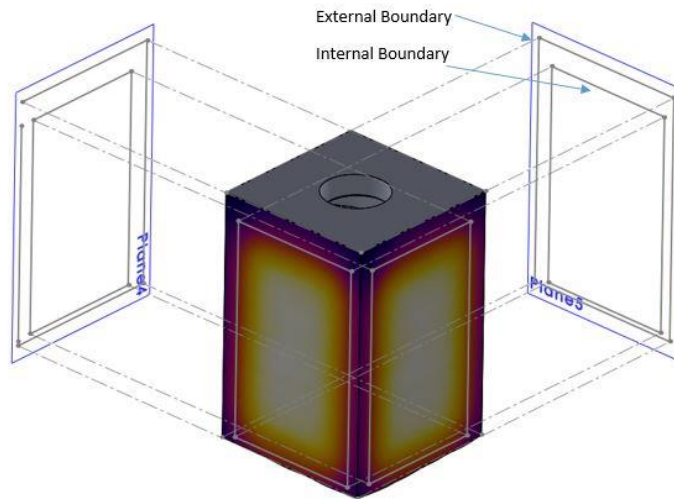


Figure 5-34: Visual representation of the projection of the internal structure

Due to this, it is important to understand the relationship between the two faces/projections, and how they correspond with each other. Figure 5-35 shows how points in both the projections relate to their corresponding points in the 3D reconstruction.

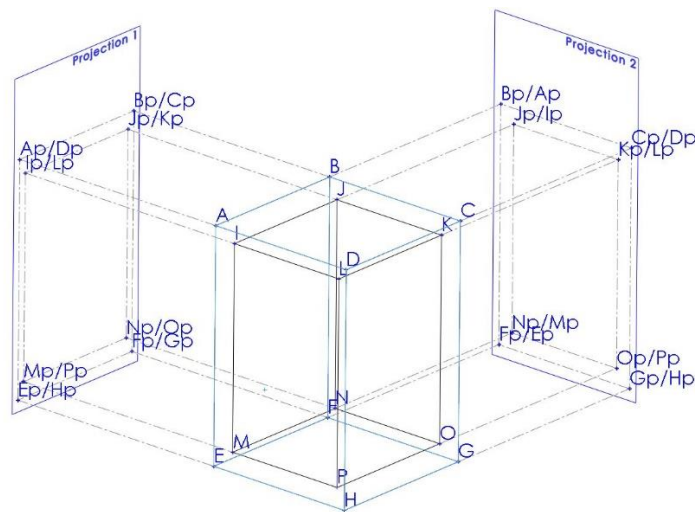


Figure 5-35: Points from the projection planes and their corresponding points in 3D

From information extracted from the two perpendicular thermograms, referring to Figure 5-35, the coordinates for faces ILMP, ADEH, DKPO, and DCHG have been recovered. The remaining points in Figure 5-35 all lie upon the projection lines for the faces mentioned above. For this shape, all the relevant data required to recreate it in 3D has been obtained. The

extracted information is now entered into a second algorithm that will arrange them accordingly. This algorithm is found in *Appendix H.f – Squareass*, with a progress flow diagram detailing its operation shown below in Figure 5-36

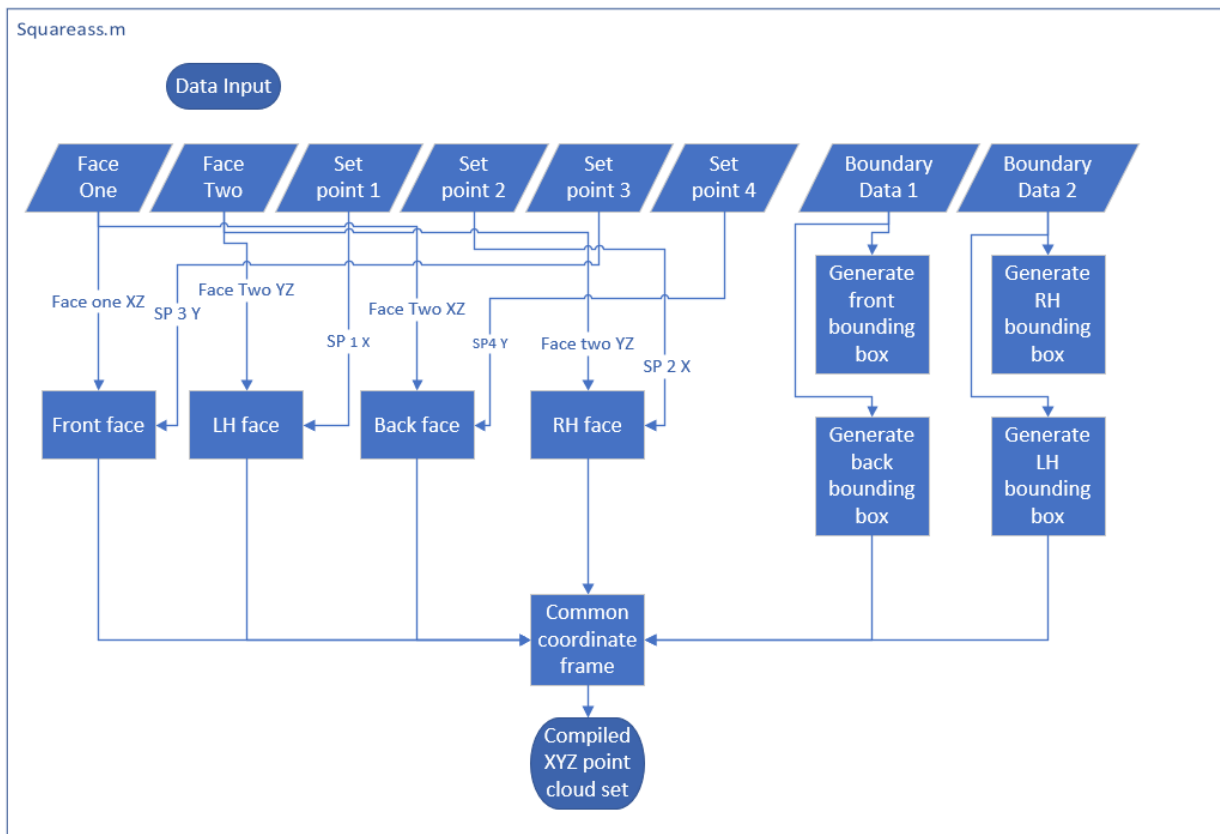


Figure 5-36: *Squareass.m* Process flow diagram

Inputted into the algorithm are the two data sets for the internal edges, the two data sets for the external surround, and four reference points that will indicate the 3D offset between the internal and external faces. In the algorithm, the two external faces are combined, with their coordinates transposed from XY to XZ or ZY based upon the face's orientation. The same process is applied to the coordinates for the internal faces, with the additional step of adding the reference point value to offset the internal face from the external. As the remaining points/faces required for a full 3D representation lie on the same projection lines as the two extracted faces, the algorithm generates new points based on these lines and their corresponding intersection points.

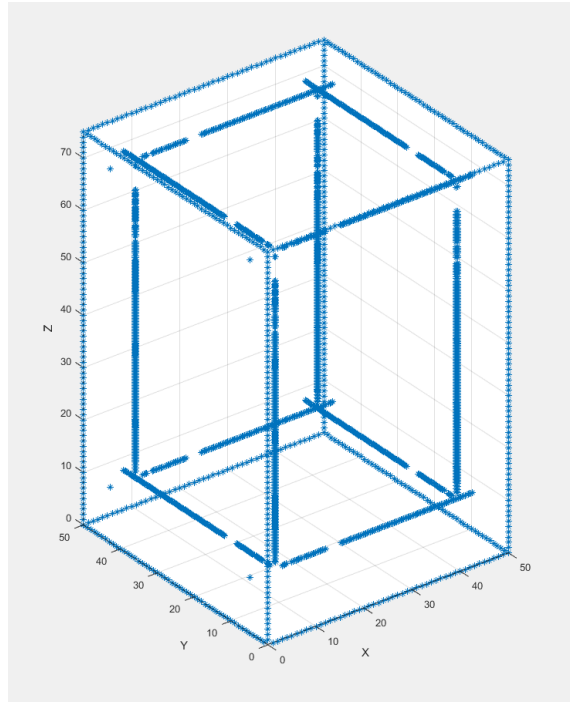


Figure 5-37: Complete 3D set compiled from two orthographic projections

Figure 5-37 shows the final 3D representation of the two extracted faces. Finally, all the points, for both faces and the newly created ones, are combined into a single XYZ point cloud set. At this stage the XYZ point cloud can be exported and recombined with the PCD from the external scan. This process is detailed in *Appendix G*.

5.4. Aluminium Version and external heating

As seen in Chapter 4 internal geometric extraction for highly conductive materials such as aluminium did not produce results as definitive as those found when using to materials with much lower thermal conductivity.

However, this was mainly true when using core heating techniques to excite the surface temperature gradients. As was seen in section 4.5 externally heating the artifact to excite the surface temperature gradients, much more stable results over time were observed. In this section both core heating and external heating techniques are performed on an aluminium version of the square artifact that was used in section 5.3. This artefact can be seen in Figure

5-38 and the actual dimensions of the artifact can be found *Appendix E*. This aluminium artifact was machined in two halves from 5083, a typical grade of aluminium. After inspection the artifact was pressed together, with the designed interference fit ensuring it locked together and that heat transfer would be continuous throughout the part.



Figure 5-38: Aluminium test artifact

The first heating cycle performed on this aluminium artefact was the same core heating cycle performed on the PLA variant seen in section 5.3.

After adding the heating medium (boiling water $\approx 100^{\circ}\text{C}$), the surface temperature of the viewed face rose extremely quickly. After 55.2s the maximum surface temperature had been reached. Figure 5-39 shows the thermogram at $t=55.2\text{s}$, and for comparison a thermogram of the PLA artifact taken at the same point in time. Figure 5-40 shows the surface temperature profile at $t=55.2\text{s}$ (orange plot), plotted against the surface temperature profile for the PLA (blue plot) artifact again for comparison.

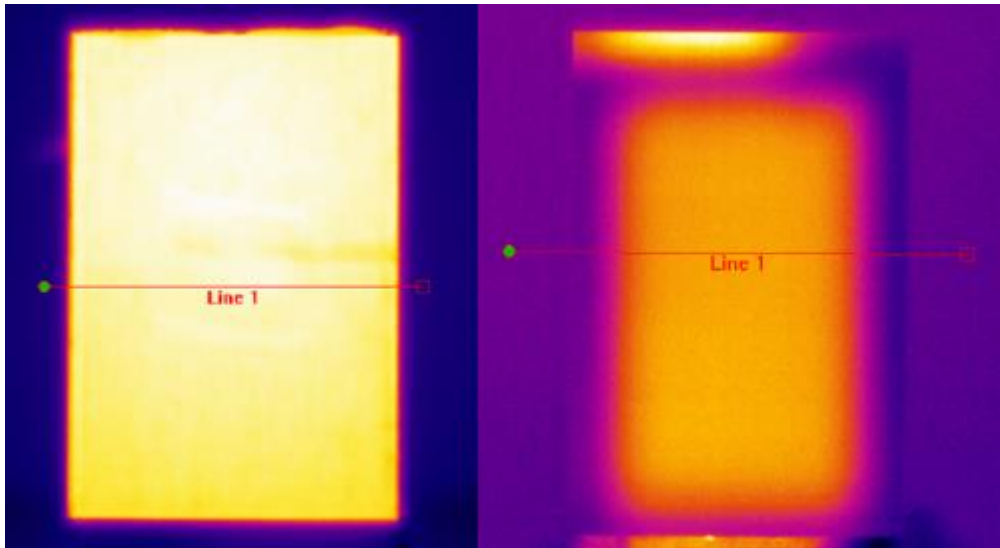


Figure 5-39: L - Aluminium artifact at $t=55.2s$, R - PLA artifact at $t=55.2s$

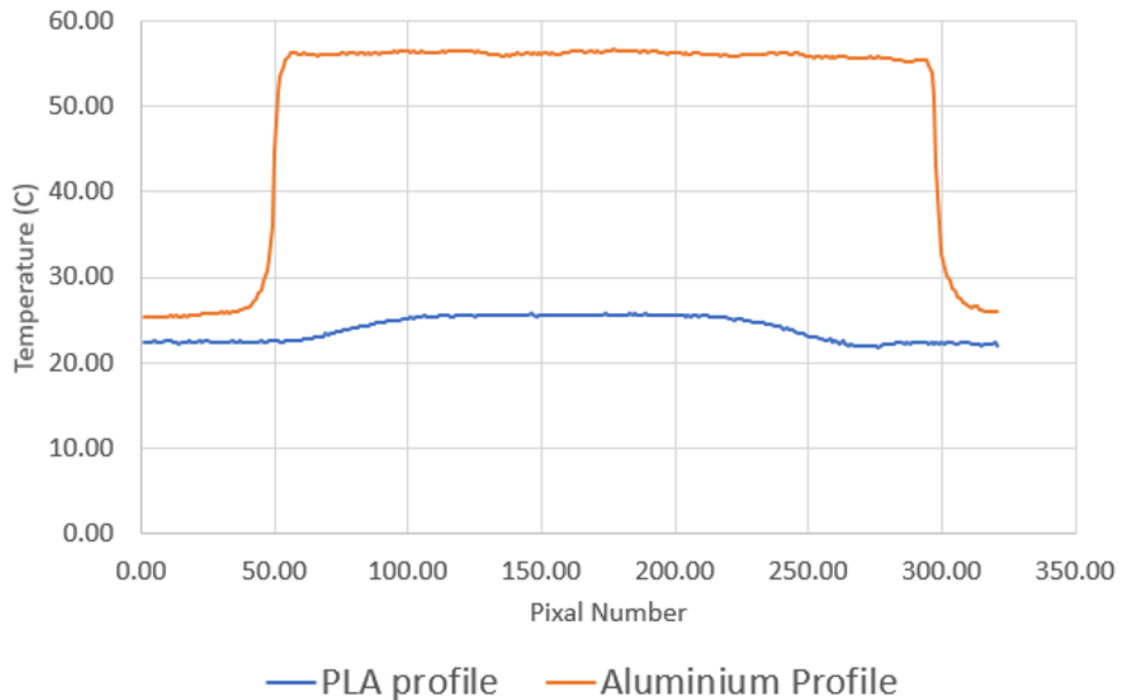


Figure 5-40: Surface temperature profiles from "line 1" in Figure 5-39 at $t=55.2s$ for PLA and aluminium

Whilst the maximum temperature that was shown in Figure 5-40 happen at $t=55.2s$, homogeneity occurred even faster at $t=32.8s$, just after added the medium had finished, which occurred at $t=20$ Therefore it was at the section of thermal capture between $t=20s$ and $t=32.8s$ that was focused on to determine if any of the surface temperature profiles could produce

geometric internal dimensions. Several thermograms from this period were extracted and entered into the FEX algorithm.

From the thermograms entered into the FEX, the first thing that was made apparent was the number of false positives that the algorithm returned. Figure 5-41 shows example thermograms with the high points from the differentiated temperature imposed over the top.

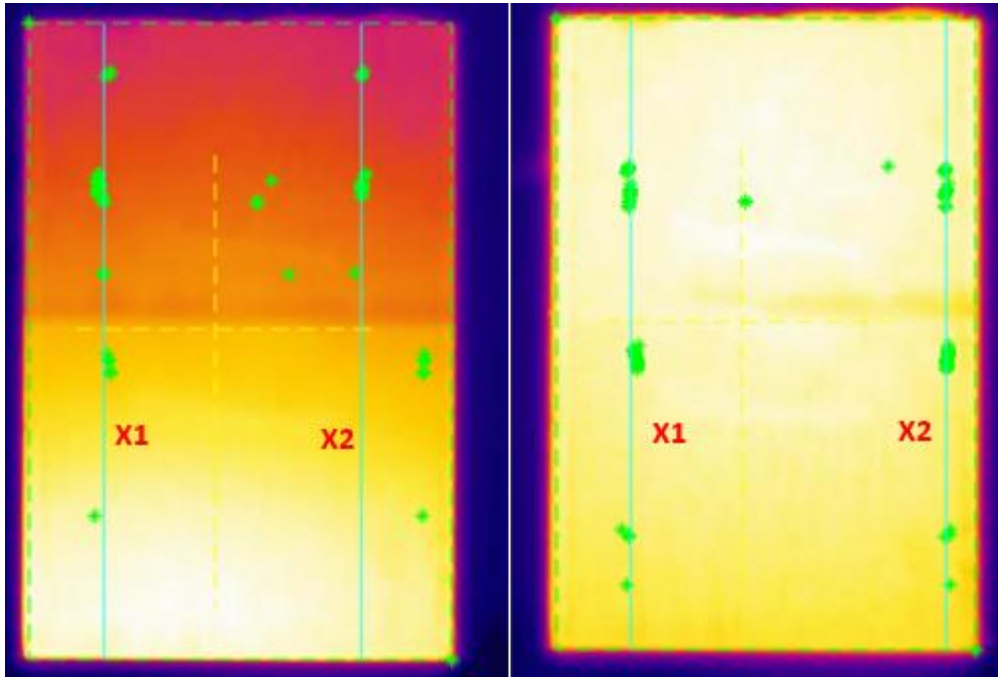


Figure 5-41: Example thermograms from the aluminium heating cycle. Potential edge positions imposed over the top

As can be seen in Figure 5-41 both images show numerous false positives, that when added into the average edge position from all the points found led to larger geometric errors. For example, the images on the left in Figure 5-41, the average geometric position for X1 and X2, with the false positives included give:

Table 5-6: Recovered results from aluminium artifact with false positive error

	Recovered	Actual	Error
X1	8.6mm	7.5mm	1.1mm
X2	38.2mm	42.32mm	4.12mm

However, it was found that by removing these outlying false positives, by setting a limit with respect to the overall mean, the average geometric positional error was reduced, as can be seen in Table 5-7.

Table 5-7: Recovered results from aluminium artifact without false positive error

	Recovered	Actual	Error
X1	7.75mm	7.5mm	0.25mm
X2	41.54mm	42.32mm	0.78mm

Whilst removing these outlying false positives did reduce the error for X1 and X2, no results were recorded for the horizontal edge dimensions of Z1 and Z2. Several thermograms which resolved dimensions for X1 and X2, did not produce any usable differentiated surface temperature data from which geometric information could be deduced. Figure 5-42 shows a surface temperature profile used in the horizontal edge extraction, along with the corresponding differentiated temperature data.

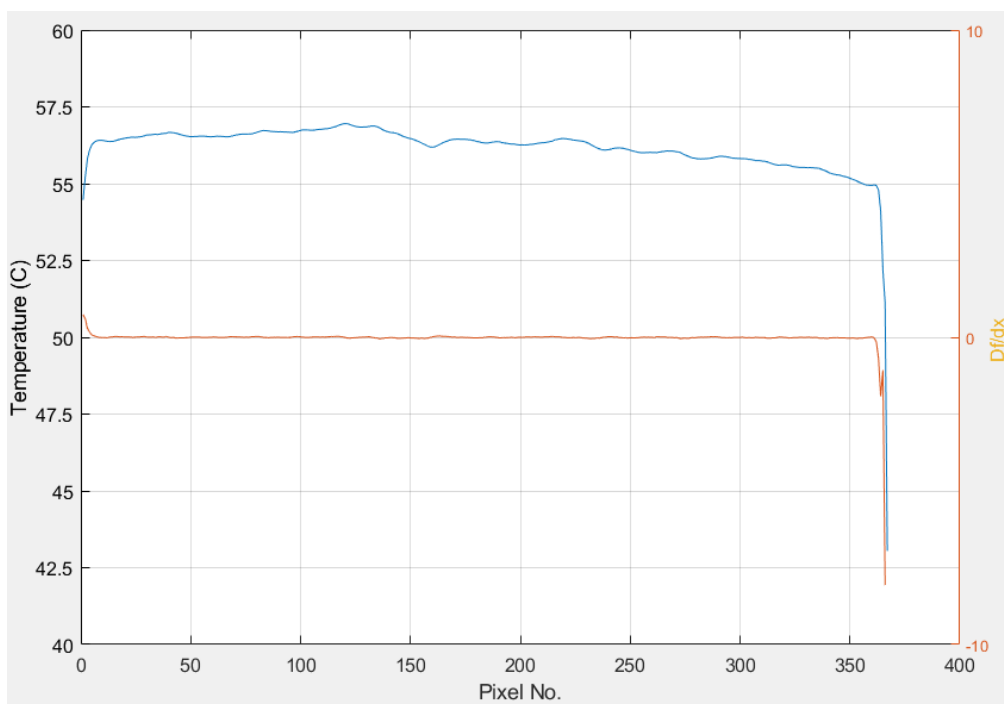


Figure 5-42: Surface temperature profile with differentiated temperature data

As can be seen in Figure 5-42 the differentiated temperature data shows no peaks and is almost perfectly flat. This is the reason that the peak detection function failed to determine their location. Due to this, and thus having only a partial data set taken for the X dimensions a complete geometric reconstruction for this face of the aluminium artifact was not possible.

Given the above result, and what that the computational results showed with regards to core heating verses external heating, this test was repeated but instead of using boiling water to heat the core, the artifact would be externally heated from one side, with the opposite side being viewed. The computational results in section 4.5 showed that heating a high thermally conductive part externally produced much more stable results over a longer period than was observed when the same part was core heated.

To validate whether this style of heating method was still viable for this artifact, the CAD model of the artifact was run in an external heating simulation. 90°C of heat power was added to 20mm x 20mm square representing the ceramic heater, with all other surfaces being exposed to 6W/m²*k of convective heat transfer as can be seen in Figure 5-43. The simulation run time was 40s in keeping with the pervious external heating simulation.

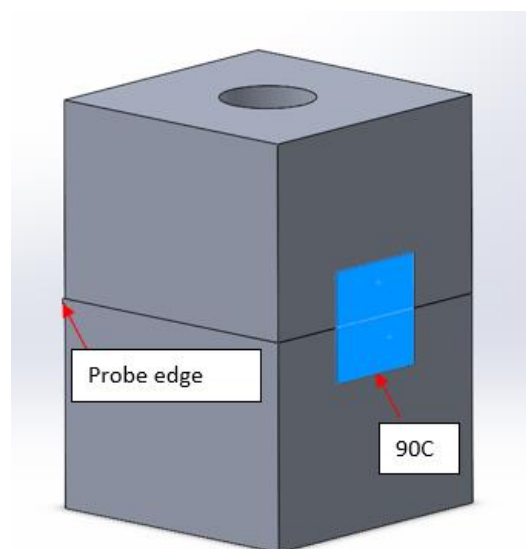


Figure 5-43: CAD model of aluminium artifact showing heating patch and probe edge

Figure 5-44 shows the resulting thermal model at $t=40s$, with the corresponding surface temperature profile, and Figure 5-45 shows the internal edge positions extracted from the temporal surface temperature gradients.

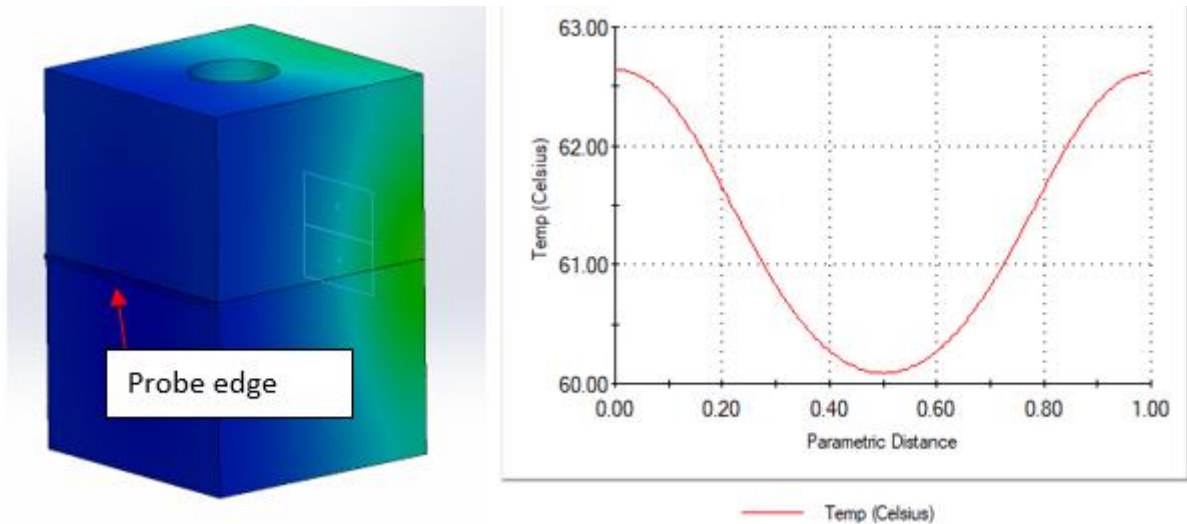


Figure 5-44: L - Resultant thermal model of aluminium artifact at $t=40s$, R - corresponding surface temperature profile

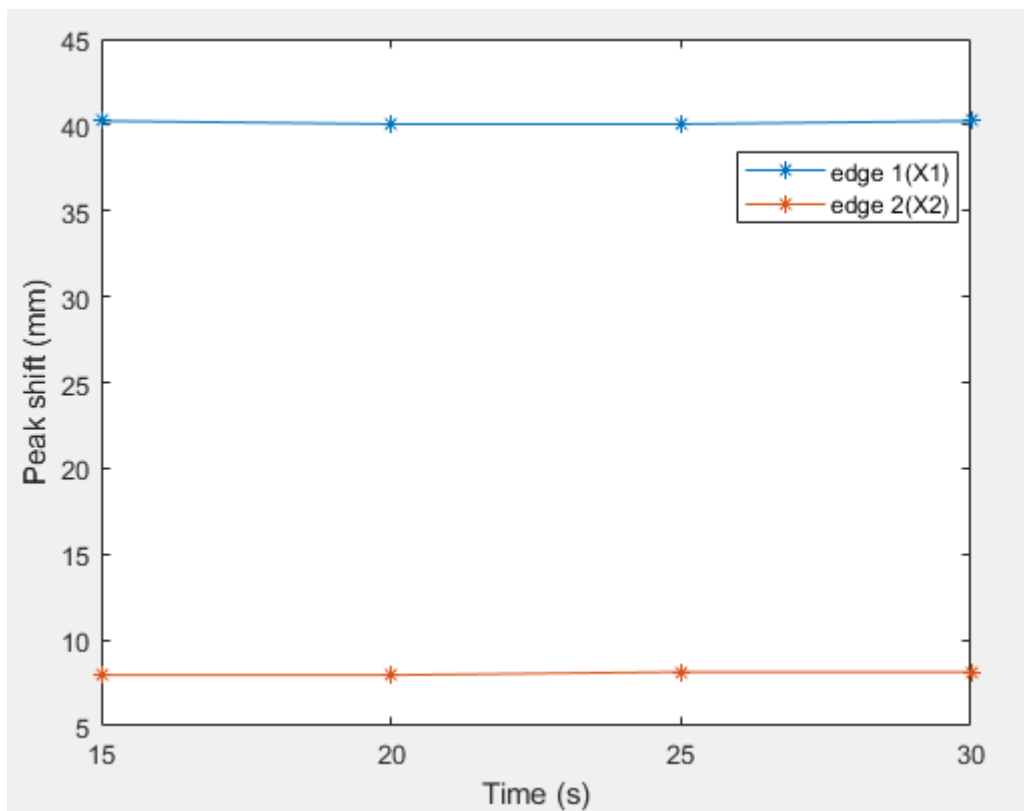


Figure 5-45: Resultant internal edge positions from simulation

From Figure 5-44 it can be seen that surface temperature gradients are induced using this heating method, and Figure 5-45 shows that internal distances can be extracted over this period. To perform this test physically a 24W metal ceramic heater was used to generate the 90°C of heating power. This was affixed to a metal backboard and then had 20V passed across it. This resulted in the heater having average surface temperature of 88.3°C. The heater was fixed to a backboard (Figure 5-46) and not the artifact itself to allow to the heater to get to its maximum temperature before the artifact was placed up to it. This technique was more representative of the above simulation that had its external heat source applied instantaneously.

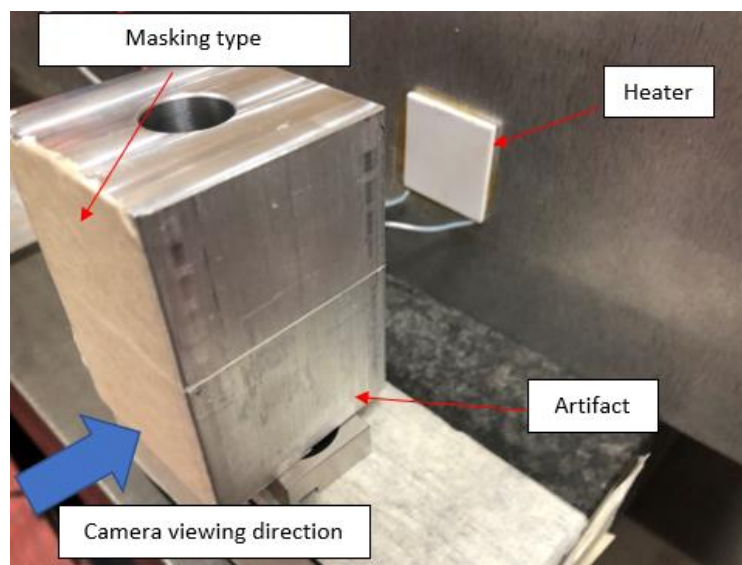


Figure 5-46: External heating set up (artefact moved so heater is visible)

With the heater up to its maximum temperature the artifact was placed firmly up to it. The heat transfer was then recorded using the A655SC for 40s.

A thermogram were extracted at $t=15,20,25,30s$, in accordance with the timings from the computational simulation, and entered into the FEX. Not a single extracted thermogram provided extracted geometric data. When reviewing the surface temperature profiles extracted at those values of t , it becomes clear why it was not possible to extract any geometric information from the thermal data. Figure 5-47 and Figure 5-48 show the actual surface

temperature gradients from the physical heating cycle, and the surface temperatures gradients from the simulation.

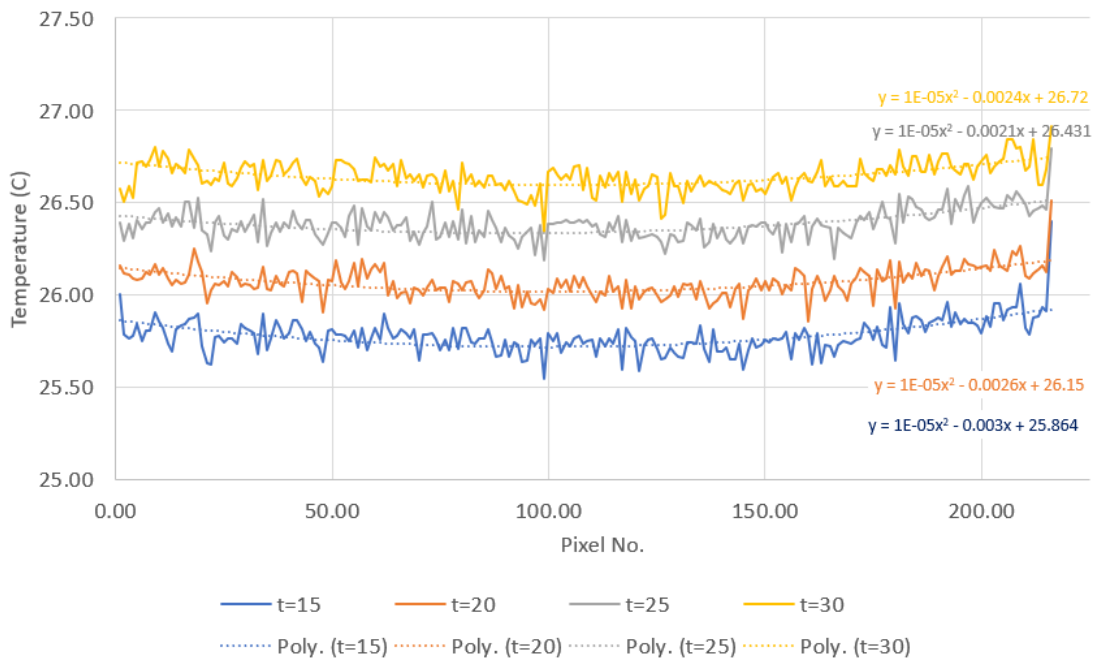


Figure 5-47: Actual surface temperature profiles for $T=15, 20, 25, 30s$

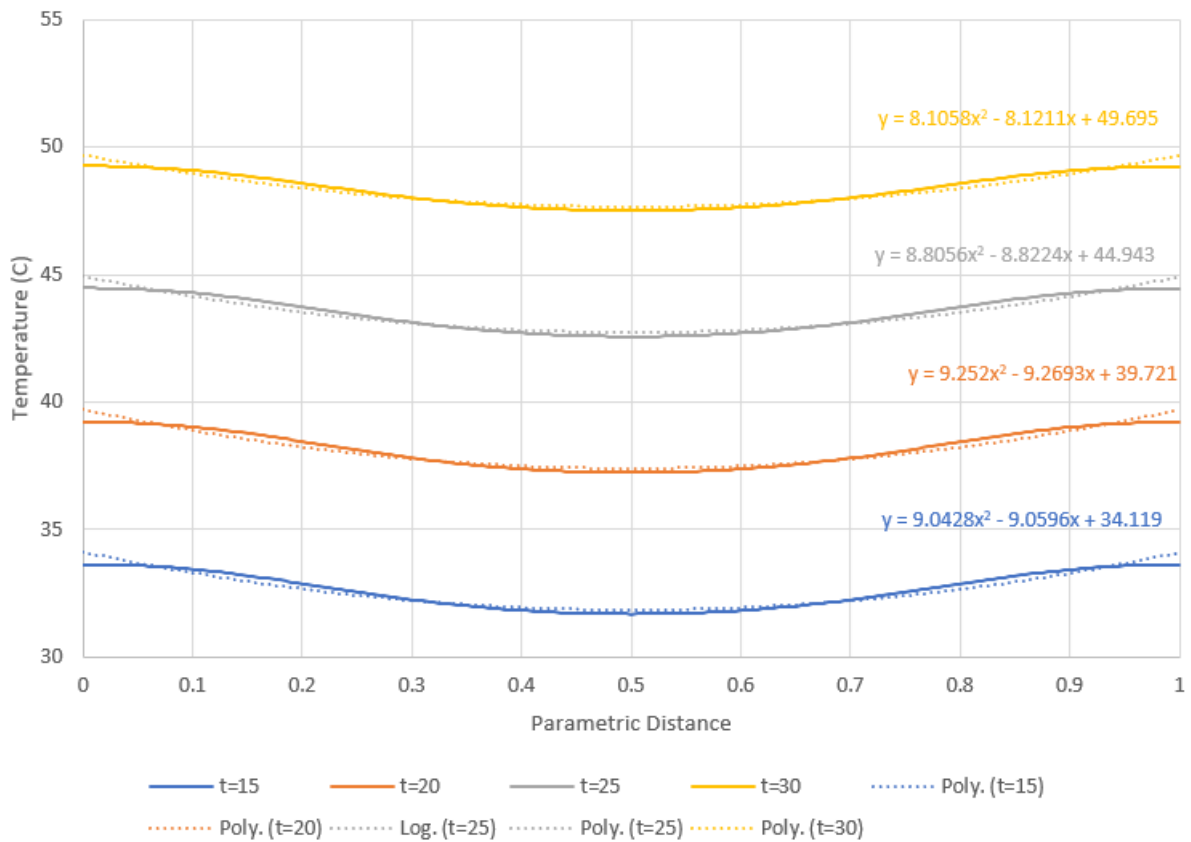


Figure 5-48: Simulated Surface temperature profiles for $T=15, 20, 25, 30s$

As can be seen in Figure 5-47 and Figure 5-48 not only is the simulated temperatures much higher than was actually observed, the gradients of each surface temperature profile are much lower in the actual data then compared with the computational surface temperature gradients. When the actual surface temperature data is differentiated, as can be seen in Figure 5-49 any “peaks” normally associated with internal edge detection are not apparent, undetectable in the noise level.

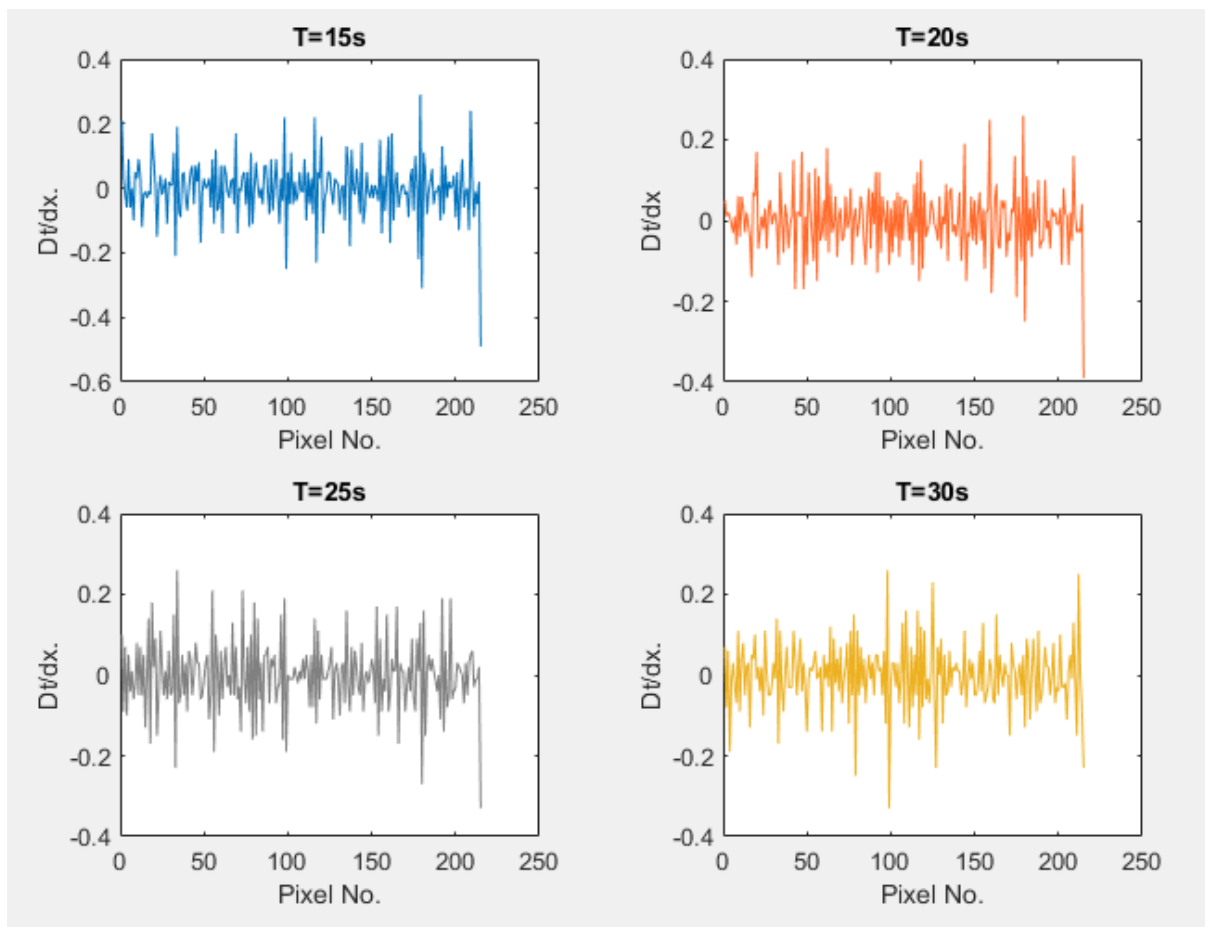


Figure 5-49: Differentiated temperature data from Figure 5-47

As the above external heating test did not produce any internal geometric dimensions and given the observed differences between the computational results and actual results with regards to the surface temperature profiles, this test was repeated but with the ceramic heater now fixed to the artifact itself. As said before the heater was fixed to a back board to order to allow it to reach its maximum temperature before the artifact was introduced. However, even though the

artifact and the heater were firmly mated together there was the potential for a small air gap between the two that could have acted as an insulator during the heating process. With the heater now fixed directly to the part, any air gap will have been eliminated.

With the heater attached to the artifact the same test was repeated. Thermograms were again extracted at $t=15,20,25,30$ s. Once again none of the extracted thermograms ($t=30$ s thermogram shown in Figure 5-50) produced usable surface temperature gradients from which internal geometric dimensions could be deduced.

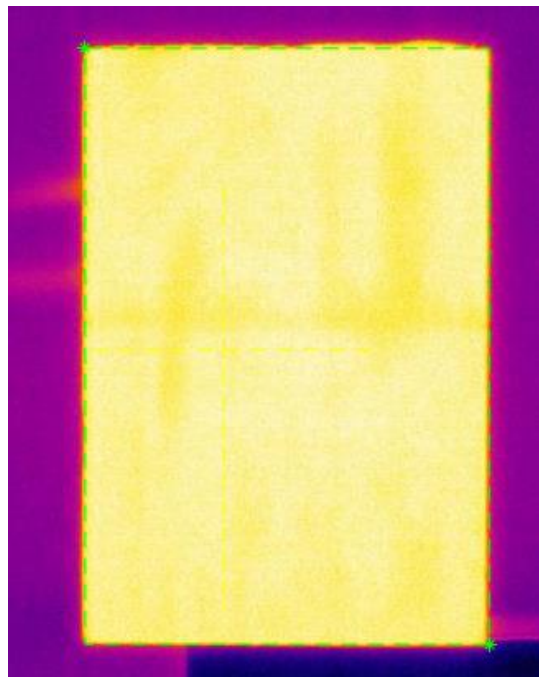


Figure 5-50: Thermogram using external heating at $t=30$ s

Reviewing the extracted surface temperature profiles for the various values of t , the results, shown in Figure 5-51, show even less gradient than was seen in the previous test. These results show that by fixing the heater directly to the artifact, the artifact appears to heat up evenly across its viewed face over time. Given this, and the apparent lack of any temperature gradient in the differentiated temperature series, no noticeable peaks from which internal dimensions can be deduced were observed (Figure 5-52).

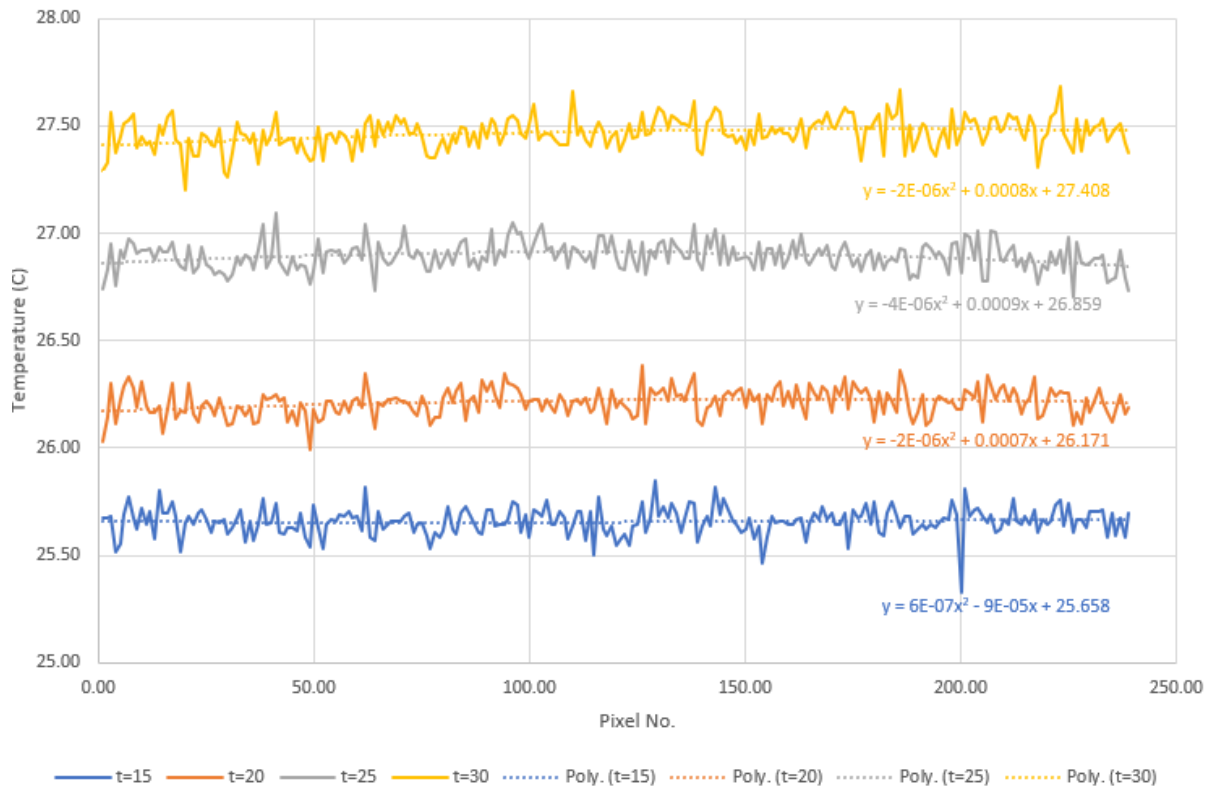


Figure 5-51: Surface temperature profiles from external heating (heater fixed)

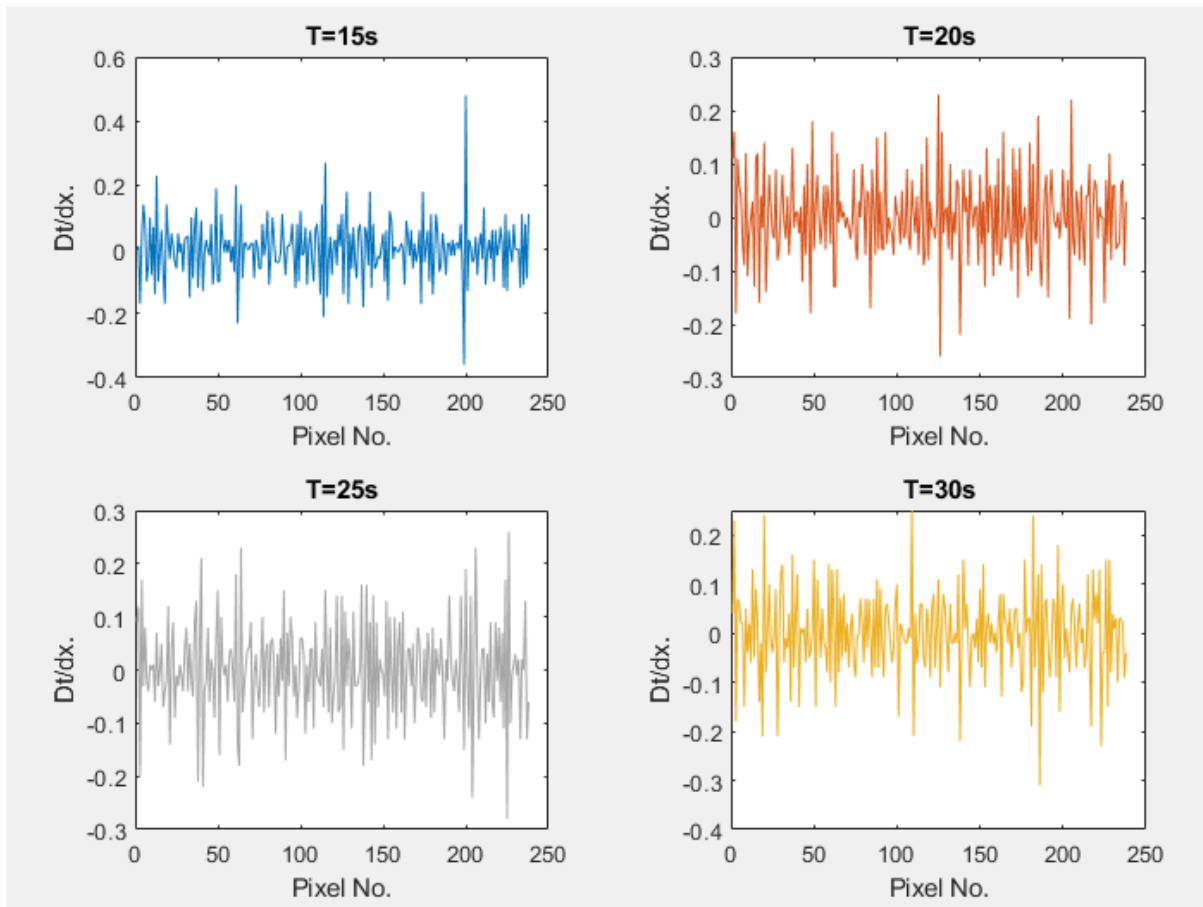


Figure 5-52: Differentiated temperature data from

At this stage it is not known why there is such disparity between the simulated and the actual test results, given that all constraints such as material properties, heating conditions and heating time, were kept as consistent as was possible. One hypothesis was that the internal bulk temperature of the artifact internal structure, which will affect convection, was changing as the artifact was heated. To test this hypothesis the simulation, describe in this section was rerun with an internal bulk temperature of 40°C (double that of the external ambient). The simulation results proved inconclusive with regards to the resultant surface temperature profile, as there was no discernible difference in surface temperature.

5.5. Second Artefact - Cuboid

The process that has been described in sections 5.3 and 5.4 was then repeated using a cuboidal shape to verify that the extraction algorithms can work consistently when the artefact under scrutiny has differing dimensions. The new artefact (Figure 5-53) is a cuboid, with external dimensions 74.34x74.02x50.35mm. The shape is again hollow, with a 5mm wall separation between the inner and outer faces.



Figure 5-53: Cuboid artefact

The same process in section 5.3.4 was repeated with this artefact. A heating medium (water at 100°C) was added, and the thermographic response was recorded. The two recovered thermograms, one for each projection, are shown in Figure 5-54.

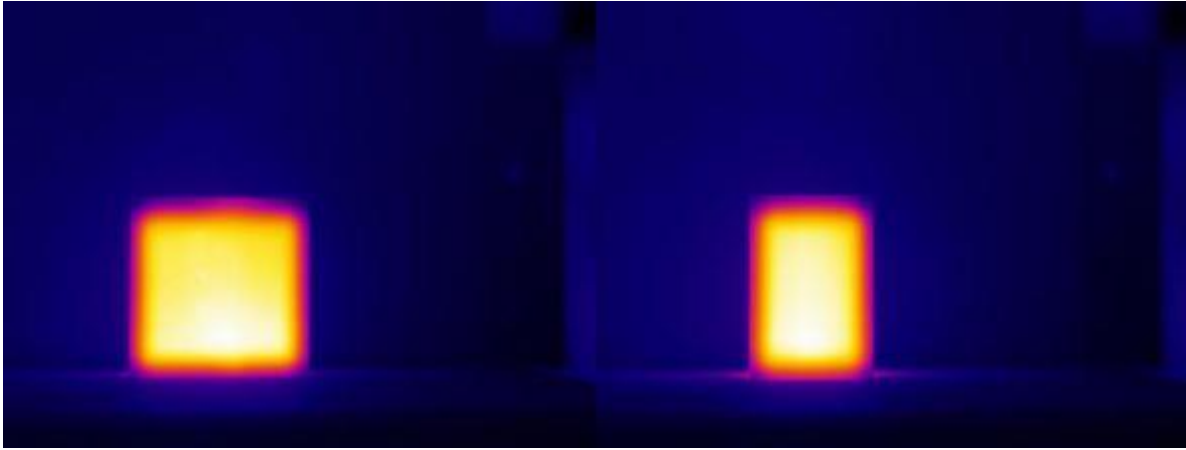


Figure 5-54: L- Front face, R- Side face

The two thermograms and the corresponding temperature data are then separately inputted into the feature extraction software, followed by the assembly algorithm. Figure 5-55 shows the resultant outputted CPD with corresponding XYZ values.

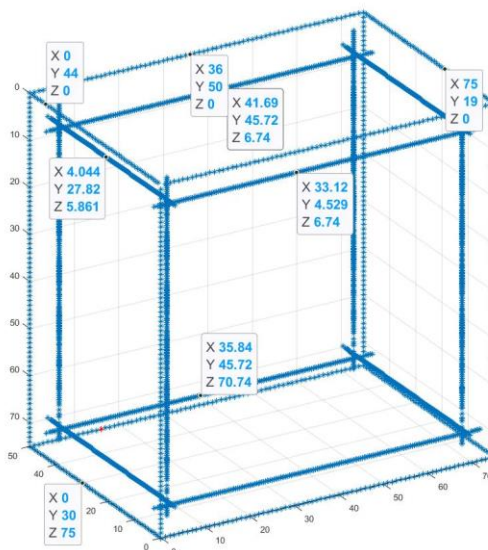


Figure 5-55: Resultant CPD

Using the dimension convention shown in Figure 5-56, the recovered results are shown in Table 5-8.

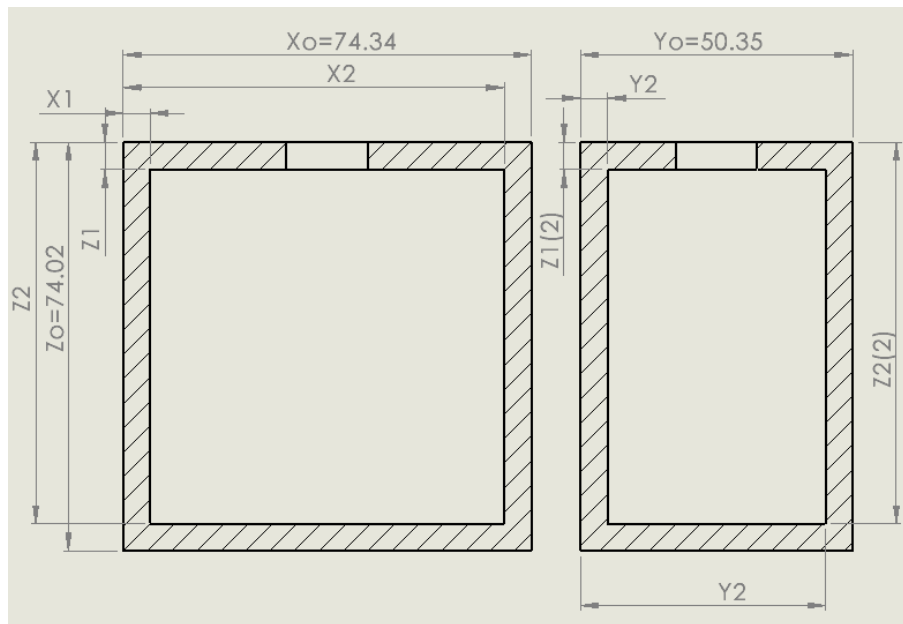


Figure 5-56: Dimension sign convention

Table 5-8: Cuboid artifact geometric results

Dimension (mm)	Actuals (mm)	Recovered (mm)	Error (mm)
X1	4.89	4.1	0.79
X2	69.45	70.5	-1.05
Y1	4.67	4.17	0.5
Y2	45.16	45.51	-0.35
Z1	5.26	6.22	-0.96
Z1(2)	5.26	5.8	-0.54
Z2	69.37	70.4	-1.3
Z2(2)	69.37	70.16	-0.79

As seen from Table 5-8 the geometric results from the cuboidal scan show max error of -1.3mm for Z2, and a min error -0.35mm for Y2. These results give a conditional average error of 0.79mm.

5.6. Third Artefact – L-shape

To further validate this extraction process, a third, more complex artefact has been created. Shown in Figure 5-57, this artefact has an L-shaped internal cavity. To reconstruct the internal geometry of this artefact a minimum of three planer views will be required.

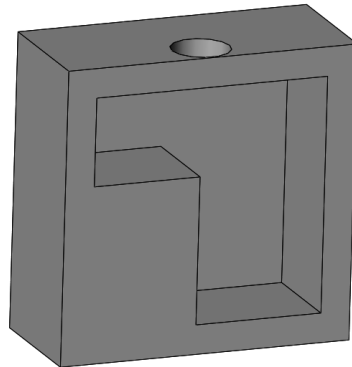


Figure 5-57: Third artefact - Cuboid with L-shaped hollow

The same heating process was then performed. The internal cavity of the artefact was heated to 100°C whilst being monitored by the IR camera to capture the heat transfer. The cameras frame rate was set to 5Hz. Figure 5-58 shows the four resultant thermograms representing the four vertical sides of the artefact.

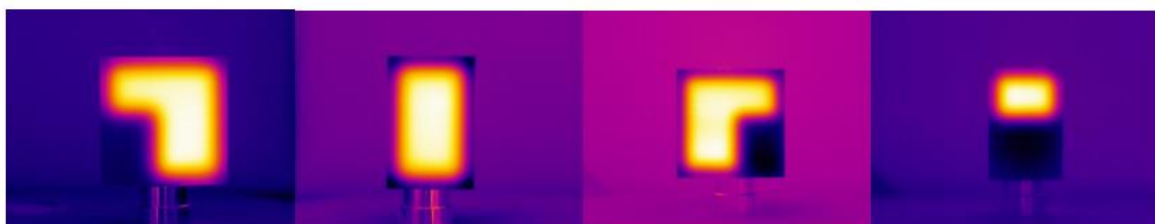


Figure 5-58: Four-perpendicular thermogram representing the four vertical sides

Each thermogram is then run through the extraction algorithm in turn. The following figures show the extracted edges for each of the above thermograms.

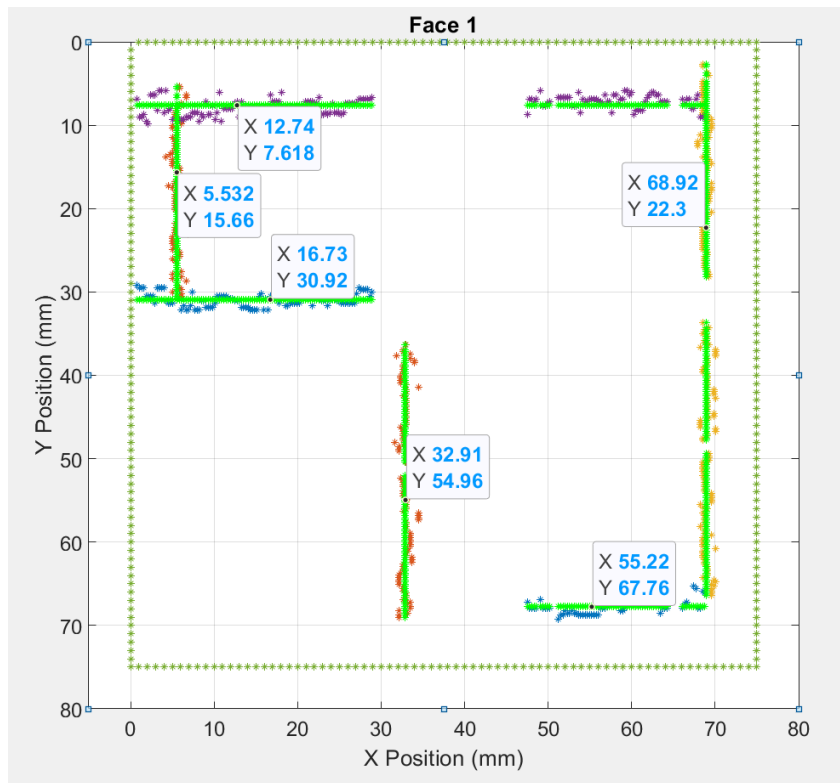


Figure 5-59: Face 1 feature extraction results

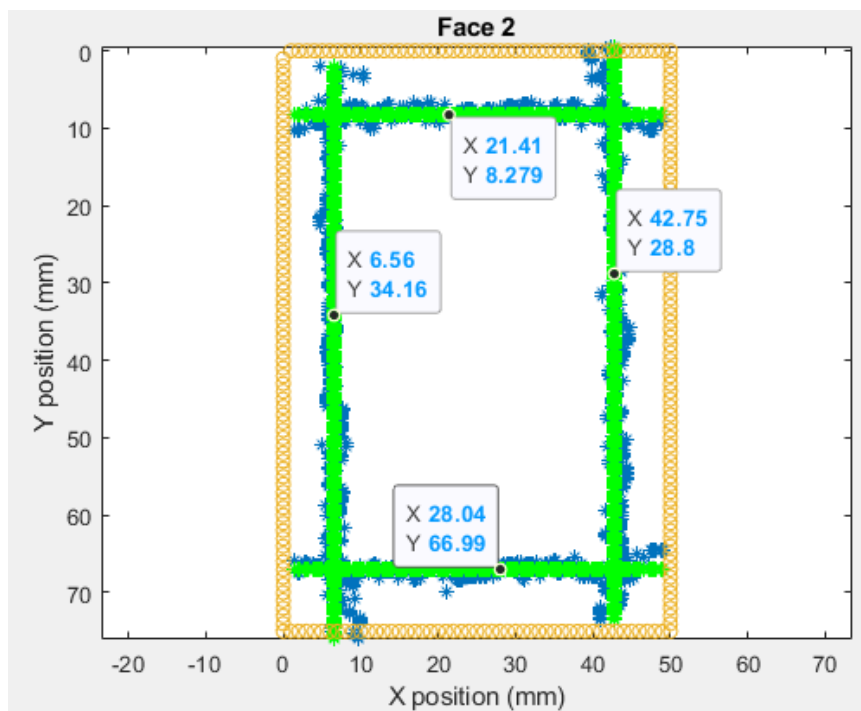


Figure 5-60: Face 2 feature extraction results

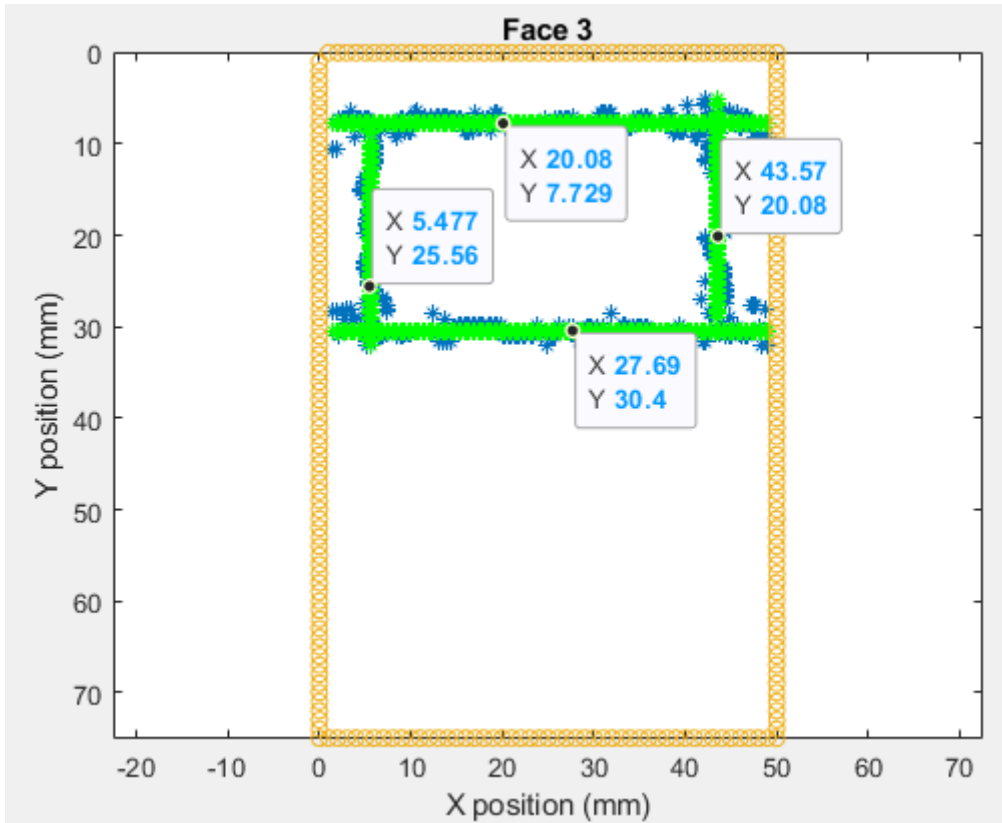


Figure 5-61: Face 3 feature extraction results

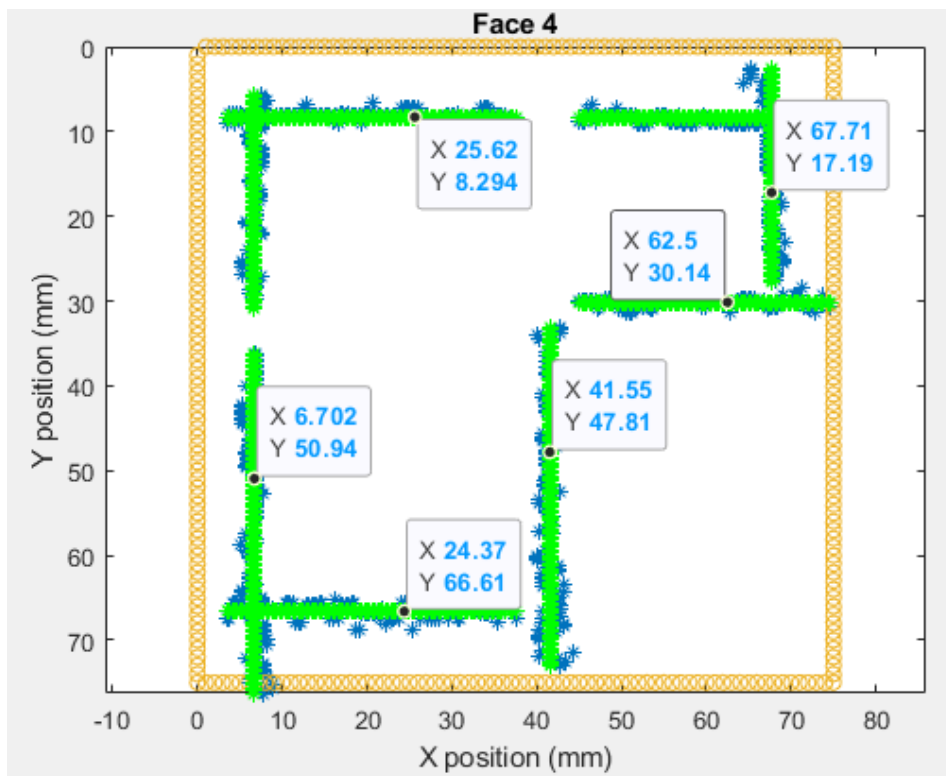


Figure 5-62: Face 4 feature extraction results

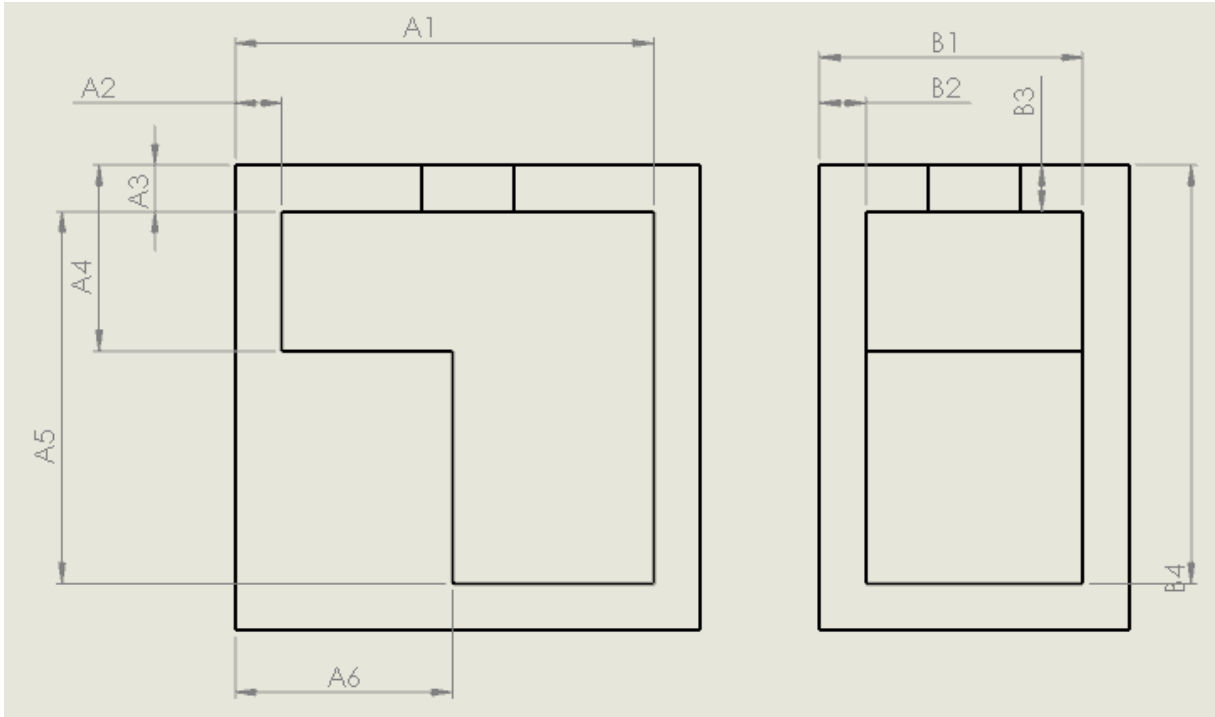


Figure 5-63: L-shape artefact sign convention for faces 1 and 2

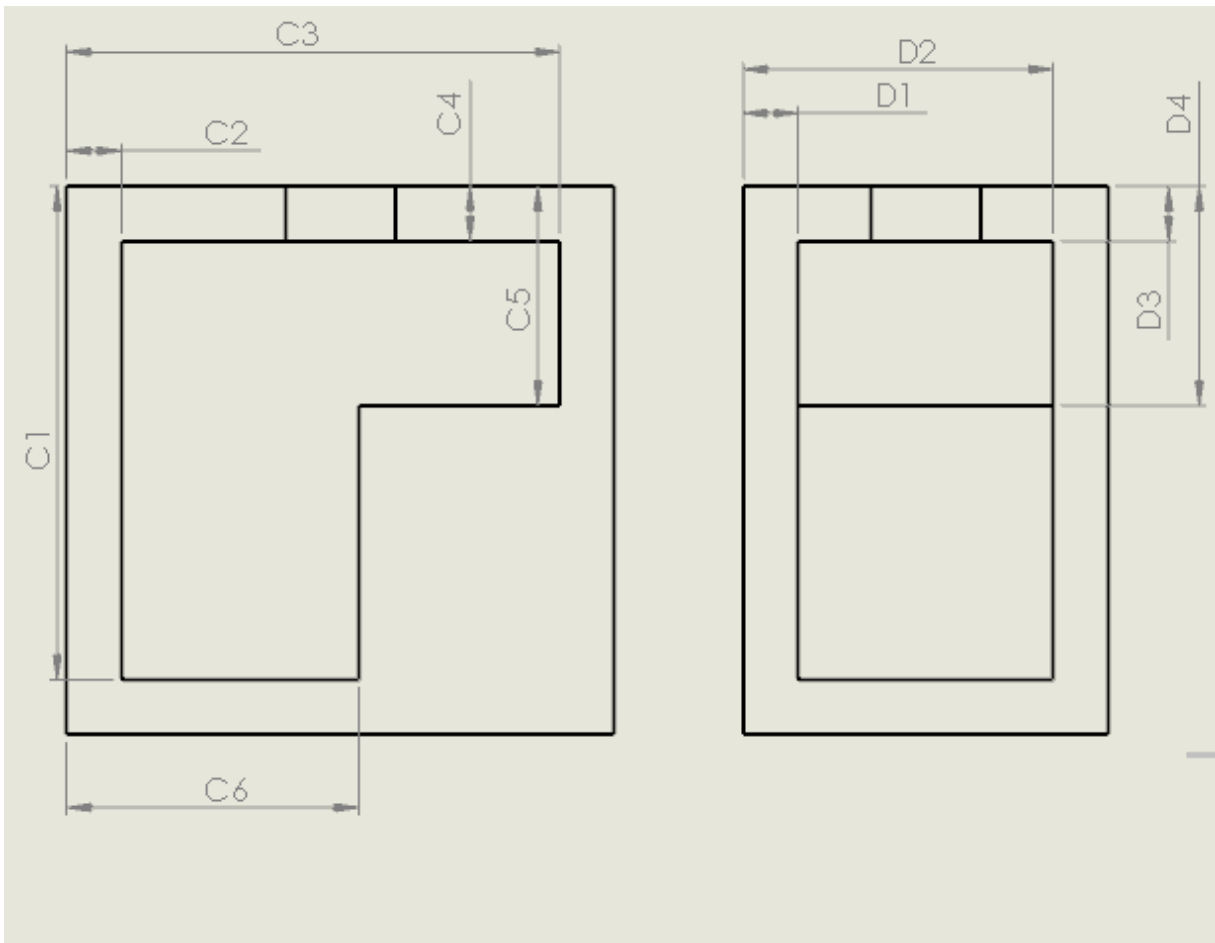


Figure 5-64: L-shape artefact sign convention for faces 3 and 4

With the geometric position of all the edges found for each face of the object, using the sign convention shown in Figure 5-63 and Figure 5-64, the tabulated results are shown below in Table 5-9. The dimensions A-D relate the dimensions as shown in Figure 5-63 and Figure 5-64, with the same dimensions in () relating to the calibration results in *Appendix E*.

Table 5-9: Geometric results for L shaped artifact

Dimension	Actuals (mm)	Recovered (mm)	Error (mm)
A1(X3)	67.19	68.9	-1.71
A2(X1)	7.36	5.53	1.83
A3(Z1)	7.54	7.62	-0.08
A4(Z2)	29.84	30.92	-1.08
A5(Z3)	67.47	67.76	-0.29
A6(X2)	34.6	32.91	1.69
B1(Y2)	42.3	42.75	-0.45
B2(Y1)	7.38	6.56	0.82
B3(Z1)	7.54	8.23	-0.69
B4(Z3)	67.47	66.99	0.48
C1(Z3)	67.47	66.61	0.86
C2(Xo-X3)	7.54	6.7	0.84
C3(Xo-X1)	67.37	67.7	-0.33
C4(Z1)	7.54	8.23	-0.69
C5(Z2)	29.84	30.14	-0.3
C6(Xo-X2)	40.13	41.55	-1.42
D1(Yo-Y2)	7.12	5.47	1.65
D2(Yo-Y1)	42.04	43.57	-1.53
D3(Z1)	7.54	7.73	-0.19
D4(Z2)	29.84	30.4	-0.56

From the results shown in Table 5-9 the conditional average error for all recovered dimensions is 0.875mm, with a max error of 1.83mm associated with A2.

Following the successful identification of the internal edge location for all four faces, the four sets of data are inputted into the assembly code for reconstruction. The assembly code then combines the internal face CPDs' and the CPD for the external surround into single comprehensive CPD set. This is shown in Figure 5-65. The complete CPD can now be exported.

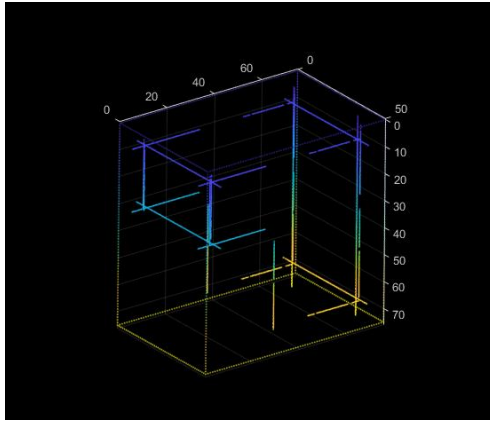


Figure 5-65: L-Shaped artefact final CPD

5.7. Accuracy, and repeatability

The previous sections have shown the capture and processing techniques necessary to extract geometrical dimensions from thermograms and combine them into a useable data format from several artifacts of differing shape and material. However, the overall accuracy and repeatability of the system still requires validation.

To achieve this, the artifact used in section 5.3.4 and 5.4.5. was rescanned five additional times, to determine the systems repeatability and accuracy when compared to the reference values gathered in section 5.2. The individual thermograms can be found in *Appendix J*. Using the same sign convention as Table 5-2, the results shown in Table 5-10 were obtained:

Table 5-10: Accuracy and repeatability results from square artifact

	Z1(mm)	Z2(mm)	X1(mm)	X2(mm)
Run 1	10.04	69.39	6.25	42.70
Run 2	7.94	69.65	6.22	43.19
Run 3	8.81	70.10	6.48	42.80
Run 4	11.62	69.50	6.06	43.11
Run 5	8.64	68.81	5.09	41.95
av	9.41	69.49	6.02	42.75
stdev	1.18	0.38	0.44	0.40
av stdev	0.60			
nominals	10.62	69.76	7.62	42.25
err from nom	1.21	0.27	1.6	0.5
av err	0.89			
MAX err	1.6			

MIN err	0.27			
range	1.33			

As can be seen from Table 5-10, the results from the five heating cycles have resulted in average standard deviation of 0.6mm, an average error of 0.89mm, with a max error of 1.6mm. This accuracy and repeatability study was then repeated on the L-shaped artifact to determine a comparison. This artifact has more internal dimensions and as seen in section 5.6 gave the biggest error when compared to the actual.

The same heating cycle was applied to this artifact 5 times, with the results being shown below in Table 5-11 and the sign conversion for those dimensions shown below in Figure 5-66. Individual thermograms for this test can be found in *Appendix K*.

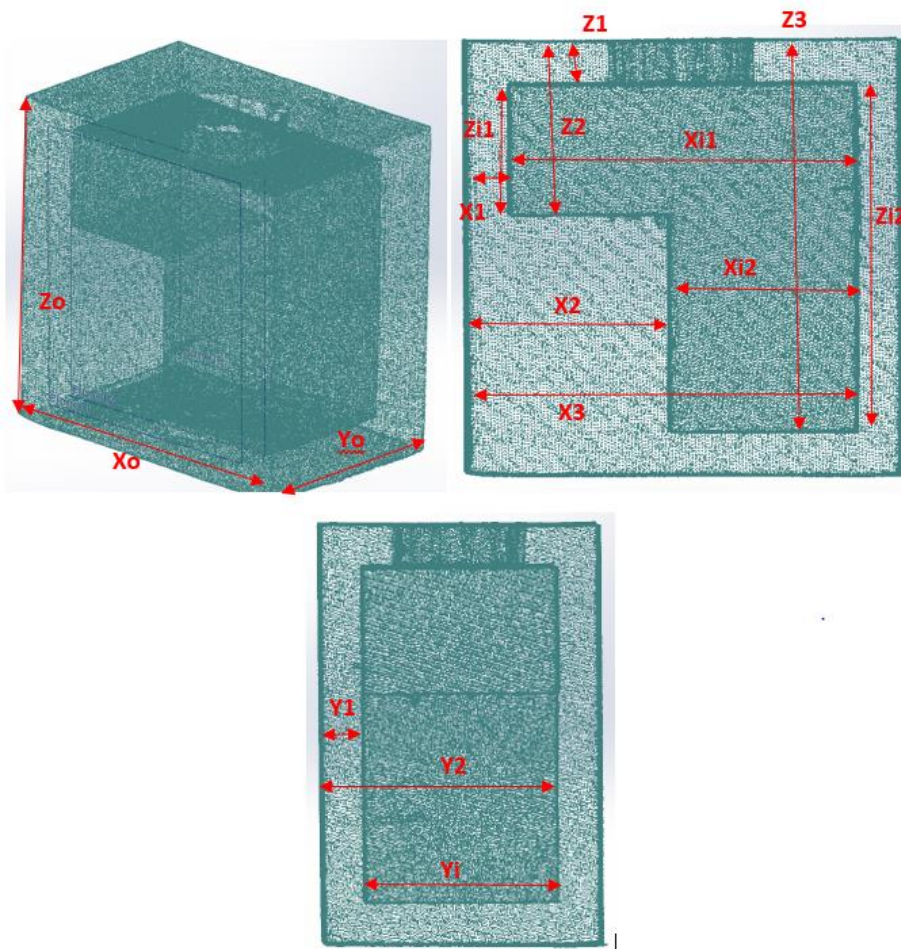


Figure 5-66: CT scan of L shaped artifact with sign convention

Table 5-11: Accuracy and repeatability results from the L shaped artifact

	Z1(mm)	Z2(mm)	Z3(mm)	X1(mm)	X2(mm)	X3(mm)
Run 1	7.02	31.46	68.64	6.37	32.99	68.93
Run 2	6.8	29.51	66.13	6.52	32.12	66.64
Run 3	6.96	31	67.53	6.26	32.62	67.37
Run 4	7.01	31.5	68.67	6.31	33.78	69.12
Run 5	7.05	29.61	69.23	6.58	33.29	69.14
Av	6.98	30.62	68.04	6.41	32.96	68.24
Stdev	0.09	0.88	1.11	0.12	0.56	1.036
av stdev	0.63					
nominals	7.54	29.84	67.47	7.36	34.6	67.19
err form nom	0.57	0.78	0.57	0.95	1.64	1.05
av err	0.93					
MAX err	1.64					
MIN err	0.57					
Range	1.07					

The results from Table 5-11 show similar results to those taken from Table 5-10. The average standard deviation across the five runs was 0.63mm, with the average error 0.93mm, and a max error of 1.64mm.

5.7.1. Accuracy and repeatability using a lower resolution camera

Until now all the practical experimentation has been performed by a high end FLIR A622SC, which has a high thermal sensitivity and resolution (see Table 5-3). To determine the accuracy and repeatability of the of the system when using lower spec equipment, the repeatability study with the square artifacts was repeated, but this time using a FLIR A35. The A35 is a small process control camera, designed mainly for quality assurance and condition monitoring. At a quarter of the retail price of the A622SC, the A35's specifications are understandable lower than that of the A622SC. The specifications for the A35 [72] are shown below in Table 5-12, along with the specifications for the A622SC for comparison.

Table 5-12: A35 Specifications (Specifications for A255SC for comparison)

Property	A35	A655SC
Thermal Sensitivity	0.05°C @30°C	0.03°C @30°C
Detector Type	Uncooled VOX microbolometer	Uncooled Microbolometer
Dynamic Range	8 bit	16 bit
Spectral Range	7.5–13 μm	7.5 – 14.0μm
Standard temperature range	-25°C to 135°C	-40°C to 150°C
Accuracy	5% of reading	2% of reading
f-number	f/1.2	f/1.0
Detector pitch	25 μm	17 μm
Field of view (FOV)	13° × 10.8°	25° x 19° (31° diagonal)
Frame rate	60Hz	50Hz
Resolution	320 × 256 pixels	640x480 pixels
Minimum Focus Distance	NA	0.25 m
Focal length	35 mm	24.6mm
Spatial Resolution (IFOV)	0.714 mrad	0.69 mrad

Using this camera one aspect that was immediate event was that due to a smaller FOV the coma effect was much more prominent. As can be seen in Figure 5-67, placing the artifact at the extremes of the A35’s FOV, results in severe distortions in the form of pronounced curvature in the resultant thermogram. At his stage placing the artifact centrally as possible in the frame becomes even more important. However, the coma effect is still prominent even then. To reduce this effect the subject can be moved further back, however this reduces the amount of the frame the artifact fills, in turn reducing the resolution.

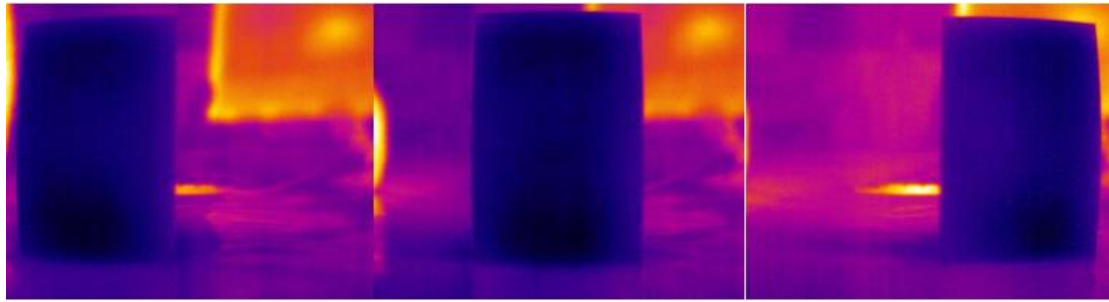


Figure 5-67: 3 images showing the effect of the coma as the subject is moved around the A35's FOV

With the subject placed in the best position with regards to the trade-off between the coma effect and resolution, the heating cycle was performed five times. The resolved values were compared to the nominal values gathered in section 5.2. The individual thermograms can be found in *Appendix L*. Using the same sign convention as Table 5-2, the results obtained are shown below in Table 5-13.

Table 5-13: Accuracy and repeatability results from using the A35

	Z1(mm)	Z2(mm)	X1(mm)	X2(mm)
Run 1	8.03	68.14	6.43	43.17
Run 2	8.21	68.62	5.78	42.03
Run 3	9	69.74	6.16	42.98
Run 4	8.43	68.23	6.62	42.59
Run 5	8.6	69.77	4.61	42.33
av	8.45	68.9	5.92	42.62
stdev	0.33	0.71	0.71	0.41
av stdev	0.54			
nominals	10.62	69.76	7.62	42.25
err form nom	2.17	0.86	1.7	0.37
av err	1.27			
MAX err	2.16			
MIN err	0.37			
range	1.79			

As expected, the average error and max error are higher using this camera than was found using the higher spec'd A655SC, being 1.27mm and 2.16mm respectively. However, the repeatability

when using this camera is comparable to the repeatability when using the A655SC with only 0.05mm between the two values.

As said, it was expected that the error when using this camera would be higher, given its lower specifications. The main contributor to these higher error values, it is hypothesized, is the lower camera resolution. The lower resolution, and the test setup used, means a single pixel can have a 0.41mm (average conversion factor) effect on the resultant geometric values. This is double the amount a single pixel effects the result when using the A644SC, as the average conversion factor used there is 0.22mm. How these additional pixels can be accumulated during the feature extraction process, thus leading to errors, is explained in the next section.

5.8. Potential Error Sources

From the previous section, using either camera resulted in large error when compared to the actual values taken during part calibration. To better understand this deviation and show the mitigations used to reduce them, this section lists the identified potential error source inherent in system.

- Setup – Alignment/parallax error

How the camera views the artefact is critical. If the object and the lens of the camera are not parallel with one another, the thermogram could be recorded at an angle, distorting the recorded thermogram. In these experimental setups, to ensure that the camera and the artifact are parallel with one another, a mirror was placed in front of the artifact (parallel with the viewed plane), and a light source mounted on the camera. By manually rotating the artifact the light was reflected away from camera, but when the artifact was true to the camera, the light reflected from the camera would flair out the resultant thermogram. With this setup this was the best method to ensure parallelism between the camera and the artifact.

In future this issue could be resolved by rotating the artefact when the thermographic capture is being performed as part of pre setup operation. Thermograms at set rotation intervals could be entered into the FEX and the separation distance between edges that are extracted could be plotted. It would be expected that this would result in a nominal distribution of separation distances as the object is rotated, with the peak of the distribution being when the artefact and the camera are truly parallel.

- Setup – Camera resolution

In all the test performed so far, the IR cameras frame is filled with the artifact, as much as the minimum focal distance allows. This ensured the greatest Pi/mm resolution, whilst maintaining focus. Ensuring the largest Pi/mm possible means that any pixel variation during selection (disused below) will have less effect on accuracy than having a low Pi/mm, as was seen using the lower resolution camera, the A35. However, placing the object at further distances from the minimal focal plane will reduce the Pi/mm which will affect the accuracy of the final result. Placing the object further away will also add in the possibility of additional environmental effects influences the captured thermogram.

- Setup – Camera Focus

During the initial setup focusing the camera correctly on the subject is also critical. Thermograms are inherently noisy and having the subject incorrectly focused will only serve to increase that noise.

At the onset of the each test the artifacts are normally at the ambient room temperature leading to difficulties with the camera focus as the camera cannot distinguish between the subject and the background, other than based on emissivity. To solve this issue a highly emissive object (such as a mirror) is placed next to the subject, allowing for a greater contrast between the

subject and the background. This then allows the camera to focus correctly on the approximate front face of the object. The highly emissive object is then removed before the test starts.

- Setup – Coma Effect

Comatic aberration is an inherent factor when using cameras with parabolic lenses. Rays hitting the lens at any angle that is not perfectly parallel to the optical axis will show an aberration to some degree in the resultant image.

At this stage it is not known what influence the coma effect will have of the geometric results. From observation there is no obvious influence from coma effect showing on the captured thermogram when using A655SC, but when using the A35, the coma effect added huge curve effects to the resultant thermograms if the subject was not centred correctly. However, its effect will in the future need investigation, but it could be difficult to quantify exactly as the effect would change from lens to lens depending on the curve of the parabola.

In these tests one mitigation that taken to reduce the coma effect was to have the subject place in the centre of the Field of view

- Setup – fill level/water temperature.

It is postulated that variations of the amount (fill level) and temperature of the heating medium could lead to variations in repeatability. The heating medium is added by eye so there is no guarantee that the exact same amount is added each heating cycle. Additionally, whilst the heating medium is heated to the same temperature each cycle, the time taken from heating to filling also varies, meaning the heating medium may have cooled by different amounts, from one heating cycle to another.

- Processing – boundary selection

As seen at the start of the FEX processing operation, the thermogram is subjected to an edge detection, highlighting the boundary of the subject within the thermogram. From here manual intervention is used to select that boundary. This manual selection of the thermograms boundary has the potential to add one or two additional pixels to the conversion calculation. This in turn will affect not only the converted geometric distance, but also the zero point from where the pixel count is started. In future this error source could be alleviated by the addition of an automatic boundary recognition program.

- Processing – Noise Levels

As previously stated thermograms are inherently noisy. The noise levels in thermograms can lead to the FEX algorithm to return false positives. Currently to reduce this down sampling is used smooth the captured temperature profile. However, sampling must be controlled as too much sampling can smooth the temperature profile to the point where no differentiation is observed, and too little will, as said above lead to false positives.

- Artifact - Thermal expansion

The act of using this system to measure internal features will itself induce thermal expansion, due to the heating cycle used to excite surface temperature gradients. This inherent fact will cause the expansion of all artifact dimensions, and it is the actual expanded dimension that will be captured. This expansion error will also change from part to part, based on part size and part material. However, calculating thermal expansion is a straightforward process, providing several factors about the part, such as thermal expansion coefficient, change in temperature and initial of final dimensional conditions, are known. In future iterations of the system additional corrective algorithm could be added to consider thermal expansion and correct the final outputted value.

5.9. Chapter Summary

In this chapter, the preliminary steps of a novel imaging process for internal measurement are presented. Four separate artefacts with differing internal profiles and materials were processed by this new system resulting in the successful extraction of all internal edges. This chapter also shows the techniques necessary to take that resultant CPD and combine it with other externally captured CPD data in a usable data or CAD format.

One issue that has been highlighted in this chapter is the heating and features extraction from parts with high thermal conductivity. As was expected through the simulation work in chapter 4, and was observed in section 5.4, core heating with such parts resolved poor responses for the internal dimensions. Whilst the core heating test in section 5.4, did provide small number of samples from which geometric distances could be resolved, the data recovered was inundated with false positives and provided information in one direction only. It was hoped based on the computational results for external heating, that such a heating method would resolve much more stable and consistent results. However, as seen in section 5.4 no peak detection (leading to internal edge extraction), was possible due to the lack of temperature gradient in the observed surface temperature profile. This was disappointing result, as computationally external heating provided much more stable results over time, and practically was a more viable solution with regards to heating methods. As mentioned in section 5.4, it is unknown why there was such large disparity between the simulated results and the actual test results.

From the accuracy and repeatability tests, it was found that from two separate tests, each consisting of five runs, the average error, and max error were consistent at around 0.9mm and 1.6mm respectively, with an average repeatability around 0.6mm. These results are consistent with average error and max errors from the other two shapes tested in this chapter. The cuboid

artifact had an average error of 0.8mm with a max error of 1.43mm, and the L-shaped artifact had an average error 0.88mm, with a max error of 1.83mm. These tests have also shown that, as expected cameras of lower resolution will produce lower accuracies and repeatability's.

These accuracy and repeatability tests have shown that whilst this system in its current state is not particularly accurate, its repeatability is moderately high given the technology readiness level of this system.

This work performed in this chapter has also highlight several error sources associated with this thermographic capture process and some of the mitigations that were used in attempts to minimise these errors. As this is not an exhaustive list, a full error analysis of this system will be required in the future to fully ascertain this error sources and determine an error budget.

This chapter has shown that is approach of PIDV using thermal imagery is potentially viable. However, so far all of the artifacts used thus far have all consisted of planer features normal to the projection plane. Whilst circular and angles artifacts were created, it was hypothesized that this spatial approach, using only a single thermographic frame, would be unsuitable given the transient edge drift noticed in such shapes shown in chapter 4. Therefore, the spatial process describe in this chapter was further developed to compute multiple thermograms simultaneously. This process in described next in chapter 6.

Chapter 6. Temporal Thermal Imagery (TTI)

TTI is a combination of algorithms that allows for the extractions of internal edge positions over time, using the same techniques as shown in the previous chapter, but in a manner like the simulations in Chapter 4.

Three sets of thermographic data are run through TTI: one planar, one curved and one angled planar. This process validated the conclusions from the simulations performed in section 4.3 and the novel method in general, allowing for the extraction of curved surfaces over time. The results for both planar surfaces and curved surfaces are also detailed here.

6.1. Introduction to TTI

The new thermal image processing capture technique in discussed Chapter 5 shows a system that can retrieve geometrical data from the internal features of an object. However, that technique is only likely to produce accurate results when the objects under investigation have internal structures comprising of planar features and consist of a low thermal conductivity material. The heat transfer between two perpendicular faces, when using such material will typically produce a uniform surface temperature distribution on the viewed face. However, internal features that are not planar and parallel meaning the separation distance between the two internal and external faces is constantly changing over the length of the feature, will lead to a temperature gradient that is proportional to the change in face separation distance (not considering the effects of thermal conductive). This was observed in the simulation work but needs validating experimentally.

TTI is a revision to the original extraction algorithm that can track the movement of these boundary regions over time and deduce their geometrical position. The simulation work showed that for materials with low thermal conductivity that preserve a measurable

temperature gradient the change in position of the boundary regions indicates the shape of the internal cavity. If they do not alter their geometric positions, then it can be assumed that the internal geometry is of planar design. However, if over time the boundary regions do shift, then depending on the rate of change of that shift, curvature or angularity can be determined.

6.2. TTI Software

TTI works on the same Feature Extraction algorithm (FEX). A single JPEG file and temperature data file are exported from the FLIR software and then entered into the FEX. However, with TTI, every frame captured by the camera is loaded into the algorithm. For example, the artefact used in Chapter 5 was monitored for four minutes, with the cameras capture frequency around 6Hz (the actual frame rate can vary around the set point). This resulted in 1500 individual thermograms. The first 340 frames are discarded as they show the addition of the heating medium to the artefact. The remaining 1160 frames are then exported from the FLIR software as both JPEGs' and temperature data sets.

Figure 6-1 shows the front panel of the new TTI algorithm. There is a loading feature that loads in all the temperature data files/JPEG's automatically (1). (2) is the viewing area, and images can be cycles though using the slider (3). The sliders at (4), when adjusted, automatically convert the viewed image into grayscale and then perform edge detection to highlight the boundary of the artifact in black and white. From here the area denoted at (5) allows the boundary of the area of interest to be selected and then thermal edge detection process. The selection points are shown in Figure 6-1 as two green points with the boundary being highlighted as a dashed green line around the artifact's thermogram. Once the area of interest has been selected, the initial cross section can be selected (6), (from Chapter 5, this locates the highest peaks in the differentiated temperature data), this initial cross section is shown as a yellow dashed line in Figure 6-1. Once the initial cross section is established the vertical and

external edges can be extracted. This is the process from Chapter 5 performed automatically with the controls shown at (7). Different line filters can be applied here to ensure best results, which can then be shown in the viewing area (2). Currently Figure 6-1 shows the thermogram with the extracted vertical edges. Once the user has the results for this initial image using the correct settings, “apply to all” can be selected (8). Now the process will be repeated automatically for every loaded frame. The result is the vertical and horizontal positional data for the internal edges for every frame over time. An indication of the final result is then shown in (9). This process is summarised in Figure 6-2.

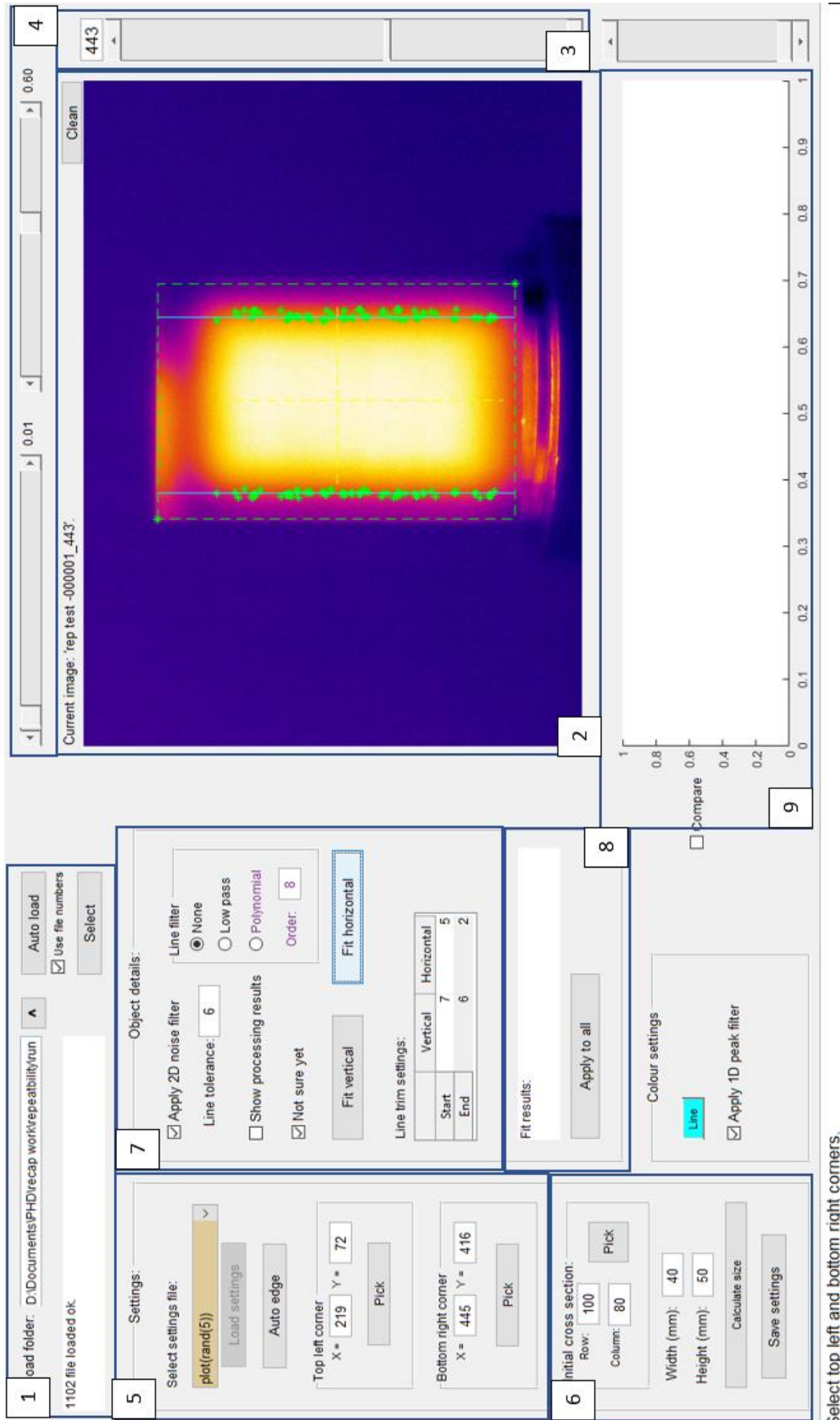


Figure 6-1: TTI front panel

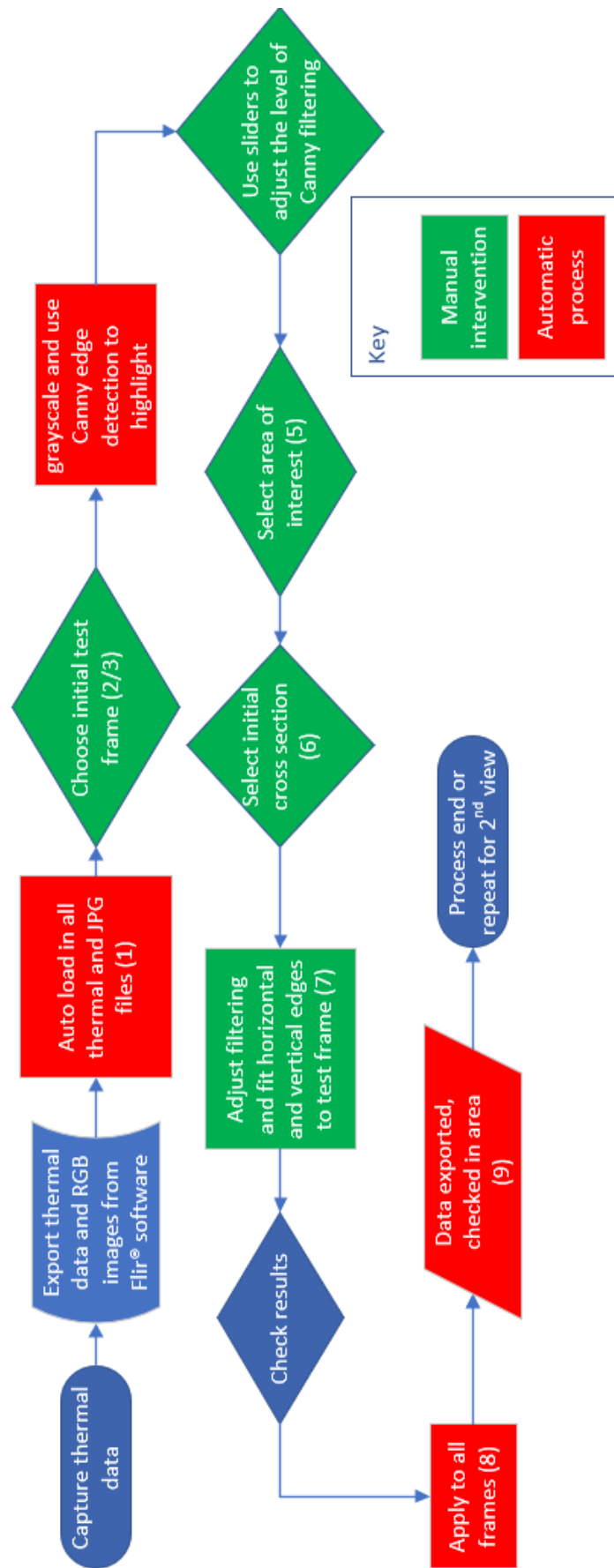


Figure 6-2: TTI operational flow chart

As can be seen in Figure 6-2 the main computational steps in this process are now automated (highlighted in red), but several steps still require user intervention (highlighted in green). Computation time can vary, dependent on the number of frames loaded into the program, but for the examples given below the TTI program can resolve on average 1000 frames every 300s. This process is for a single projection only. For a second projection, a second set of data (from either repeating and capturing the heating cycle, or from a 2nd camera capturing that second projection), will need to be inputted into the TTI program.

6.2.1. TTI Planar cavity example

The temperature and image data from the first artefact that was used in Chapter 5 was entered into TTI. Figure 6-3 shows TTI after all 1160 data files/JPEGs' have been loaded, the area of interest has been cropped (green dash), the initial cross section has been selected (yellow dash), and the sample feature extraction in the vertical direction has been performed (green points). The 1160 files represent all the files from a single orientation heating cycle. For the 2nd orientation a second heating cycle would be required.

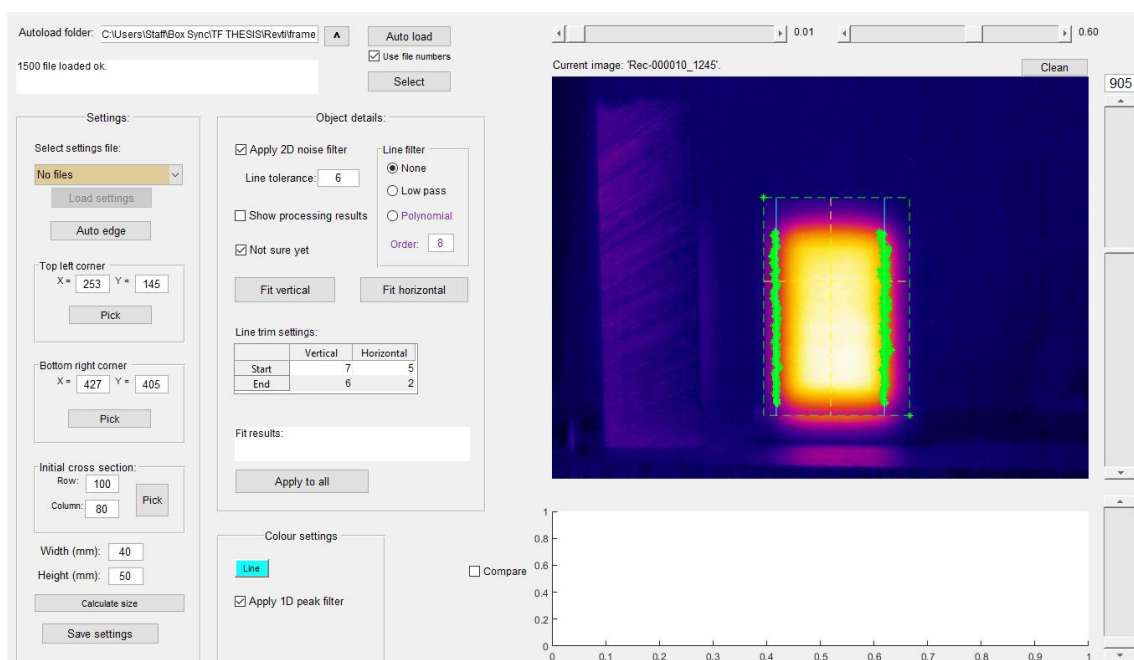


Figure 6-3: TTI after image/data loading and image preparation

After clicking “Apply to all”, the algorithm analyses all 1160 data sets with the same parameters as the used in the image shown.

Once TTI has finished analysing all the files in the sequence, it will return two data sets containing an average positional value for the horizontal and vertical edges for every thermographic frame that was loaded. It also returns an indication of the number of frames that were rejected, as no internal edges were detected. In this instance, the number of rejected frames was 377, returning “Not A Number (NaN)” into the data output. When reviewing the data output almost all the NaN values are found at the beginning of the frame sequence. This is because the majority of the thermograms are similar to the image shown in Figure 6-4 and have negligible temperature gradients and relatively high noise levels. This in turn leads to the boundary regions normally located by the maximum and minimum values in the differentiated temperature being undetectable.

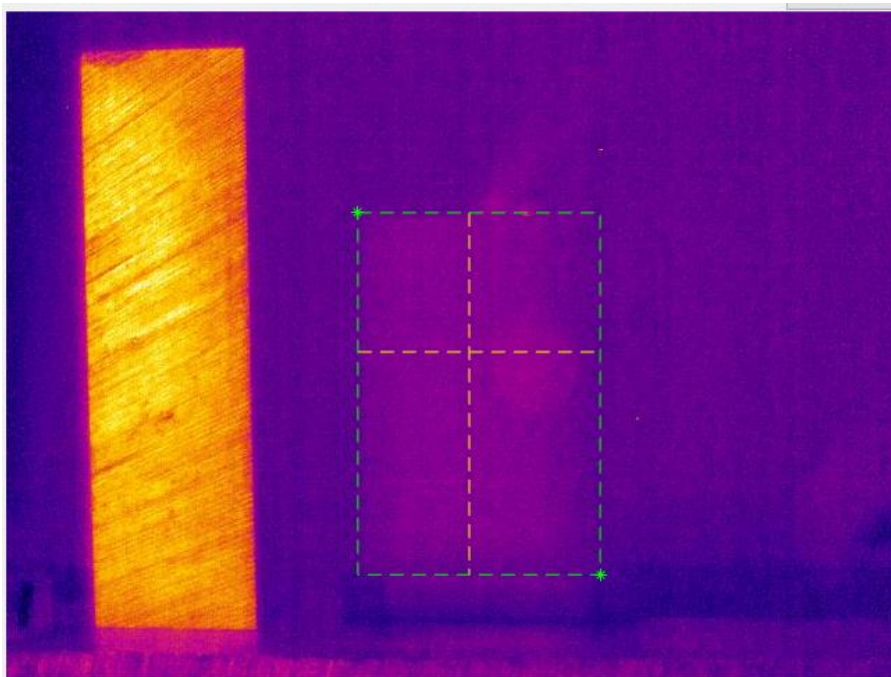


Figure 6-4: Example of an initial frame for the loaded sequence. Images like this will return a NaN value.

For the frames that do return values for the vertical and horizontal edges, the average positional value is calculated for each edge in each frame. These averaged positional values are then presented sequentially over time, as shown in Figure 6-5.

The geometrical position for all four edges (RH, LH, TOP, BOTTOM) does not vary greatly over time. The mean values for each of the edges as well as the maximum and minimum geometrical variation for this thermogram are shown in Table 6-1.

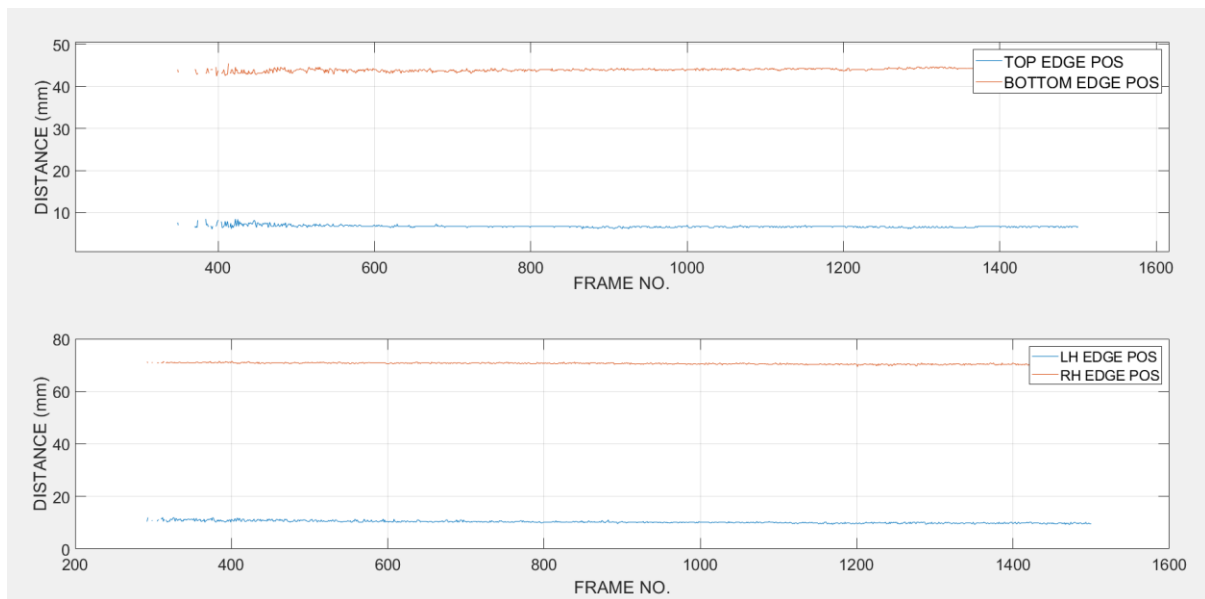


Figure 6-5: Edge position over time

Table 6-1: MAX/MIN/MEAN Results for square artefact

VALUE/EDGE	LH	RH	TOP	BOTTOM
MAX	8.45	46.35	11.95	71.41
MIN	6.03	41.68	9.22	69.37
MEAN	6.69	43.98	10.27	70.59

As expected, the internal edge positions do not vary significantly over time or indicate any gradient. This indicates that the distance between the internal surface and the external surface is uniform and that the feature is a planar primitive, perpendicular to the viewed external face, which is correct.

From the results shown in Table 6-1, the mean values are consistent with the previous experimental work.

Referencing again Table 6-1, large variations between the maximum and minimum values can be observed. In the case of the RH edge, a difference of nearly 5mm has been recorded. Most of the differentiation between values within any of this time series data is found at the start of the thermal data capture (Figure 6-6), when the recorded surface temperature and resulting gradients are low. During the initial heating of the object, the heat conduction from the internal area becomes visible on the thermogram. At this stage, the thermal gradient across the thermogram starts to rise but the signal to noise ratio in the thermogram is large. Whilst edge position can be deduced at this point, until the signal to noise ratio reduces, visualised by a quality colour contrast, the edge position results will vary. When the signal to noise ratio is reduced by the temperature gradient increasing, consistent results are recovered. This is shown in Figure 6-6.

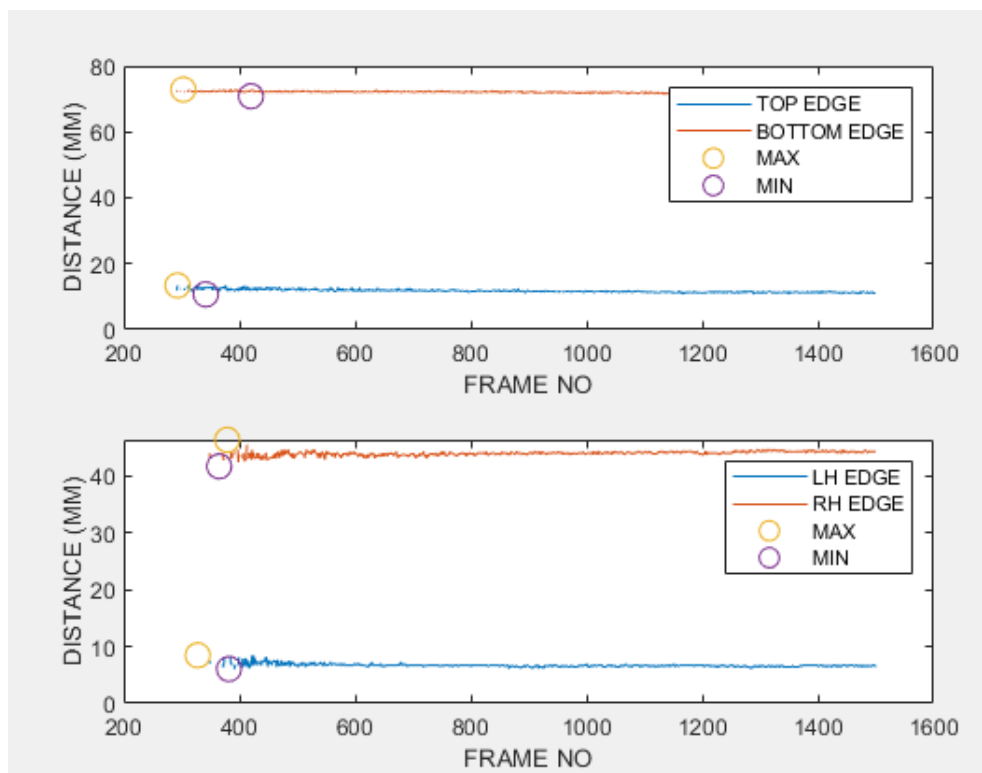


Figure 6-6: Showing the locations of the MAX/MIN location the data set.

In this example, as seen above, results could be gathered from frame 400 onwards. However, for the vertical (LH/RH) edges, stable data was not recovered until around frame 600. This is due to the noise levels in the thermograms combined with the low temperatures in the observed surface gradients. The average temperature of the surface gradient in frame 400, peaked at 24.5°C, this is shown in Figure 6-7 (L).

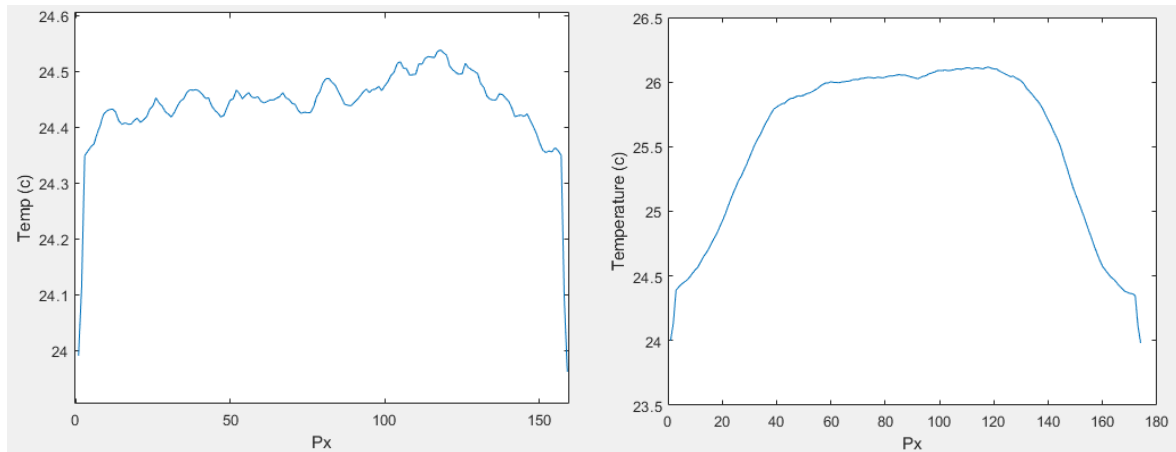


Figure 6-7: L- Average surface temperature for frame 400, R- average surface temperature for frame 600

As can be seen, large levels of noise are present and peak position is difficult to determine. Obviously, certain positions have been deduced as they are present in Figure 6-6, however these are the results that show the most error. At frame 600 in Figure 6-7 (R), when the distance (edge) positions results start to stabilise the average surface temperature has risen, with a maximum of 26°C. This shows that the average maximum temperature of the surface gradient needs to be 26°C or higher, for the signal to noise ratio to be reduced enough that accurate stable edge position results can be extracted.

6.2.2. Circular Internal Face Example

Figure 6-8 shows a cross section of a new artefact that has external dimensions 50x50x75mm and an internal cylindrical volume 35mm in diameter and 65mm in height.

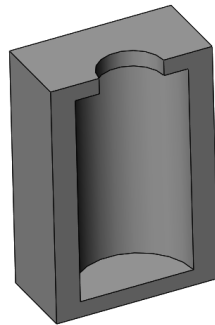


Figure 6-8: Circular Test Artefact

The same testing procedure was undertaken, this time running for approximately eight minutes; with the capture rate set to 6Hz. Figure 6-9 shows a sample of thermograms that were captured during this time.

This thermographic capture results in 3000 frames, each consisting of a temperature data set and a thermogram JPEG.

The first 262 are discarded as they show the heating medium being added. The remaining sets are then imputed into TTI. The outputted positional data for the vertical edges is shown in Figure 6-10 with a geometric conversion factor of 0.294mm/Pixel.

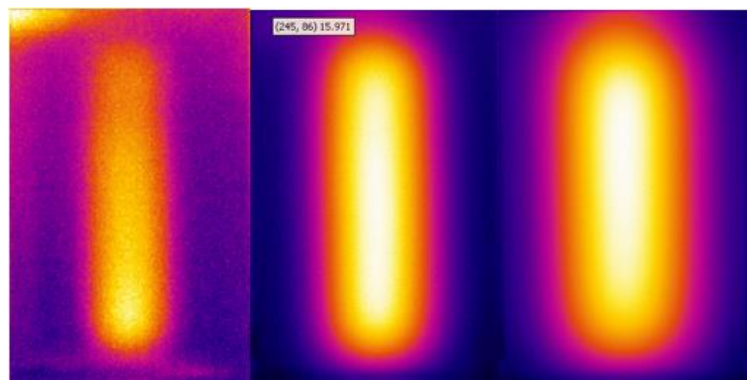


Figure 6-9: Thermogram showing the change in intensity and edge position over time

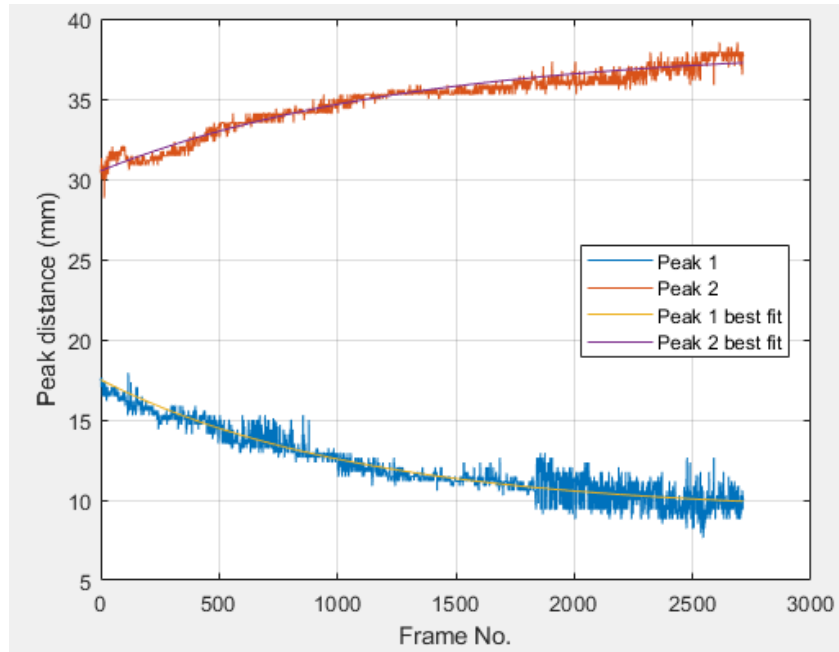


Figure 6-10: Results from TTI edge detection for curved artefact showing best fit curved comparison

Overtime, the boundary, as viewed from the thermal camera, widens indicating that the internal surface is not flat which is correct. In the simulation work, the curvature was exponential therefore the same curve fit was applied and the results of this curve fitting is shown by the yellow and purple lines in Figure 6-10 (individual results are found in *Appendix I.a*)

The fit is very good and validates the simulations in section 4.3, as well as indicating correctly that the internal structure is curved. Extending these curves, using the exponential function shown below (3), will predict the extent of the edge position drift, indication the position of the two apexes of the curved face:

$$f(x) = a * \exp(b * x) + c * \exp(d * x) \quad (3)$$

Figure 6-11 and Figure 6-12 were generated using the above function with the following generated coefficients for a, b, c, and d:

- a=8.283

- $b = -0.0009076$
- $c = 9.218$
- $d = 6.884e-17$

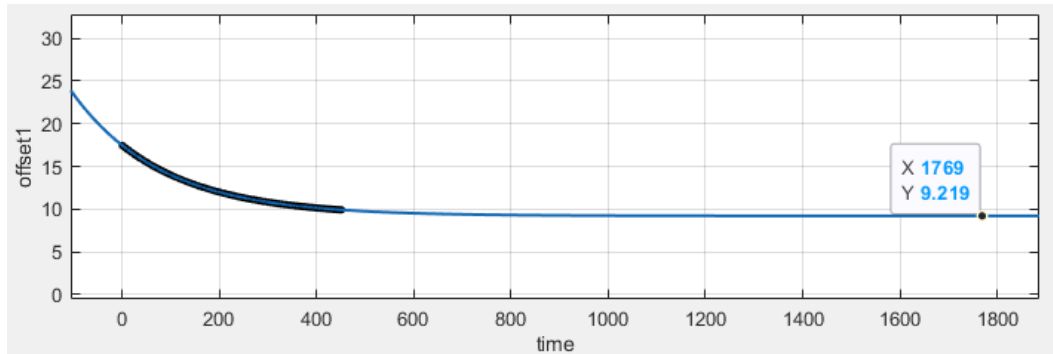


Figure 6-11: Addition of exponential curve to peak 1 (X1) best fit

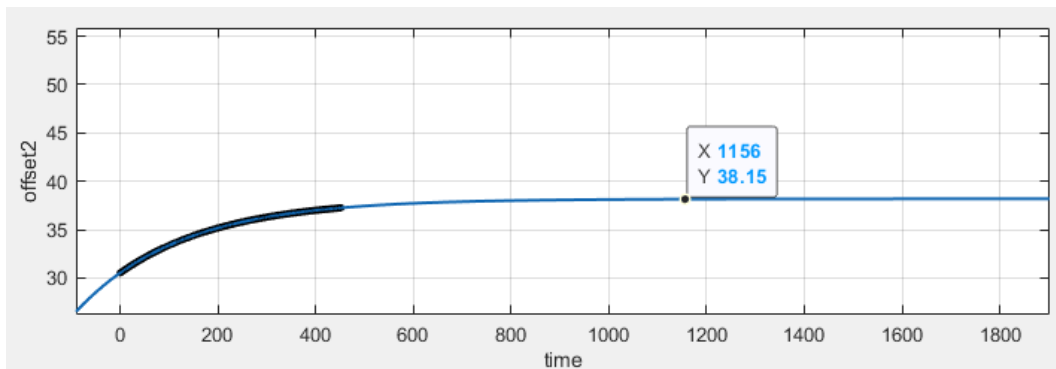


Figure 6-12: Addition of exponential curve to peak 2 (X2) best fit

Extending the best-fit curves, the predicted apex positions of the curved faces can be recovered. As previously stated, this artefact has an internal structure comprising of a cylinder with a diameter of 35mm. From the projection from which the thermograms were taken, this would lead to the apex positions being 7.5mm and 42.5mm from the outside edge. The actual values from the XCT scan gave the actual apex positions 7.59 and 42.43 giving a diameter of 34.94. Figure 6-13 shows this in relation to the part's geometry.

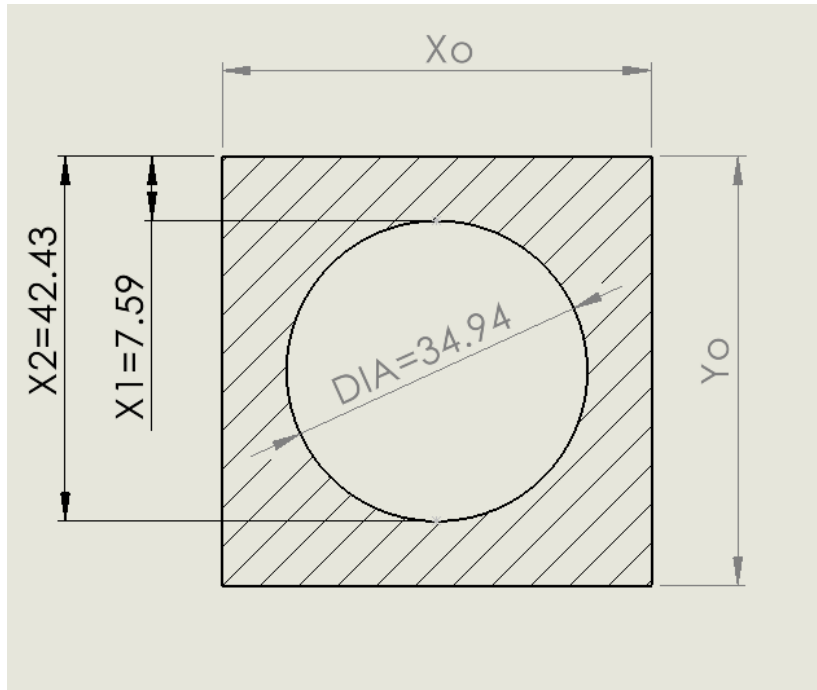


Figure 6-13: Actual dimensions of circular artifact

The geometric results recovered are shown below in Table 6-2, and compared to the actuals from the calibration

Table 6-2: Circular artifact geometric results

	Actual (mm)	Recovered (mm)	Error (mm)
X1	7.59	9.2	-1.61
X2	42.43	38.2	4.23

Using these peak positions improves the accuracy in predicting the size of the cylinder significantly but is still subject to variability caused by the depth and conductivity effects as well as the accuracy of the curve fit. There are small undulations causing deviation from the pure exponential curve, particularly in the red trace in Figure 6-10 which is likely to have caused the lower accuracy in the apex of peak 2.

6.2.3. Angled (diamond) Cavity Example

In this example, an artefact consisting of internal angled planar features is used. The internal structure is shown in Figure 6-14.

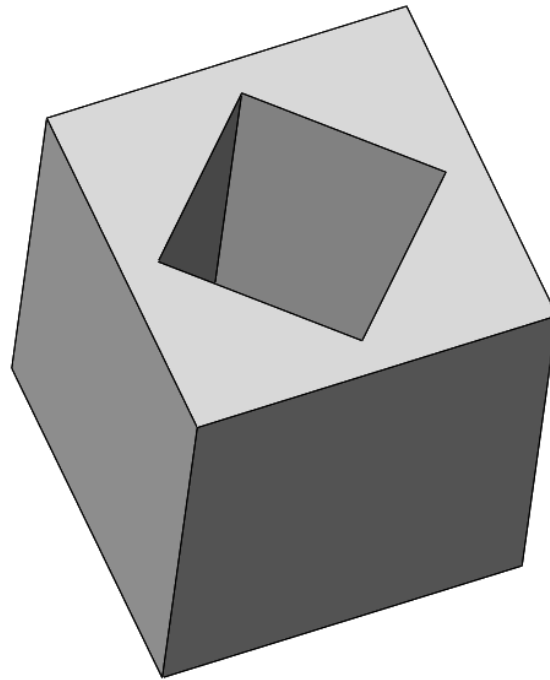


Figure 6-14: Angled planar internal features

The internal structure is 40mm from apex to apex, meaning each apex is 5mm from an outer face. The other dimensions are the same as the previous artefacts.

The same experimental process was repeated for this artefact resulting in 3000 frames being acquired. The resulting peak positions for this artefact over time are shown in Figure 6-15. The pixel conversion factor for this procedure is 0.234mm/Pixel. The X-axis only goes to 1800 frames because the remaining frames returned NaN's.

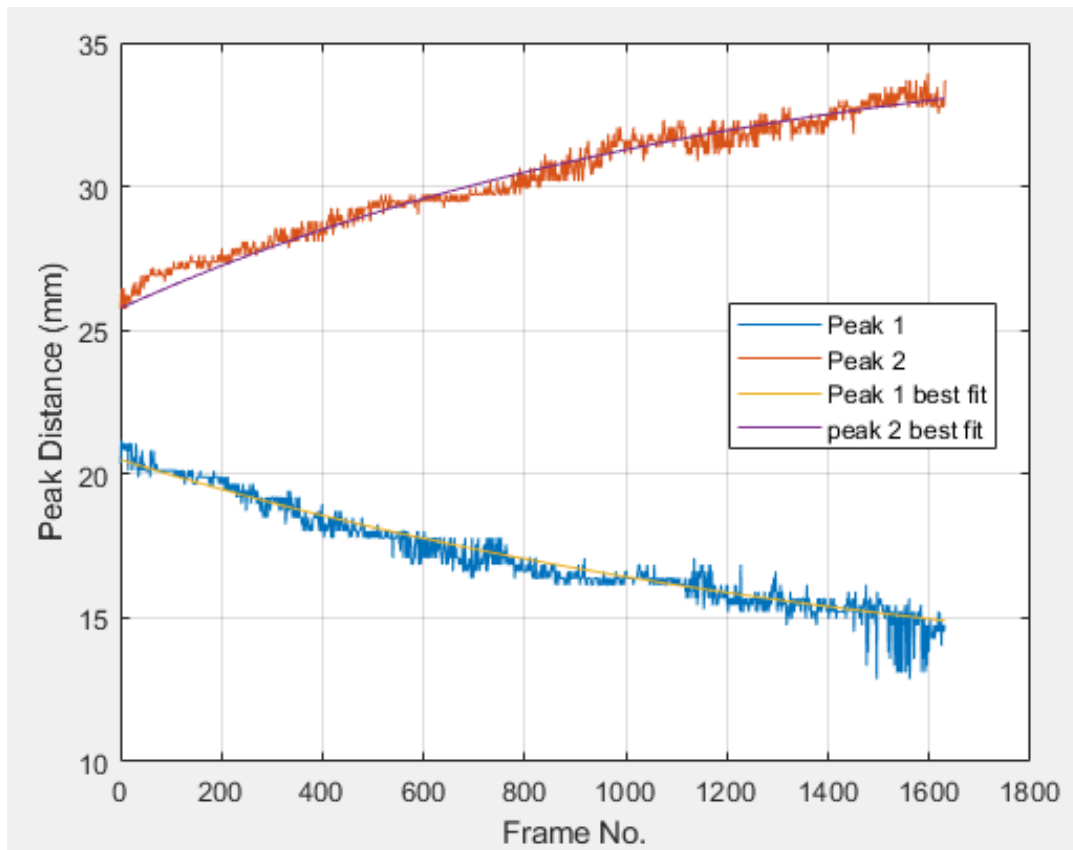


Figure 6-15: Edge position for angled planar object

Again, a best-fit curve is applied to each set of peak position data. This best fit is shown as the yellow and purple lines in Figure 6-15. Individual plots can be found in *Appendix I.b*.

In this case, exponentially extending the best-fit curve does not yield viable results for the final geometric edge position. Once the curve had flattened out, the final edge position was given to be 12mm and 36mm (nominally 5mm and 45mm respectively). The exponential curve fitting can be seen in *Appendix I.b*.

A comparison between the best fit curves from Figure 6-10 and Figure 6-15, are shown in Figure 6-16.

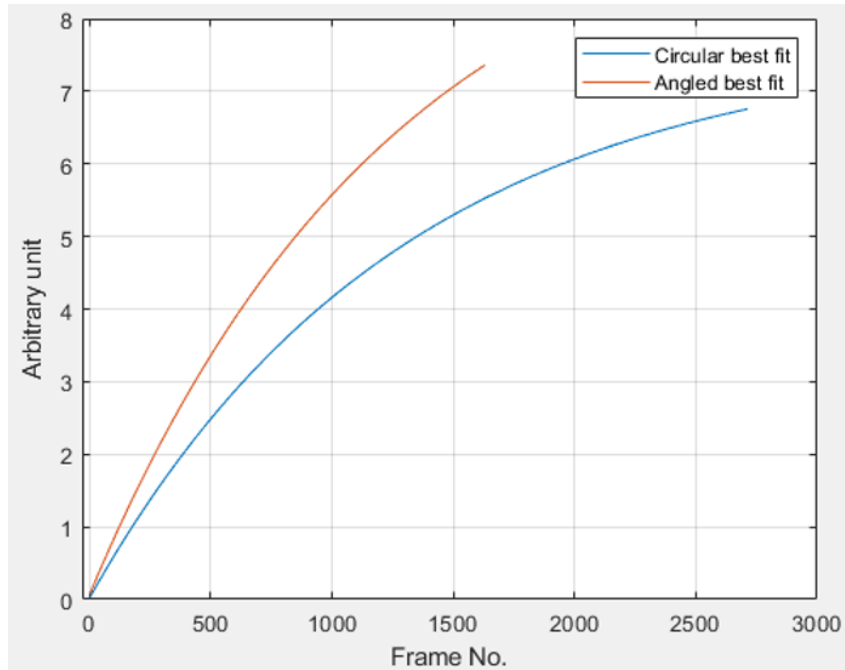


Figure 6-16: Comparison between circular best fit and angled best fit

As can be seen in Figure 6-16 the best fit curve taken from the results for the circular object, has a tighter curvature than the angled object.

These results are consistent with the finding for angled or curved features that were recovered from the computational simulations. This combination of spatial and temporal data shows that this system can differentiate between differing geometrical constructions.

In future work a more analytical characterization would be required for each curve. If values for curvature/gradient were returned for a recovered curve, they could be compared against a set of known limits that would categorise them into a curved, angled or a flat planar feature.

6.3. Chapter Summary

This chapter has introduced the automated edge recovery program TTI. Built upon the techniques used in chapter six, TTI can return an average value for geometrical edge position for every time step within a given capture period.

By using TTI, the simulations in Chapter 4 regarding shape characterisation from thermal information has been validated. It has been shown that for PLA, a material with low thermal conductivity, differing internal primitive features can be varied based upon their thermal response over time.

This system has shown that for plainer features that are parallel with the viewed face, that with this material, edge shift hardly varies over the capture time. This allows the confident estimation of the internal features edge positions for that orthographical view.

For curved and angled faces, it has been shown here and in chapter 4, that edge position shift will occur over the initial period of thermal capture. For this low conductive material, we know from sections 6.2.2 and 6.2.3, that this edge shift must be due to a change in feature depth caused by circularity or angularity.

Creating artefacts that have such features has allowed the validation of the computational simulations performed in Chapter 4. It has also shown that edge position responses from seemingly similar thermal captures, can differ depending on the internal structure. Whilst this process has been highlighted here, as previously stated, further work is required to allow for the automated classification of such shapes based upon results gained from using this time-based system.

Chapter 7. Conclusions and Future Work

This final chapter provides a general summary of the work presented in this thesis, as well as a detailed summary of each objective laid out in chapter 3 and the work performed to ensure these objectives are met.

In addition, the contributions to knowledge this work provides are also listed here as well as areas that require further investigation in the future.

7.1. Summary of Investigation/Research question

This work was envisaged as an alternative method for the PIDV of shapes consisting of internal geometry. As referred to in chapter 2, with the advent of AM becoming more mainstream in industry, one of its main barriers to that industry is a viable method of inspection. Whilst XCT currently provides the necessary tools for the PIDV of internal geometries, and at present is the most viable option, for reasons also mentioned in chapter 2, its use can also be prohibitive and considered non-viable. The aim of this investigation was to determine whether a low cost thermographical vision system could extract and deduce internal geometric dimensions, and thus in the future be considered a viable alternative method for internal geometric PIDV.

As this concept of thermographical PIDV is completely novel, the broader research questions laid out in section 3.3, with the above aim in mind, attempted to discern whether this approach would indeed be viable in anyway:

RQ1. Can internal dimensional data be extracted from a thermographic image of an object's surface if the object is subjected to a series of controlled temperature perturbations?

RQ2. If the answer to the above RQ is yes, can the system differentiate changes in geometrical and mechanical states from the captured results?

RQ3. To what extent does analysis of the transient behaviour provide additional useful information for the measurement task?

RQ4. To what level of accuracy can measurement results be obtained from such a system.

In answering the above questions, it can be stated that, yes internal dimensions can be extracted from thermographic images. Whilst this was built upon the work of *Barker et al* [55], who detailed the techniques for dimensional extraction of external features from thermographic images, this work expands upon that to extract dimensional information from the internal regions. From this ability to be able to extract internal geometric dimensions, repeating the process for the extraction of multiple features of differing factors such as shapes, size, depth, and materials etc was proven possible both analytically and practically. This result has then been further built upon allowing for the temporally extracted results to show differences between shapes of differing geometry. It was observed that circular, angled and planer shapes all show differing temporal responses throughout their respective heating cycles. Regardless of the spatial or temporal method used in the data extraction, the final geometric results produced can either be outputted numerically, or digitally. The generation of digitised data is extremely important step, as it means the captured data can be used subsequently by several third-party applications, in addition to dimensional validation. Finally, an initial value of accuracy has been determined for this system from the practical work that has been performed. In addition to this several error contributors have been identified that when resolved in the future could increase the accuracy of this system.

7.2. Summary of achieved objectives

In addition to the research questions answered above, the following is a summary of the results for each of the research objectives.

7.2.1. Objective i

- i- Verify computationally that changes in surface temperature are detectable to the extent that internal geometry profiles can be extracted in the resultant surface temperature profile. Performing this will validate whether or not geometric information can indeed be extracted from thermal data from the very basic first instance.*

This first objective was to determine whether this concept of a thermographic vision system would indeed be possible. To obtain the outcome for this objective, an FEA simulation was designed (section 4.1 and 4.2), taking this idea of internal heating, and then monitoring the external face, capturing the resultant surface temperature profile. As seen in section 4.2, the extracted temperature data was used to determine the geometric dimensions of the internal cavity. The results for one edge were extremely close to the nominal, whilst the other showed a higher level of discrepancy. Additional simulations were then performed to vary certain FEA specific simulation factors such as mesh density and simulation time, to try and reduce this discrepancy, or ensure that these factors had no bearing on the initial results obtained. Whilst this initial simulation did not provide exact dimensional results, this objective did show that geometric information could be extracted from surface temperature data with a high enough degree of accuracy to continue this investigation forward. Continuing this work would allow for the addition of several other factors that could influence the accuracy of the resulting geometric data.

7.2.2. Objective ii

- ii- Verify that changes in internal geometry, such as shape, depth from surface, size, and material properties, such as thermal conductivity, still allow for internal geometry profile extraction. Building upon the information gained from objective*

one, changing a multitude of factors will indicate the limitation of system, and offer insight into the where this system will yield best results, and where potential pitfalls may exist.

This objective built upon the work from the objective i. By reusing the simulation used in objective i, several factors such as depth from surface, size, thermal properties, and shape could be altered. As seen in sections 4.2.4, 4.2.5, and 4.2.6 the change in these factors did have an effect on the capture results. Changes in width did result in increases of size in the resultant geometric data showing that size differences can be distinguished. Changes in depth did affect geometric results for in aluminium, increasing the error band, but had less of an effect of less conductive materials. In addition to that, changes in thermal conductivity showed the effective monitoring time required for different materials. For example, the surface temperature gradients from aluminium showed geometric information extraction was only viable up to around 10s. After that the surface temperature had saturated yielding no further results. Conversely PLA, with a much lower thermal conductivity, was still able to yield geometric results 600s after heating start.

These simulations have also shown that different heating techniques provide better results depending on the material. Core heating for highly conductive materials leads to surface temperature saturation very quickly, given as said before only 10s to extract any usable data. However, external heating on same material, where the internal structure acts as an air cavity, provided a much steadier heating cycle, allowing for geometric data to be captured for a longer period. Conversely though, external heating on low conductive materials yields no useable results even though the heating time was massively extended.

Performing these simulations has shown that computationally, under perfect conditions, this system is capable of discerning changes in internal structures, considering differing material properties, shapes, etc. However, it has also shown that differing materials produce different results, and that different heating solutions are applicable when considering different materials.

With this in mind this thermographic vision system was considered suitable for be taken forward practically for validation.

7.2.3. Objective iii

- iii- Design, simulate, and manufacture test artefacts that can be validated experimentally, based upon the information gathered in objectives one and two. These artifacts will need to be calibrated before any experimental validated do determine their actual internal dimensions.*

Following on from objectives one and two, several test artifacts were designed, simulated under the same conditions as in objectives one and two, and then manufactured (section 5.1).

The design aspects considered, were a large enough internal structure to ensure suitable heat generation but be small enough to fill the frame of the thermal camera during heating. Given the most stable and consistent results found in object two were from simulations using plastics, most artifacts manufactured in the stage was 3D printed from PLA. This allowed not only a low thermal conductivity and emissivity, which seemed to be more conducive when using the thermographic system, but also meant these artifacts could be manufactured quickly and cost-effectively. From the artifacts manufactured several factors were altered in each one, such as shape (planer, curved, angled), and symmetry (cuboid, L-shaped). In addition, one artifact was duplicated in aluminium. As found during simulations aluminium gave completely converse results compared to PLA. It has the highest thermal conductivity of any material used, and it is highly emissive. This artifact would also allow for the validation of the external heating idea simulated in section 5.4.

After manufacture all artifacts were calibrated using a X-TEK XCT scanner, to find their actual internal dimensions. This is shown in section 5.2 and *Appendix E*.

7.2.4. Objective iv

- iv- Design an experiment around the manufactured artefacts that will validate the finding of objective one and two. Emphasis will need to be made upon the thermal*

data capture technique, and the technique used in manipulating the object internal temperature relative its external temperature.

The design around the practical aspect of this investigation was based on the above-mentioned need and the factors and levels outlined in Table 3-2. As envisaged from the conception of this investigation, the thermal capture would be performed by a thermal imaging (thermographic) camera. This work had used a FLIR A655SC since the specification was adequate and it was available for the research. Further work to see whether a better-performing camera could provide better results is outside the scope of this thesis. The factors to consider for the design of the practical work were constrained by the artifacts designed in objective three. Certain levels, such as internal heating temperature, and monitoring time, were influenced by the results from the simulation work in objective ii but were dependent on material. The FOV level was determine by the choice of lens, in this case a 24.6mm wide angled lens. Using this lens gave a wider field of view allowing for the artifact to fill the frame as much as the minimal focal distance would allow. This is turn would allow for the highest resolution possible. It was envisaged and proven that this setup would return the expected response of being able to capture surface temperature profiles form which internal geometric information can be deduced.

7.2.5. Objective v

- v- *Investigate ways in which the recovered data can be used and manipulated into deduced geometric data sets of the internal geometry, which if needs can be combined with other external data sets to form complete 3D renditions of the object in question. This will show how versatile the system is, and its practical imitations; can it be used for single 2D stills or can it produce complex 3D models that can be combined with third party information.*

By using the experimental setup detailed from objective four, both spatial and temporal surface temperature profiles were successfully extracted (Chapter 5 and Chapter 6). With regards to the spatial capture of all artifacts tested, each one presented result's showing that 2D geometric dimensions can be extracted from induced surface temperature profiles projections using this

technique to within a certain degree of accuracy. In addition to this, following several successful geometric extractions from differing projections, several 2D data sets can be stitched together to form a single 3D PCD of the object in question. In the first instance this PCD can provide tangible 3D geometric information, but as shown it can also be combined with externally captured information to form a complete 3D rendition of object comprising of both internal and external geometric features. This in turn can then go on to form a 3D solid model which can then be used in a multitude of differing applications.

Whilst the above result shows that this system can extract geometric information from thermal data, all the artifacts used in the spatial extraction consisted of planar features. It was hypothesised that introducing curved and angled features would lead to the features being unresolvable spatially, due to the transient nature of the extractable edge as it moved across the curved or angled face. Therefore, the spatial extraction program was modified to allow for geometric extraction from every thermographic frame that was inputted as part of a single heating cycle. By transiently monitoring the heat propagation generated by the internal features, the internal boundaries of that feature can be tracked over time. By performing this transient monitoring process on artifacts consisting of planar, curved, and angled internal features, it has been observed that each different feature presents a different response over time. This difference has shown that when monitored transiently, seemingly similar thermal responses can divulge different geometric profiles that must be dependent on the internal structure. Such observed differences, pending on future work, could allow for the automatic classification of features.

7.2.6. Objective vi

- vi- *Determine the accuracy and repeatability of the system. As this is a critical part of any metrology tool, if the experiment from objective four is successful, it will need to be repeated several times to ascertain its accuracy and repeatability.*

To determine the accuracy, repeatability, and reusability of the system at this proof-of-concept stage of development the experiment detailed in section 5.3 was repeated five times. For each of the five runs, the X/Y positions for the internal feature was recorded. From this the standard deviation, average error and max error were deduced. The average standard deviation over the five runs was 0.6mm. The average error was found to be 0.9mm with a max error of 1.6mm. These results are consistent with the average and maximum errors from additional experiments performed in Chapter 5. For the cuboid and L-shaped artifacts the average and maximum errors were 0.8mm and 1.4mm, and 0.9mm and 1.8mm (average and max), respectively. In addition, several error sources have been identified and where possible, steps have been taken to mitigate their effects. Further work is required to fully understand the effects of these error sources on the overall uncertainty, and what additional steps and mitigations can be put in place to minimise their overall effect.

7.3. Conclusions and Contributions to Knowledge

7.3.1. Conclusions

From this investigation, the following conclusions have been drawn, in order of importance:

- For low materials with thermal conductivity less than 0.5 W/m k, internal geometric dimensions of an object under investigation can be determined from the temperature data recovered from induced differential spatial temperature gradients when the cavity is heated to ≈ 100 °C. For materials with thermal conductivity greater than 0.5W/m k, computationally internal geometric dimensions have been recovered. However practically the validation of successful internal geometric extraction remains inconclusive as only partial results were obtained.
- Using this system, the internal geometrical dimensional accuracy of object has been tested and has been determined to with max error of 1.8mm with an average error of

0.9mm. Whilst the exact reason behind such large errors is yet undetermined, several error sources have been identified that will warrant further investigation and resolution.

- For materials with low thermal conductivity less than 0.5 W/m k, the internal structure of the object can be determined (either curved, angled or flat) based upon its differential temporal thermal response.
- Multiple 2D geometric profiles, individually recovered from single projection thermograms can be integrated together to form a single 3D point cloud entity, capable of detailing all internal geometric features
- This single point cloud of the internal geometry can be combined with additional data concerning the external features to generate a complete 3D solid model of the geometry in question, that can be used in further applications.
- Further work is required to devise a more suitable heating technique. Most tests in the investigation successfully used core heating to excite surface temperature profiles. Whilst this method has resolved numerous internal data sets for low thermally conductive materials, it has only provided partially successful results high thermally conductive materials. Furthermore, it is potentially not universally suitable moving forward, and some form of external heating would be a more attractive solution. However, as has been found, external heating in this investigation proved inconclusive with regards to internal data extraction. Therefore, moving forward more research will be required in this area to determine a practical heating solution that can resolve internal geometric data extraction for materials of varying thermal conductivity.

7.3.2. Contributions to Knowledge

1. The creation and validation of a novel thermal vision system capable of extracting internal geometric dimensions.

- Prior to this research, the dimensional validation of an objects internal features could only be performed by either XCT scanning, or destructive measurement. The new method exploits relatively inexpensive and accessible equipment to perform non-destructive internal measurement. To the author’s knowledge thermography and dimensional measurement have never been combined to ascertain the internal layout or geometric structure of an object.
 - It has been found that differing internal shapes resolve different temporal responses. As has been seen in this investigation differing internal structure present different resulting responses from their surface temperature profiles when observed over time. This change in the resultant captured data, can form the basis for a feature detection algorithm capable of determining internal feature geometry based on temporal thermal responses.
2. The creation of filtering and edge detection algorithms for ill-defined edges in noisy thermal image data
- Current edge detection algorithms are imaged based and designed to return values greater or lower than a set threshold. This is impractical for this investigation as any threshold value would be unknown. For this reason, a novel peak detection algorithm has been created in MATLAB, which can detect a predefined number of “peaks” in a differentiated temperature data set. This algorithm provides an autonomous function that can repeat the above process and return results for every row or column in a given data set. These methods can be seen in Chapter 5 and Chapter 6 with the MATLAB algorithms presented in *Appendix H*. This process could be adapted for edge detection in any noisy data set where typical edge detection methods are unsuitable.
3. Detailed simulations on the effects that differing part geometries and differing heating techniques have on resulting surface temperature gradients.

- By performing multiple FEA simulations in Chapter 4 a baseline for the relationship between discerned internal geometric edge position, and other variables such as thermal conductivity, applied temperature and exposure time has been established. In addition, differing internal geometry can be determined based upon the resultant shape and gradient of the temporal results for edge position. This information can be used in further investigations for internal geometry measurement, or for potential studies in thermal conductivity dynamics.
4. Representation of recovered geometry and point cloud integration.
- For the reconstruction of the individual recovered data, as seen in Chapter 5, a new MATLAB algorithm has been created. This algorithm takes all of the 2D X/Y data, exported from the algorithm mentioned in contributions 1 and 2 and combines them into a representative 3D point cloud model of the object in question. This data can then be exported to additional third-party software's for additional computational operations.
 - To register two sets of cloud point data together, first, they need to be tessellated. If the data is sparse, such as the internal geometry data in this investigation, accurate tessellation is impossible. In Chapter 5 (and *Appendix D* and *Appendix G*) a process is developed that allows the generation of a dense tessellated mesh from minimal point cloud data points. Combined with the generation of meaningful representative features, such as planes or axis lines, this allows for the registration of both the internal and external meshes, resulting in a single tessellated mesh. From this, a single CAD solid model can be produced. This technique is applicable to any point cloud data set consisting of minimal points.

7.4. Closing Statement

This investigation has led to the design and initial implementation of a novel vision system capable of extracting internal geometric dimensions from objects consisting of internal features. By manipulating the internal temperature of a hollow object and observing the surface temperature gradient resulting from the conductive heat transfer, it has been shown that the profile of the internal structure can be extracted and inspected. By compiling this information and organising it three dimensionally, the gathered geometrical data will then represent the internal structure. This information can then be combined into existing techniques for the external geometry, allowing for the realisation of a complete CAD solid model. Experimental validation showed that all recovered dimensions are within $\pm 2\text{mm}$ of their corresponding actual measurements, with an average error for all artifacts measured, of around 0.9mm , and the largest error found in this investigation of 1.8mm .

This investigation has also shown that different internal structures can be identified based upon the resultant information gathered from their respective heat transfer results.

Whilst this investigation has mainly focused on low conductive materials, as at this stage they produce the most easily observable results, it has been shown that the inspections of hollow objects is possible using this non-destructive technique. It has also been shown that using this technique with other more conductive materials can produce geometric results, but further work is required for the method to be refined and for these results to become fully validated.

7.5. Future Work

The preceding chapters in this investigation have introduced a novel system for the non-destructive holistic measurement for the PIDV of hollow objects. During this investigation,

several areas that would complement this solution have been identified for further investigation.

This section proposes areas of further research that have arisen from this thesis in order of importance.

7.5.1. Thermal conductivity, edge position relationship.

As was seen in Chapter 4, materials with low values for thermal conductivity provided the most unambiguous and stable results over time. In these examples, periods of several minutes could elapse in which edge positions could be extracted that would be considered within tolerance. However, with increased thermal conductivity, this period in which accurate edge position results can be extracted, rapidly decreases. As was seen with models designed from aluminium, the results that were captured for edge position included large values of drift over time. Whilst repeatedly simulating the model with materials that had lower values for thermal conductivity showed this drift decreasing, it was only when the material's thermal conductivity was at its lowest did edge position results stop being unambiguous.

Therefore, going forward, to ensure that this system can work on a much wider range of materials, other than low conductive polymers, a corrective factor would be needed that considers the relationship between thermal conductivity, temperature, and time.

By adding a corrective factor that takes into account thermal conductivity and temperature, it is envisaged that stable actual results for edge position can be found at any time step regardless of drift.

7.5.2. Edge position response curves characterisation

As was noted in Chapter 5, with low conductive materials, where the edge position drift is caused by internal shape geometry, it is possible to determine the characteristics of the internal

features based upon the response of the edge positions over time. In Chapter 5, this was performed as a validation to the simulation examples undertaken in Chapter 4. In a real-world example, the internal shape would not be known. Therefore, for future usage it would be important to employ classifications to these response curves. By relating the curvature and gradient of the recovered curve, it can be compared against a set of predefined standards, that could classify the internal feature as, curved, angled or flat etc.

7.5.3. Heating methods

As was shown in Chapter 4, a simulation was performed where the object was not heated from the internal cavity but on one of the external faces. The simulation was performed on an object with the material properties set to those of aluminium. Normally results from aluminium show large amounts of edge position drift and quick homogenisation. However, by heating the object on an external face, much more stable and accurate results were obtained. When performed experimentally however, this external heating technique did not provide the stable results expected, with the surface temperature gradient not being induced, and the surface temperature raising uniformly.

Even though in this investigation external heating did provide the results expected, it is still maintained that moving forward, and with further investigation, it would be a more attractive and suitable heating method, due to the control it can offer and the removal of adding water to what could be potentially delicate items. Heating techniques that could be exploited with regards to this such as joule heating [73] or pulsed thermography [74].

7.5.4. Large scale scanning

As said at the onset of this investigation, one constraint of XCT scanning is the size of object these devices can accommodate. This was one of the rationales behind performing this investigation, by envisaging a system that was not limited by such size constants. Whilst it is

true that the thermal imagery part of this investigation does not define any size limitations (although resolution will reduce as the size of the object increases), this process has not yet been performed on any large-scale objects. To ascertain this system's full viability, one area of future work would be to perform the full scanning process on a large-scale object.

A preliminary simulation has been performed to show that even very large object can have internal edge positions deduced from excited surface temperature gradients. The internal void was heated to 100°C, with Figure 7-1 showing the temperature distribution of a 5m hollow cube (the size of such parts found in the civil nuclear industry), and Figure 7-2 shows the recovered edge positions over time. Whilst this simulation shows that internal feature extraction is possible with this technique, raising the internal temperature of such as object would require large amounts of energy.

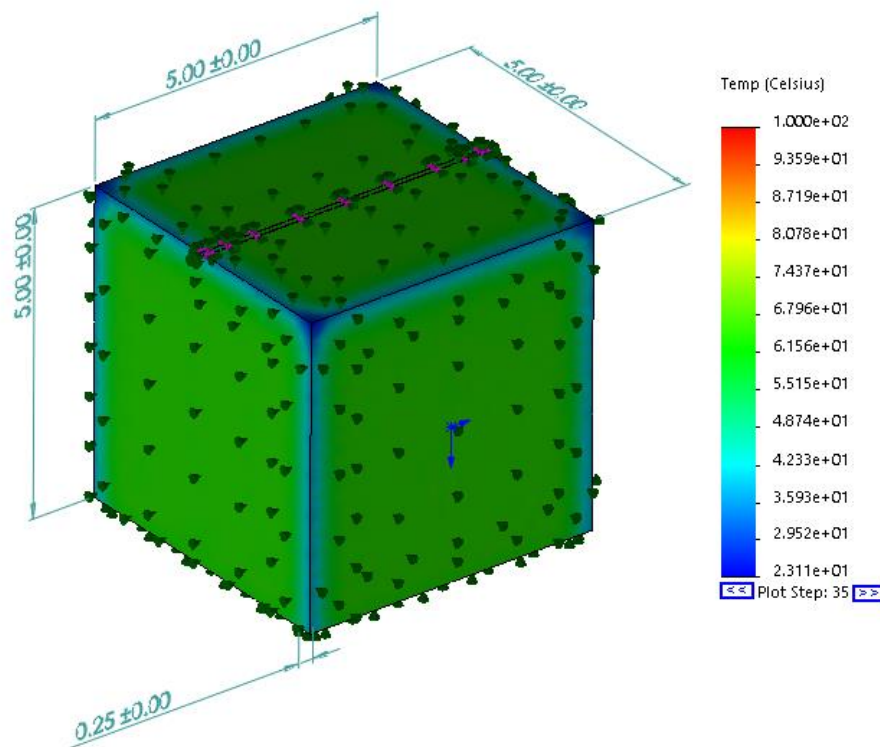


Figure 7-1: Example of large component edge recovery. All dimensions are in metres

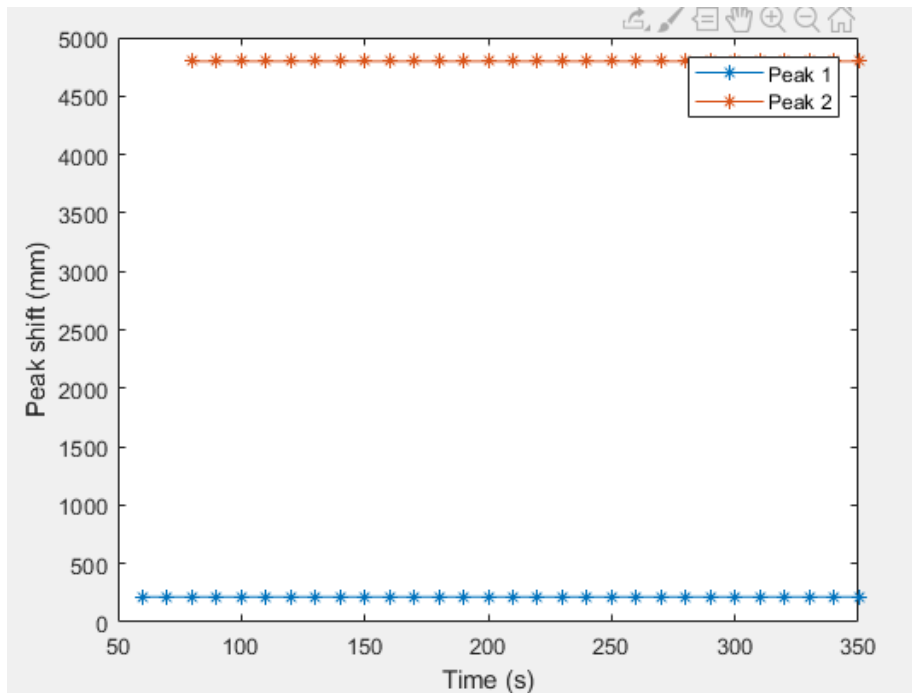


Figure 7-2: Edge position of large part

7.5.5. Uncertainty analysis

To be used as a metrology tool, this system would require a full uncertainty evaluation to be undertaken. Several areas of uncertainty have already been highlighted during this investigation. Thermal expansion, the effects of emissivity, parallax error between the object and the camera, the coma effect of the camera lens, filtering errors in the extracting algorithms are just a few of the systematic errors that would influence uncertainty in a measurement using this system. These systematic errors would need to be fully evaluated and quantified before a review of random errors that could arise by using this system, could be undertaken.

7.5.6. Enhanced small scale scanning

From previous research done in the areas where thermography and PIDV do overlap, one area of commonality between them is the use of a combined system, i.e., the thermal camera and visible light scanner that are intrinsically linked (see [54]). This allows the use of a common global registration between the two devices. During this investigation, the external scanning and internal capture were performed separately. Ideally, the most optimal device would be one

that has the visible light scanner and the thermal camera linked on a single stage with the object under investigation placed between them and allowed to rotate. This concept is shown in Figure 7-3.

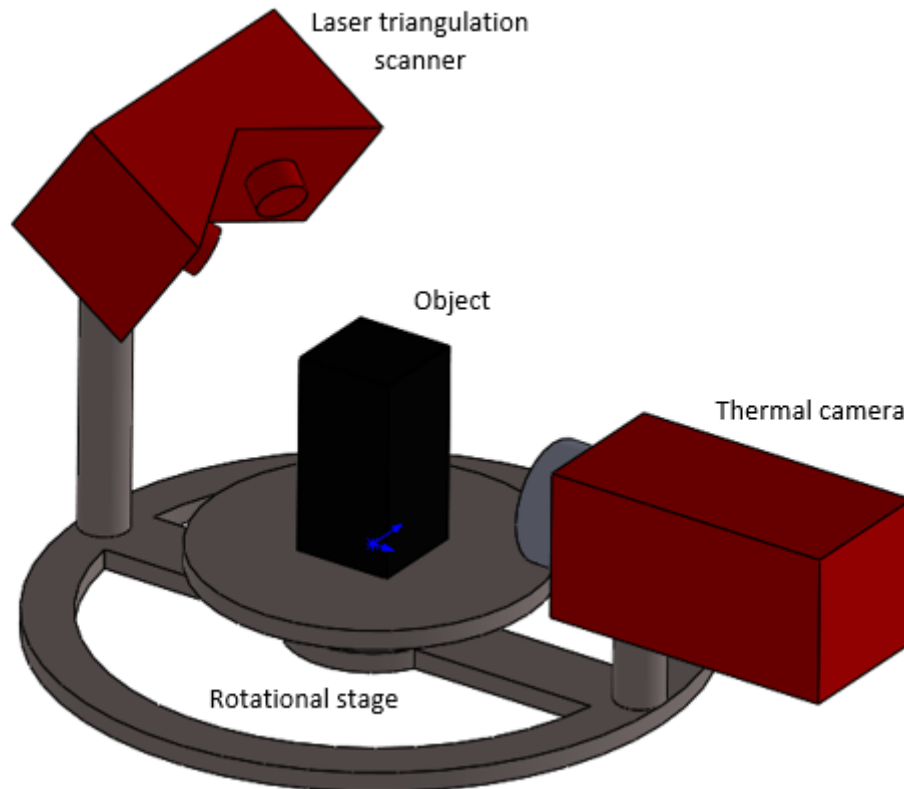


Figure 7-3: Concept of small object thermal scanner

By linking, the thermal camera and the scanner head to a single stage, a global coordinate frame could be established between the two. As the object rotates, the laser triangulation scanner can capture a complete scan in a single pass. The thermal imaging camera would take thermograms at the same rate as the stages rotational intervals. In this sense, it is similar to the operation of XCT scanner. Computationally the thermograms are then assembled in accordance with the rotation intervals, allowing the reconstruction not from four orthographic views but many multiple views. From this, a more accurate reconstruction of the internal structure might be resolved. The external scan CPD can then be registered with the CPD resolved from the thermal scans in the same way it was performed in Chapter 5.

References

- [1] ISO 10360-1:2000 *Geometrical Product Specifications (GPS) — Acceptance and reverification tests for coordinate measuring machines (CMM) — Part 1: Vocabulary*, ISO, 2000.
- [2] Y. Jun, “A Piecewise Hole Filling Algorithm in reverse engineering,” *Computer Aided Design*, vol. 37, pp. 263-270, 2004.
- [3] L. Spampinato, S. Calvari, C. Oppenheimer and E. Boschi, “Volcano Surveillance using Infrared Cameras,” *Earth-Science Reviews*, vol. 106, pp. 63-91, 2011.
- [4] S. Telfer, J. Pallari, J. Munguia, K. Dalgarno, M. McGeough and J. Woodburn, “Embracing additive manufacture: implications for foot and ankle orthosis design,” *BMC Musculoskeletal Disorders*, vol. 13, no. 84, 2012.
- [5] G. N. Levy, R. Schindel and J. P. Kruth, “RAPID MANUFACTURING AND RAPID TOOLING WITH LAYER MANUFACTURING (LM) TECHNOLOGIES, STATE OF THE ART AND FUTURE PERSPECTIVES,” *CIRP Annals*, vol. 52, pp. 589-609, 2003.
- [6] W. Geo and et al, “The status, challenges, and future of additive manufacturing in engineering,” *Computer-Aided Design*, vol. 69, pp. 65-89, 2015.
- [7] D. Li and Et al, “Optimal design and modeling of gyroid-based functionally graded cellular structures for additive manufacturing,” *Computer-Aided Design*, vol. 104, pp. 87-99, 2018.
- [8] S. K. Everton, M. Hirsch, P. Stravroulakis, R. Leach and A. Clare, “Review of in-situ process monitoring and in-situ metrology for metal additive manufacturing,” *Materials and Design*, vol. 95, pp. 431-445, 2016.
- [9] K. Naresh, K. A. Khan and W. J. Cantwell, “The use of X-ray computed tomography for design and process modeling of aerospace composites: A review,” *Materials and Design*, vol. 190, pp. 2-26, 2020.
- [10] Y. An and G. S. Schajer, “Feature-Specific CT Measurements for Log Scanning: Theory and Application,” *Experimental Mechanics*, vol. 54, pp. 753-762, 2014.
- [11] T. Flohr, “CT Systems,” *Advances in CT imaging*, vol. 1, pp. 52-63, 2013.
- [12] A. du Plessis, S. Gerhard le Roux and A. Guelpa, “Comparison of medical and industrial X-ray computed tomography for non-destructive testing,” *Case Studies in Nondestructive Testing and Evaluation*, vol. 6, pp. 17-25, 2016.

- [13] J. P. Kruth, M. Bartscher, S. Camignato, R. Schmitt, L. De Chiffre and A. Weckenmann, "Computed tomography for dimensional Metrology," *CIRP Annals - Manufacturing Technology*, vol. 60, pp. 821-842, 2011.
- [14] J. P. Kurth, M. Bartscher, S. Carmignato, R. Schmitt, L. De Chiffre and A. Weckenmann, "Computed tomography for dimensional metrology," *CIRP Annals - Manufacturing Technology*, vol. 60, pp. 821-842, 2011.
- [15] J. Hiller, M. Maisl and L. Reindl, "Physical characterization and performance evaluation of an x-ray micro-computed tomography system for dimensional metrology applications," *measurement science and technology*, vol. 23, pp. 1-18, 2012.
- [16] Carl Zeiss industrielle Messtechnik GmbH, "Zeiss Volumax specifications," Carl Zeiss, 2017. [Online]. Available: <https://www.msiviking.com/documents/ZEISS/CT/VoluMax.pdf>. [Accessed 27 04 2019].
- [17] G. Moroni and S. Petro, "Design for X-ray Computed Tomography," in *29th CIRP design*, Póvoa de Varzim, 2019.
- [18] V. Aloisi and S. Carminato, "Influence of surface roughness on X-ray computed tomography dimensional measurements of additive manufactured parts," *Case Studies in Nondestructive Testing and Evaluation*, vol. 6, pp. 104-110, 2016.
- [19] E. N. Landis and D. T. Keane, "X-ray microtomography," *Materials Characterization*, vol. 61, pp. 1305-1316, 2010.
- [20] A. Thompson, I. Maskery and R. K. Leach, "X-ray computed tomography for additive manufacturing: a review," *Measurement Science and Technology*, vol. 27, pp. 1-17, 2016.
- [21] W. Dewulf, Y. Tan and K. Kiekens, "Sense and non-sense of beam hardening correction in CT metrology," *CIRP Annals*, vol. 61, pp. 495-498, 2012.
- [22] L. De Chiffre, S. Carmignato, J. Kruth, R. Schmitt and A. Weckenmann, "Industrial Applications of Computed Tomography," *CIRP Annals - Manufacturing Technology*, vol. 63, pp. 655-677, 2014.
- [23] K. Artyushkova and j. E. Fulghum, "Quantification of PVC-PMMA polymer blend compositions by XPS in the presence of x-ray degradation effects," *SURFACE AND INTERFACE ANALYSIS*, vol. 31, pp. 351-361, 2000.
- [24] L. Geraldo, C. Dos santos and K. Yoshio, "Degradation of polyacrylonitrile by X-ray radiation," *Polymer Degredation and Stability*, vol. 44, no. 1, pp. 27-32, 1994.
- [25] Y. Nishikawa, Y. Hatanaka, S. Lizuka and M. Takahashi, "Survey of contrasts of polymers under a high-contrast X-ray computerized tomography," *Polymer*, vol. 53, no. 19, pp. 4287- 4292, 2012.

- [26] Y. Nishikawa, S. Baba and M. Takahashi, "Optimization of X-Ray Computerized Tomography for Polymer Materials," *International Journal of Polymeric Materials and Polymeric Biomaterials*, vol. 62, pp. 295-300, Osaka.
- [27] T. Varady, R. M. Martin and J. Coxt, "Reverse Engineering of Geometric Models - an Introduction," *Computer-Aided Design*, vol. 29, pp. 255-268, 1997.
- [28] D. Algernon, B. Grafe, F. Mielentz, B. Kohler and F. Schubert, "Imaging of the Elastic Wave Propagation in Concrete Using Scanning Techniques: Applications for Impact-Echo and Ultrasonic Echo Methods," *Journal of Nondestructive Evaluation*, vol. 27, no. 1-3, pp. 83-97, 2008.
- [29] "Non-destructive testing of welds — Ultrasonic testing — Techniques, testing levels and assessment (ISO 17640:2010)," European Committee For Standardization, 2011.
- [30] H. Neshat, D. W. Cool, L. Gardi, K. Barker, N. Kakani and A. Fenster, "A 3D ultrasound scanning system for image guided liver interventions," *Medical Physics*, vol. 40, no. 11, pp. 1-13, 2013.
- [31] T. J. Eason, L. J. Bond and M. G. Lozev, "Ultrasonic thickness structural health monitoring photoelastic visualization and measurement accuracy for internal pipe corrosion," in *Smart Structures and Materials + Nondestructive Evaluation and Health Monitoring*, San Diego, 2015.
- [32] M. Lian, H. Liu, T. Zhang, Q. Bo, T. LI and Y. Wang, "Ultrasonic on-machine scanning for thickness measurement of thin-walled parts: modeling and experiments," *The International Journal of Advanced Manufacturing Technology*, vol. 104, pp. 2061-2072, 2019.
- [33] B. S. Marcio, P. Nienheysen, D. Habor and R. C. C. Flesch, "Quality assessment and deviation analysis of three-dimensional geometrical characterization of a metal pipeline by pulse-echo ultrasonic and laser scanning techniques," *measurement*, vol. 145, pp. 30-37, 2019.
- [34] D. W. McRobbie, *MRI from Picture to Proton*, New York: Cambridge University Press, 2007.
- [35] K. Rathnayaka, K. I. Momot, H. Noser, A. Volp, M. A. Schuetz, T. Sahama and B. Schmutz, "Quantification of the accuracy of MRI generated 3D models of long bones compared to CT generated 3D models," *Medical Engineering and Physics*, vol. 34, pp. 357-363, 2012.
- [36] S. Bagavathiappan, B. B. Lahiri, T. Saravanan, J. Philip and T. Jayakumar, "Infrared thermography for condition monitoring – A review," *Infrared Physics and Technology*, vol. 60, pp. 35-55, 2013.
- [37] C. Meola, *Infrared Thermography Recent advances and Future Trends*, Bentham Science, 2012, p. 3.

- [38] R. Gade and T. B. Moeslund, "Thermal cameras and applications: a survey," *Machine Vision and Applications*, vol. 25, no. 1, pp. 245-262, 2014.
- [39] InfraTec, "Infrared theory," Infratec, 2006.
- [40] I. Ridpath, *A dictionary of Astronomy* (3 ed.), Oxford University Press, 2018.
- [41] J. Law and R. Rennie, *A Dictionary of Physics* (7 ed.), Oxford University press, 2015.
- [42] P. E. Liley, "Emissivity of Solids," [Online]. Available: http://hedhme.com/content_map/?link_id=22144&article_id=530. [Accessed 11 05 2019].
- [43] M. Vollmer and K. P. Mollman, *Infrared Thermal Imaging: Fundamentals, Research and Applications*, 2nd, Ed., Wiley-VCH, 2017.
- [44] S. Fletcher, A. p. Longstaff and A. Myres, "Measurement methods for efficient thermal assessment and error compensations," in *Thermal Effects in precision systems*, Maastricht, 2007.
- [45] O. Aubreton, A. Bajard, B. Verney and F. Truchetet, "Infrared System for 3D Scanning of metallic surfaces," *Machine Vision and Applications*, vol. 24, pp. 1513-1524, 2013.
- [46] I. Ihrke, K. N. Kutulakos, H. P. A. Lensch, M. Magnor and H. Wolfgang, "Transparent and Specular Object Reconstruction," *Computer Graphics Forum*, vol. 29, pp. 2400-2426, 2010.
- [47] C. Chen, "Variations of spherical aberration and central coma of conceptual thin lenses," *Applied optics*, vol. 55, no. 36, 2016.
- [48] D. Gonzalez-Aguilera, P. Rodriguez-Gonzalvez, J. Armesto and S. Laguela, "Novel Approach to 3D Thermography and Energy Efficiency Evaluation," *Energy and Buildings*, vol. 54, pp. 426-443, 2012.
- [49] A. G. Krefer, M. M. L. Lie, G. B. Borba, H. R. Gamba, M. D. Lavarda and M. A. De Souza, "A method for generating 3D thermal models with decoupled acquisition," *Computer Methods and Programs in Biomedicine*, vol. 151, pp. 79-90, 2017.
- [50] S. Laguela, J. Martinez, J. Armesto and P. Arias, "Energy Efficiency studies through 3D laser Scanning and thermographic technologies," *Energy and Building*, vol. 43, pp. 1216-1221, 2011.
- [51] S. Yu, J. Kim and S. Lee, "Thermal 3D Modeling system based on 3-view geometry," *Optics Communications*, vol. 285, pp. 5019-5028, 2012.
- [52] S. Zhang and P. S. Huang, "Novel method for structured light system calibration," *Optical Engineering*, vol. 45, no. 8, 2006.
- [53] R. Hartley and A. Zisserman, *Multiple view geometry in computer vision*, Cambridge : Cambridge university press, 2000.

- [54] V. Stephen and P. Moghadam, "Heatwave: A handheld 3D thermography system for energy auditing," *Energy an Buidlings*, vol. 66, pp. 445-460, 2013.
- [55] E. Barker, X. Maldague and D. Laurendeau, "Shape reconstruction from a single thermal image," *Optical Engineering*, vol. 34, no. 1, pp. 154-158, 1995.
- [56] S. K. Everton, M. Hirsch, P. Stravroulakis, R. K. Leach and T. A. Clare, "Review of in-situ process monitoring and in-situ metrology for metal additive manufacturing," *Materials and Design*, vol. 95, pp. 431-445, 2016.
- [57] N. Mian, S. Fletcher, A. P. Longstaff and A. Myers, "Efficient estimation by FEA of machine tool distortion due to environmental temperature perturbations," *Precision Engineering*, vol. 37, pp. 372-379, 2013.
- [58] A. Bejan, *Convection Heat Transfer*, 4 ed., New Jersey: John Wiley & Sons, Incorporated, 2008, pp. 30-95.
- [59] Dassault systems, "Solidworks material library," Dassault Systems, 2019.
- [60] S. Frash, D. G. Anderson and R. Langer, "Physical and Mechanical Properties of PLA, an their functions in widesprea applications - A Comprehensive review," *Avanced Drug Delivery Reviews*, vol. 107, pp. 367-392, 2016.
- [61] D. Hahn and O. Necati, *Heat conduction*, 3rd, Ed., Hoboken: N.J. Wiley, 2012, p. 5.
- [62] A. D. Girgidov, "STRUCTURE AND THERMAL CONDUCTIVITY OF AIR FLOW IN A VENTILATED HPP BUILDING FACADE," *Power Technology and Engineering*, vol. 49, pp. 52-56, 2015.
- [63] R. V. Morgan, R. S. Reid, A. M. Baker, B. Lucero and J. D. Bernardin, "Emissivity Measurements of Additively Manufactured Materials," USDOE OSTI, Los Alamos, 2017.
- [64] Simplify 3D, "Properties Table," [Online]. Available: <https://www.simplify3d.com/support/materials-guide/properties-table/>. [Accessed 08 2020 06].
- [65] BCN3D Technologies, "BNC3D SIGMA R19," 2020. [Online]. Available: <https://www.bcn3d.com/bcn3d-sigma-r19/>. [Accessed 03 06 2020].
- [66] FLIR Systems .inc, "FLIR A655SC specification," [Online]. Available: <https://flir.netx.net/file/asset/10275/original>. [Accessed 24 10 2019].
- [67] FLIR Systems .inc, "IR lens, f=24.6 mm (25°) with case specifications," [Online]. Available: https://www.flircameras.com/pub/media/productattach//t/1/t197922-en-us_usl.pdf. [Accessed 24 10 2019].

- [68] rgb2gray, “Mathworks.com,” The Mathworks.inc, [Online]. Available: <https://uk.mathworks.com/help/matlab/ref/rgb2gray.html#d117e1253144>. [Accessed 07 01 2020].
- [69] G. Hao, L. Min and H. Feng, “Improved Self-Adaptive Edge Detection Method Based on Canny,” in *2013 Fifth International Conference on Intelligent Human-Machine Systems and Cybernetics*, Hangzhou, 2013.
- [70] Mathworks, “Wiener2 2.d adaptive noise-removal filtering,” Mathworks.inc, [Online]. Available: <https://uk.mathworks.com/help/images/ref/wiener2.html>. [Accessed 09 01 2020].
- [71] A. M. Chandra, *Engineering Graphics - Solving the Intricacies of Orthographic Projection*, New Academic Science, 2018, pp. 12-13.
- [72] F. Systems, *User’s manual FLIR Ax5 series*, vol. T559770, Flir Systems , 2018.
- [73] T. Sakagami and K. Ogura, “New flaw inspection techniquw based on infrared thermal images under joule effect heating,” *JSME international journal* , vol. 37, pp. 380-388, 1994.
- [74] Z. Wang, G. Tian, M. Meo and F. Ciampa, “Image processing based quantitative damage evaluation in composites with long pulse thermography,” *NDT and E International*, vol. 99, pp. 93-104, 2018.
- [75] “Romer Absolute Arm factsheet,” Hexagon, 2015. [Online]. Available: <https://www.hexagonmi.com>. [Accessed 01 09 2019].
- [76] Y. Wnag and H.-Y. Feng, “Effects of scanning orientation on outlier formation in 3D laser scanning of reflective surfaces,” *Optics and Lasers in Engineering*, vol. 81, pp. 35-45, 2016.
- [77] L. Xuegang, L. Hongchao and L. Yaogang, “Reverse Engineering Design,” in *Fifth Conference on Measureing Technology and Mechatronics Automation*, 2015.
- [78] T. Varady, R. R. Martin and J. Coxt, “Rerverse Engineering Of geometric Models - An Introduction,” *Computer Aided Design*, vol. 29, pp. 256-268, 1997.
- [79] R. M. Daniel, “The Little Can That Could,” *Invention & Technology Magazine.*, vol. 3, 1987.
- [80] C. F. Geust, “<http://lend-lease.airforce.ru/>,” [Online]. [Accessed 21 November 2016].
- [81] L. Kerber, “Epic Tu-4,” in *War Literature memoirs. No5*, 1990.
- [82] J. Dow, *The Arrow*, James Lorimer & Company, 1997, p. 67.
- [83] T. Varady, R. R. Martin and J. Coxt, “Reverse Engineering of Geometric Models - An Introduction,” *Computer Aided Design*, vol. 29, pp. 256-268, 1997.

- [84] R. M. Daniel, "The Little Can That Could," *Invention & Technology Magazine*, vol. 3, 1987.
- [85] T. Varady, R. R. Martin and J. Coxt, "Reverse Engineering of Geometric Models - An Introduction," *Computer Aided Design*, vol. 29, pp. 256-268, 1997.
- [86] T. Varady, R. R. Martin and J. Coxt, "Reverse Engineering of Geometric Models - An Introduction," *Computer Aided Design*, vol. 29, pp. 256-268, 1997.
- [87] J. Berglund, E. Lindskog and B. Johansson, "On the Trade-off Between Data Density and Data Capture Duration in 3D Laser Scanning for Production System Engineering," in *48th CIRP Conference on Manufacturing Systems - CIRP CMS 2015*, 2015.
- [88] M. Dodosz and A. Wozniak, "CMM Touch Trigger Probes Testing Using a Reference Axis," *Precision Engineering*, vol. 29, pp. 281-289, 2005.
- [89] J. G. D. M. Franca, M. A. Gazziro, A. N. Ide and J. H. Saito, "A 3D System Based on Laser Triangulation And Variable Field of View," in *IEEE international Conference on Image Processing*, 2005.
- [90] J. Garcia-Fernandez, "An assessment of Errors and Their Reduction in Terrestrial Laser Scanner Measurements in Marmorean Surfaces," *3D Reserch*, vol. 7, no. 2, 2016.
- [91] E. L. Monique Johnson, "Suspect Height Estimation Using the Faro Focus 3D Laser Scanner," *Journal of Forensic Sciences*, vol. 60, no. 6, pp. 1582-1588, 2015.
- [92] A. Yamamoto, C.-C. Kuo, K. Sunouchi, S. Wada, I. Yamaguchi and H. Tashiro, "Surface Shape measurement by Wavelength Scanning Interometry Using an Electronically Tuned Ti Sapphire Laser," *Optical review*, vol. 8, no. 1, pp. 59-63, 2001.
- [93] M. A. Hassan, H. Martin and X. Jiang, "Surface Profile Measurement Using Spatially Dispersed Short Coherence Interferometry," *Surface Topography: Metrology and Properties*, vol. 2, 2014.
- [94] S. C. Park and M. Chang, "Reverse Engineering with a Structuerd light System," *Computers and Industrial Engineering*, vol. 57, pp. 1377-1384, 2009.
- [95] S. Rianmora and P. Koomsap, "Structured light system-based selective data acquisition," *Robotics and Computer-Integrated Manufacturing*, vol. 27, pp. 270-880, 2011.
- [96] A. M. Khalil, "Two-dimensional displacement measurement using static close range photogrammetry and a single fixed camera," *Alexadria Engineering Journal*, vol. 50, pp. 219-227, 2011.
- [97] J. baqersad, P. poozesh, C. Niezrecki and P. Avitabile, "Photogrammetry and optical methods in structural dynamics - A review," *Mechanical Systems and Signal Processing*, vol. 86, pp. 17-34, 2017.

- [98] Y. An and G. S. Schajer, "Feature-specific CT measurements for log Scanning Theory and Application," *Experimental Mechanics*, vol. 54, pp. 753-762, 2014.
- [99] M. Yu, Y. Zhang, Y. Li and D. Zhang, "Adaptive sampling method for inspection planning on CMM for free-form surfaces," *The International Journal of Advanced Manufacturing Technology*, vol. 67, no. 9-12, pp. 1967-1975, 2013.
- [100] P. Keller, M. Bertram and H. Hagen, "Reverse engineering with subdivision surfaces," *Computing*, vol. 79, pp. 119-129, 2007.
- [101] N. Werghi, "Assessing the Regularity of 3D Triangular Mesh Tesselation Using a topological Structured pattern," *Computer Aided Design and Applications*, vol. 8, pp. 633-648, 2011.
- [102] Y. Zhang, H. Wang, H. Zhou and J. Li, "Finite Triangular Surface Mesh Simplification With Geometrical Feature Recognition," *PROC IMECHE*, vol. 223, pp. 2627-2636, 2009.
- [103] H. Zhao, N. Anwer and P. Bourdet, "Curvature-based registration and segmentation for multisensor coordinate metrology," *12th CIRP Conference on Computer Aided Tolerancing*, vol. 10, pp. 112-118, 2013.
- [104] G. Kavoue, F. Dupont and A. Baskurt, "A new CAD mesh segmentation method, based on curvature tensor analysis," *Computer-Aided Design*, vol. 37, no. 10, pp. 975-987, 2005.
- [105] H. Woo, E. Kang, S. Wang and H. L. Kwan, "A new segmentaion method for point cloud data," *International Journal of Mahcine Tools and Manufacture*, vol. 42, no. 2, pp. 167-178, 2002.
- [106] T. Varady, R. R. Martin and J. coxt, "Reverse Engineering of Geometric Models - an introduction," *Computer Aided Design*, vol. 29, no. 4, pp. 255-268, 1997.
- [107] R. Fontana, M. Gambino, G. Gianfrate, M. Greco,, L. Marras, M. Materazzi, E. Pampaloni and . L. Pezzat, "Time-of-Flight Laser Scanner for Architectural and Archaeological Applications," *Optical Metrology for Arts and Multimedia*, vol. 5146, pp. 185-193, 2003.
- [108] K. Knoerzer, M. Regier, E. H. Hardy, H. P. Schuchmann and H. Schubert, "Simultaneous microwave heating and three-dimensional MRI temperature mapping," *Innovative Food Science & Emerging Technologies*, vol. 10, pp. 537-544, 2009.
- [109] A. Saidatul, C. Azlan, M. S. Megat Amin, B. J. Abdullah and K. H. Ng, "A survey of radiation dose to patients and operators during radiofrequency ablation using computed tomography," *Biomedical Imaging and Intervention Journal*, pp. 1-4, 2010.
- [110] F. Javidrad and A. R. Pourmoayed, "Contour curve reconstruction from cloud data for rapid prototyping," *Robotics and Computer-Integrated Manufacturing*, vol. 27, pp. 397-404, 2011.

This page has been left intentionally blank

Appendix A. Mesh modification

In order to recover more accurate results, mesh density should be optimum, especially along the probe edge of the object. Increasing the mesh density will increase the resolution of the result extracted from the probe edge. This simulation has been re-run with element lengths of 0.25mm, 0.5mm, and 2mm, examples of which are shown in Figure A-1. The results of edge position accuracy by varying the mesh density are shown below in Figure A-2.

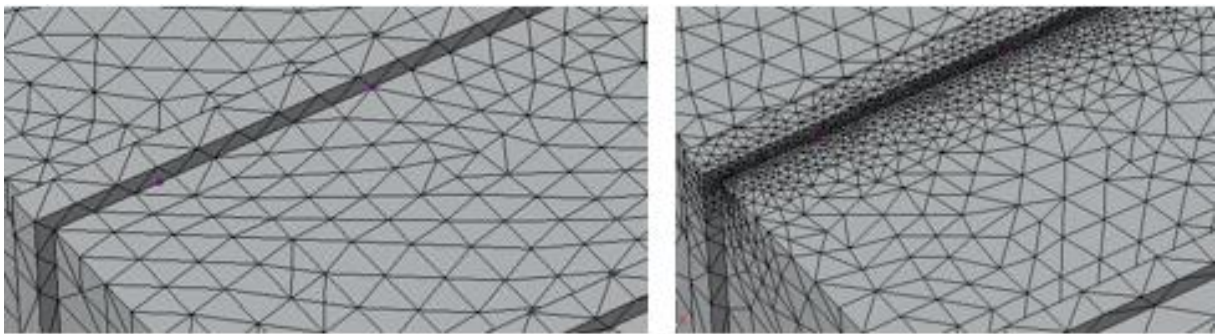


Figure A-1: Examples of mesh density. LH - 2mm, RH-0.25mm

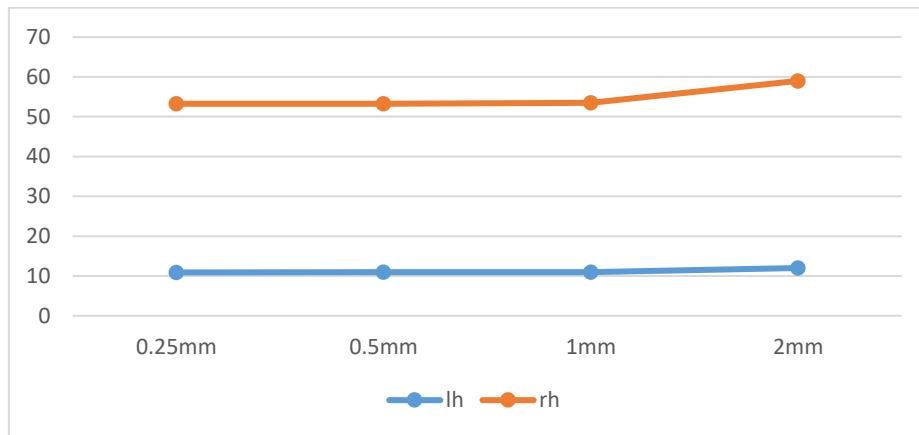


Figure A-2: Edge position by varying mesh density

As can be seen in Figure A-2, modifying the mesh density of the object around the probe line does very little in varying the position results of the internal edges. It also does not correct the positional error of the LH edge, which shows a geometrical position of between 10-11mm regardless of mesh element size.

This has shown that whilst reducing the element size has no apparent effect on the result of the simulation, increasing the element size produces a marginal effect. Therefore, further simulations will have an element size set at 1mm. Any larger than this resolution may be lost, and smaller will provide better insight, but will needlessly increase the computational time of the simulation.

Appendix B. Initial simulation dimensions

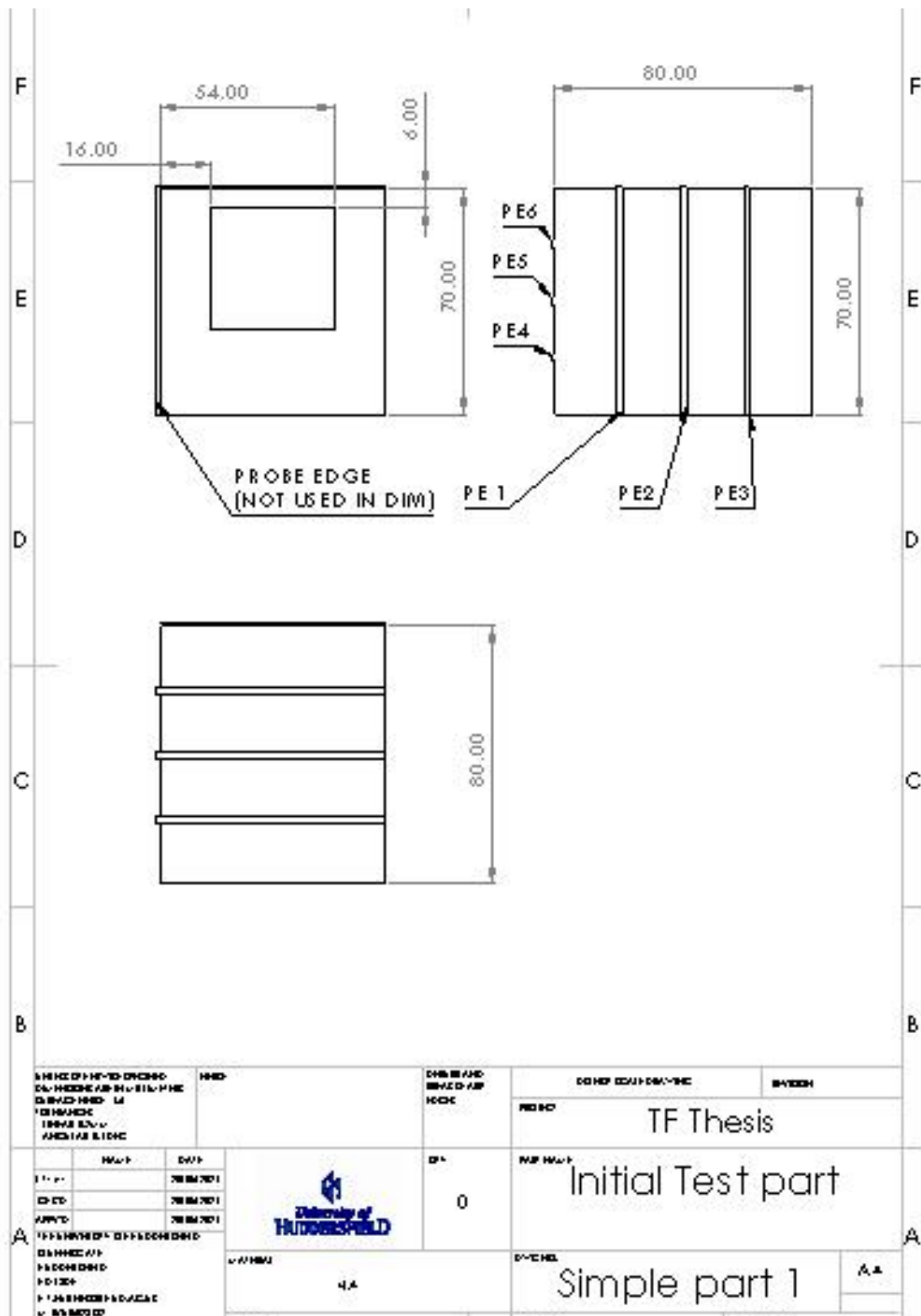


Figure B-1: Drawing of initial test part

Appendix C. FEA results

a. Change in cavity depth

i. Aluminium depth – 2mm

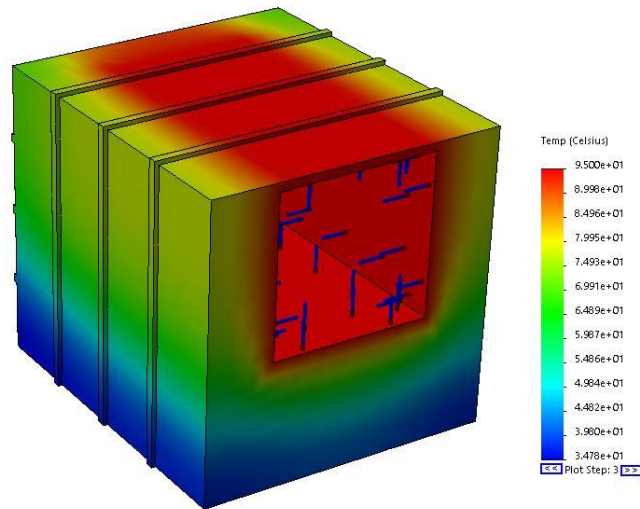


Figure C-1: Thermal distribution at X=2mm

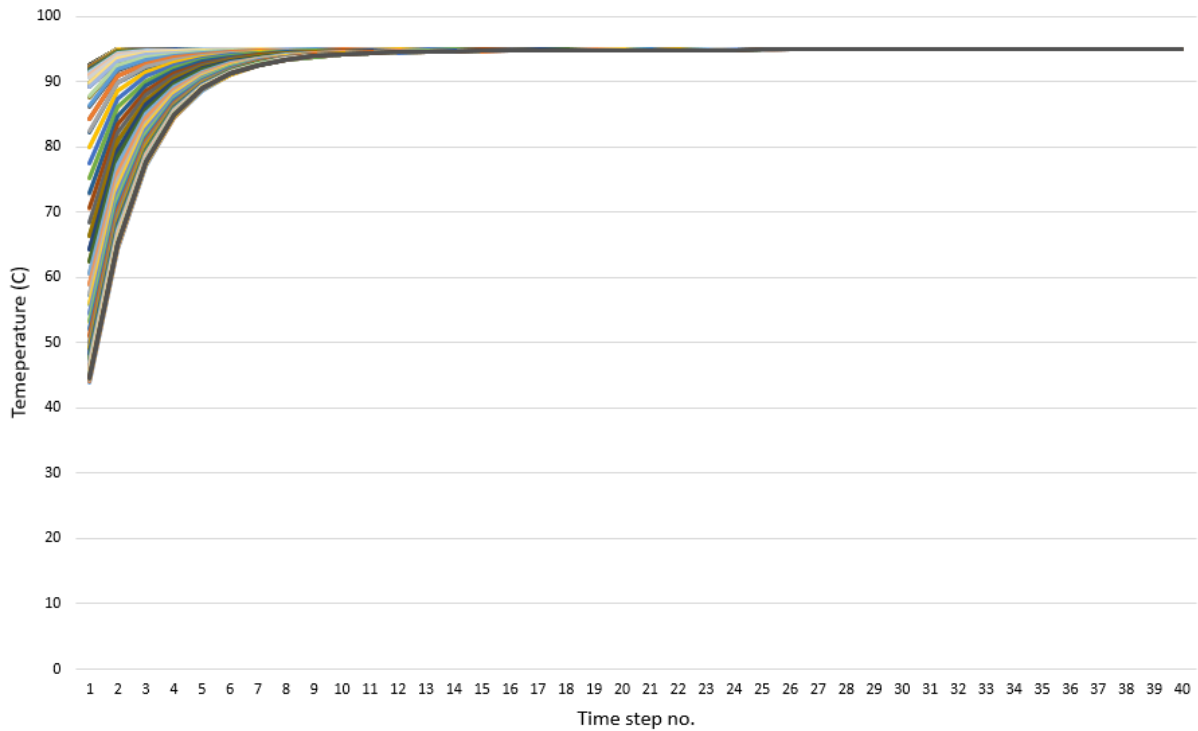


Figure C-2: Nodal temperature over time for X=2mm

ii. Aluminium Depth – 8mm

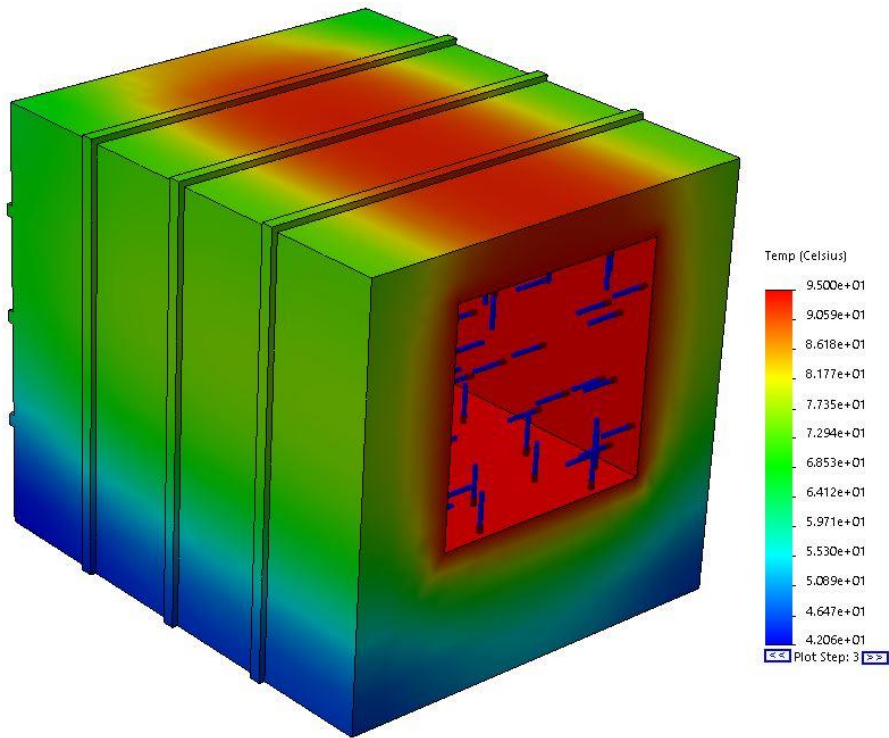


Figure C-3: Thermal distribution at X=8mm

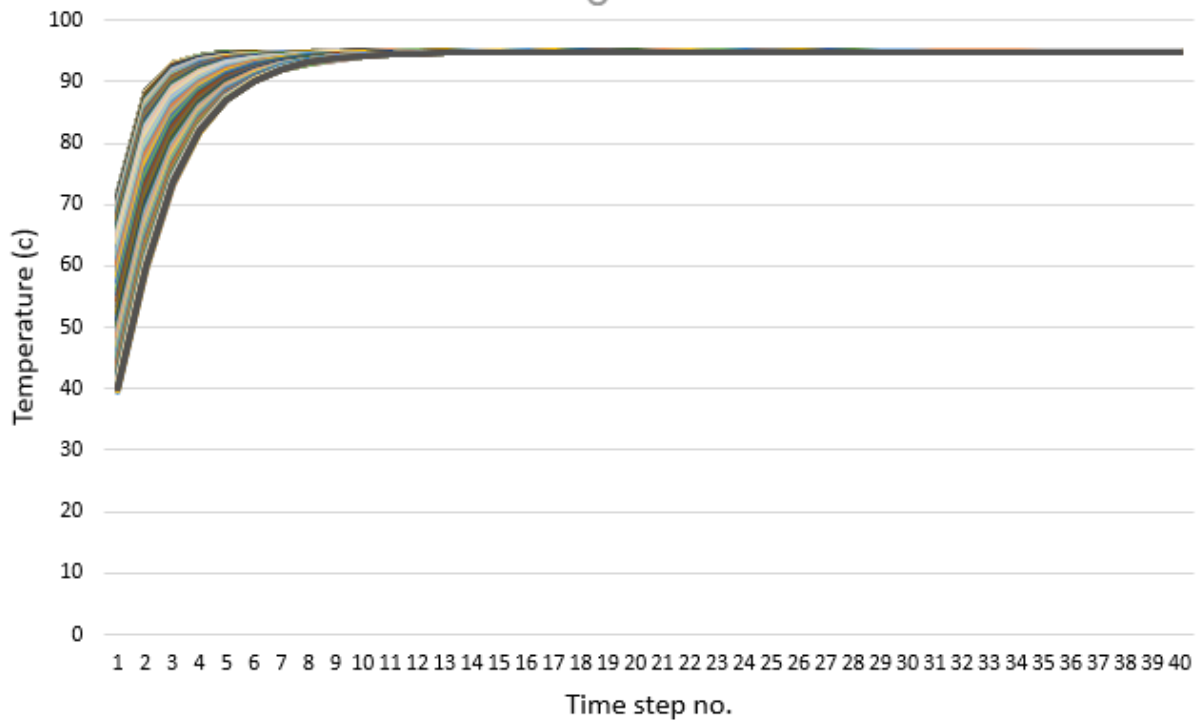


Figure C-4: Nodal temperature over time for X=6mm

iii. Aluminium Depth – 16mm

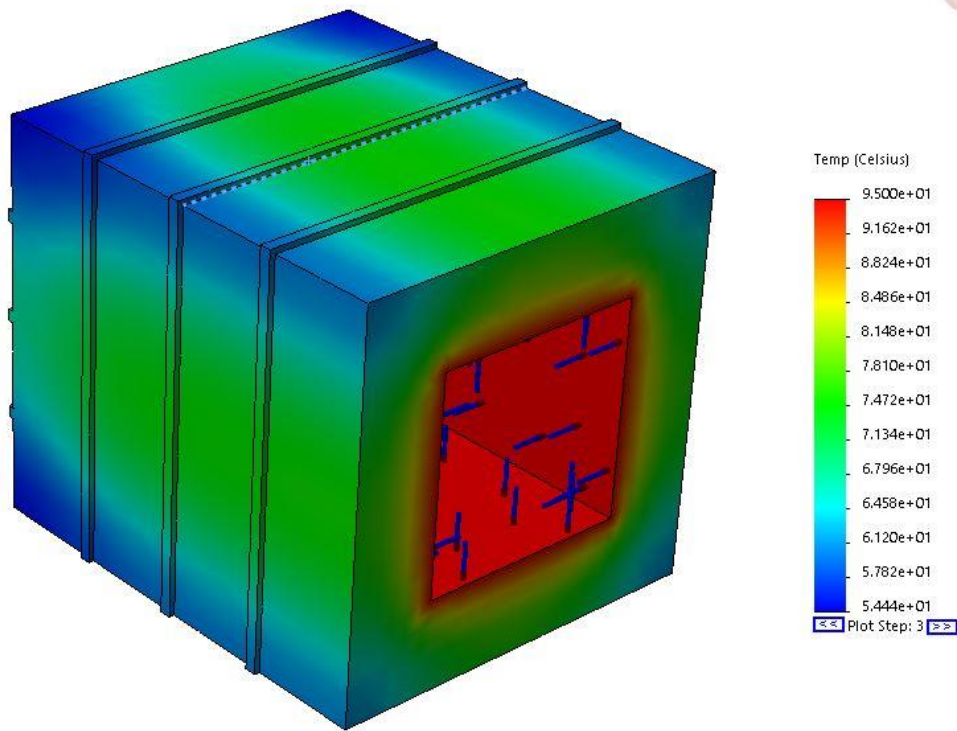


Figure C-5: Thermal distribution at X=14mm

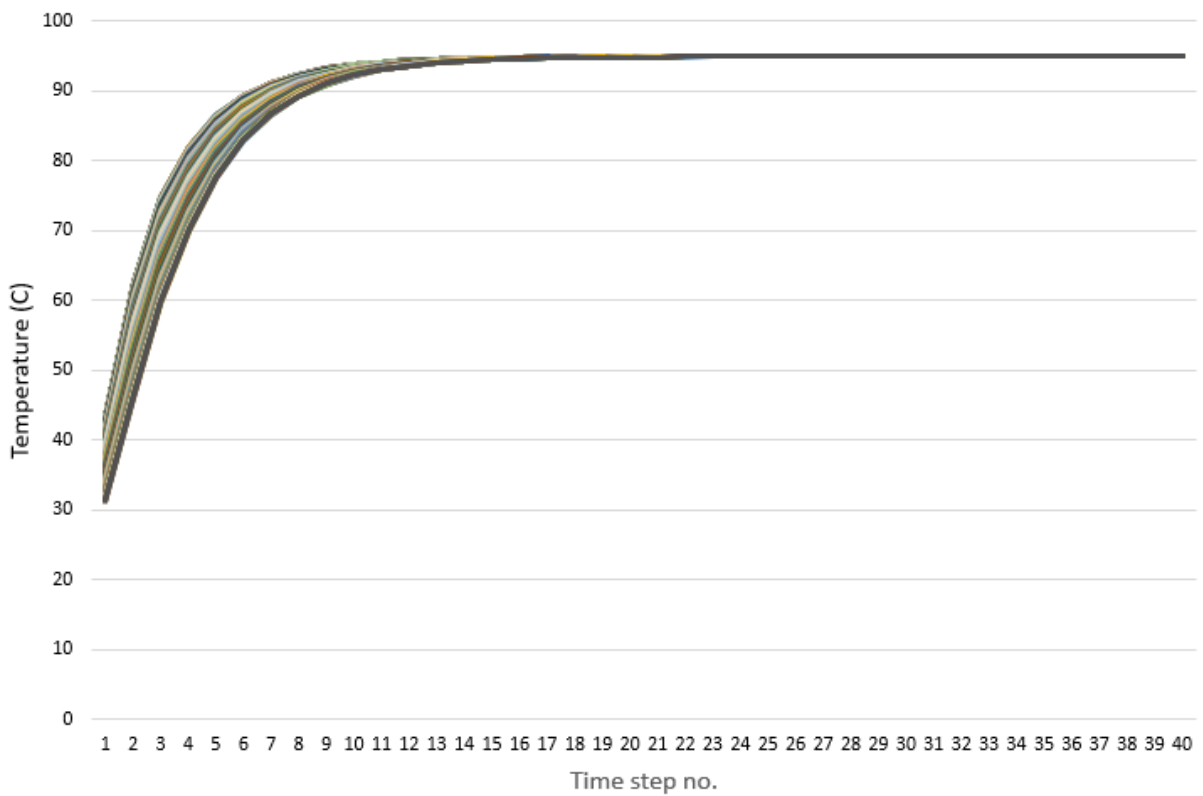


Figure C-6: Nodal temperature over time for X=16mm

iv. PLA Depth – 2mm

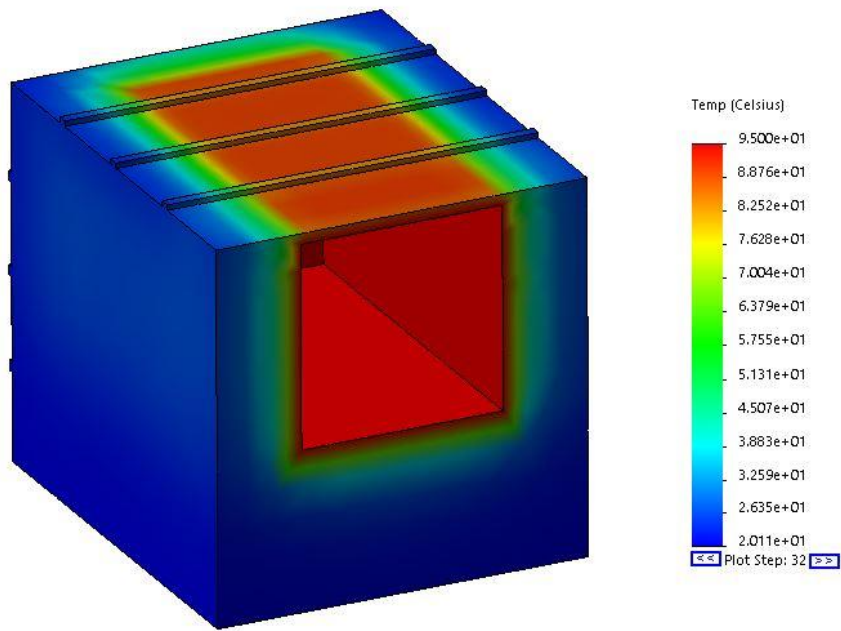


Figure C-7: Thermal distribution at X=2mm with PLA

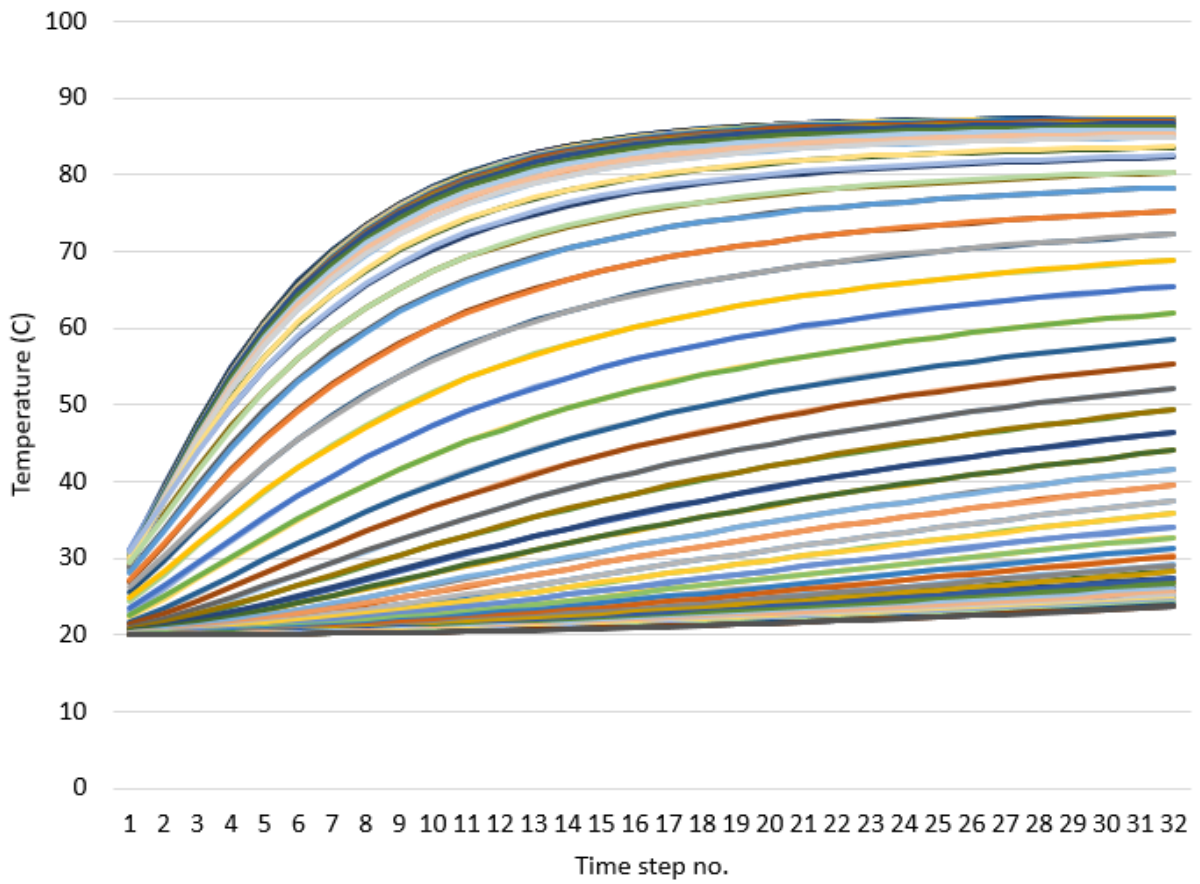


Figure C-8: Nodal temperature over time for X=2mm with PLA

v. PLA Depth – 8mm

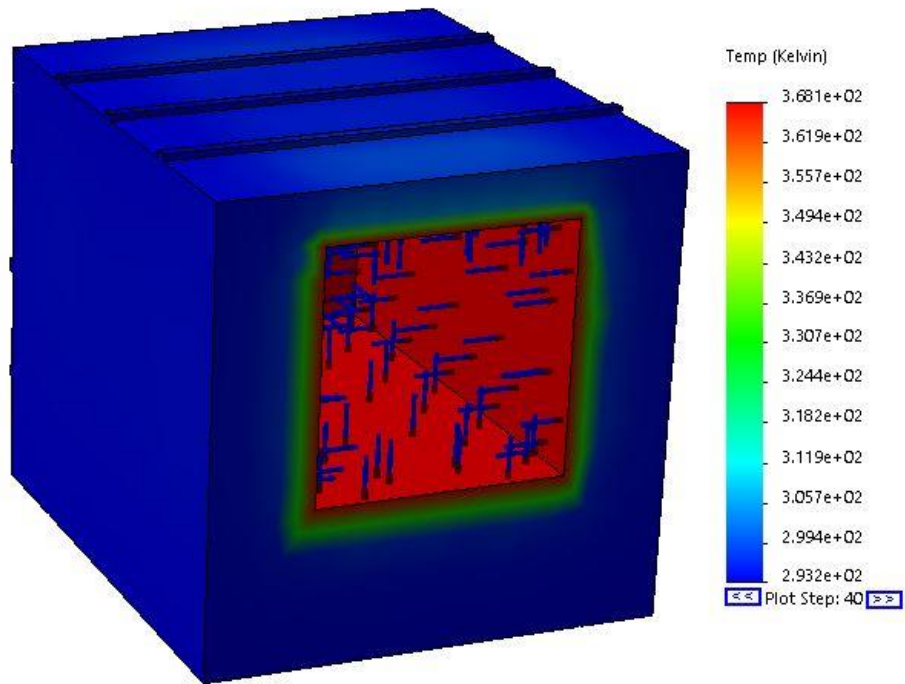


Figure C-9: Thermal distribution at X=8mm with PLA

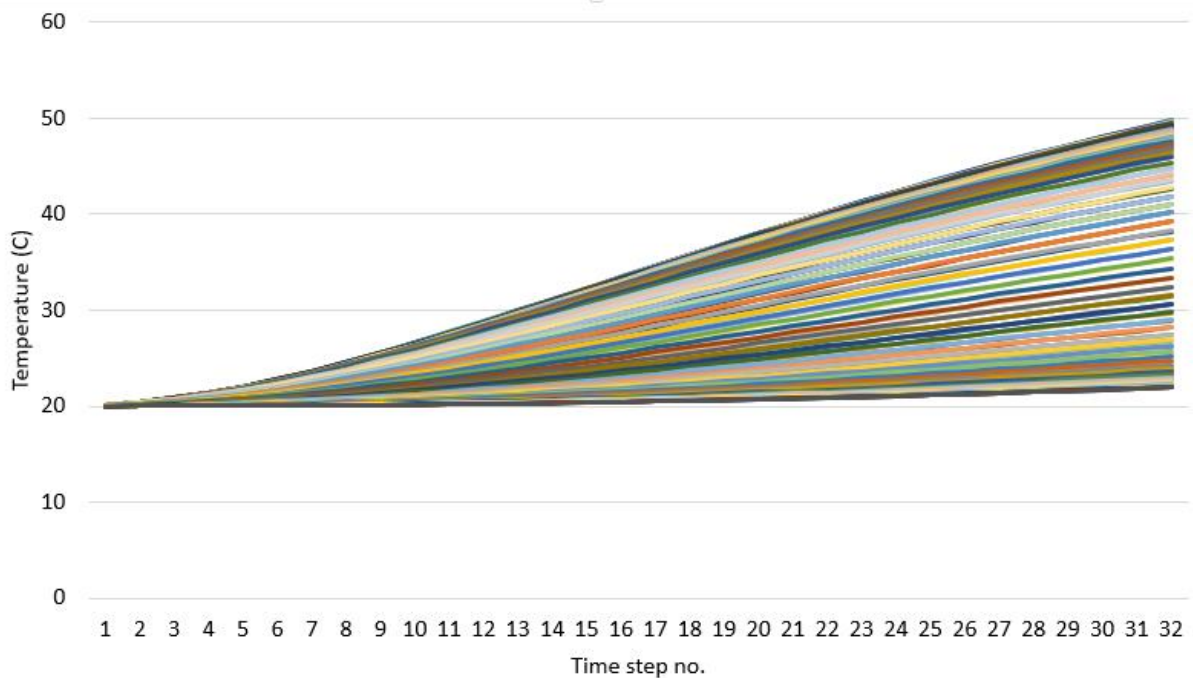


Figure C-10: Nodal temperature over time for X=8mm with PLA

vi. PLA Depth – 16mm

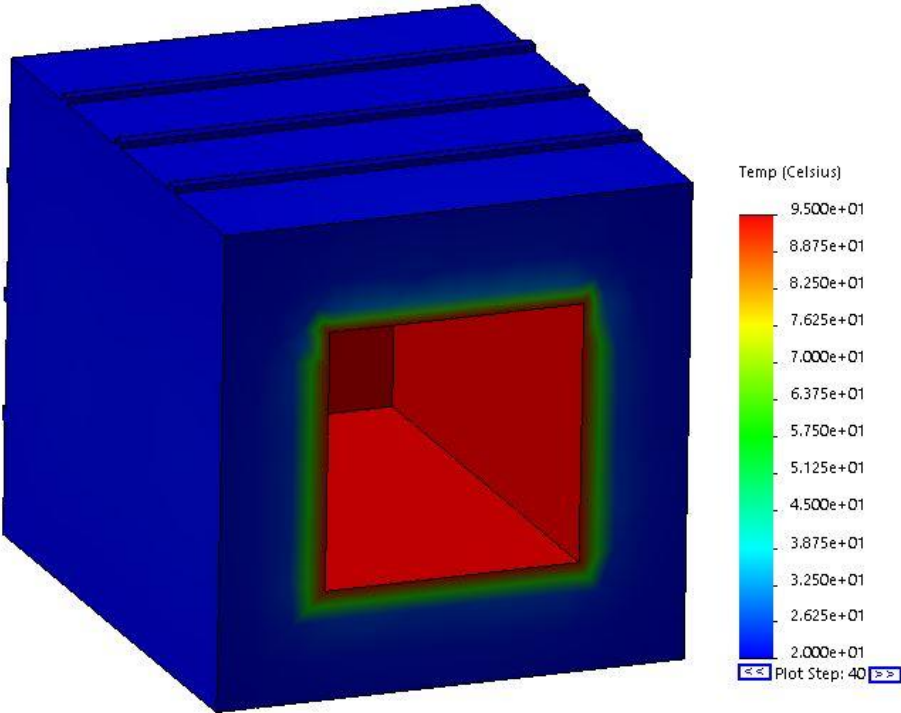


Figure C-11: Thermal distribution at X=16mm with PLA

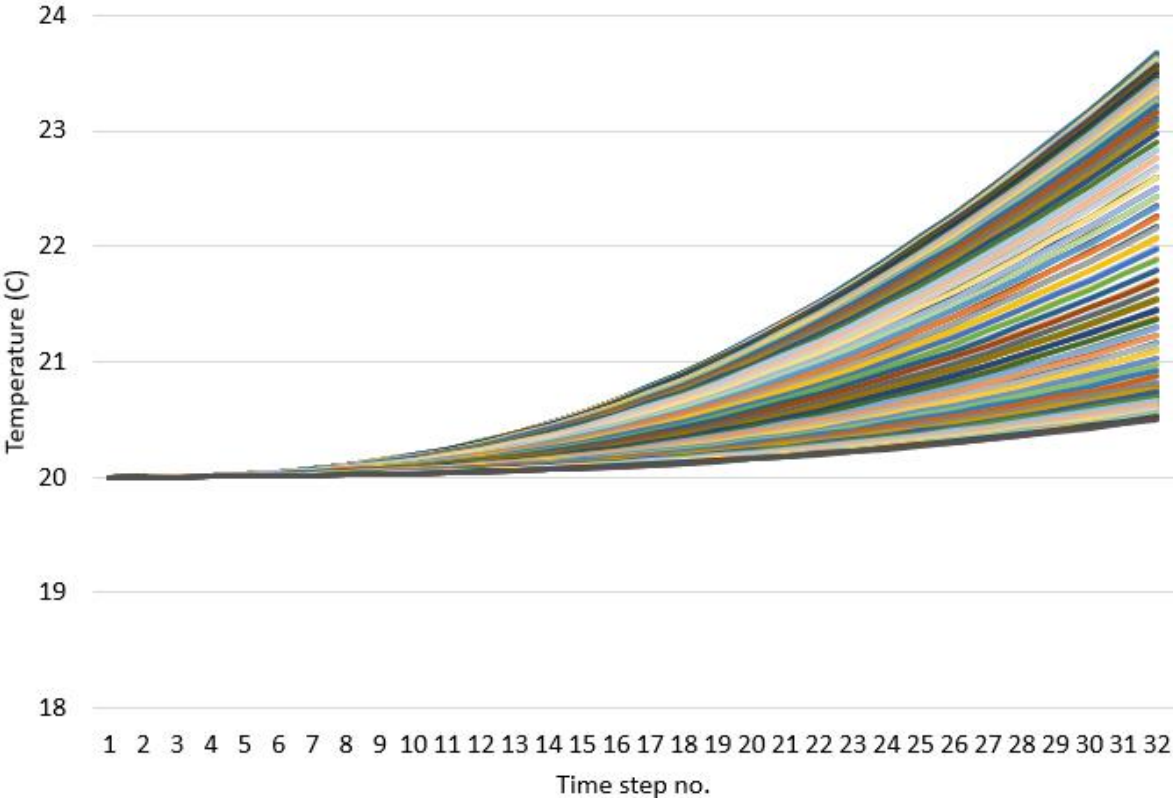


Figure C-12: Nodal temperature over time for X=16mm with PLA

b. Change in width results

i. Width - 10mm

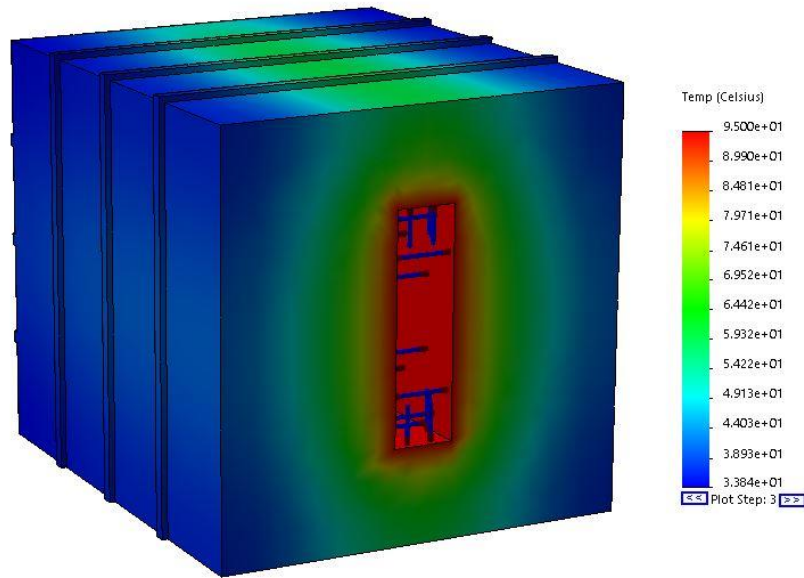


Figure C-13: Thermal distribution at X=10mm

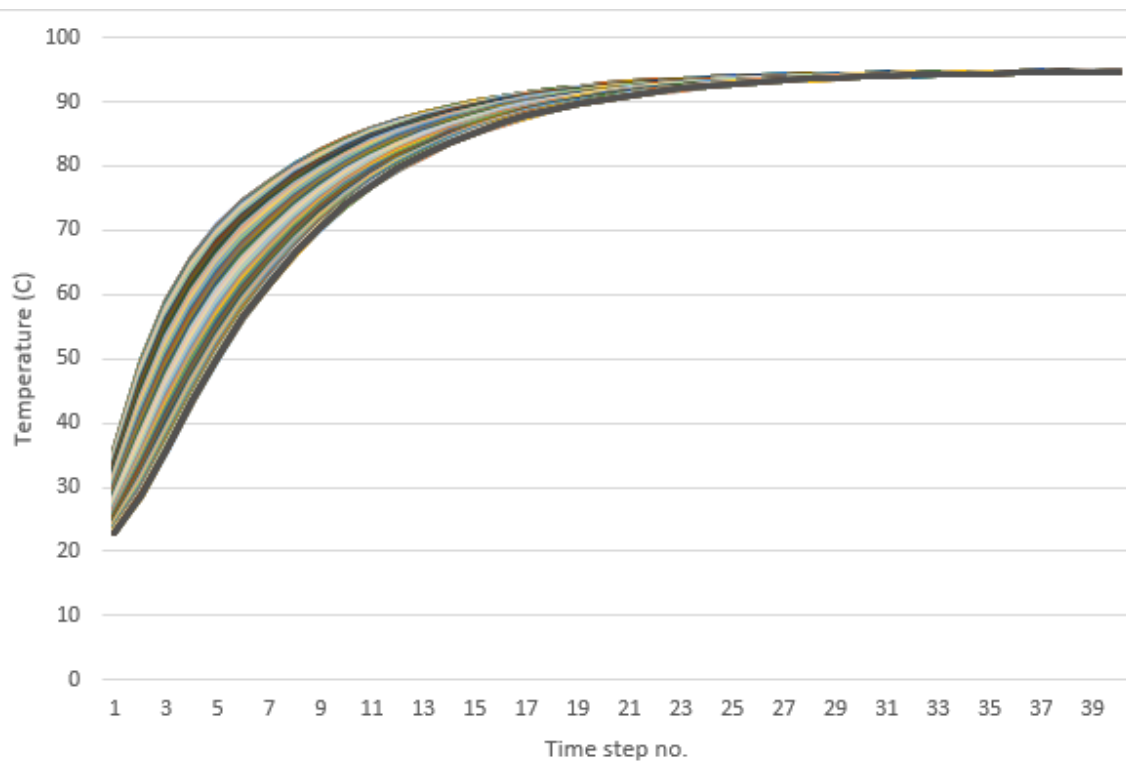


Figure C-14: Nodal temperature over time for X=10mm

ii. Width – 30mm

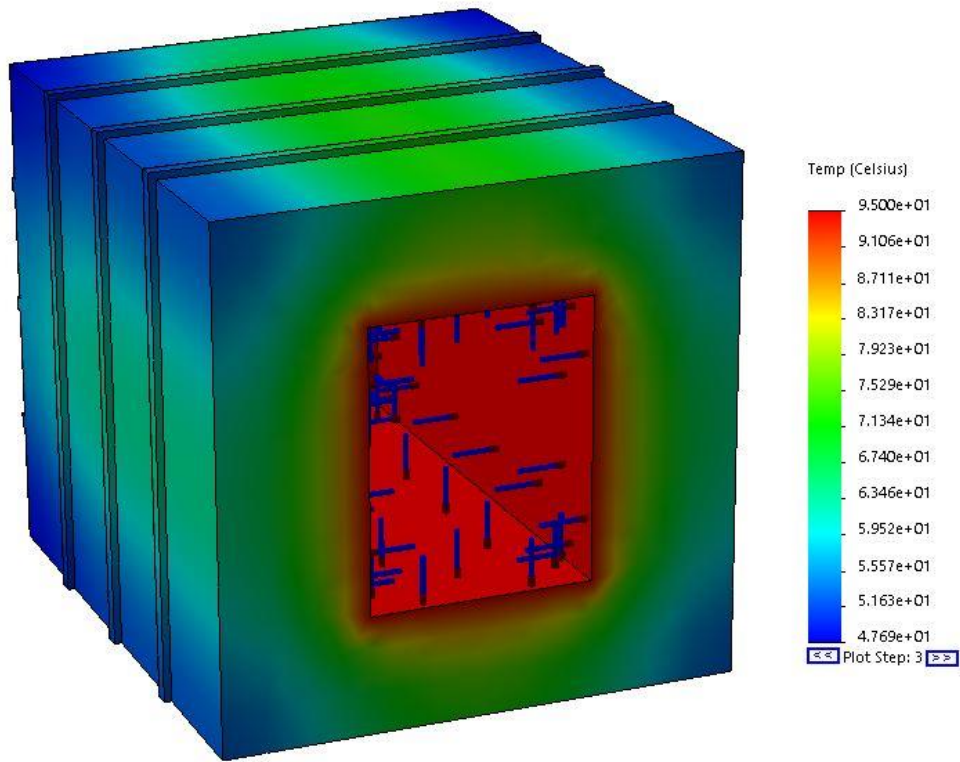


Figure C-15: Thermal distribution at X=30mm

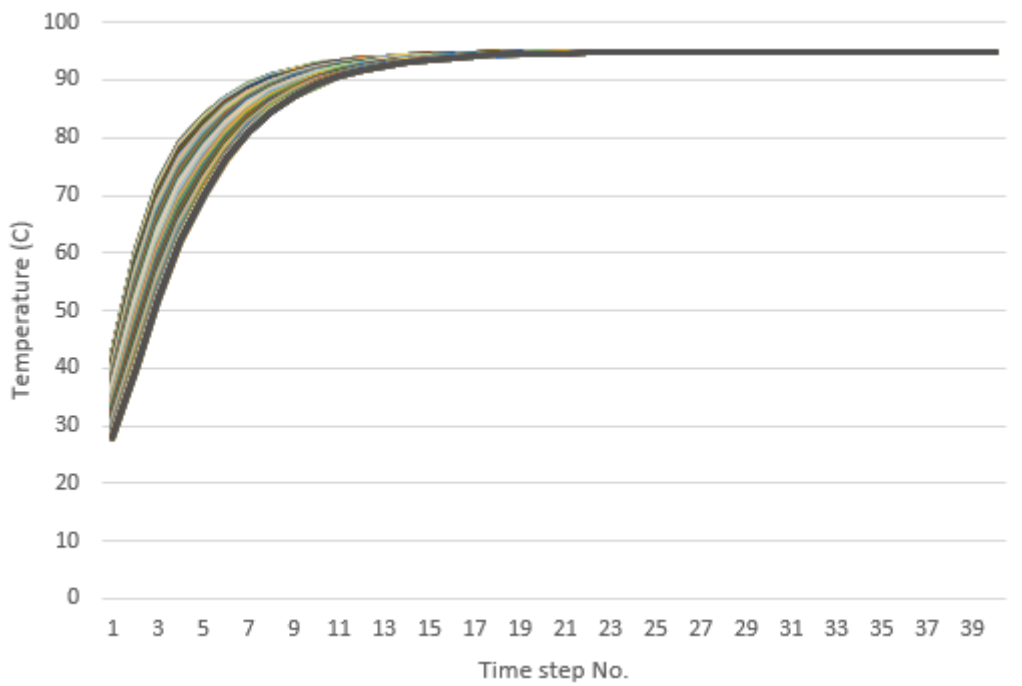


Figure C-16: Nodal temperature over time for X=30mm

iii. Width – 60mm

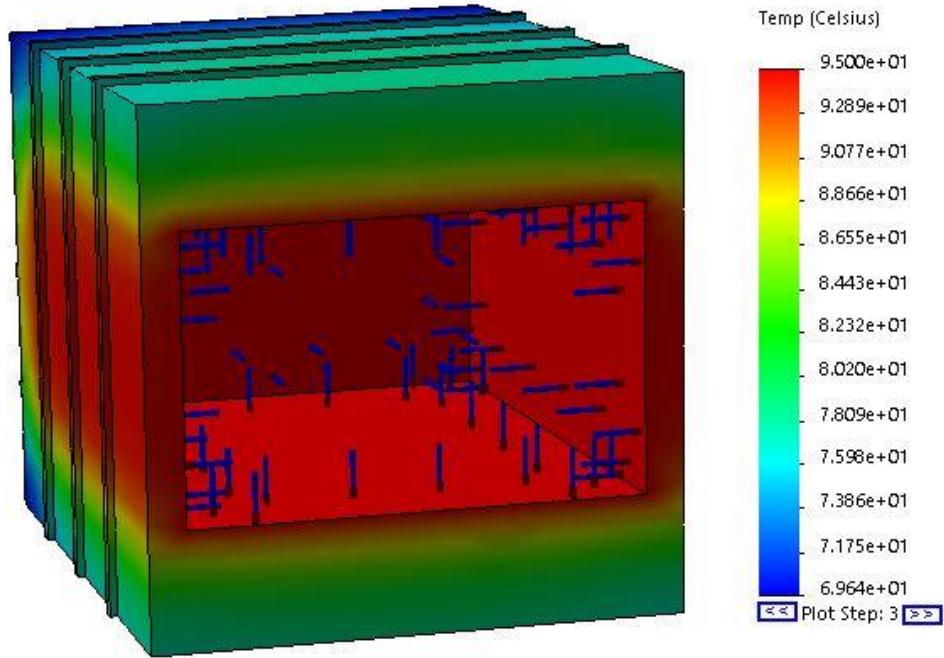


Figure C-17: Thermal distribution at X=60mm

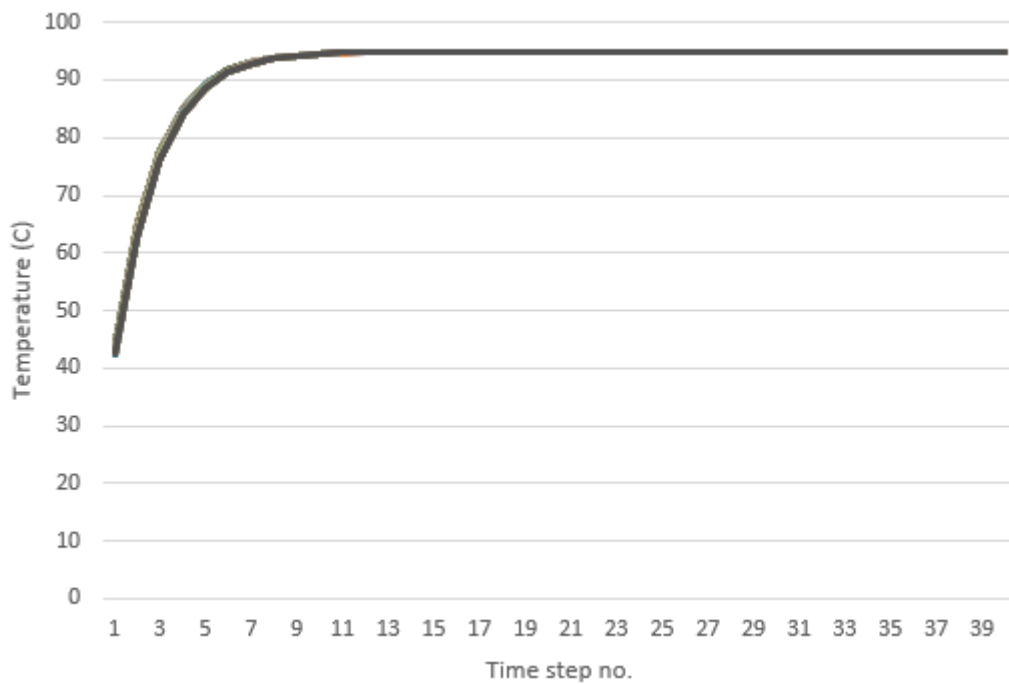


Figure C-18: Nodal temperature over time for X=60mm

c. Change in material results

i. Aluminium

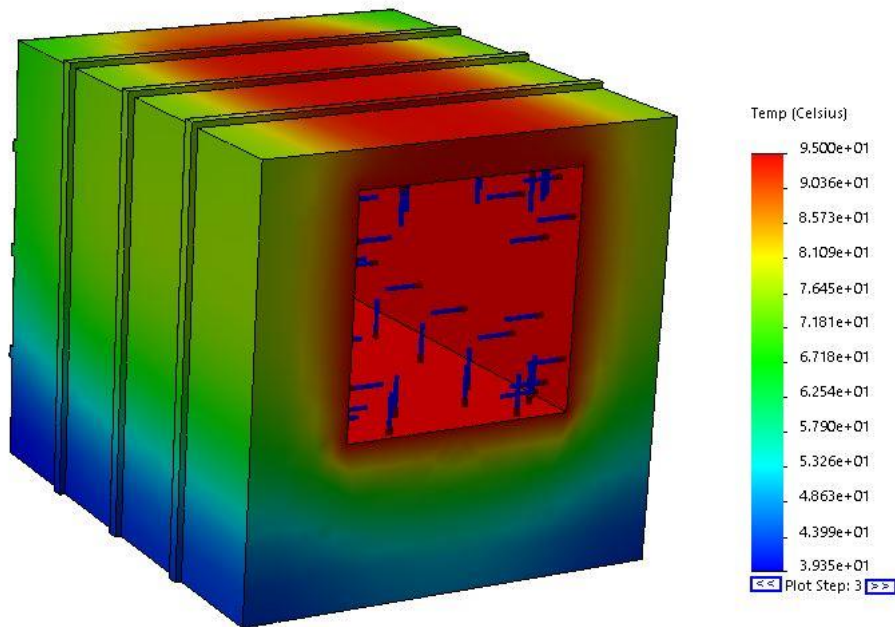


Figure C-19: Thermal distribution of aluminium

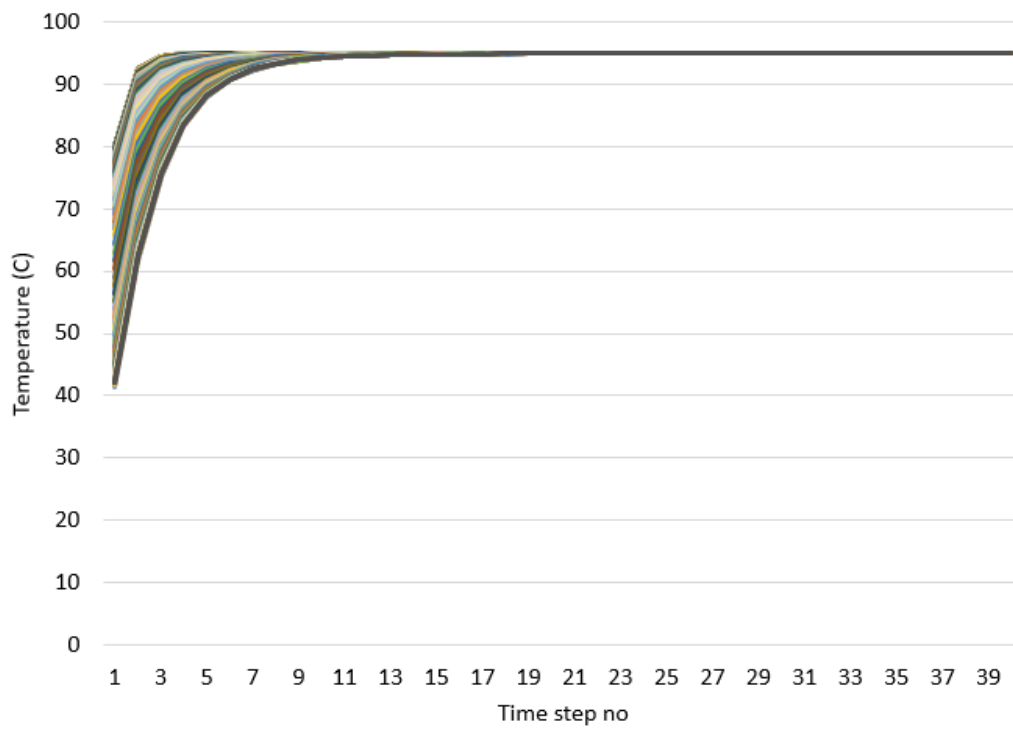


Figure C-20: Nodal temperature of aluminium over time

ii. Copper

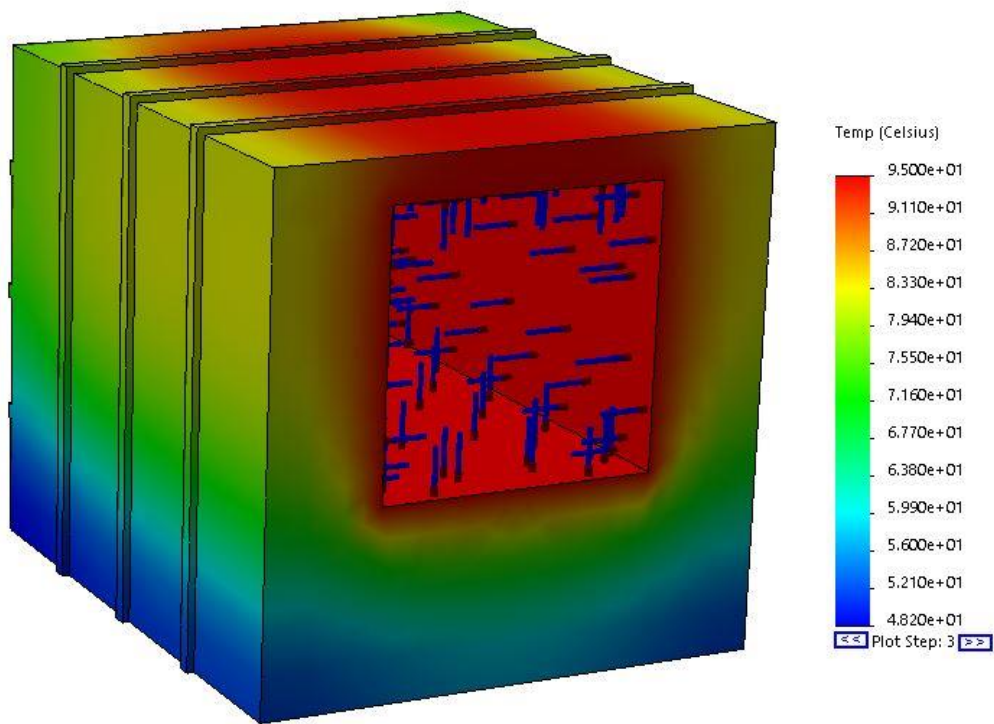


Figure C-21: Thermal distribution of copper

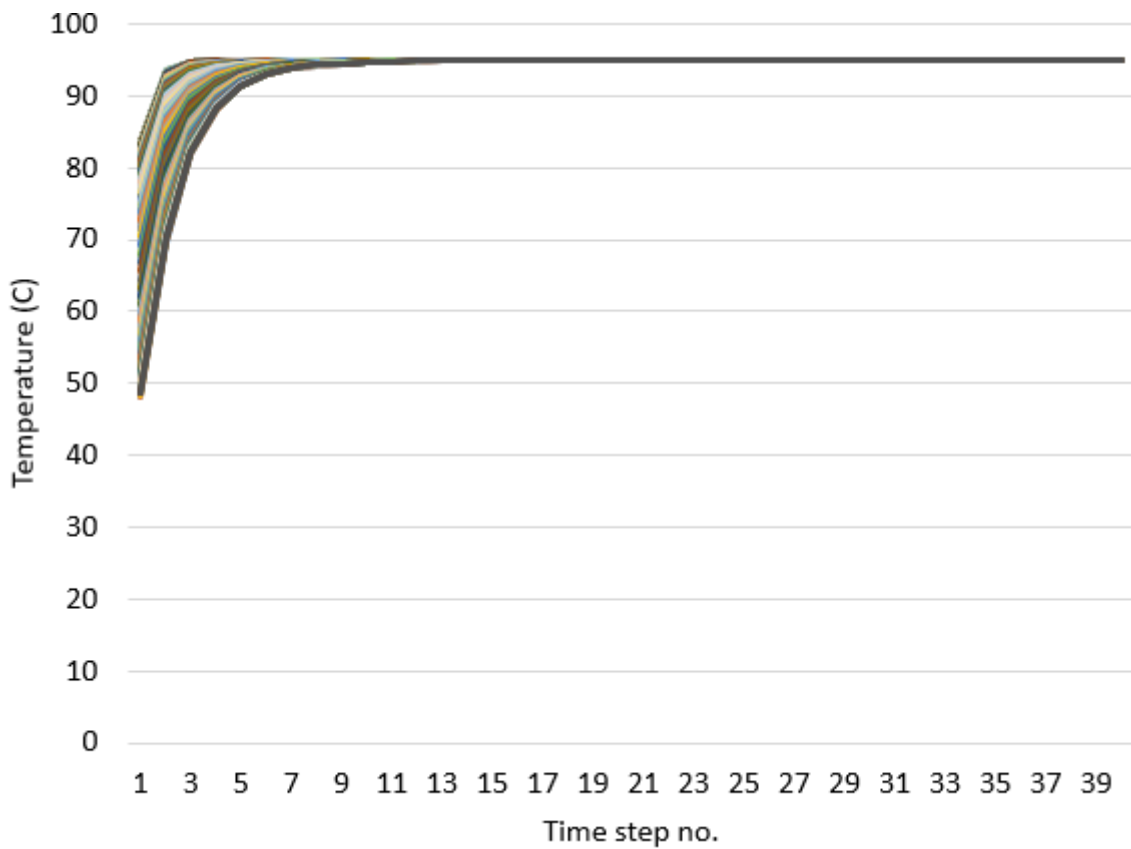


Figure C-22: Nodal temperature of copper over time

iii. Ceramic

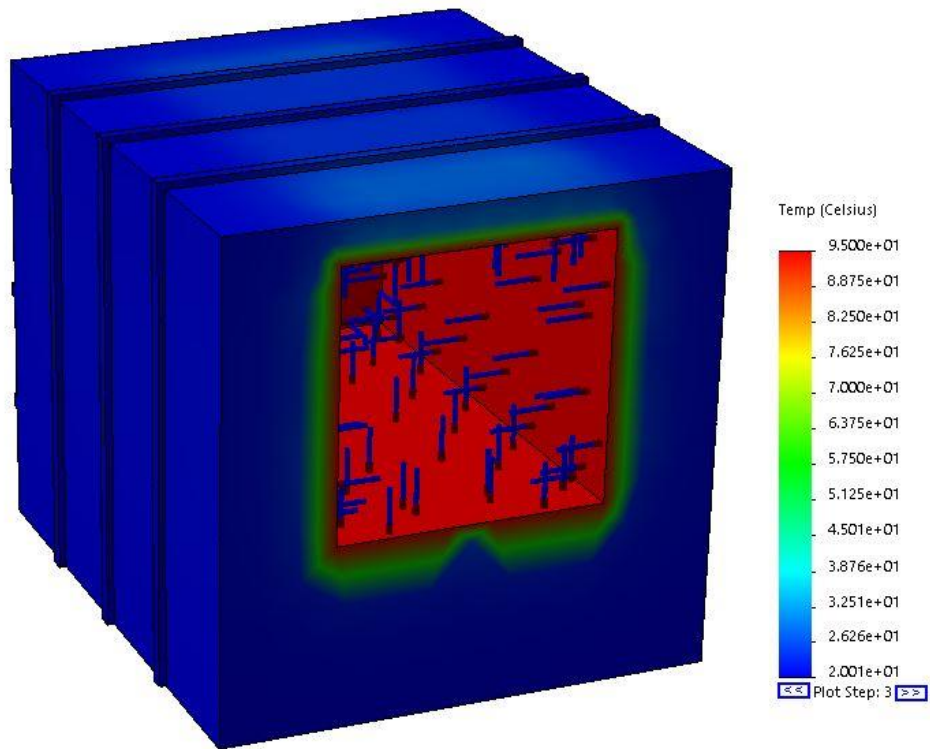


Figure C-23: Thermal distribution of ceramic

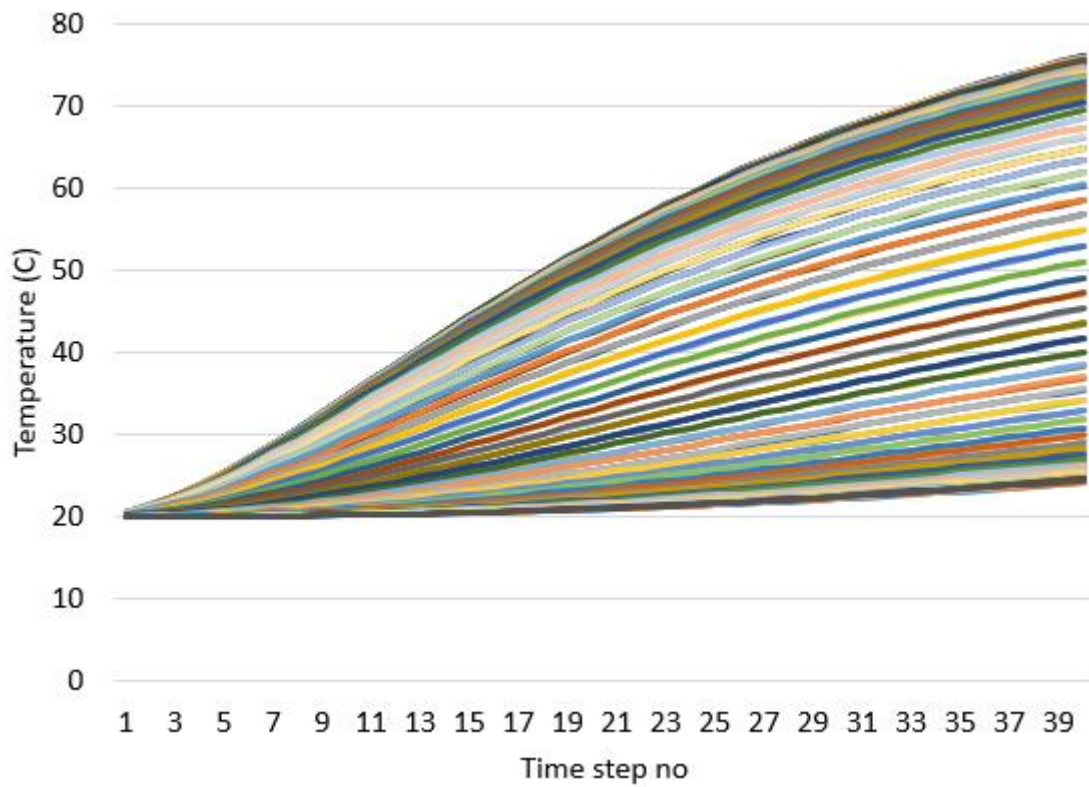


Figure C-24: Nodal temperature of ceramic over time

iv. Nylon

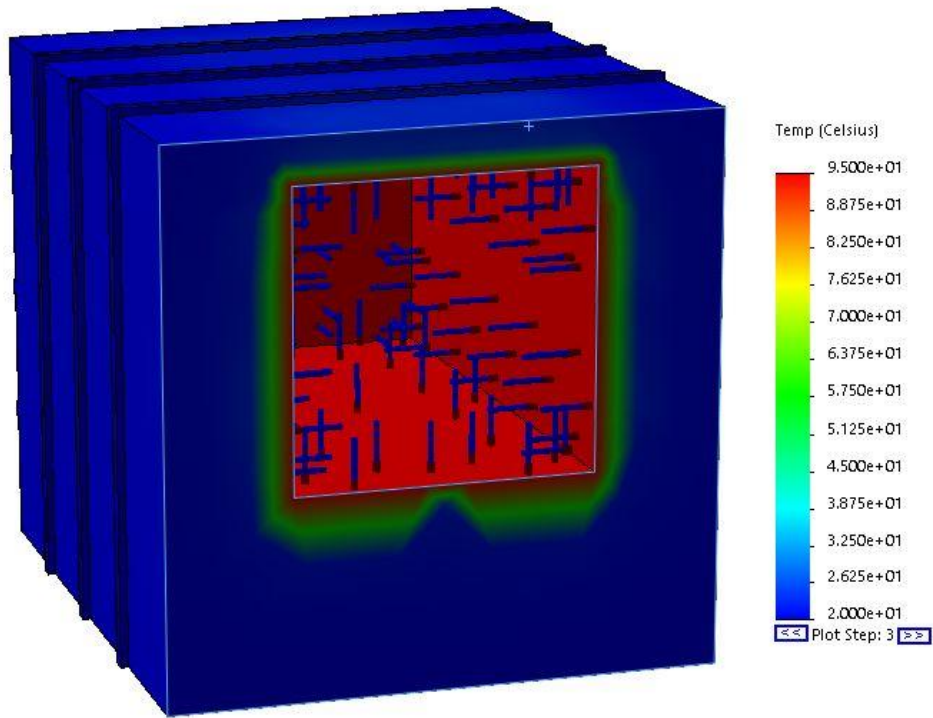


Figure C-25: Thermal distribution of nylon

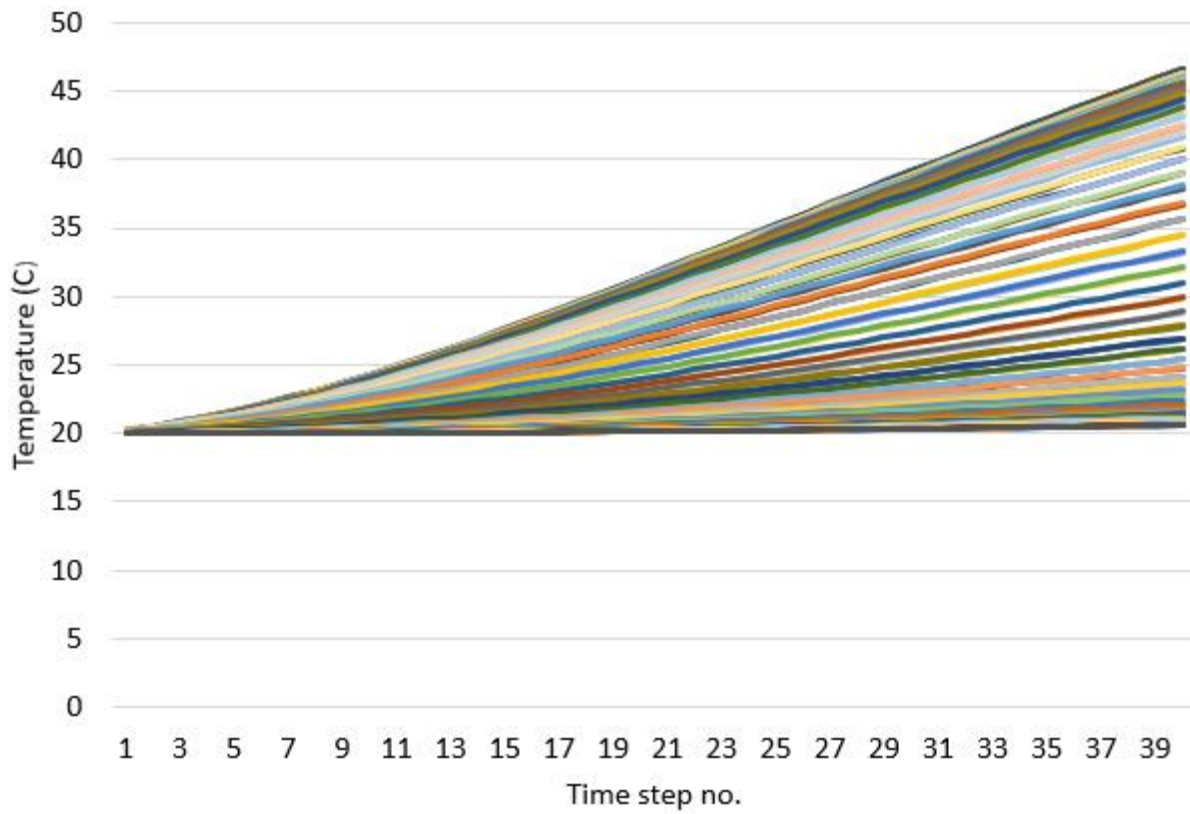


Figure C-26: Nodal temperature of nylon over time

v. PLA

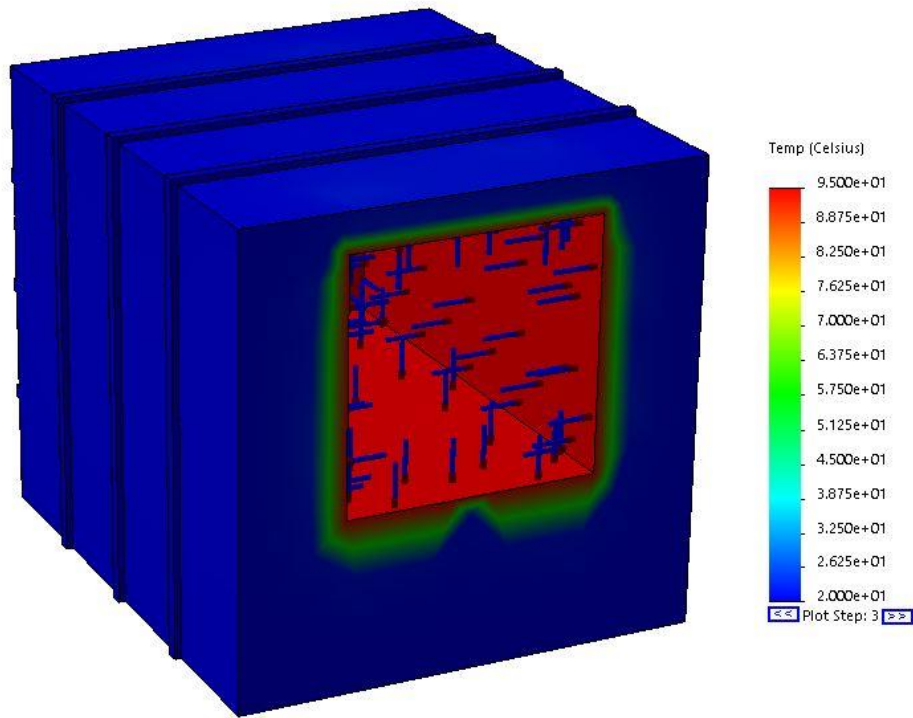


Figure C-27: Thermal distribution of PLA

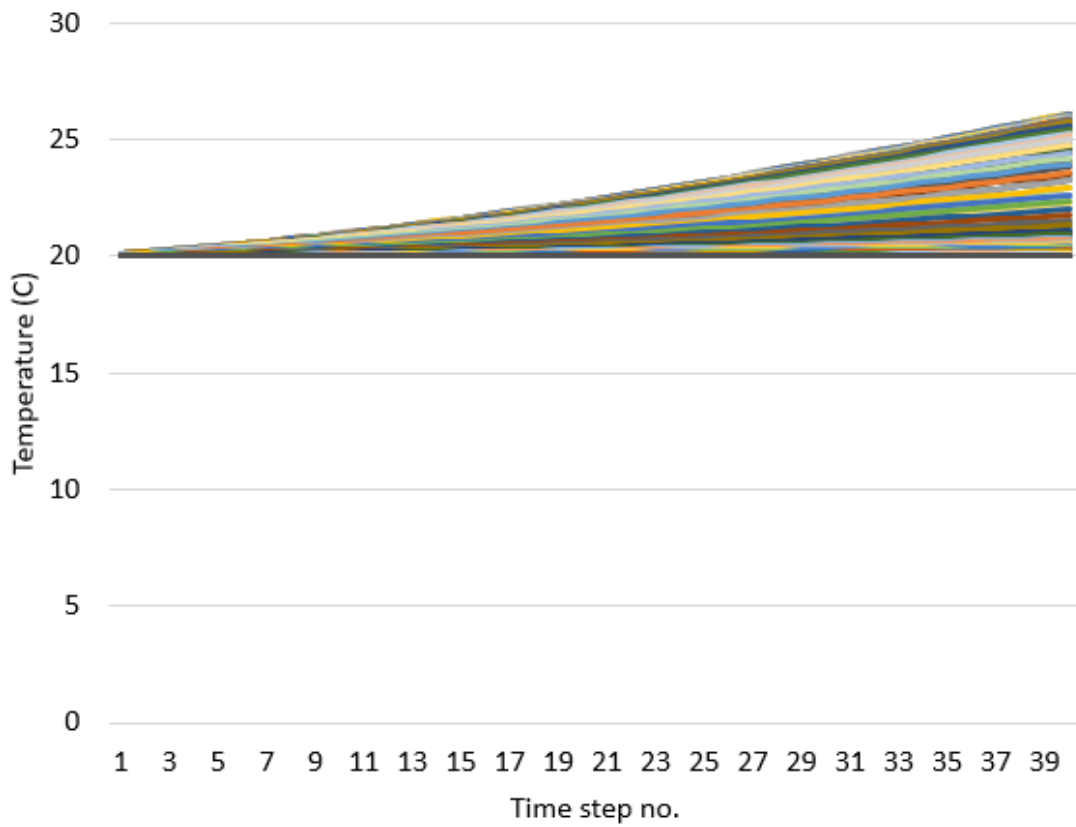


Figure C-28: Nodal temperature of PLA over time

vi. Steel

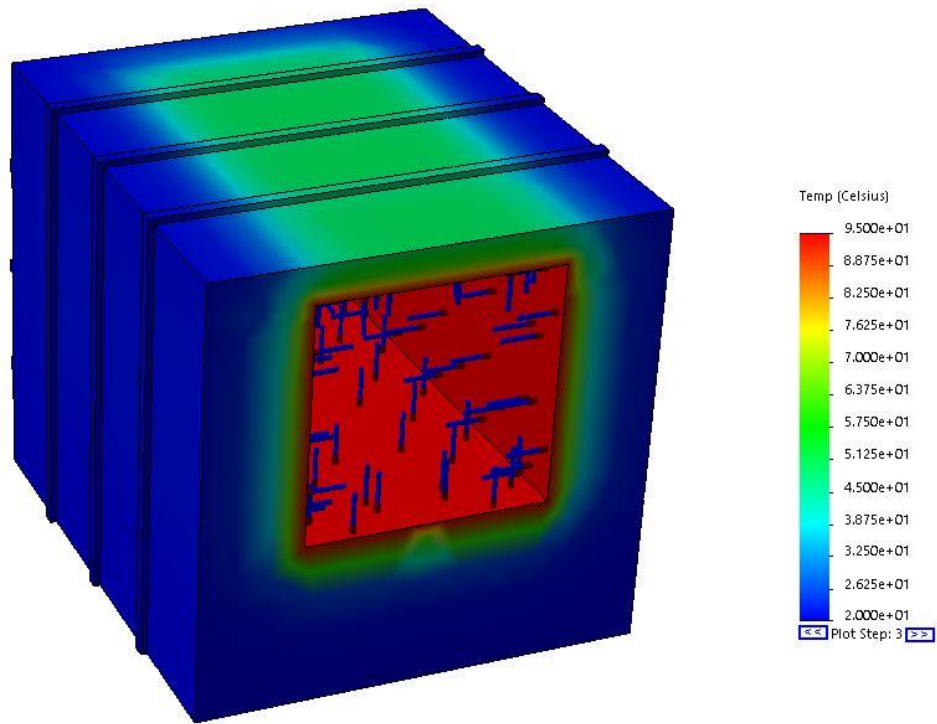


Figure C-29: Thermal distribution of steel

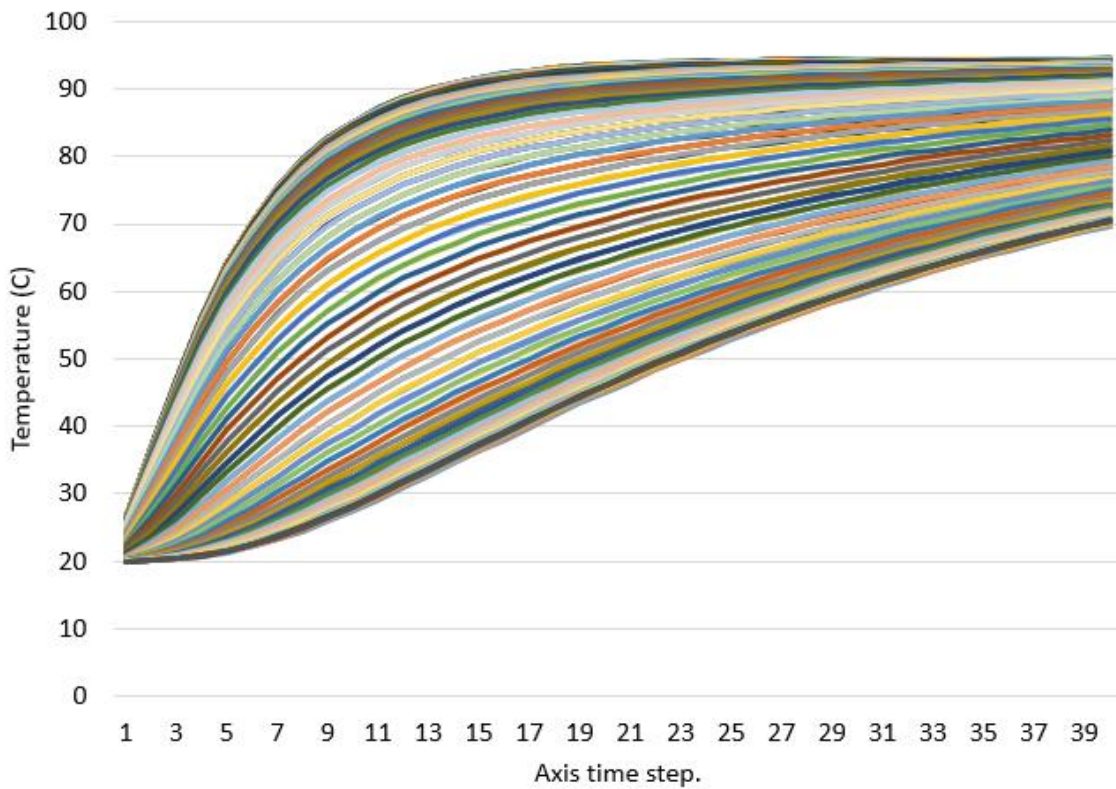


Figure C-30: Nodal temperature of steel over time

d. Edge position differences for difference profiles

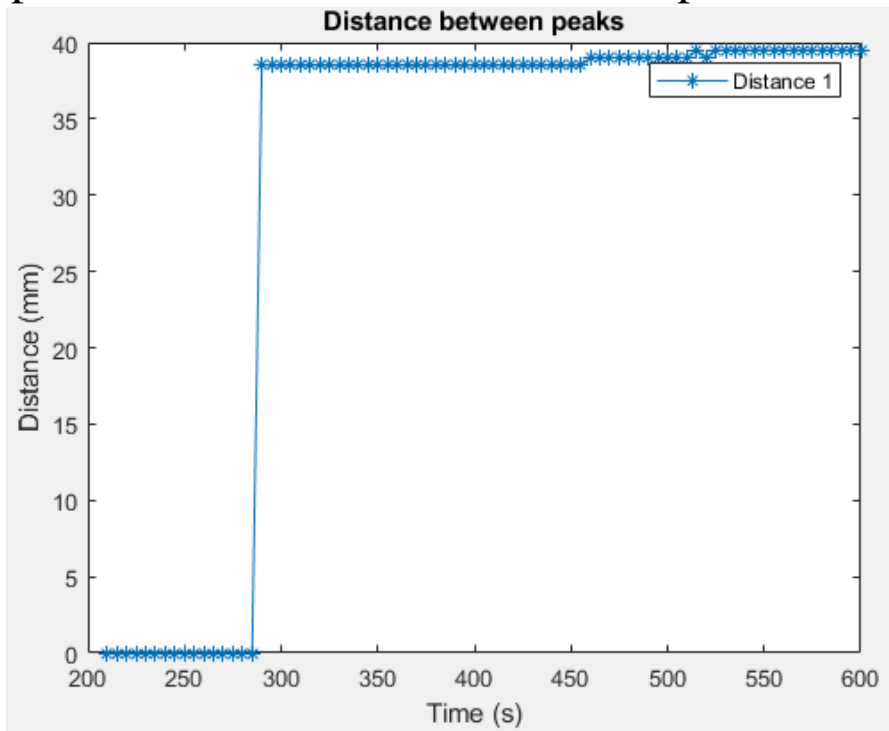


Figure C-31: Parallel planar - difference between peaks

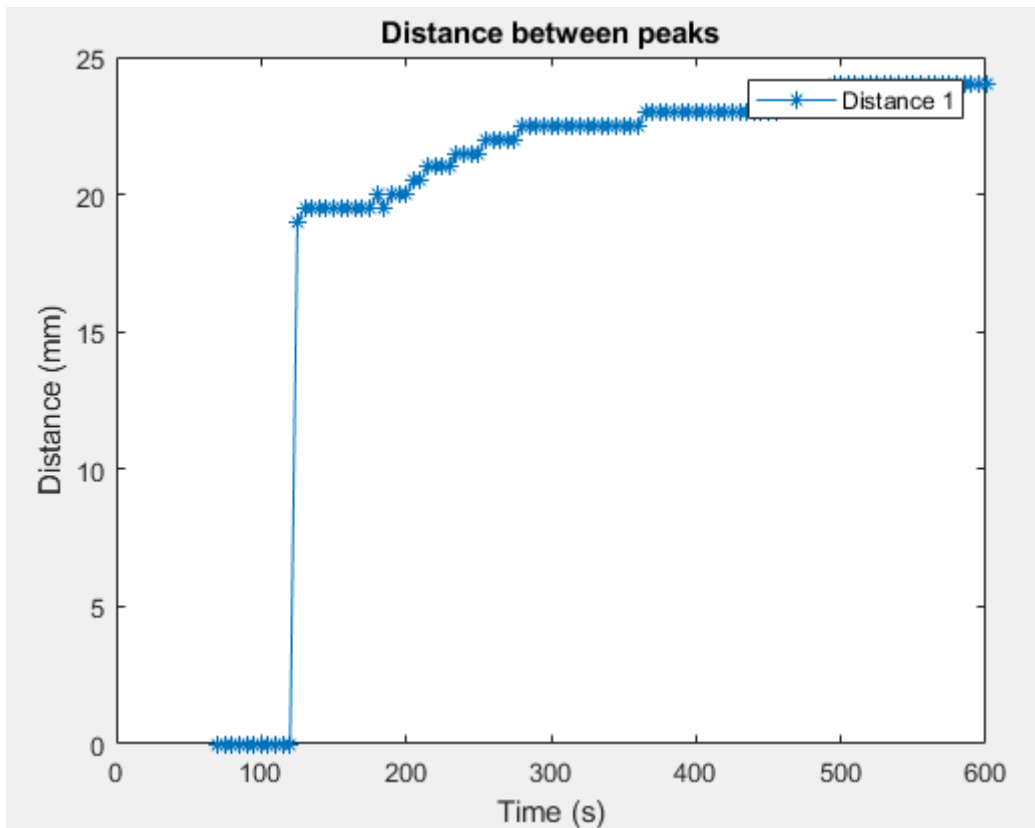


Figure C-32: Circular - difference between peaks

15.5	55	20.5	48.5	27	43.5
15.5	55	20.5	48.5	27	44
15.5	55	20.5	48.5	27	44
15.5	55	20.5	48.5	27	44
15.5	55	20.5	49	27	44
15.5	55	20.5	49	26.5	44
15.5	55	20.5	49	26.5	44
15.5	55	20.5	49	26.5	44

e. External heating results

i. 20mm cavity width

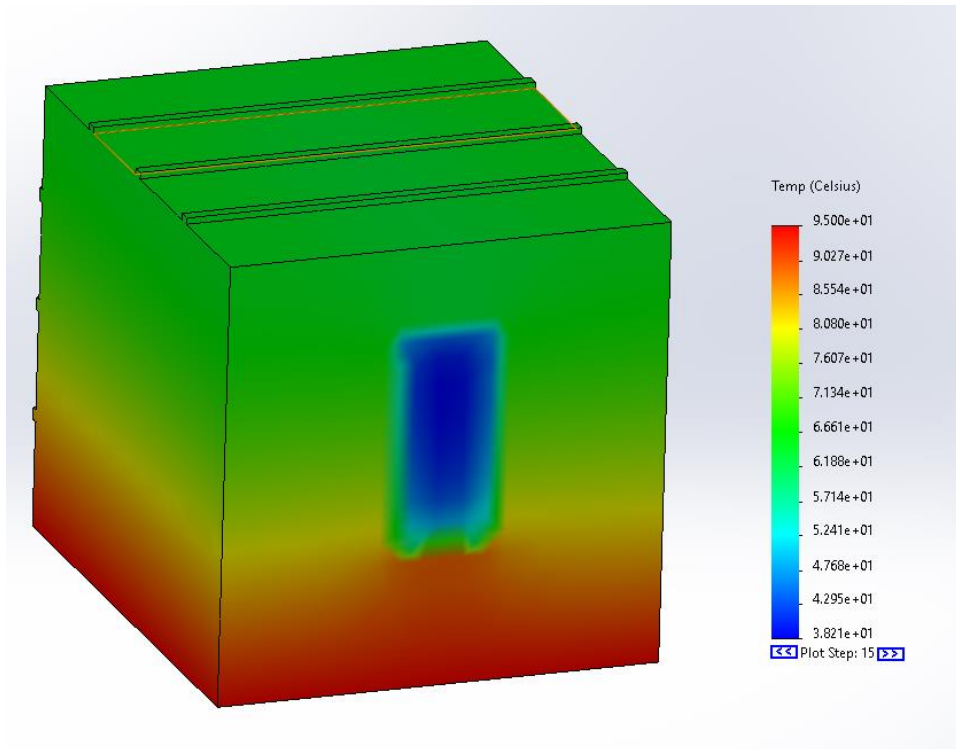


Figure C-34: Side heating thermal distribution 20mm cavity width

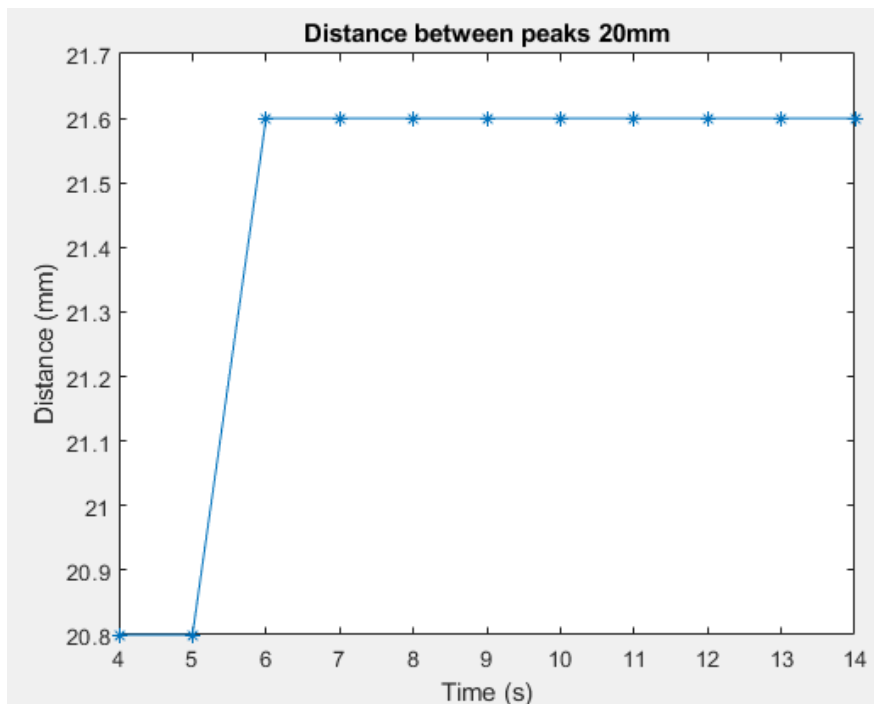


Figure C-35: 20mm internal edge position results

ii. 25mm cavity width

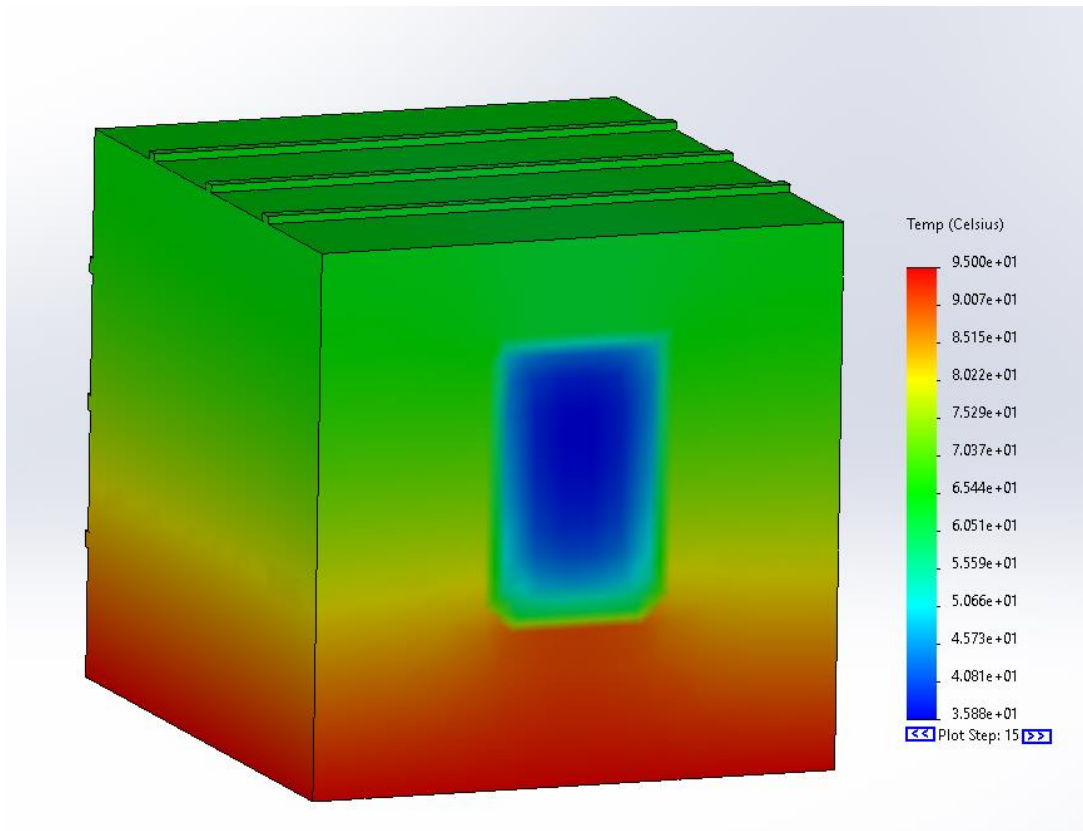


Figure C-36: Side heating thermal distribution 25mm cavity width

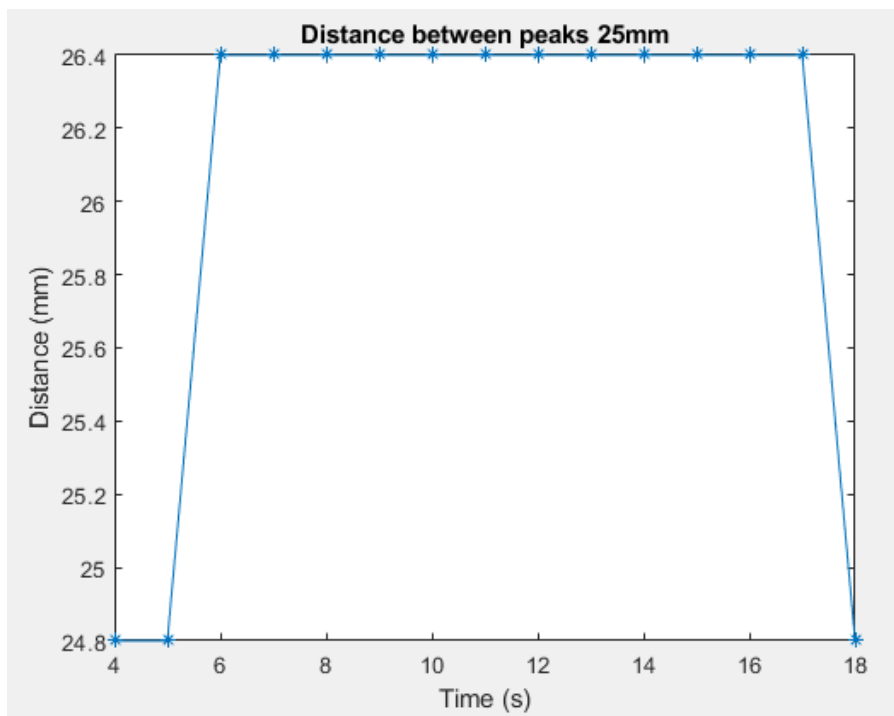


Figure C-37: 25mm internal edge position results

iii. 30mm cavity width

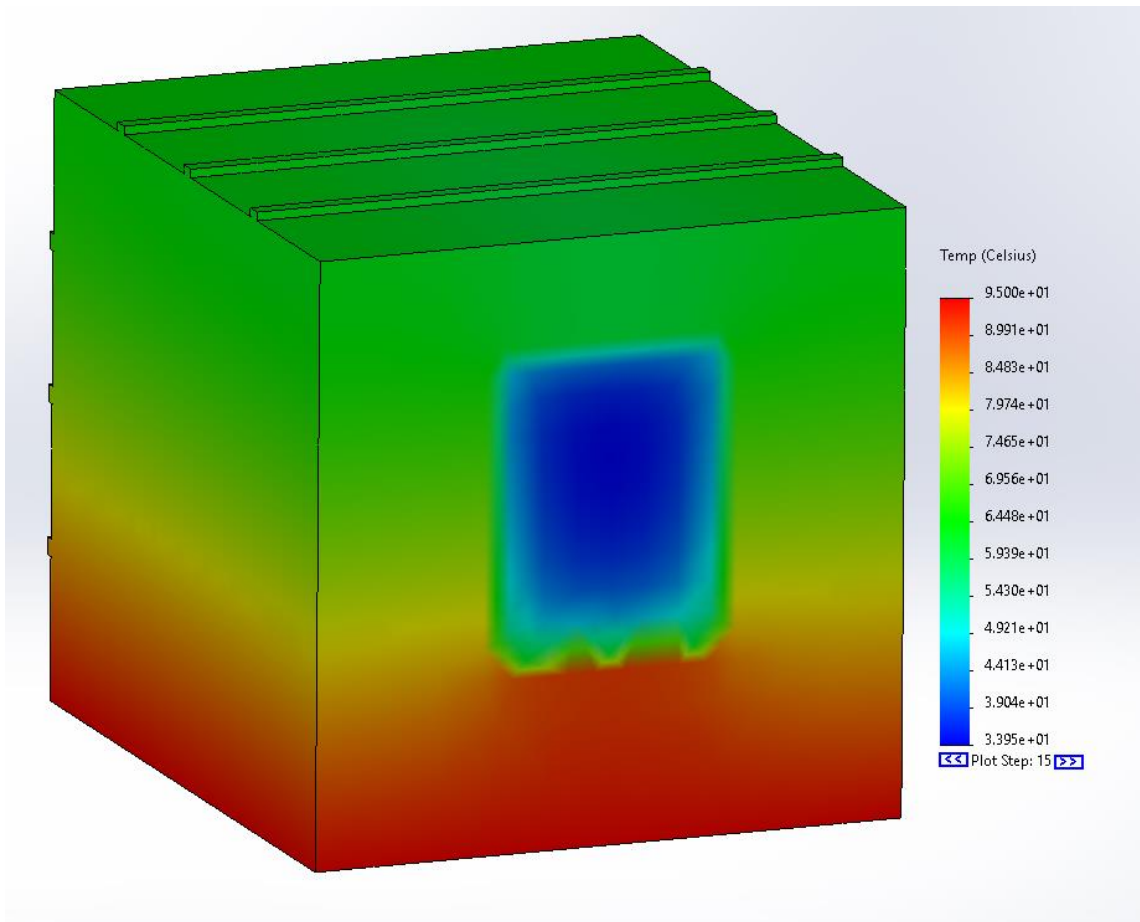


Figure C-38: Side heating thermal distribution 30mm cavity width

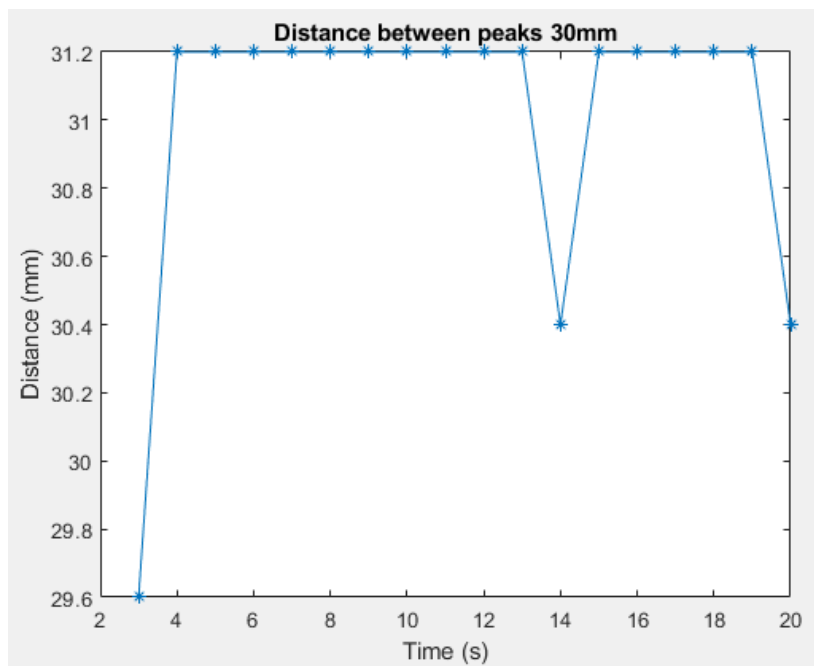


Figure C-39: 30mm internal edge position results

iv. 35mm cavity width

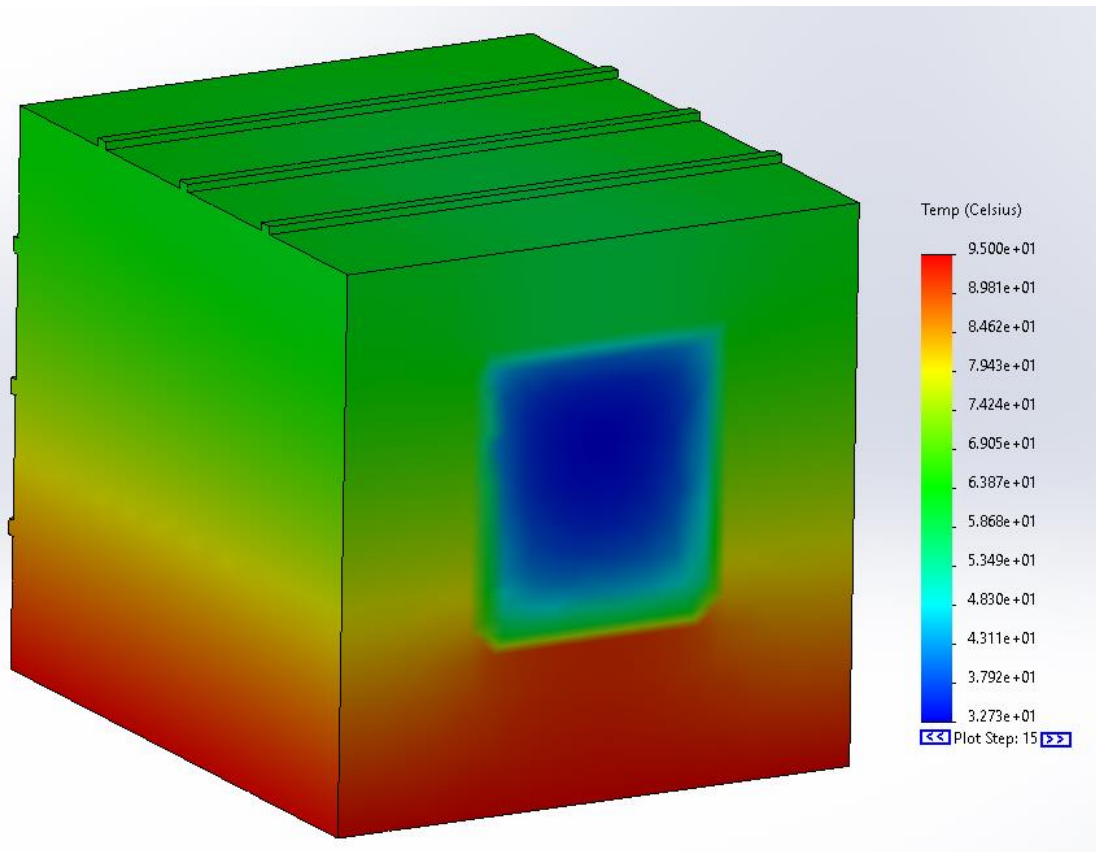


Figure C-40: Side heating thermal distribution 35mm cavity width

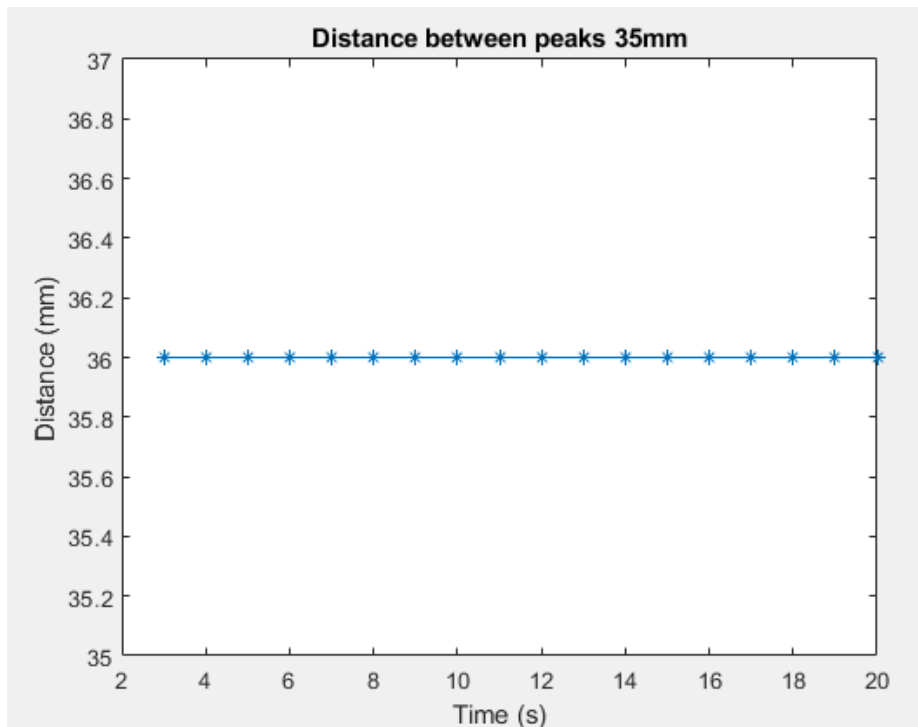


Figure C-41: 35mm internal edge position results

v. 40mm cavity width

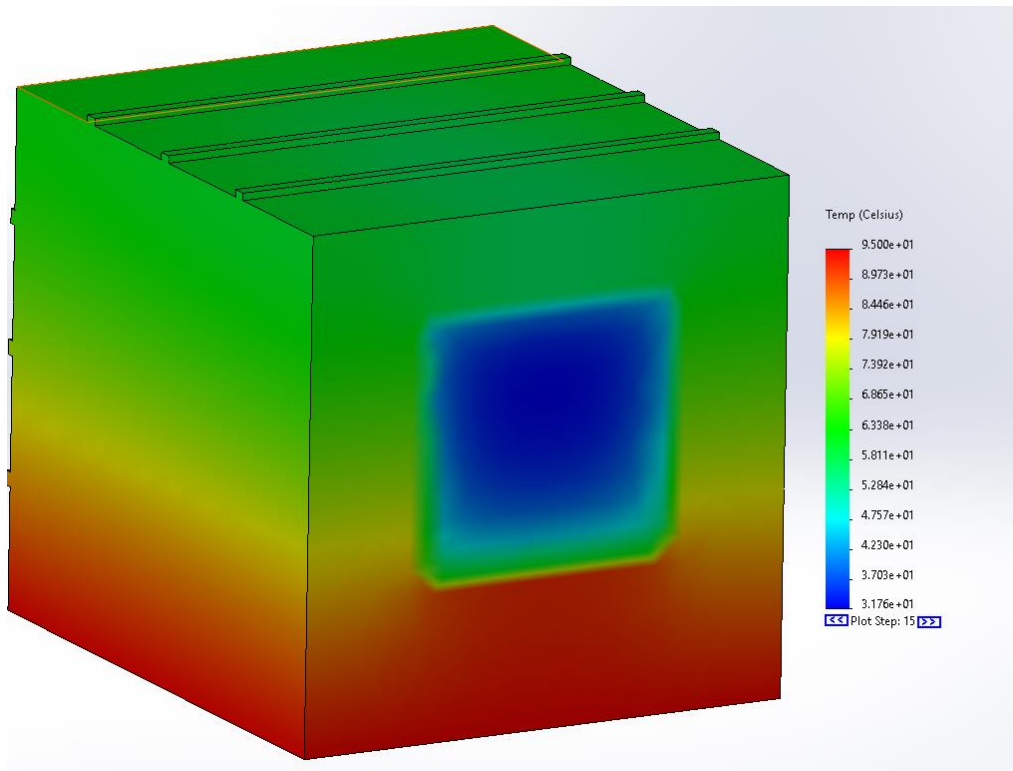


Figure C-42: Side heating thermal distribution 40mm cavity width

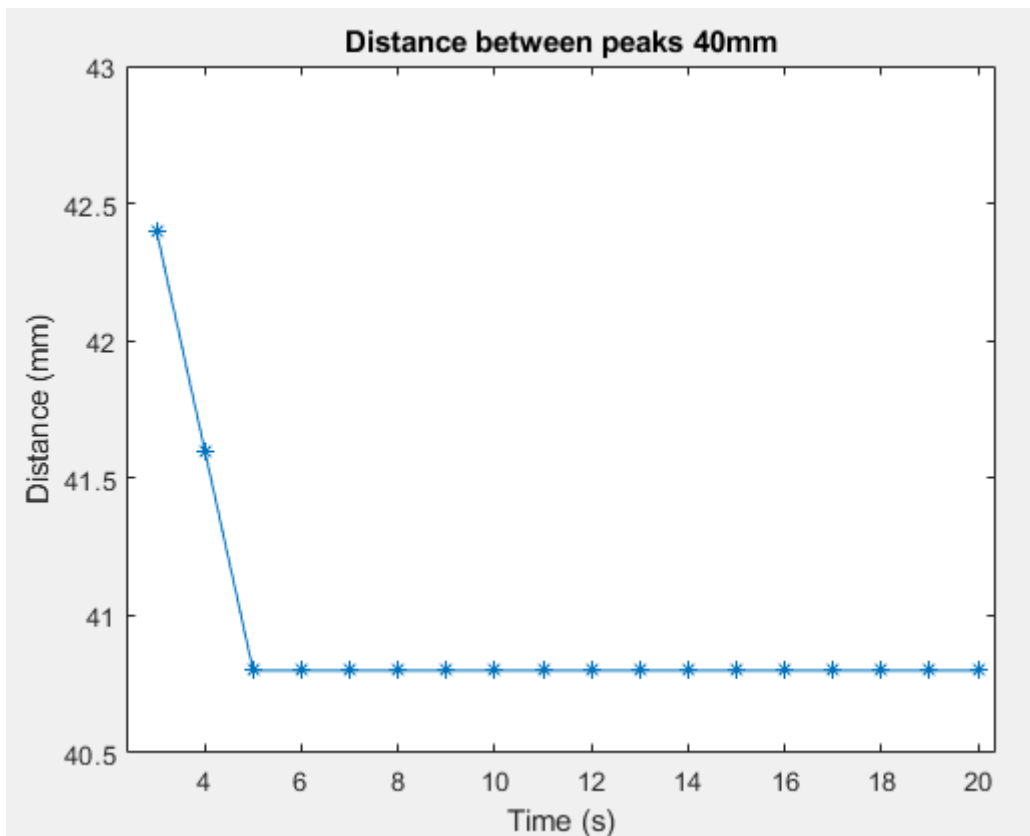


Figure C-43: 40mm internal edge position results

vi. 45mm cavity width

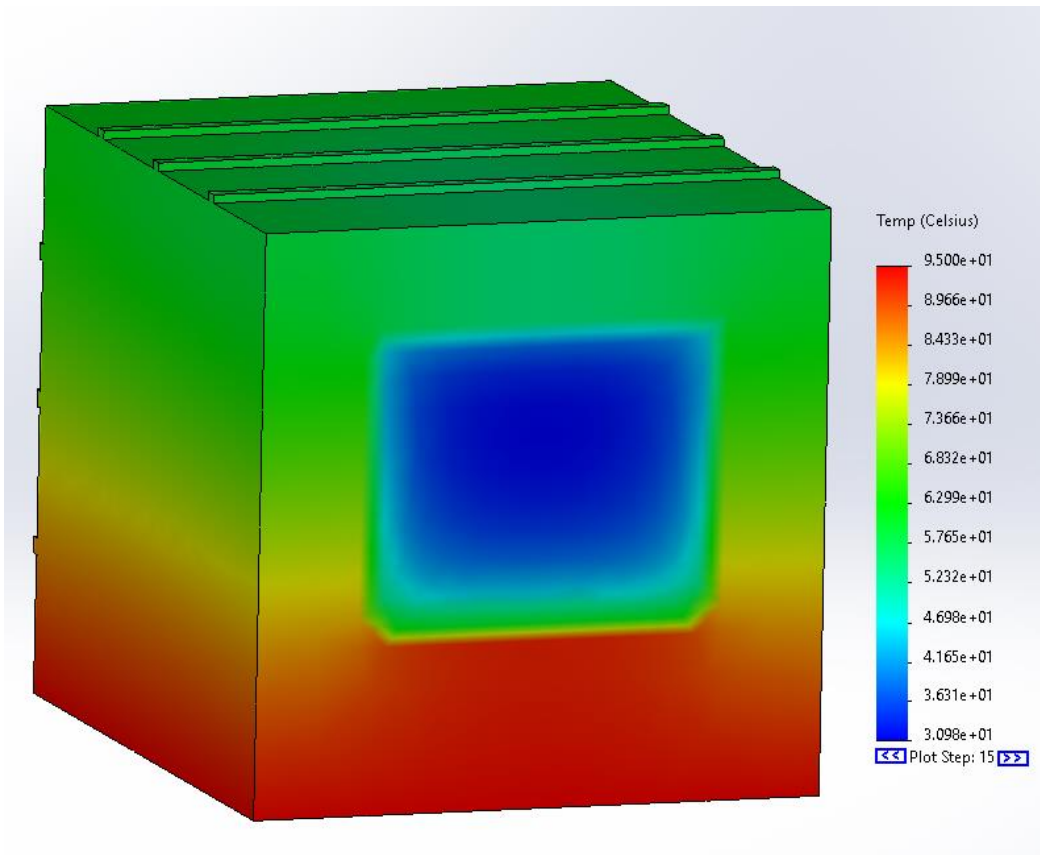


Figure C-44: Side heating thermal distribution 45mm cavity width

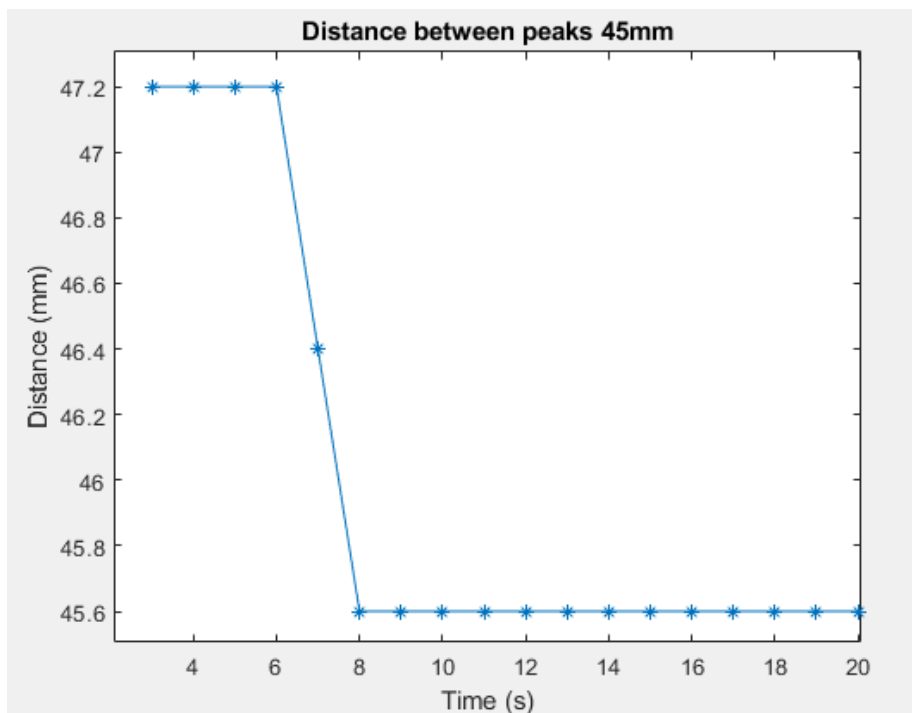


Figure C-45: 45mm internal edge position results

vii. 50mm cavity width

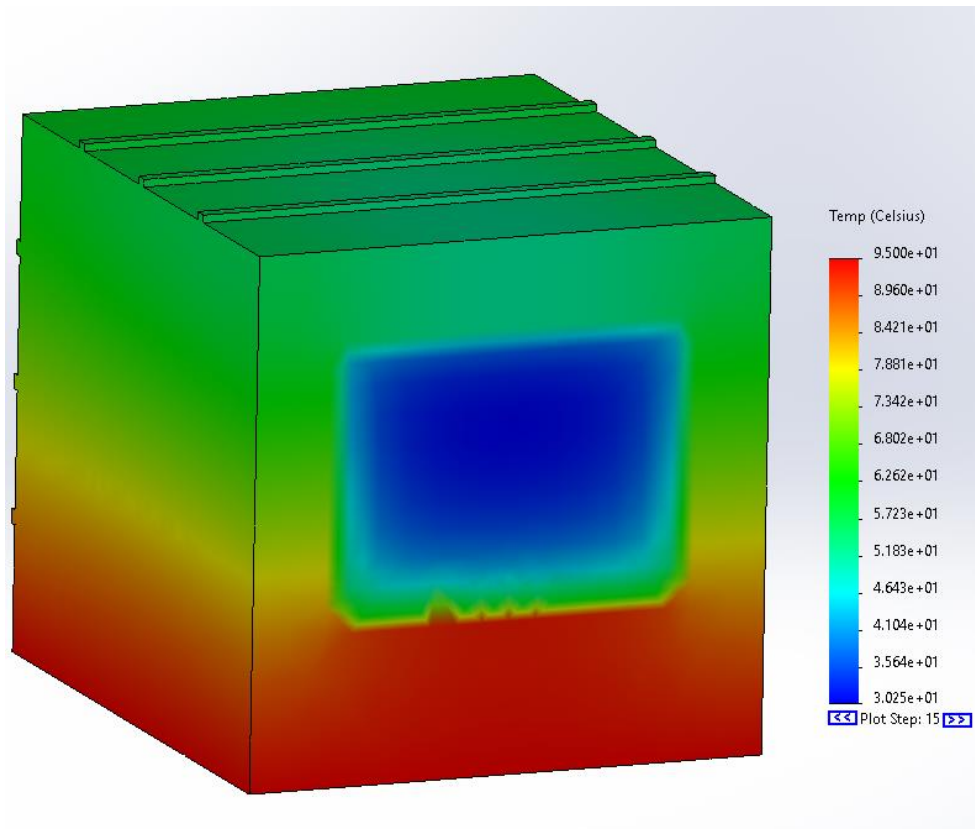


Figure C-46: Side heating thermal distribution 50mm cavity width

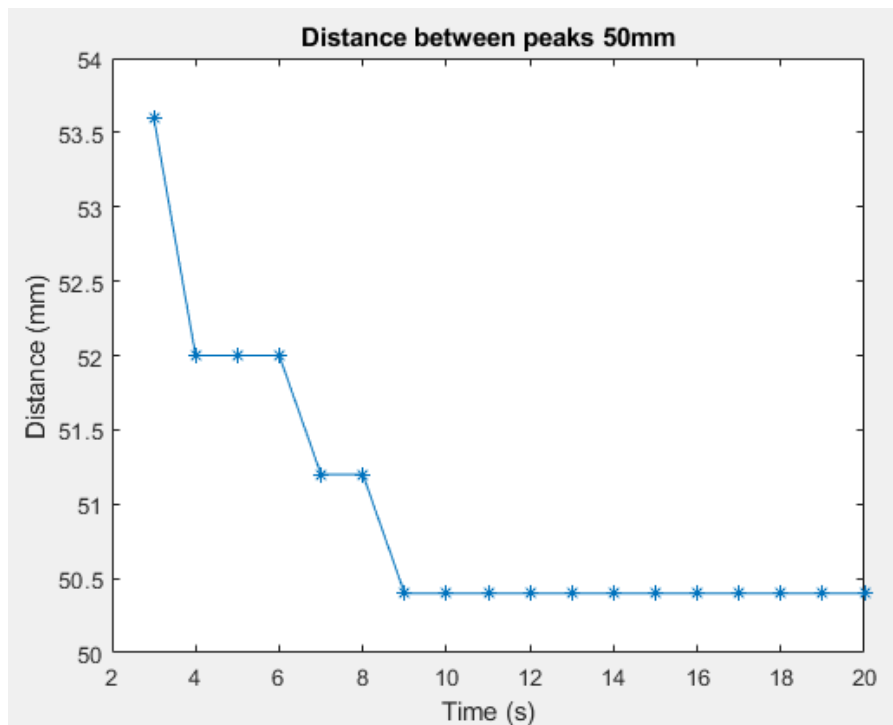


Figure C-47: 50mm internal edge position results

viii. 55mm cavity width

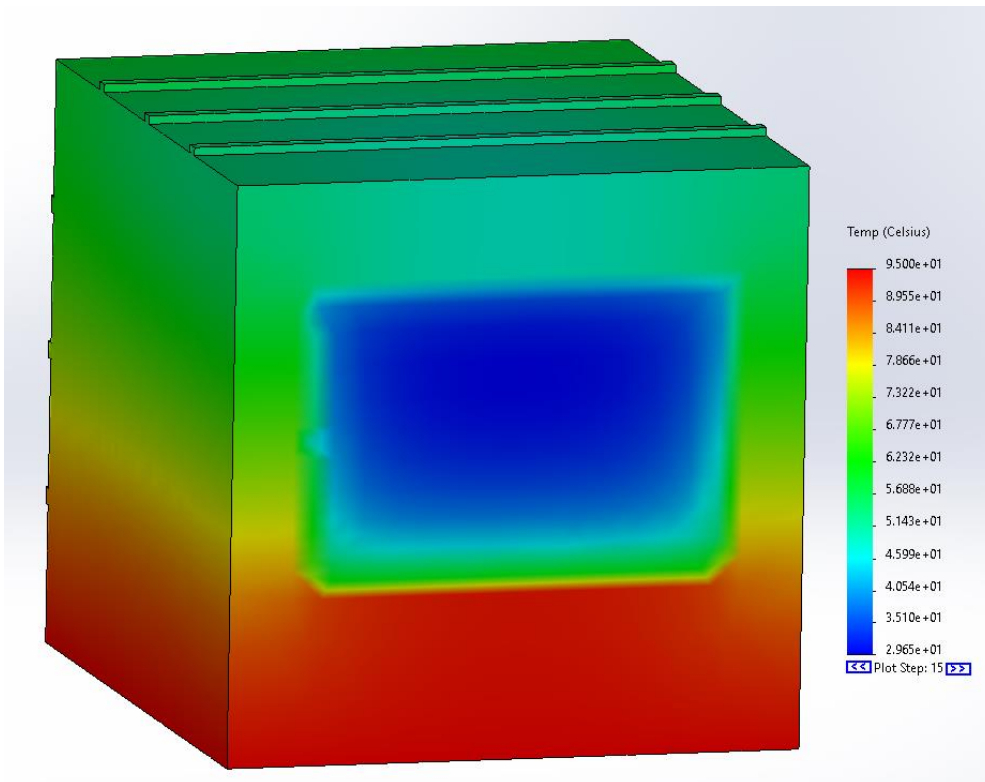


Figure C-48: Side heating thermal distribution 55mm cavity width

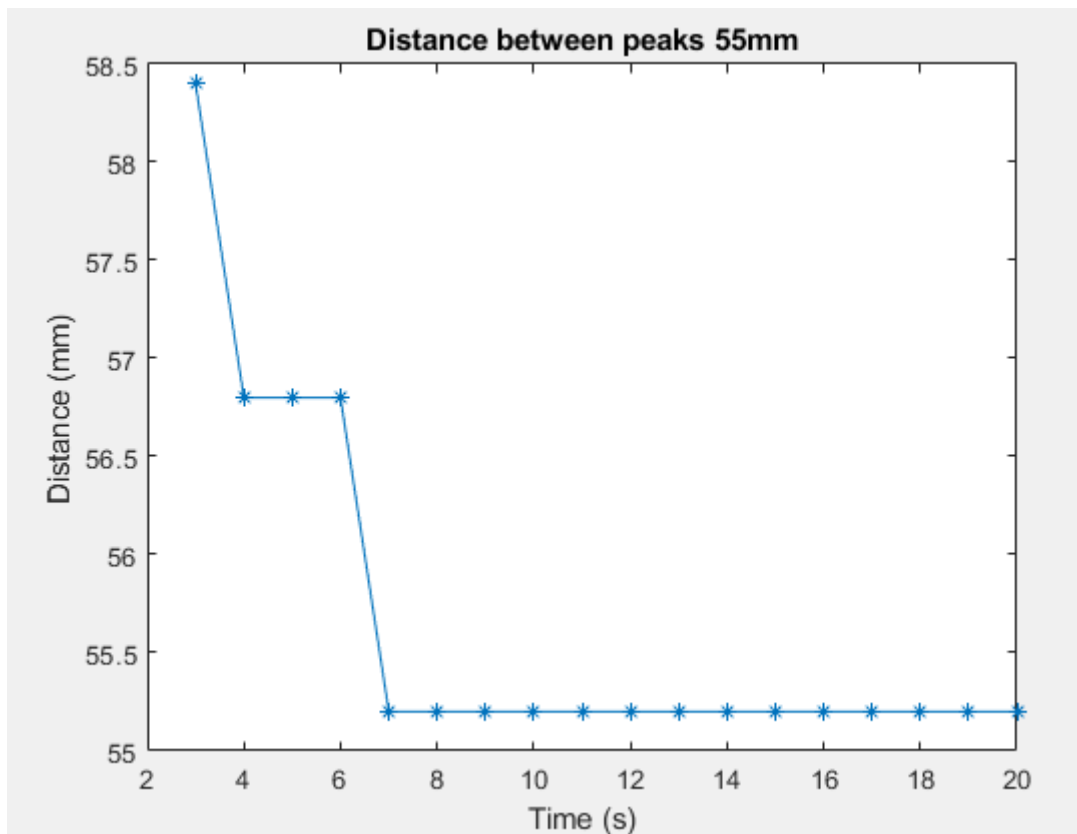


Figure C-49: 55mm internal edge position results

ix. 60mm cavity width

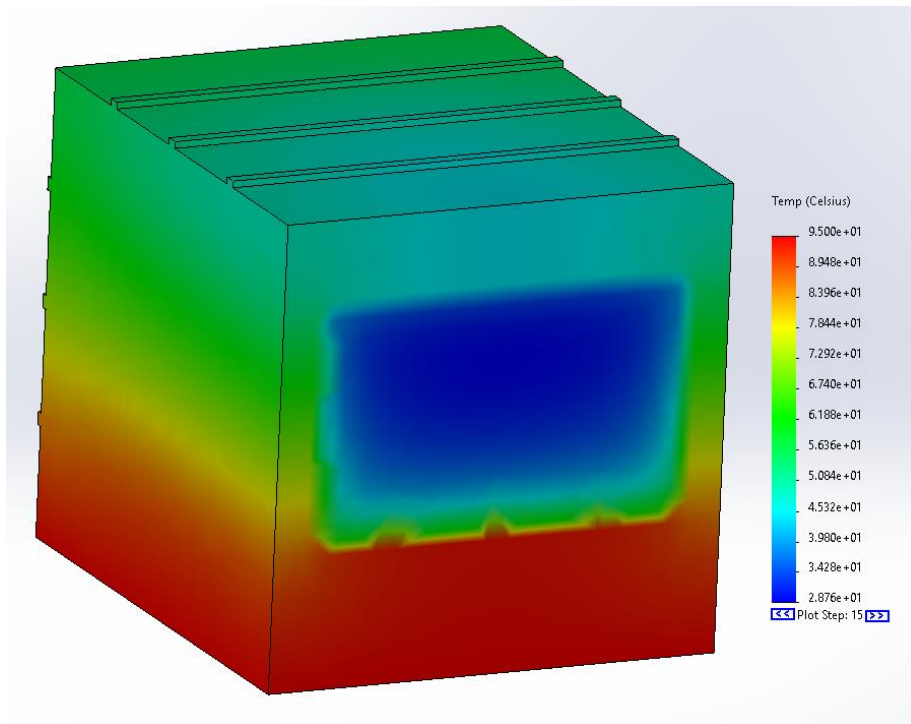


Figure C-50: Side heating thermal distribution 60mm cavity width

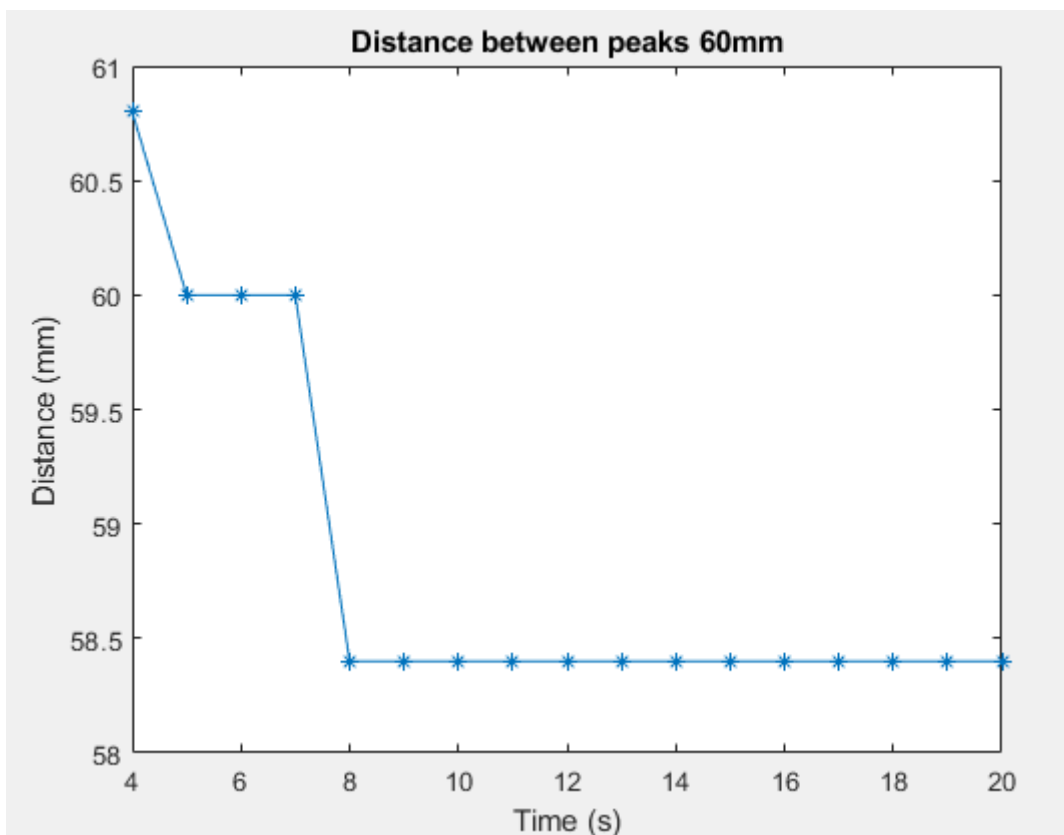


Figure C-51: 60mm internal edge position results

x. PLA $t=1200s$

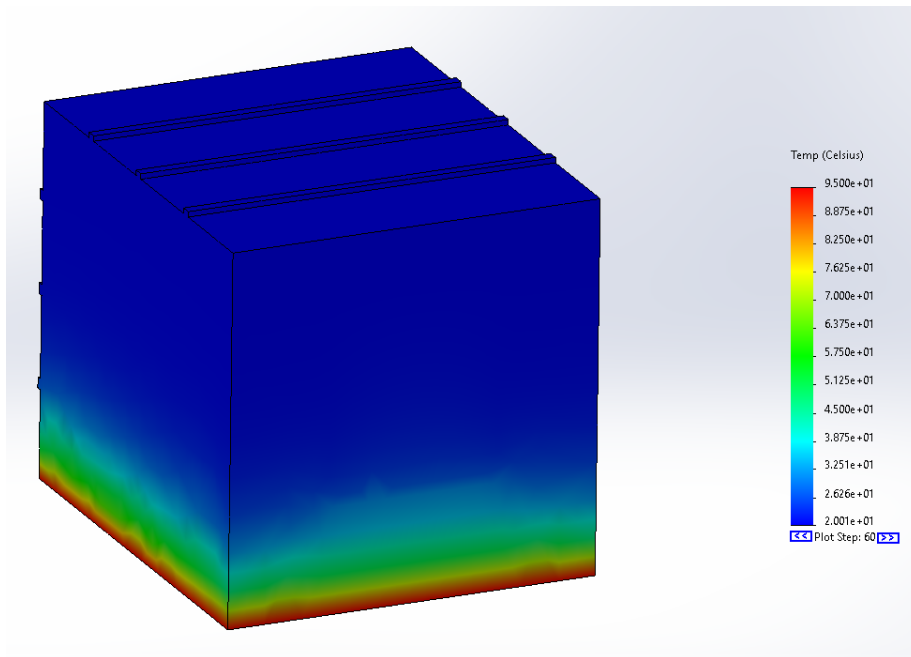


Figure C-52: Thermal distribution, external heating, PLA, $t=1200s$

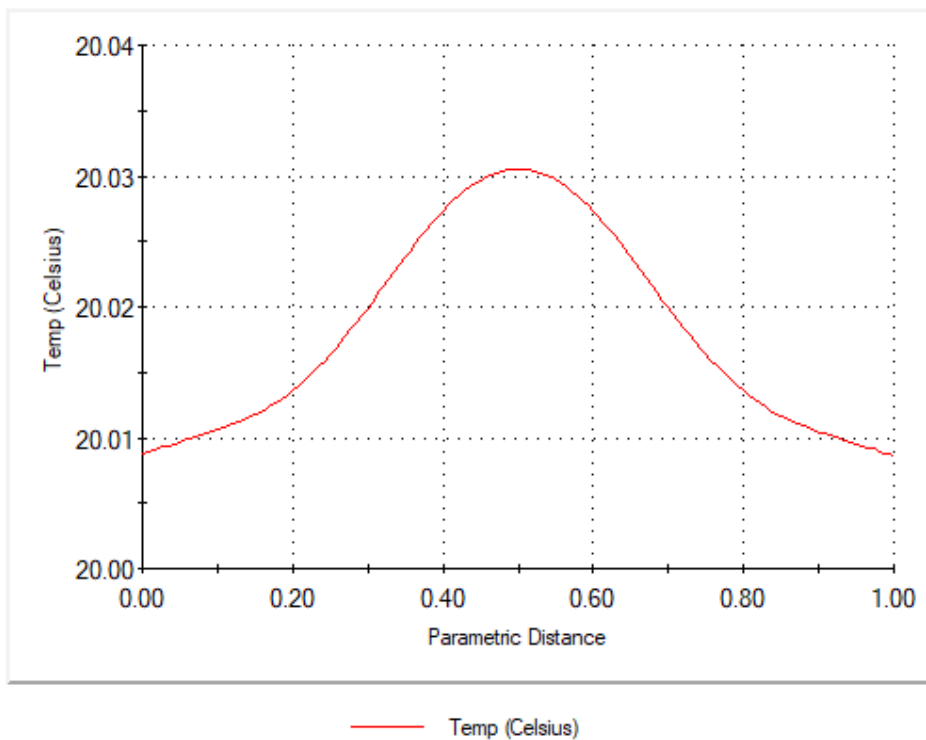


Figure C-53: Temperature profile from probe edge $t=1200s$

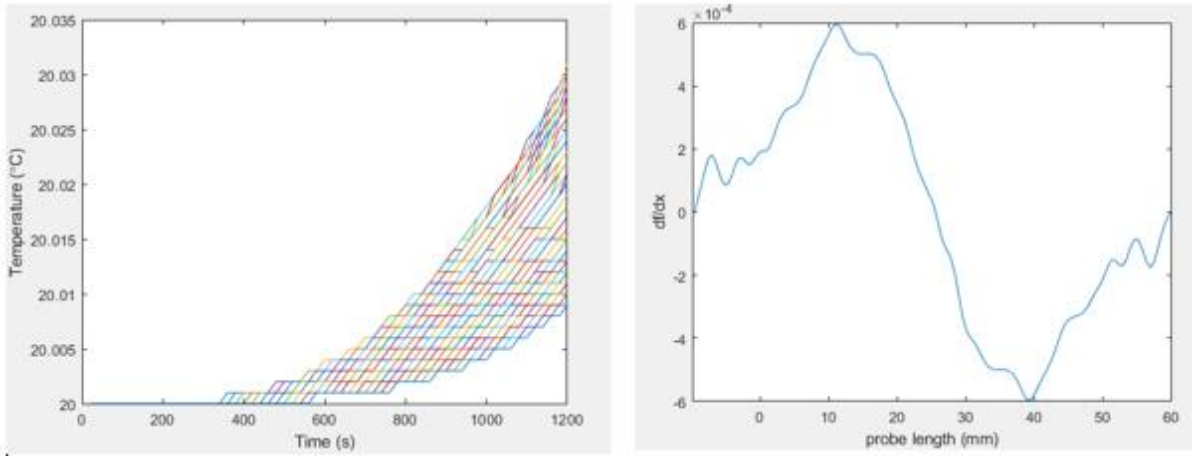


Figure C-54: (L) nodal temperature over time, (R) differentiated temperature data at $t=1200s$

xi. PLA $t=2400s$

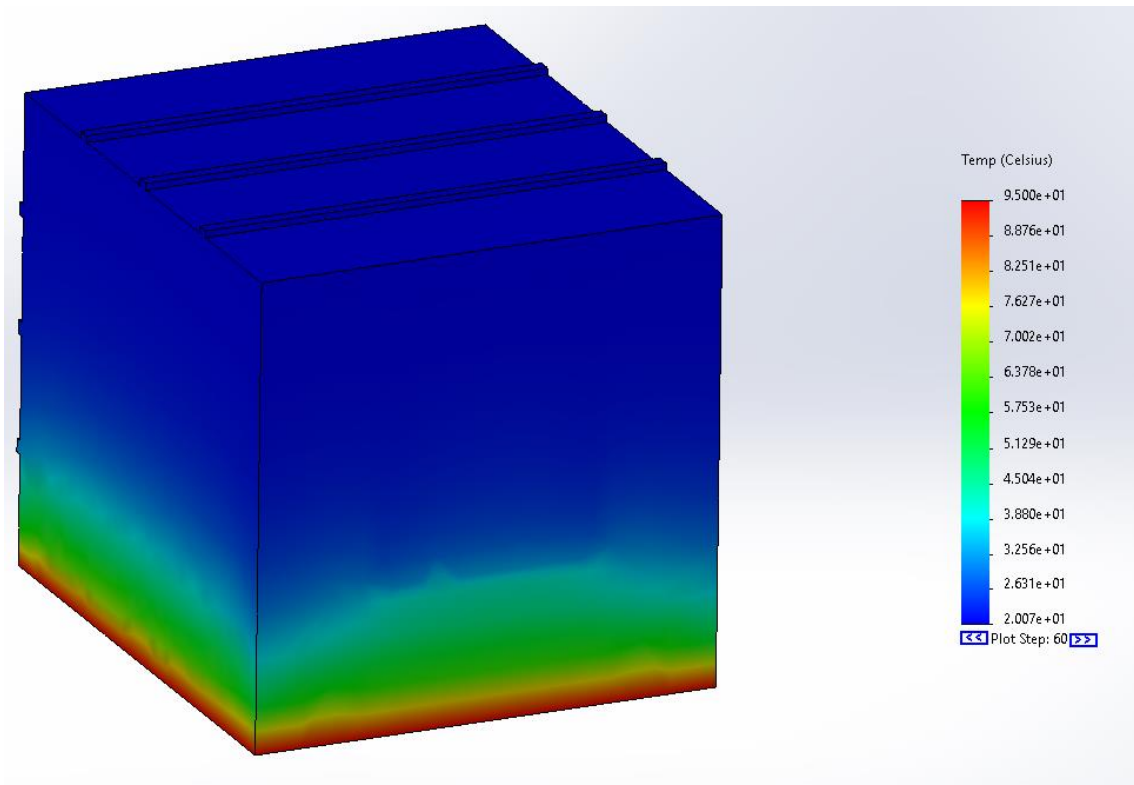


Figure C-55: Thermal distribution, external heating, PLA, $t=2400s$

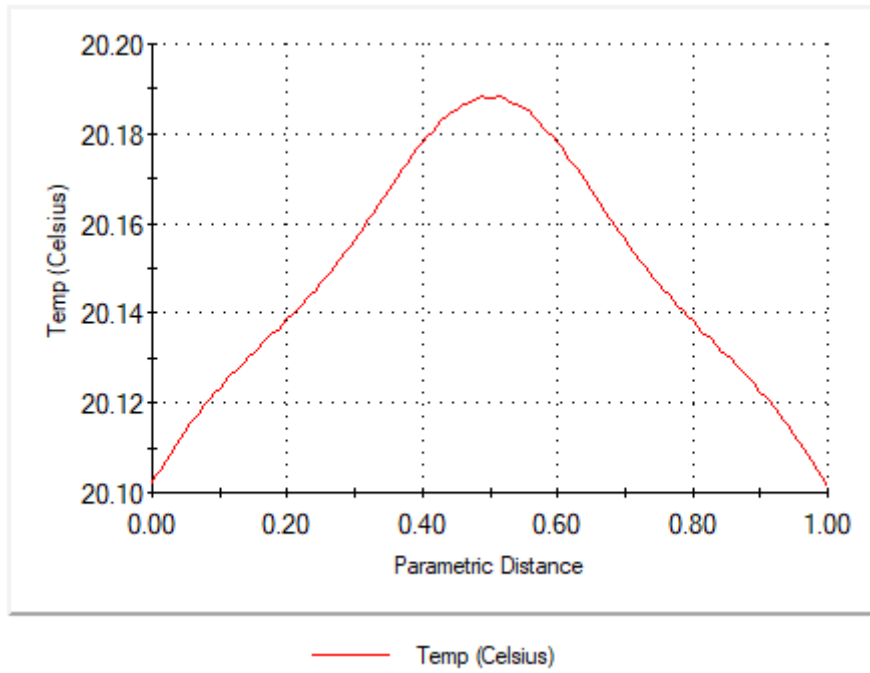


Figure C-56: Temperature profile from probe edge $t=2400s$

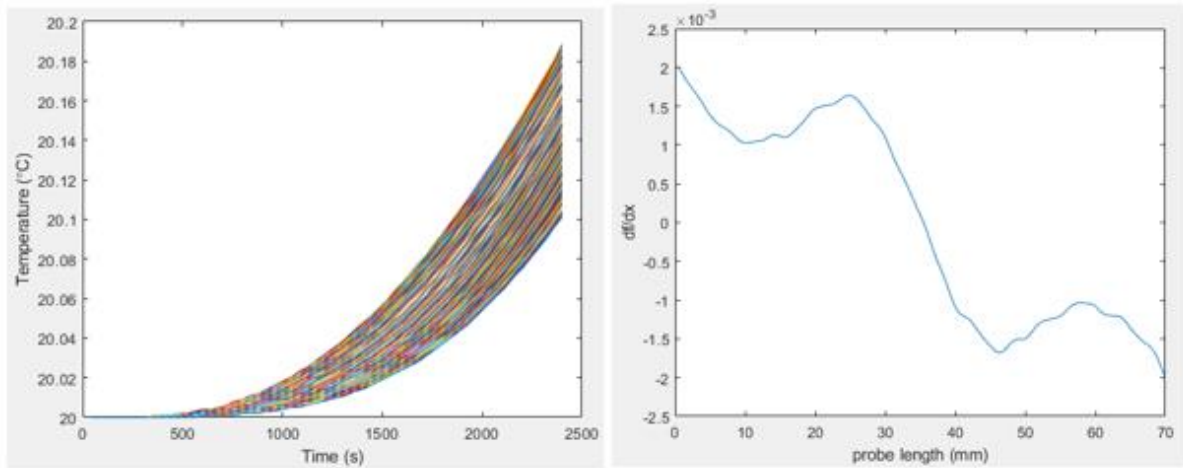


Figure C-57: (L) nodal temperature over time, (R) differentiated temperature data at $t=2400s$

xii. PLA $t=4800s$

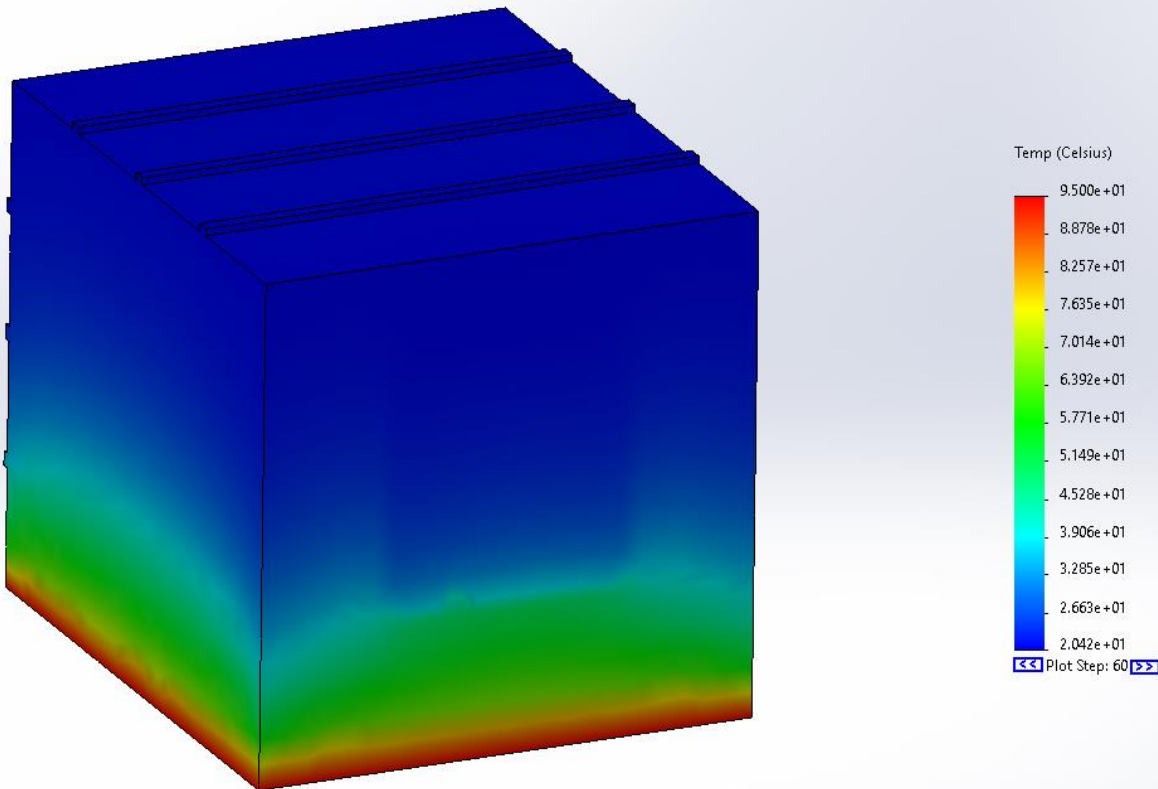


Figure C-58: Thermal distribution, external heating, PLA, $t=4800s$

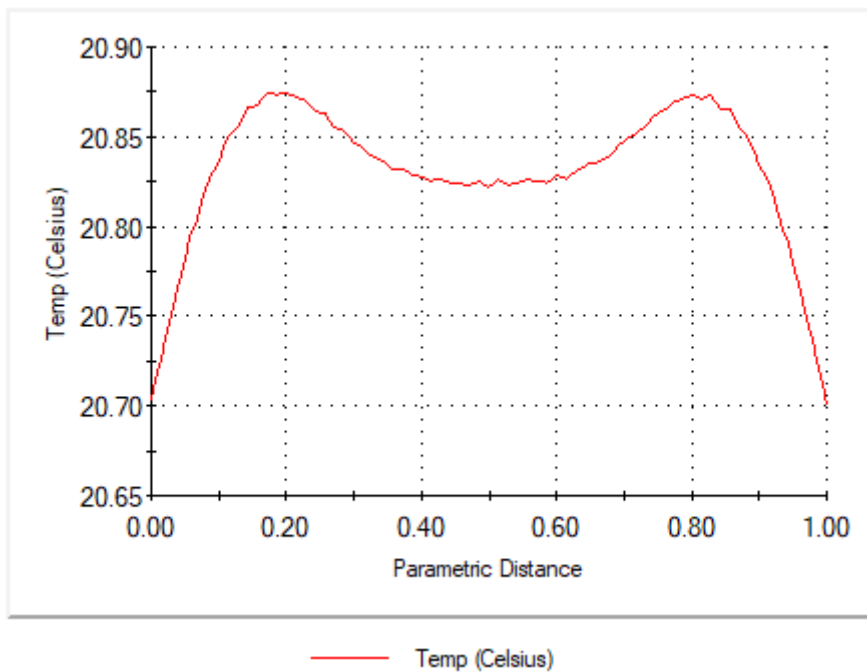


Figure C-59: Temperature profile from probe edge $t=4800s$

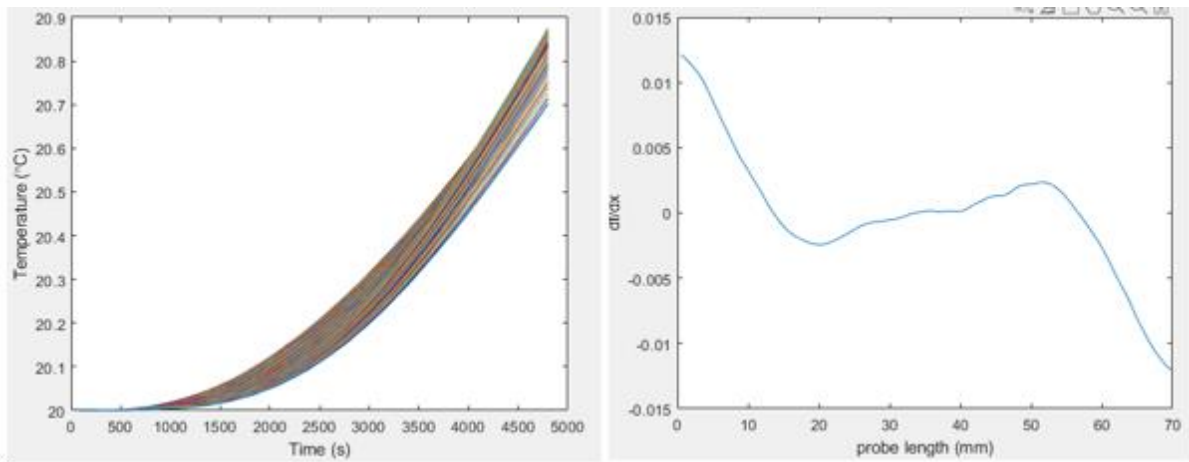


Figure C-60: (L) nodal temperature over time, (R) differentiated temperature data at $t=4800s$

xiii. PLA $t=9600s$

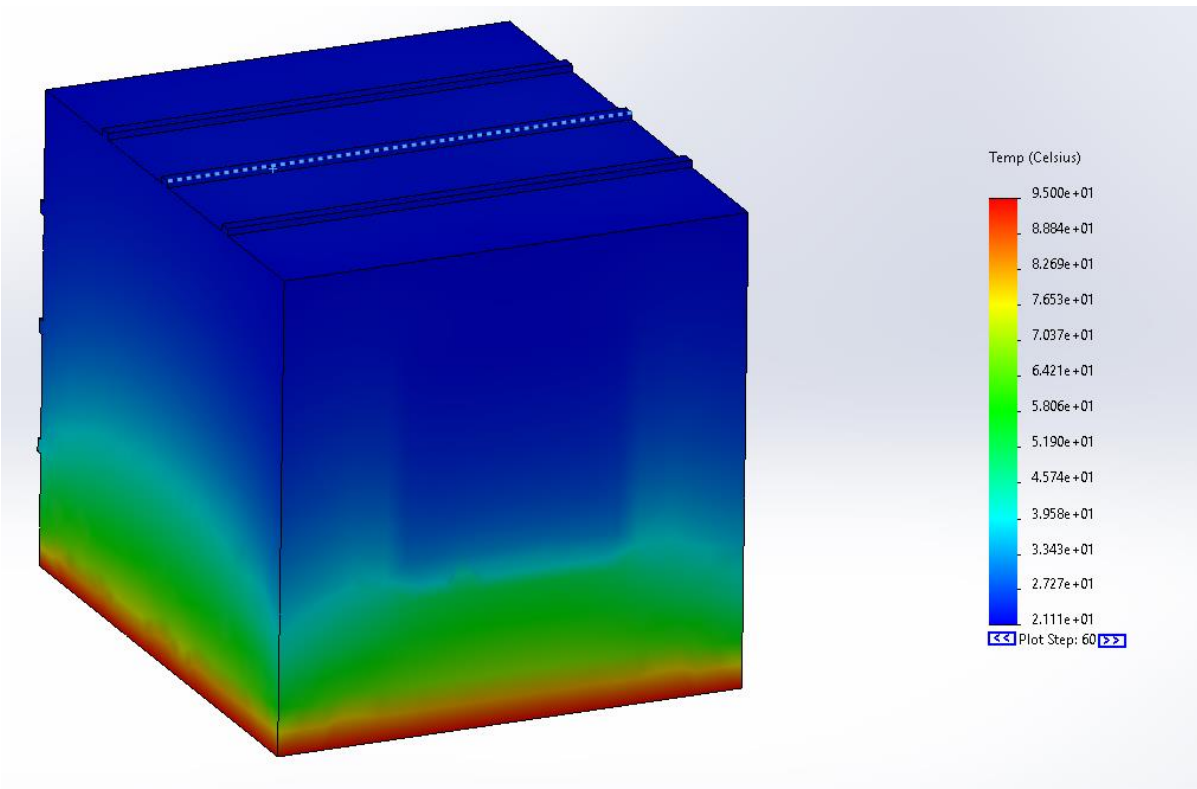


Figure C-61: Thermal distribution, external heating, PLA, $t=9600s$

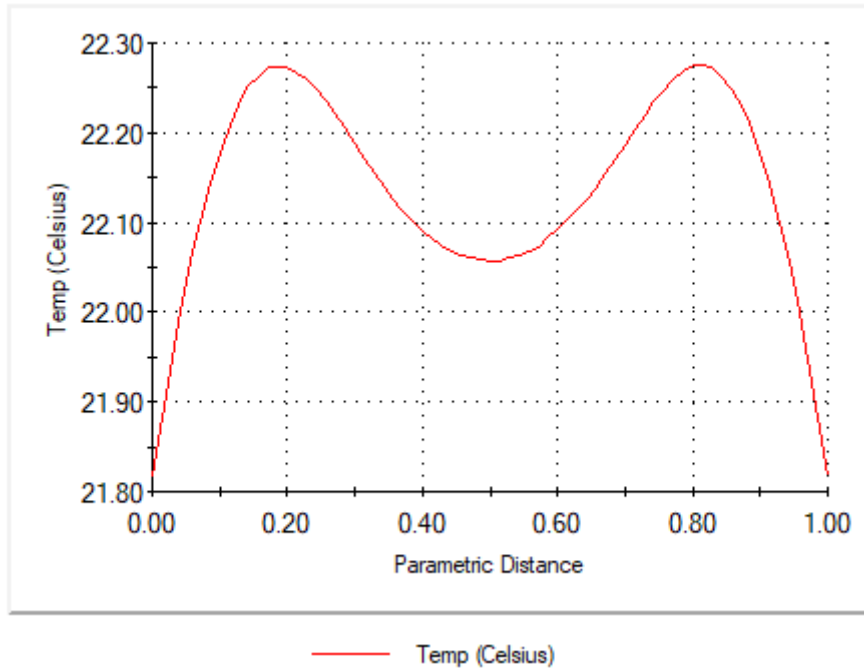


Figure C-62: Temperature profile from probe edge $t=9600s$

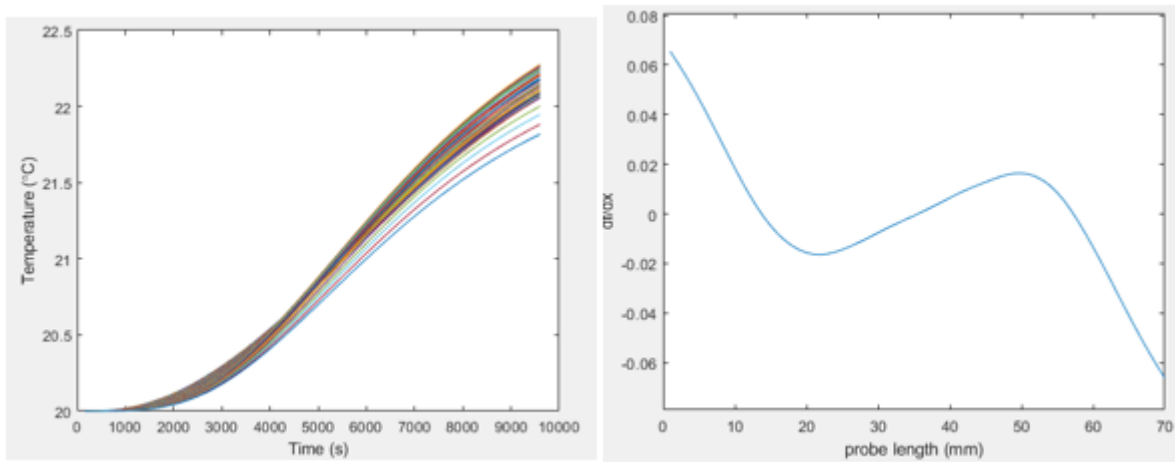


Figure C-63: (L) nodal temperature over time, (R) differentiated temperature data at $t=9600s$

f. Experimental artefact result

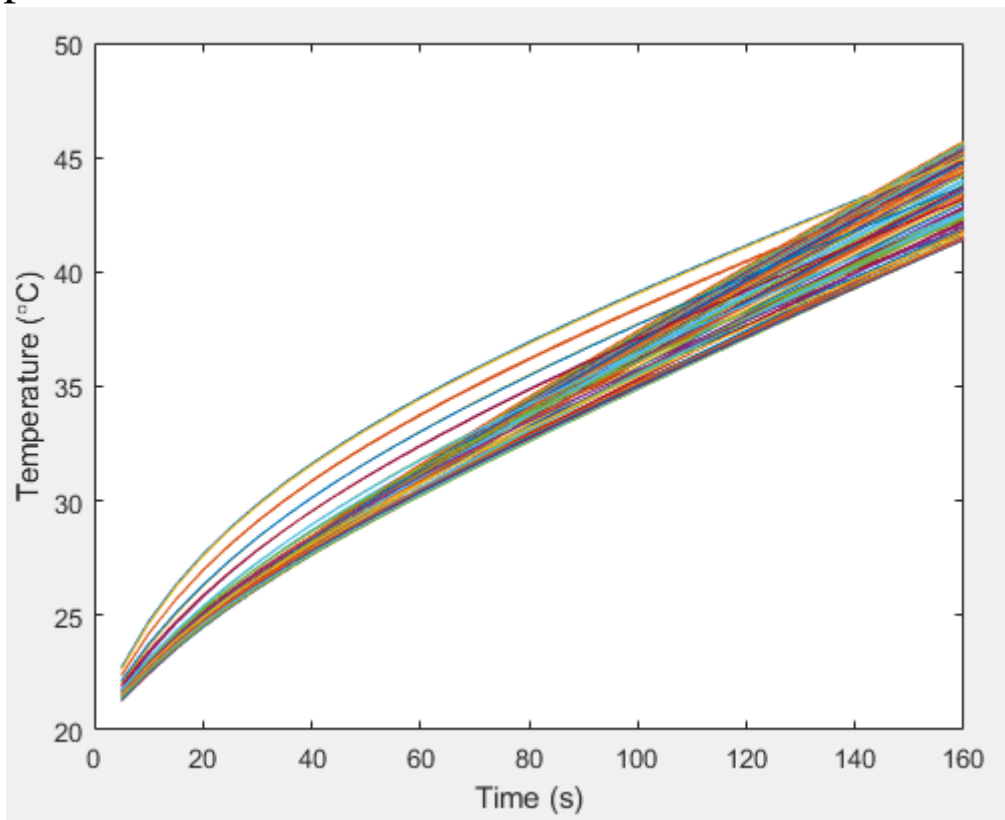


Figure C-64: 160s artefact simulation - nodal temperature

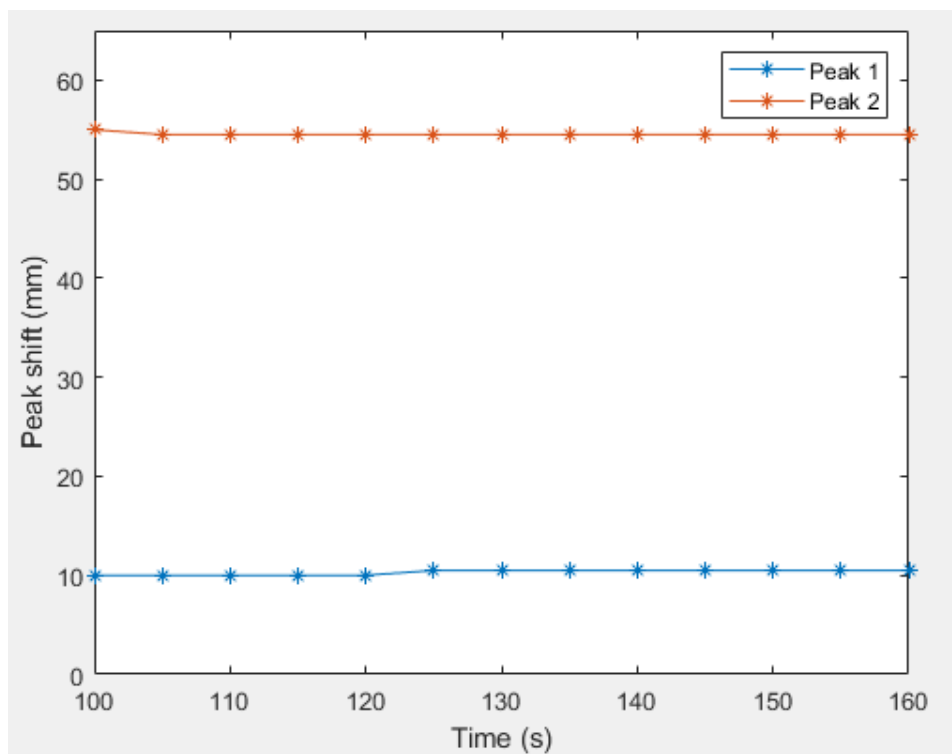


Figure C-65: 160s artefact simulation - edge position

Appendix D. 3D external scanning

The following details the process that was undertaken to capture and digitise the external geometry as highlighted in Chapter 5 section 5.3.1

a. Digitisation

The first step in this RE process is the recreation of the external geometry. In this investigation, this was performed using a *Hexagon Metrology Romer® Absolute 7525* measurement arm (Figure D-1).



Figure D-1: Romer Absolute 7525 Arm with RS3 laser line scanner

This articulated measurement arm has an integrated triangulation laser-line scanner, the RS3, built into the grip. This laser line scanner is used to capture the external geometry of the artefact. Table D-1 outlines the RS3's scanning specifications [75].

Table D-1: Romer arm and RS3 specifications

Property	Value
Max. point acquisition rate (points/s)	460,000
Points per line	4600
Line Rate (Hz)	100
Line Width (mid-range) (mm)	65
Stand-off (mid-range) (mm)	150±50
Minimum point spacing (mi-range) (mm)	0.014
Accuracy (µm)	2σ or 30
Measurement range of arm (m ³)	2.5

The artefacts were then placed on a stand so that the measurement arm could capture all four side faces, the top face, and a partial capture of the bottom face (shown in Figure D-2).



Figure D-2: External scanning of artefact

At this point, the process is repeated three times, one for each of the three artefacts. As the process for the RE of the external geometry is the same each time, it will only be described

once. The results of the external capture for all three artefacts will be presented at the end of this section.

After scanning the first artefact, a CPD consisting of around twenty-two million points was recovered (Figure D-3).

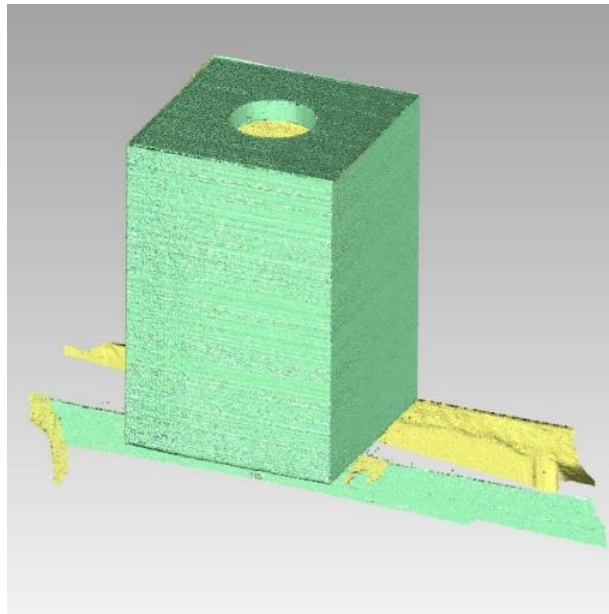


Figure D-3: Captured external CPD of artefact

b. CPD Editing

Following a successful external CPD capture, the CPD is subjected to several sampling techniques to reduce the number of points and remove any unnecessary out-liars. The software used in this part of the 3D recreation is Geomagic® Studio.

As the shape in question is rudimentarily prismatic, the sampling routines can be quite aggressive. The loss of large numbers of points will not detract from the CPD's overall shape. To begin with, the points that make up the stand the artefact was situated on are deleted, as they are not required. This is a manual operation, requiring the user to trim the points as close as possible to the target CPD without deleting any of the primary CPD points. Secondly, out-liar points are removed. Out-liars are any spurious points not connected to the primary scan data.

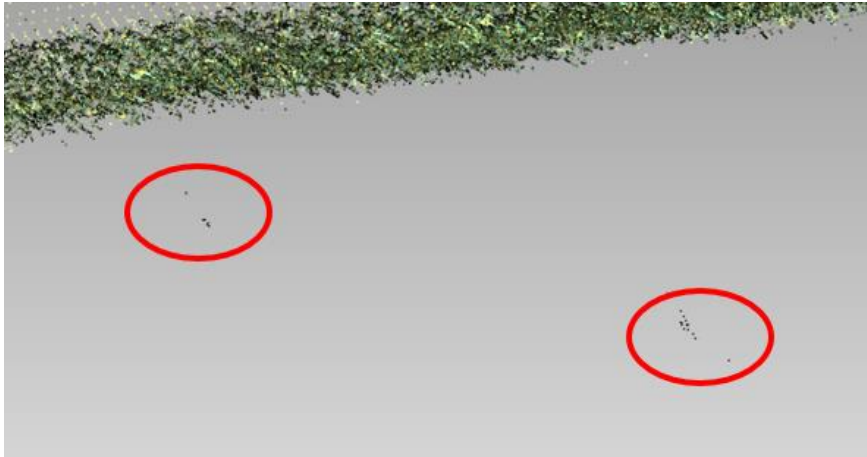


Figure D-4: Out-liars separated from the main bulk of the primary

As can be seen in Figure D-4, these out-liars, highlighted in red, are undesirable due to their separation from the main bulk of the CPD. During tessellation, these out-liars will cause irregularities in the mesh and lead to ghost patches.

Out-liars are generated from specular reflection. Sharp edges, high reflectivity, colour variation and translucency can all lead to the laser light profile being distorted. This in turn leads to mixed or multi-path reflections that are detected by the scanner receiver [76]. Selecting the out-liars is done by a distance-based algorithm. Points that are found to be further away from a large percentile of other points by a pre-prescribed distance are selected and in turn deleted.

After out-liar removal, the remaining points are sampled, reduced in number, and reordered. As the shape presented is prismatic in nature, a grid sampling routine is used to reduce the number of points in the CPD. Grid sampling will reduce the mesh evenly, spacing the remaining sampled points by a pre-defined set distance. The routine reduces the number of points regardless of curvature or original CPD density. This could potentially be detrimental as the object was made up of free-form shapes or areas with high curvature and detail could be lost. As the shape presented consists of planar features, grid sampling is ideal.

After sampling, the CPD is subject to a final noise reduction routine. Again, as the object is prismatic, an aggressive noise reduction can take place, as this will not affect the simple planar features.

From the initial circa twenty million points, the resulting CPD, which is now ready for meshing, has been reduced to 100,588 points (Figure D-5).

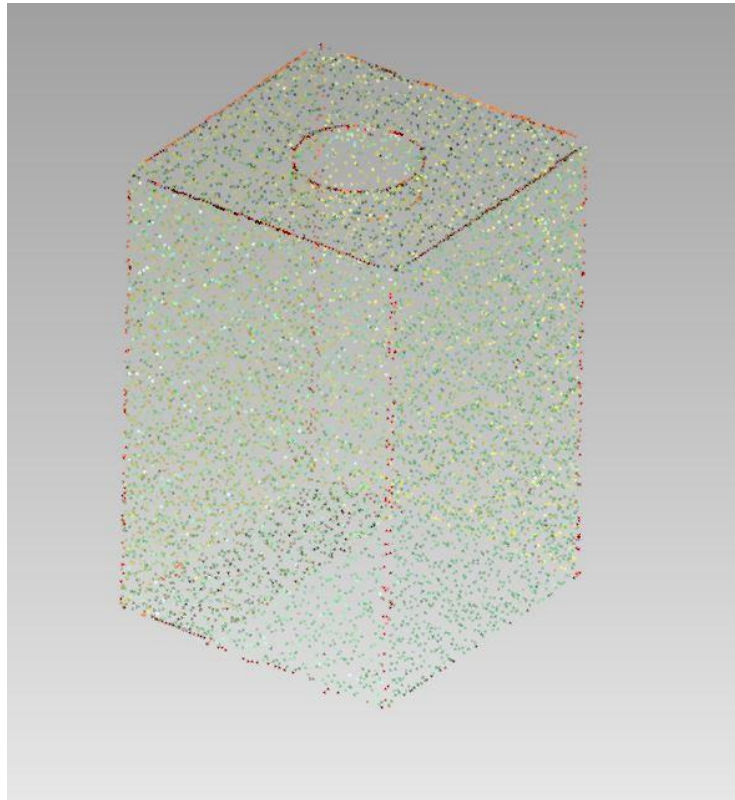


Figure D-5: Final Sampled CPD - The red areas indicate additional out-liars that require deletion

c. Mesh creation

From the sampled CPD a tessellated triangular mesh (TTM) can be created. In the first instance, the raw TTM consists of 199,999 triangles.

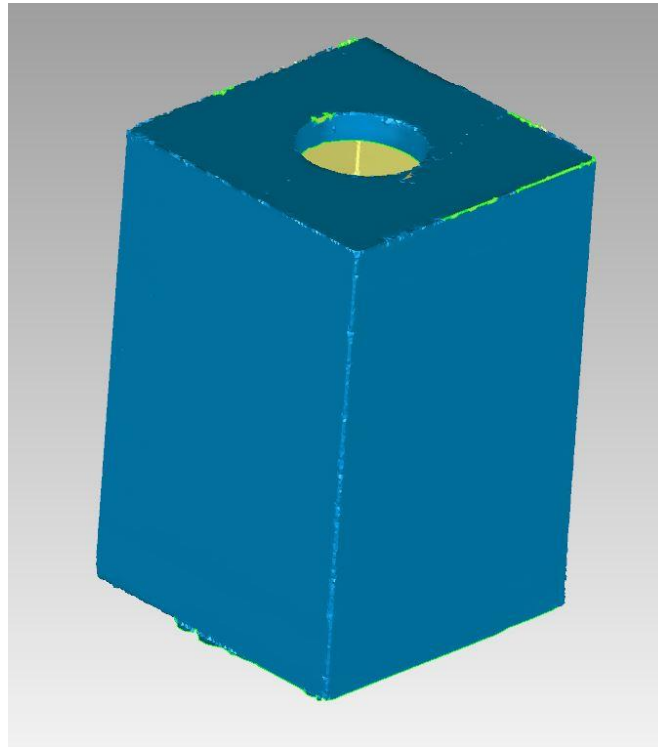


Figure D-6: Initial TTM after wrapping

For mesh reconstruction, Geomagic has a useful built-in tool for analysing the composition of the tessellated triangle. “Mesh Doctor” can identify manifolds, self-intersections, highly creased edges, small holes, and spikes. It is an autonomous function that can detect the anomalies as mentioned above and repair it with no user interface. After running the TTM through the Mesh doctor, larger holes remain, including the area where the object was in contact with the stand. These areas are then manually filled using the hole fill command. As the holes are on planar surfaces this is performed using no curvature, which results in a flat fill. The manual “sanding tool” is then used to smooth the edges around the fill, removing shape vertices. Mesh Doctor is run again. This ensures any irregularities that may have occurred during the hole filling procedure are removed.

Finally, the edges of the TTM can be sharpened. This is performed by the “Sharpening Wizard” function built into Geomagic Studio[®]. To begin with, the function breaks down the geometry of the TTM into regions. Region separation is determined by curvature, minimum surface area, and separator sensitivity. The value of curvature determines how the regions are separated based upon area flatness. A higher value will result in more areas of flatness to be separated. This can also be achieved by setting the region’s minimum surface area. A lower value for surface area will result in the TTM being subdivided into more regions. Regions can also be determined by defining the separator sensitivity. The separator highlights the boundary between regions. To ensure that the fillets, normally found in the mesh where two boundaries merge, are replaced with a sharp edge, the separator must be wide enough to encompass the entire fillet. Small separators could potentially define the boundary inside the radius of a fillet, and conversely, large separators could cover over small or delicate features.

Given the TTM in question, the following settings were used:

- *Curvature sensitivity: 50*
- *Separator sensitivity: 80*
- *Minimum surface area: 36mm²*

The value for curvature sensitivity was set at 50. It was found that any lower than this and the mesh radius between two perpendicular faces could be overlooked, leading to those two faces being defined as a single region. The separator sensitivity value was set high at 80. This was so that any small flat regions in the mesh radius could be defined as a separate, and therefore unwanted, region. Given the two variables above, the minimum surface area factor was automatically calculated to 36mm². Figure D-7 shows the resultant region subdivision of the TTM. Figure D-7 also helps highlight the mesh radius found between two perpendicular unsharpened faces.

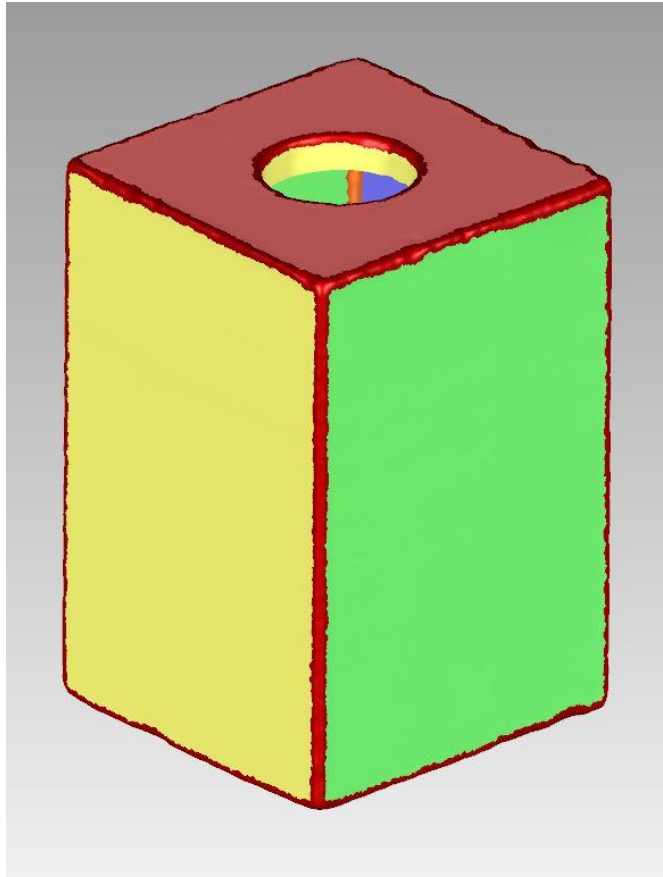


Figure D-7: Region subdivision of the TTM

The region separators highlighted in red in Figure D-7 are then replaced with placement curve lines. Nominally, these lines would be placed at the apex or the base of the mesh radius, but noisy mesh may prevent this, leading to irregularities in the continuity of the line. This issue can be edited manually until the placement curve line in question best replicates the required edge. When the placement curve lines have been placed, and if necessary, edited, they are to be “extended”. The extension of the placement curve line introduces two additional tangent curve lines on either side of the master curve line. These additional curve lines encapsulate the affected mesh radius, illustrating the start and the finish of area that is to be sharpened. Again, this can be manually edited, enlarging or shrinking the extension area so that the entire radius area is covered. The extended placement curve lines for this TTM are shown in Figure D-8.

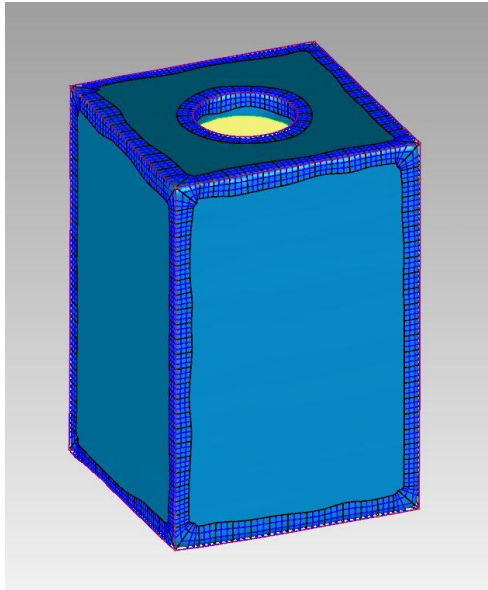


Figure D-8: Placement curve lines and their extensions

Following this function will presuppose that these regions are to be assimilated, and re-meshed to form sharp edges between the separate regions as shown Figure D-8. The final sharpened mesh is shown in Figure D-9. The external 3D scanning is now complete for this part of the reconstruction. Before surfaces or features can be extracted, the internal TTM needs to be recovered and incorporated into the TTM below.

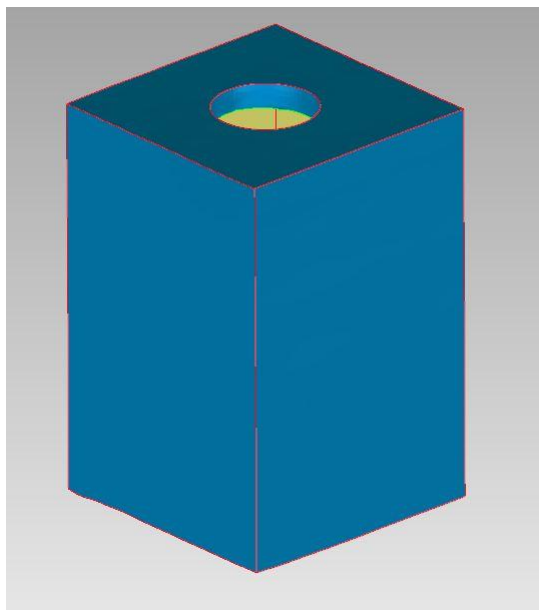


Figure D-9: Final sharpened TTM

Appendix E. Artifact Calibration Results

a. Square Artifact

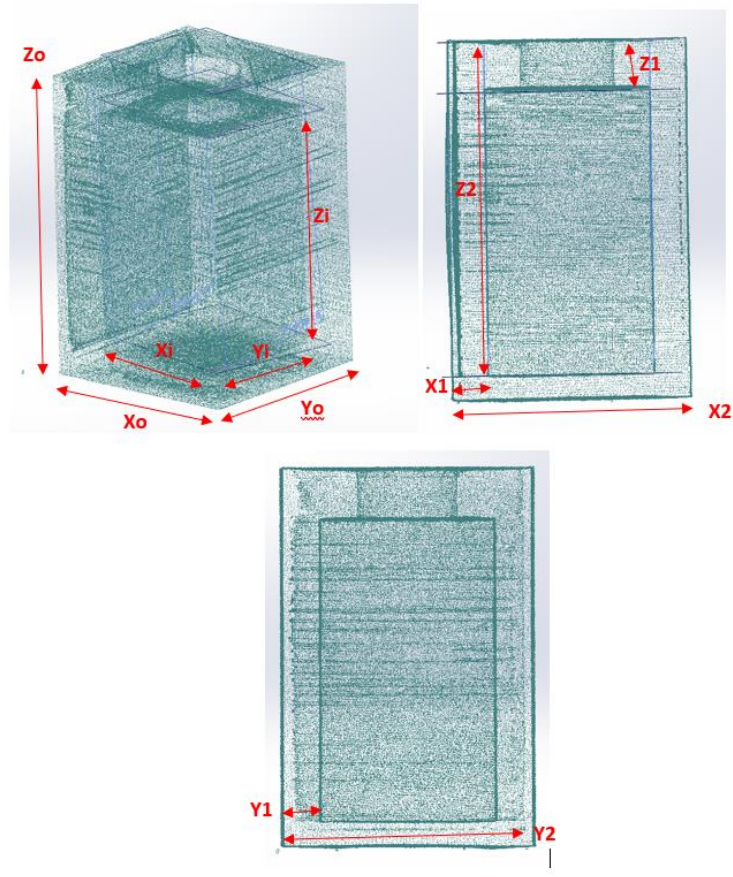


Figure E-1: PCD of Square artifact

Table E-1: Square Artifact result

SQUARE PLA	
Xo	49.75mm
Yo	49.7mm
Zo	74.87mm
Xi	34.77mm
Yi	34.58mm
Zi	59.43mm
X1	7.62mm
X2	42.25mm
Z1	10.62mm
Z2	69.76mm
Y1	7.52mm
Y2	42.26mm

b. Rectangular Artifact

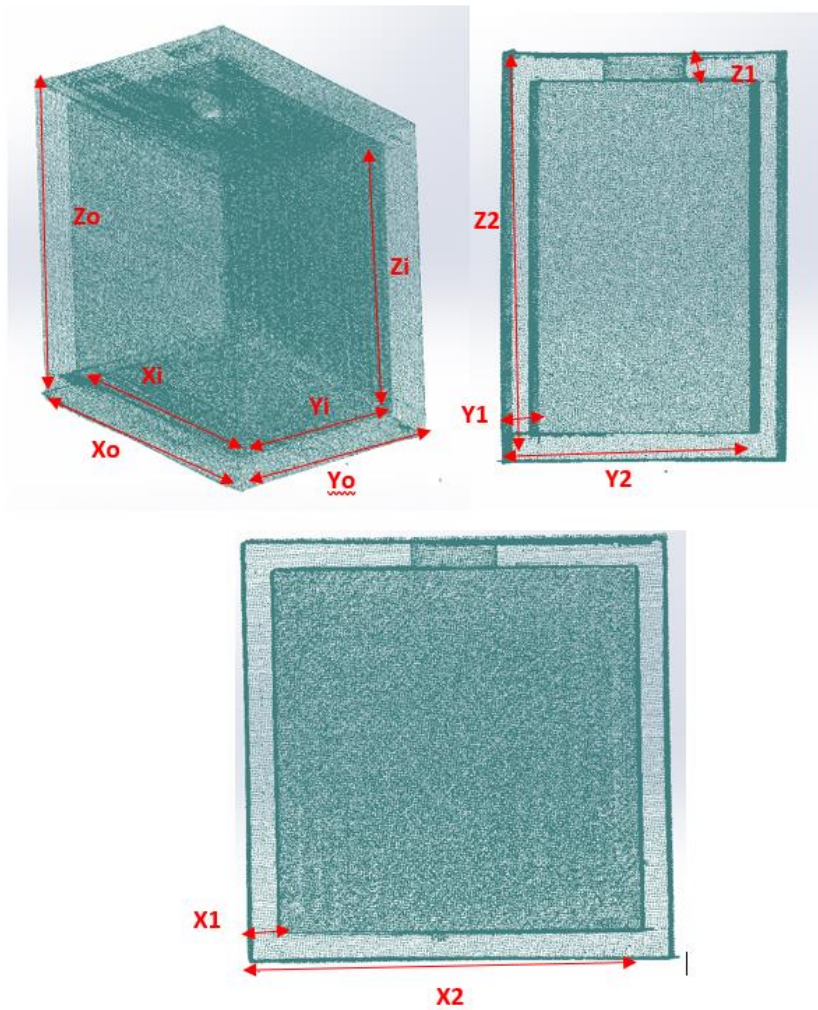


Figure E-2: PCD of rectangular artifact

Table E-2: Rectangular Artifact result

Rectangular PLA	
X_o	74.34mm
Y_o	50.35mm
Z_o	74.02mm
X_i	64.56mm
Y_i	40.4mm
Z_i	64.12mm
X_1	4.89mm
X_2	69.45mm
Y_1	4.76mm
Y_2	45.16mm
Z_1	5.26mm
Z_2	69.37mm

c. Cylinder Artifact

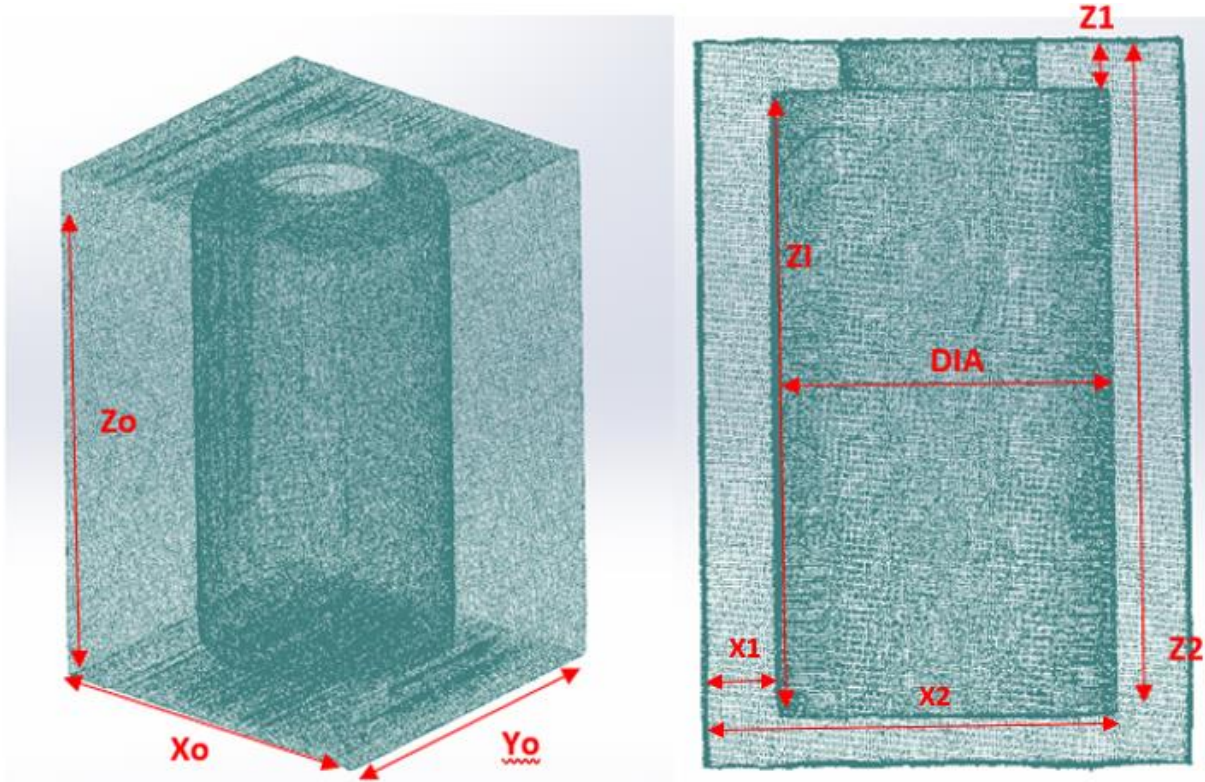


Figure E-3: PCD of Cylinder artifact

Table E-3: Cylinder Artifact result

CYLINDER	
Xo	49.94mm
Yo	49.64mm
Zo	74.77mm
Zi	64.77mm
DIA	34.94mm
Z1	5.04mm
Z2	69.81mm
X1	7.59
X2	42.43

d. Angled Artifact

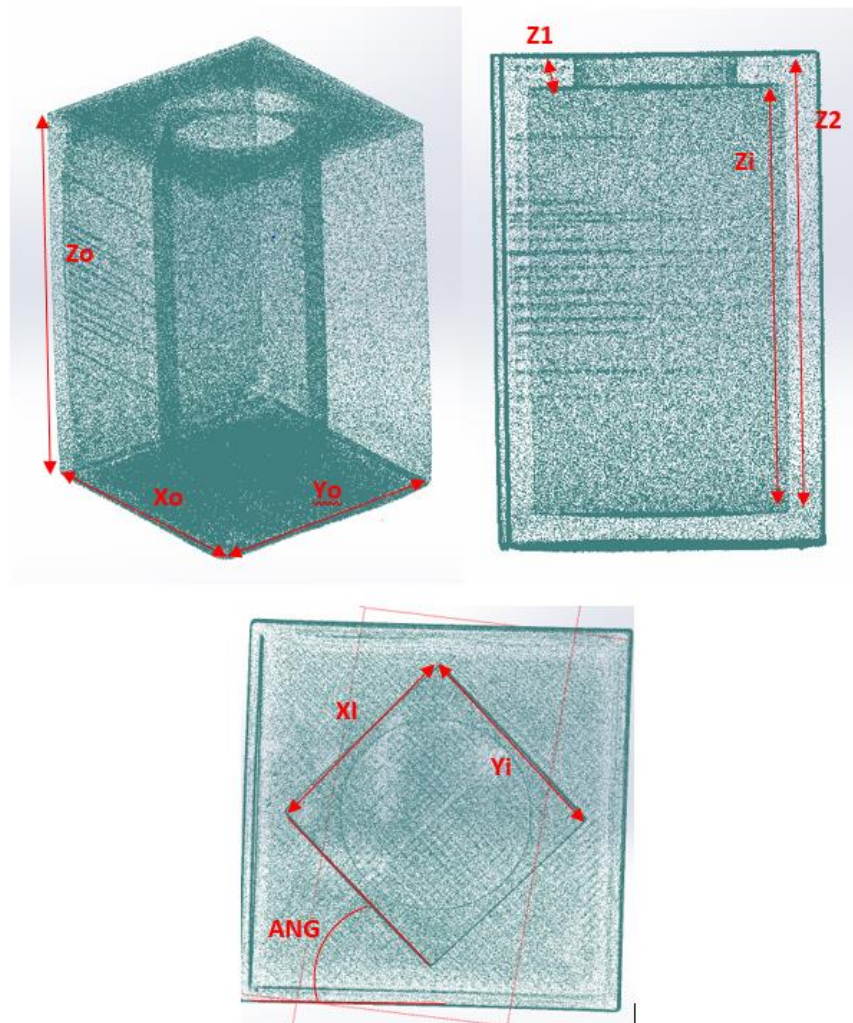


Figure E-4: PCD of Angled artifact

Table E-4: Angled Artifact result

ANGLED	
Xo	49.74mm
Yo	49.7mm
Zo	75.27mm
Xi	28.21mm
Yi	28.19mm
Zi	64.45mm
ANG	45.14°
Z1	5.4mm
Z2	69.85mm

e. L-shaped Artifact

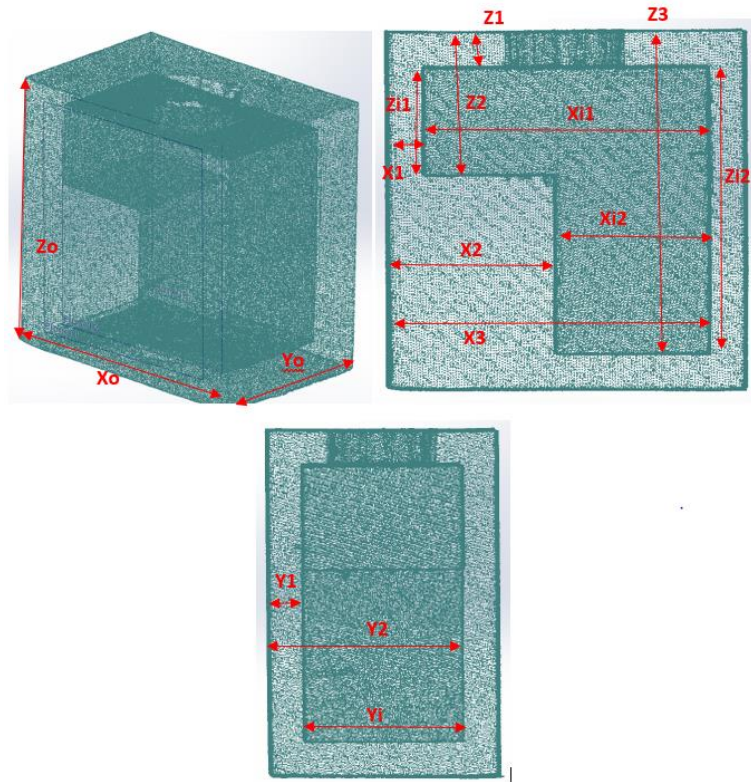


Figure E-5: PCD of L-shaped artifact

Table E-5: L-shaped Artifact result

L SHAPED	
Xo	74.73mm
Yo	49.42mm
Zo	75.17mm
Zi1	22.3mm
Zi2	59.93mm
Xi1	27.24mm
Xi2	59.83mm
Yi	34.66mm
X1	7.36mm
X2	34.6mm
X3	67.19mm
Y1	7.38mm
Y2	42.3mm
Z1	7.54mm
Z2	29.84mm
Z3	67.47mm

f. Aluminium Square Artifact

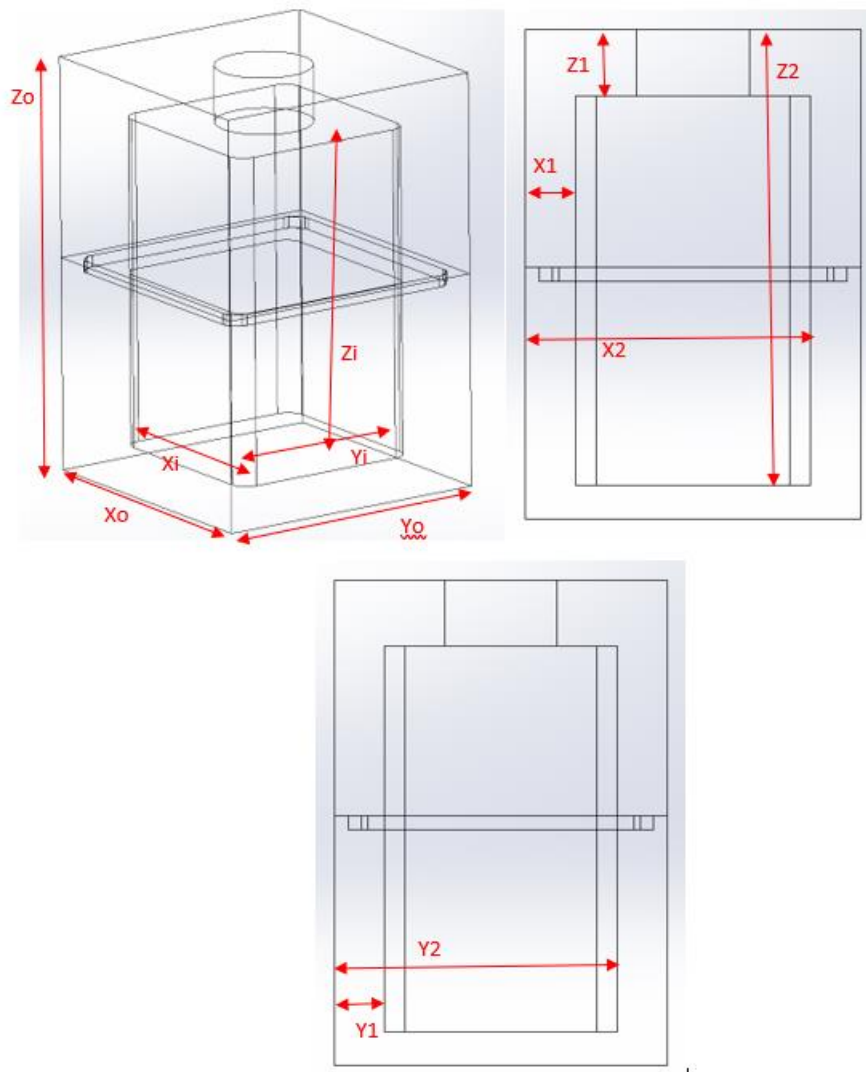


Figure E-6: Sign convention of aluminium artifact

Table E-6: Aluminium artifact results

Aluminium square	
Xo	50.92mm
Yo	50.92mm
Zo	73.87mm
Xi	34.99mm
Yi	35.02mm
Zi	57.94mm
X1	7.5mm
X2	42.32mm
Z1	9.36mm
Z2	67.32mm
Y1	7.35mm
Y2	42.32mm

Appendix F. Feature Extraction with traditional Edge Detection Algorithms

Whilst the Canny edge detection method was used to identify the external profile of the object, in the first instance traditional edge detection methods, such as Canny, were used to try to determine the internal edge position as well.

As shown in Figure 5-16, edge detection techniques require the imputed data to be an $M \times N$ array with values between 0 and 1. This was why the image in Figure 5-14 was converted from an $M \times N \times 3$ RGB image to the $M \times N$ monotone image shown in Figure 5-16. To perform internal edge detection on this thermogram; the cropped selection for edge detection is taken from the monotone image shown in Figure 5-16. This cropped selection is shown in Figure F-1.



Figure F-1: Cropped Monotone Thermogram

Having cropped the required selection, Sobel, Canny, Prewitt and Roberts edge detection algorithms were each in turn applied to the above cropped image in an attempt to deduce the internal edge position.

Figure F-2 shows the results of applying the above edge detection methods to the selection shown in Figure F-1.

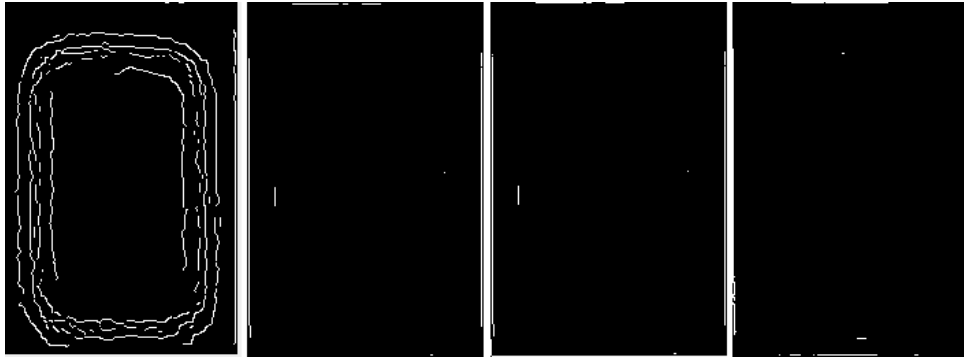


Figure F-2: Results from applied edge detection algorithm. From left to right: Canny, Sobel, Prewitt, Roberts

As can be seen in Figure F-2, without applying a sensitivity threshold factor, only the canny method returns any kind of insight into the internal shape. Even so, the results the Canny method returns are ambiguous, with no definitive indication of the internal edge. What the Canny results does show is an indication of a change in hue within the image.

This process was then repeated, but with a value for the sensitivity threshold added. The sensitivity threshold can be set between 0 and 1. The above process of applying different edge detection algorithms was then repeated but with a sensitivity threshold value of 0.01, 0.5, and 1. Figure F-3 shows the results of this varying sensitivity using the Canny method, Figure F-4 using the Sobel method, Figure F-5 using the Prewitt method, and Figure F-6 using the Roberts method.

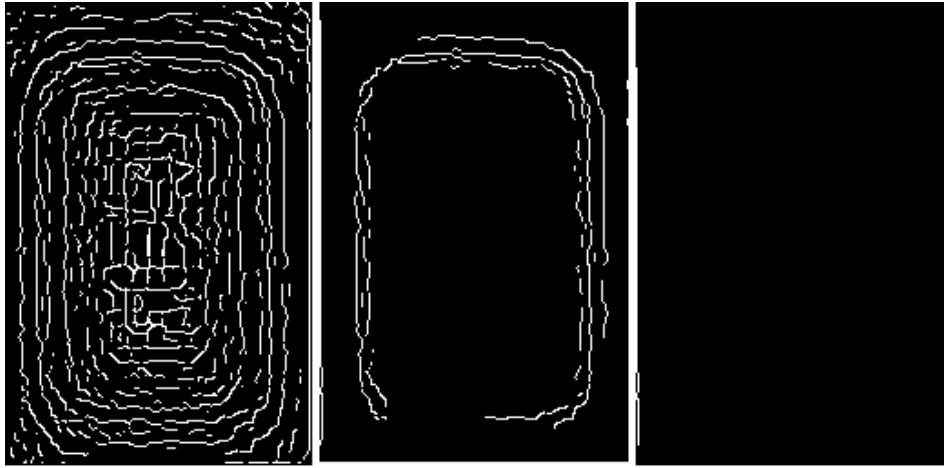


Figure F-3: L-R Canny method at 0.01, 0.5, 0.99, sensitivity threshold values

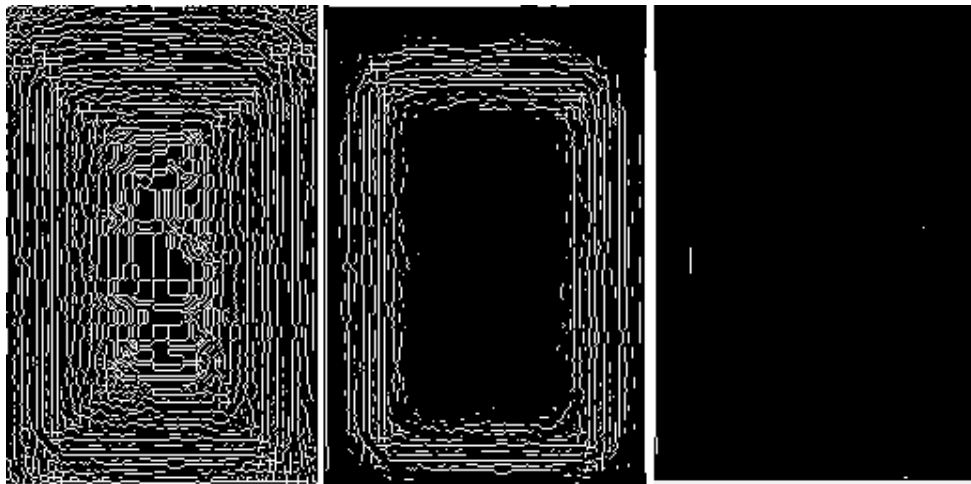


Figure F-4: L-R Sobel method at 0.01, 0.5, 0.99, sensitivity threshold values

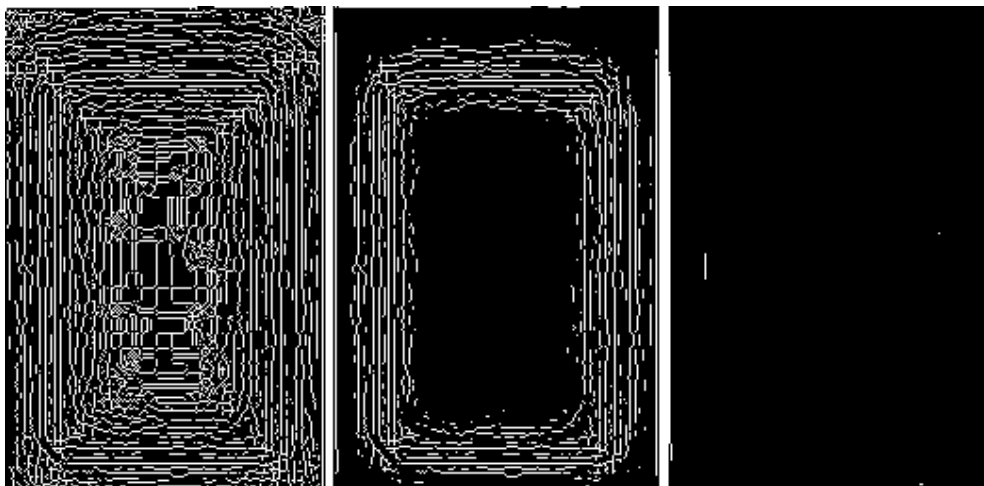


Figure F-5: L-R Prewitt method at 0.01, 0.5, 0.99, sensitivity threshold values

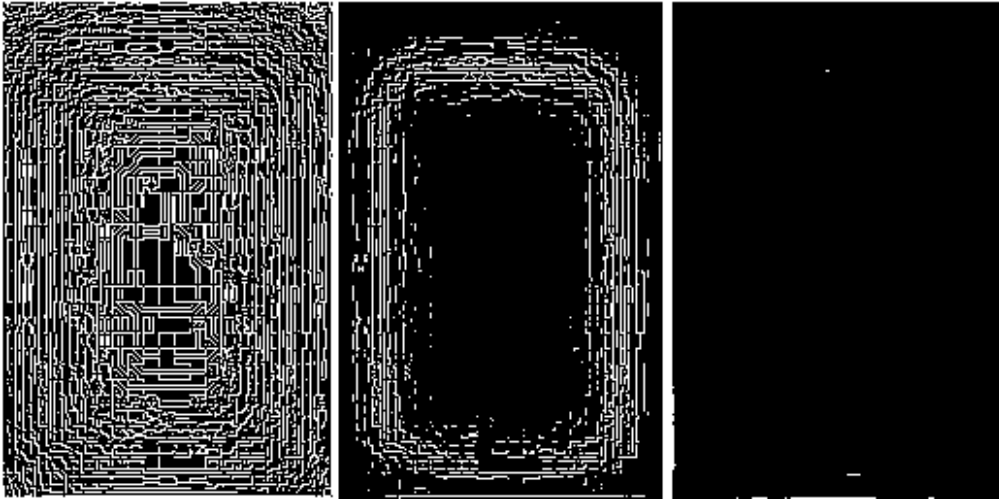


Figure F-6: L-R Roberts method at 0.01, 0.5, 0.99, sensitivity threshold values

As can be seen in the above figures, adjusting the sensitivity threshold does affect the number of edges returned. However, to accurately ascertain the internal edge position, the sensitivity threshold must be continually tuned in order to observe the most meaningful result. For example, the result using the Canny method with the sensitivity threshold set to 0.5 produced the most representative result from the above examples. By adjusting the threshold to 0.49, a marginally more representative result of the internal structure was obtained. However even with this result, shown in Figure F-7 edge position is still not definitive, as there are several recovered edges present.

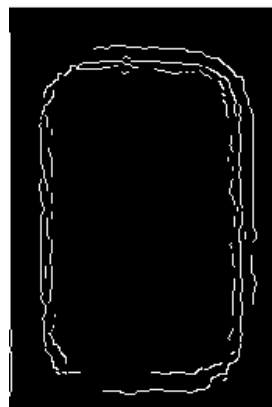


Figure F-7: Canny method with 0.49 threshold

Further adjustment in the sensitivity threshold, does provide better results for the estimation of some of the internal edges but can completely remove others. This is shown in Figure F-8, with the sensitivity increased to 0.6.

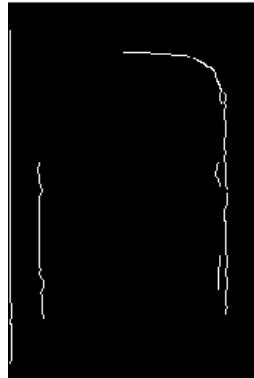


Figure F-8: Canny method with 0.6 threshold

As can be seen in Figure F-8, there is now a more definitive result for three of the internal edges, but the bottom edge has been completely eliminated. However, if positional results are taken from the three discerned edges and combined with a conversion factor of 0.285Px/mm^3 , the following edge positions are deduced (Figure F-9).

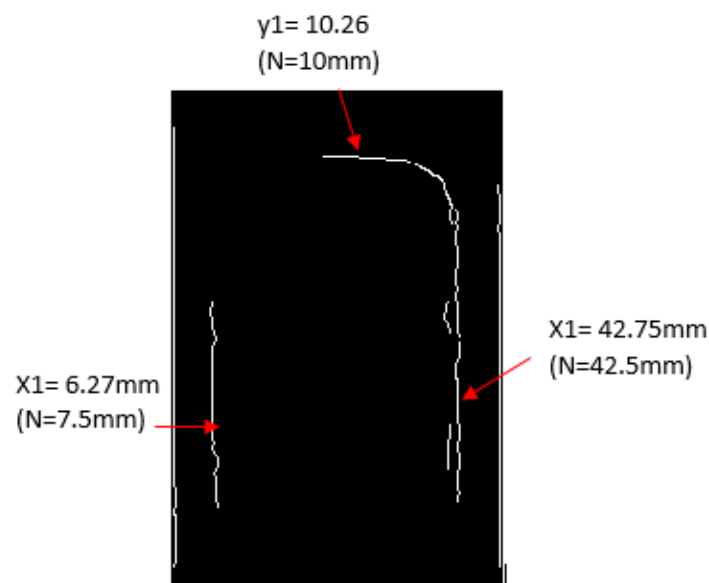


Figure F-9: Positional results from Canny method with 0.6 threshold

³ Given by the average of width of the object in mm divided by the number of pixels in X, and the height of the object in mm divided by the number of pixels in Y, $C=0.285=(50/173)+(75/259)/2$

As can be seen in Figure F-9 using the Canny method in this way has provided accurate results for the three edges that were returned. However, going forward it cannot be considered a viable method for the following reasons. By tuning the sensitivity threshold to gain definitive results for some edges, other edges could be lost. Furthermore, these settings for the Canny method are only applicable to this specific thermogram. The edge detection methods work on the image properties of the thermogram not the temperature data. With monotone images, this is based on the image's luminance. This luminance can change from one thermogram to another, therefore the setting used to gain the results shown in Figure F-9, will not be applicable to any other thermogram. Additionally, different users may use different colour palettes when visualising the thermal data. This will greatly change the hue and saturation of the RGB image, influencing the luminance in the converted monotone image used for edge detection.

By using the absolute temperature data, that the image properties of the thermograms are based upon, this will allow for an edge detection technique that is universal of all imputed thermograms.

Appendix G. Internal/External Reconstructing

With the successful extraction of the geometric data for the internal structure, and the generation of the corresponding CPD, the internal and external data sets can now be combined. To begin with, the internal CPD is imported into Geomagic® Studio. Figure G-1 shows the imported CPD, with a point count of 3051 points.

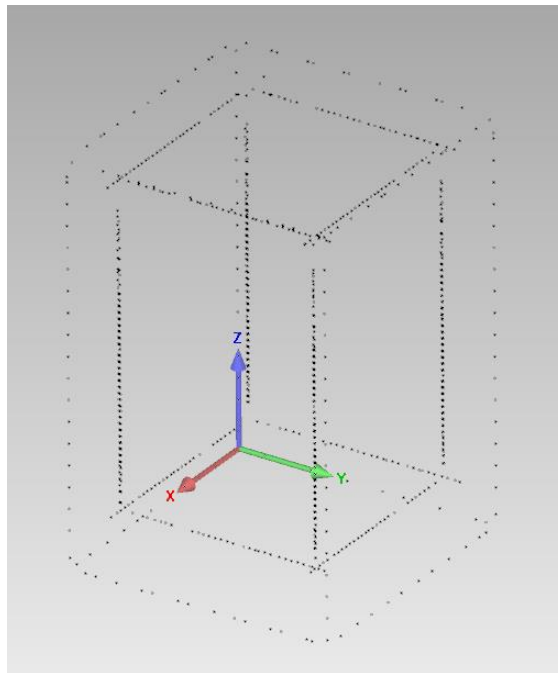


Figure G-1: Imported internal CPD

To begin with all six internal faces and three external faces are assigned plane features (Figure G-2). The planes assigned to the internal faces will allow the generation of a new TTM, and the planes assigned to the external faces will allow registration with external TTM.

The planes are applied using the best-fit method and are then converted into designated individual TTMs' (Figure G-3). The new TTMs' encompass the entirety of the plane they are built on. This, as can be seen in Figure G-3, includes a large amount of overhang, which needs to be removed. This is easily done by cropping each plane where they intersect with a corresponding perpendicular plane.

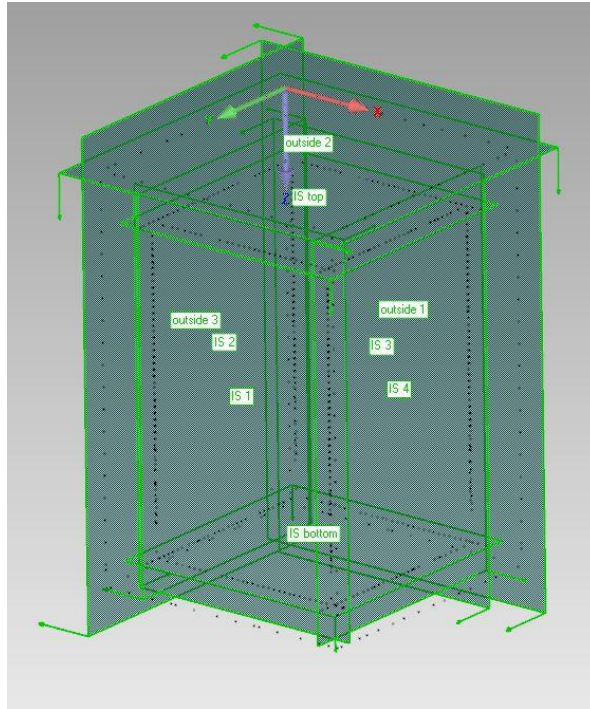


Figure G-2: Assigning planes to individual faces.

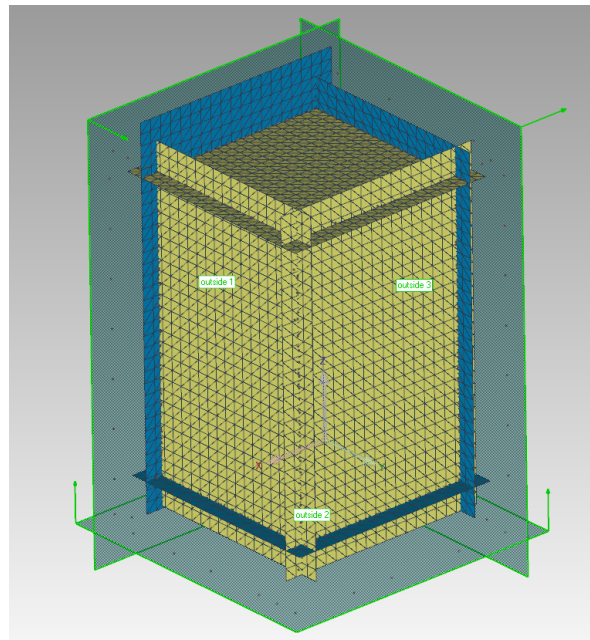


Figure G-3: Planes representing inside mesh after tessellation.

After the TTM has been cropped using perpendicular planes (Figure G-4 (L)), the inner and outer TTMs' can be registered together. Using the planes registered on the outer points of the inner data set, and planes registered on the corresponding outer faces, the two TTMs' can be combined. By combining corresponding planes on both the inner and the outer TTMs', using

a minimum of three pairs of planes the two TTMs' can be constrained both rotationally and translationally. The software then performs a best fit, ensuring the best alignment possible. The new combined TTM is shown in Figure G-4(R).

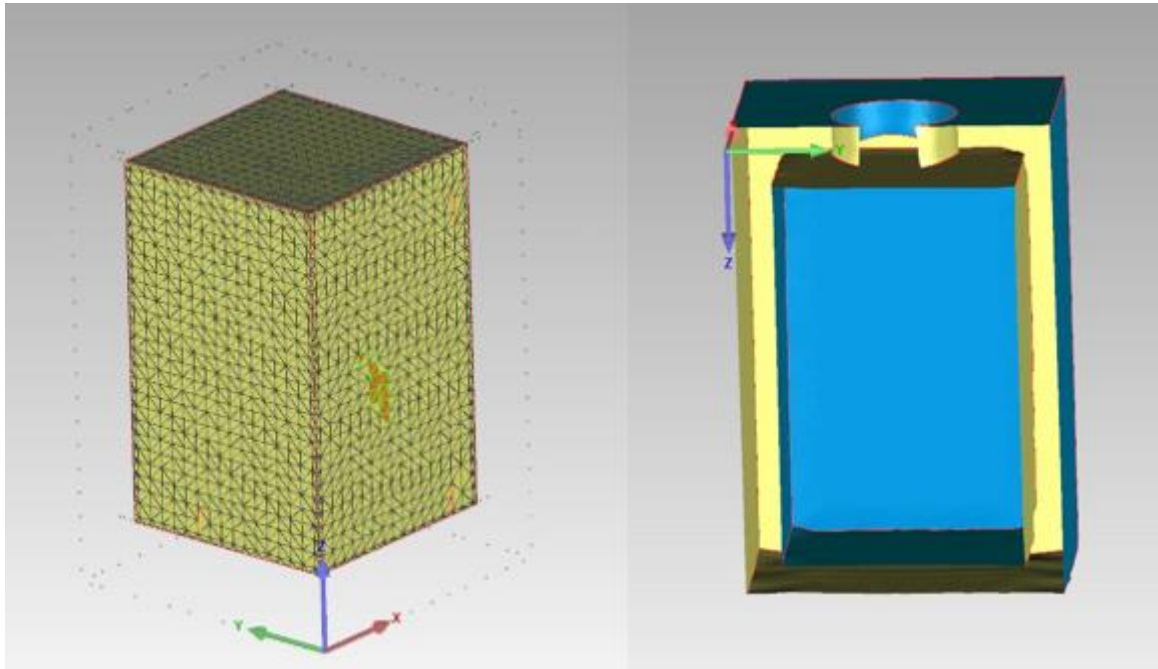


Figure G-4: L - Internal TTM after cropping, R - Section view of the new merged TTM

With the two TTMs' now registered together, the final step before parametric surfacing is to finish the TTM and connect the inner and outer segments. The hole in the top of the TTM (where the heat medium was added) was mostly captured during the external scanning. As it connects to the internal structure, the section that was captured during external scanning needs to be extended so that it intersects with the internal part of the TTM. The TTM will then need to be manipulated to ensure a constant mesh surface with no self-intersections or highly creased edges. Finally, a new boundary will need to be added to distinguish between the planer top of the internal section and the cylindrical hole.

This is performed using feature generation. The partial cylindrical section that was captured in the initial external scan, can be used to generate a best fit cylinder which, can then be extruded down (using the top surface of the TTM as a reference point) until it intersects with the top face

of the internal section of the TTM. As this stage a function can be used that will delete any part of the mesh that intersects with the constructed cylinder feature. By deleting this section of the mesh, a new circular boundary is created that is coincident with the circular boundary on the top face of the external mesh.

With the generation of this new boundary on the internal section, this boundary and the boundary that signifies the termination of the partial scan of the captured cylindrical feature can be merged together. This action denotes that the TTM, comprising of both internal and external features, is now continuous. It also ensures that the TTM has a complete selection of boundaries signifying the start and end of individual features. This will be important when assigning parametric surfaces to these features.

With the acquisition of a complete and continuous TTM, parametric surfaces can be added to the mesh. It begins with the TTM being broken down into separate regions. This function is performed by analysing the mesh and bisecting the TTM based upon the mesh curvature. Given that this TTM is made up of planar features, there is very little curvature to the mesh, so the regions are broken down according to their planar faces.

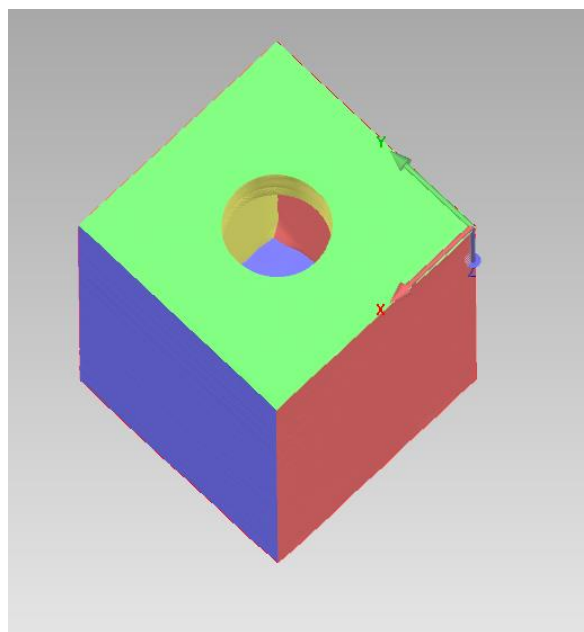


Figure G-5: TTM broken down into separate boundary regions

This is shown in Figure G-5, with each region being identified with a separate colour. With the regions identified, surfaces can be fitted to each region. This function is performed autonomously, based on the users' selection. The user selects the region that is to be fitted, and the function will fit a primitive feature that best represents that region. A colour map is then presented showing the deviation of the feature from the mesh that it is representing. As is shown in Figure G-6, the worst deviation for this set of added features is between 0.1mm and 0.18mm. This is acceptable, as the deviations appear to be in relation to surface errors on outer faces, which will have been present during the scanning phase and need to be discarded anyway.

For this TTM the surface fitting function returns twelve planar features (the internal and external walls of the object), one cylinder (the pouring hole), with a standard deviation of 0.03mm for the entire TTM.

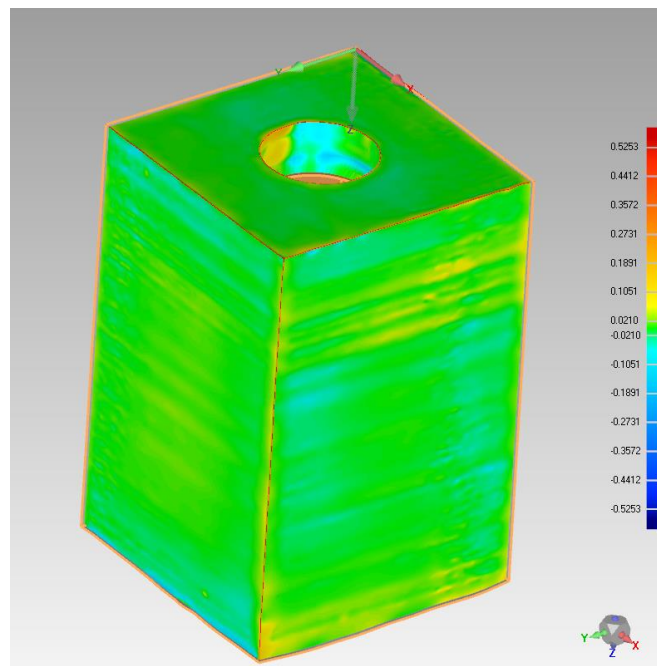


Figure G-6: L - Deviation colour map for fitted surfaces

After the surfaces have been stitched, the resultant part can be considered a complete parametric model. A section view of this is shown in Figure G-7.

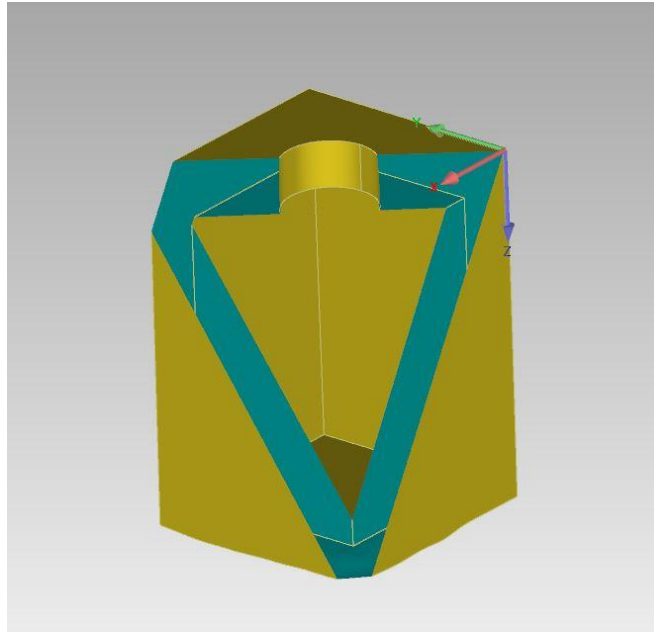


Figure G-7: Section view of the stitched model

This is a key milestone in this investigation. Up until this point, the data either gathered from the external laser scanning, or from the thermographic capture was only fit for purpose within the context of the capturing techniques. The culmination of these data sources leading to a full and complete solid model means this model can now be exported in several different file formats to be used in other engineering applications, such as FEA, CFD, drawing generation, and if needed can even be reprinted.

Appendix H. Matlab Code

a. *LoadSW* – Single Solidworks temperature extraction program

```
%Script for loading SW results files
close all
clear data t fnames

%---- OPTIONS: ----%
blnDebug = 1;
rawPlot = 1;
doFit = 1;

mmPerNode = 0.125;

%---- FOLDERS -----%
%Top surface folders:
basePath = 'C:\Users\sjwfl\Box\TF THESIS\SW sim\Results files\Cuboid
square void top thickness varying';
%Cylinders
basePath = 'D:\Documents\PHD\thermal sims\result files';

%SW FEA uses 200 nodes equally spaced along the top surface
%150 and 200W/m/k conductivity, use 1second resolution over 20 seconds or
more
% filename = 'Response Graph-Square void X50 5mm thick 36s 1800s
0,5Wmk.csv';
%filename = 'Response Graph-Square void X50 5mm thick 4s 120s 100Wmk.csv';
%filename = 'Response Graph-Square void X50 5mm thick 1s 40s 150Wmk.csv';
% filename = 'Response Graph-Square void X50 15mm thick 1s 40s 200Wmk.csv';
filename = '0.25 mm ele.csv'

%Cylinders:
% filename = 'Response Graph-Cylinder void X50 5mm thick 36s 1800s
0,5Wmk.csv'
% filename = 'Response Graph-Cylinder void X50 15mm thick 36s 1800s 0,5Wmk
AreaMatched.csv'

%%
[data,t, fnames]=floadcsv('Point', fullfile(basePath, filename));
t = data(:,1); %Extract time data from first column
a = data(:,2:end-1); %Trim
%a5_05 = a'; %Transpose to get nodes as columns
%t5_05 = t;

% am = a - mean(a,2); %Removing the mean seemed to have no effect.

if doFit
    [pmax2,pmin2]=feapeaks(a', t(2)-t(1), mmPerNode, 1, blnDebug);

    % [pmax1m,pmin1m]=feapeaks(a', t(2)-t(1), 0.5, 0);
    % [pmax_5_150,pmin_5_150]=feapeaks(a5_150, x(2)-x(1), 0.5, 0);
end
```

```

if rawPlot
    figure;
    plot(t,a);
    xlabel('Time (s)'); ylabel('Temperature (\CircC)')

    %Range plotting: (To see what gradient there is along the tope surface
    figure;
    plot(t,range(a));
end

%%
%%-----
function [data,t, fnames]=floadcsv(headerString, fnames)
% FLOADASC: Loads ascii CSV files into variable
%
% Use: [data,fnames]=floadcsv
%
% Modified: November 2018 - New version for CSV and appending
% By: Simon Fletcher
% Description: filenames outputted & file dialog string input

if nargin == 0; headerString='sec'; end;

string='Select files';

ftypes={'*.csv'};

if nargin < 2
    ver=version;
    if ver(1)>='7' %uigetfiles does not work on Matlab 2007 version or
later
        [fnames,pathName] = uigetfile({'*.csv','CSV-files (*.csv)'; ...
            '*.*', 'All Files (*.*)'}, ...
            string,...
            'MultiSelect','on');
    else
        [fnames,pathName] = uigetfiles(ftypes, string);
    end
else
    pathName = '';
end

if iscellstr(fnames)
    numfiles=size(fnames,2);
else
    fnames=cellstr(fnames);
    numfiles=1;
end
if numfiles==1;
    fname=char(fnames(1,1));
    fname=fullfile(pathName,fname);
    [t, data]=getData(fname,headerString); %data=load(fname);
    if nargin == 0
        varName=char(fname(1:size(fname,2)-4));
        assignin('base',varName,data);
    end
end

```

```

else
    data=[];
    t=[];
    for i=1:numfiles
        fname=char(fnames(1,i));
        fname=fullfile(pathName,fname);
        [newt, newdata]=getData(fname,headerString); %load(fname);
        data=[data;newdata];
        if i>1
            maxt=max(t);
        else
            maxt=0;
        end
        t=[t;newt+maxt];
    end
end

% if nargout > 1
%     t=data(:,1); data=data(:,2:end);
% end
end

function [X_Value,data] = getData(filename,headerString)

delimiter = ','; %comma

fileID = fopen(filename,'r');

%Need to auto determine number of columns to define correct format string
%Assume time column is there
frewind(fileID);
[lineFound,scratch,lineCount]=gotoLine(fileID,headerString);
dataString = fgetl(fileID);
cols=0;
while ~isempty(dataString)
    [val,dataString]=strtok(dataString,delimiter);
    cols=cols+1;
end

formatSpec_f='%f'; %Time col
formatSpec_s='%s'; %Time col
for i=1:cols-1
    formatSpec_f = strcat(formatSpec_f,'%f');
    formatSpec_s = strcat(formatSpec_s,'%s');
end
formatSpec_f = strcat(formatSpec_f,'%*s%[\n\r]');
formatSpec_s = strcat(formatSpec_s,'%s%[\n\r]');

frewind(fileID);
startRow = lineCount+1; %23;
if startRow~=11;
    warning(sprintf('Expected start row for data to be 11. Check file.
Using: %d',startRow))
end
endRow = inf;
% delimiter='\t'
%% Read columns of data according to format string.
% This call is based on the structure of the file used to generate this
% code. If an error occurs for a different file, try regenerating the code
% from the Import Tool.

```

```

try
    formatSpec=formatSpec_f;
    dataArray = textscan(fileID, formatSpec, endRow(1)-startRow(1)+1,
'Delimiter', delimiter, 'EmptyValue' ,NaN, 'HeaderLines', startRow(1)-1,
'ReturnOnError', false);
catch
    formatSpec=formatSpec_s;
    dataArray = textscan(fileID, formatSpec, endRow(1)-startRow(1)+1,
'Delimiter', delimiter, 'EmptyValue' ,NaN, 'HeaderLines', startRow(1)-1,
'ReturnOnError', false);
end

for block=2:length(startRow)
    frewind(fileID);
    dataArrayBlock = textscan(fileID, formatSpec, endRow(block)-
startRow(block)+1, 'Delimiter', delimiter, 'EmptyValue' ,NaN, 'HeaderLines',
startRow(block)-1, 'ReturnOnError', false);
    for col=1:length(dataArray)
        dataArray{col} = [dataArray{col};dataArrayBlock{col}];
    end
end

%% Close the text file.
fclose(fileID);

%% Post processing for unimportable data.
% No unimportable data rules were applied during the import, so no post
% processing code is included. To generate code which works for
% unimportable data, select unimportable cells in a file and regenerate the
% script.

%% Allocate imported array to column variable names
X_Value = dataArray{:, 1};
convert=0;
%s=size(dataArray);
if iscellstr(X_Value(1,1));
    convert=1;
end
k=1;

for j=2:cols
    data(:,k) = dataArray{:, j};
    k=k+1;
end
h = waitbar(0, 'Please wait...');
if convert
    try
        rI=1;
        for i=1:length(data)
            rowval=str2num(char(X_Value(i,1)));
            if ~isempty(rowval) & isnumeric(rowval)
                newX(rI,1)=rowval;
                for j=1:size(data,2)
                    newdata(rI,j)=str2num(char(data(i,j)));
                end
                rI=rI+1;
            end
            waitbar(i/length(data),h)
        end
        X_Value=newX;
    end
end

```

```

        data=newdata;
    catch ME
        error;
    end
end
close(h)
end

%-----
function [lineFound,line,linecount]=gotoLine(fid,lineString)

frewind(fid)
lineFound=0;
linecount=0;
while ~lineFound & ~feof(fid)
    line = fgetl(fid);
    lineFound1 = instring(lineString, line);
    lineFound2 = strfind(line, lineString);
    if any([lineFound1, lineFound2]); lineFound = 1; end;
    linecount = linecount+1;
end
end

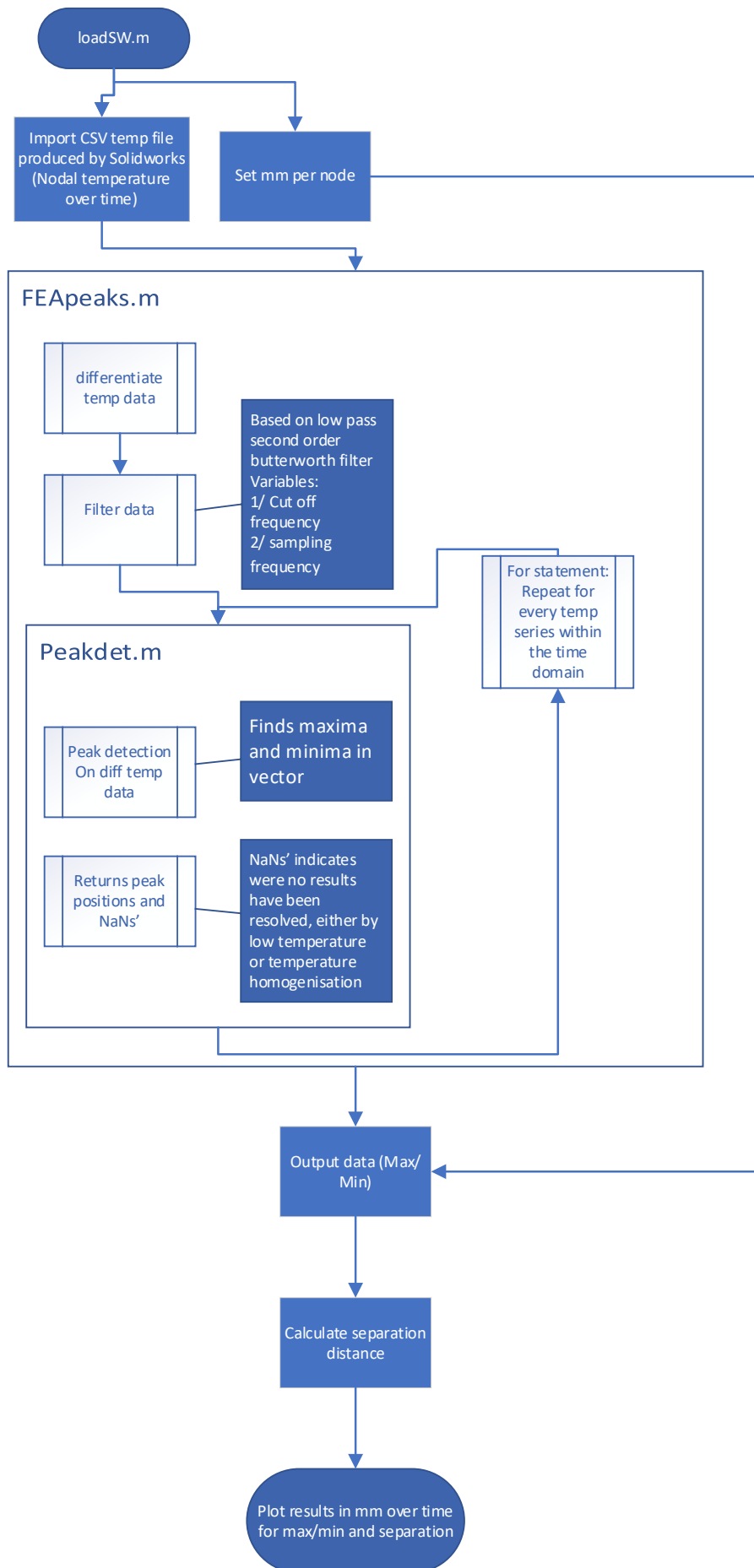
function [f,startIndex]=instring(stringBit,string,onlyFirst)

% INSTRING: checks string exists in another string.
%
% [f,startIndex]=instring(stringBit,string,onlyFirst)
% returns '1' if 'stringBit' exists in 'string'

if nargin < 3
    onlyFirst=0;
end

there=ismember(stringBit,string);
f=0; startIndex=[]; j=1;
if all(there)
    %worth looking at
    extra=length(string)-length(stringBit);
    if extra==0; extra=1; end;
    endI=length(stringBit);
    startI=endI-length(stringBit)+1;
    while endI<=length(string)
        if strcmp(stringBit,string(startI:endI))
            f=1;
            startIndex(j)=startI;
            if onlyFirst
                continue
            end
            j=j+1;
        end
        endI=endI+1;
        startI=startI+1;
    end
end
end
end

```



b. *feapeaks* – FEA peak extraction code

```
function [pmax,pmin,rawRange]=feapeaks(nodedata, timePerStep, mmPerStep,
interpFactor, doPlots)

% FEAPEAKS: get peaks of FEA node temperature data
%
% Use: [pmax,pmin]=feapeaks(nodedata)

if nargin < 2; timePerStep = 1; end;
if nargin < 3; mmPerStep = 1; end;
if nargin < 4; interpFactor = 1; end;
if nargin < 5; doPlots=0; end;

if interpFactor > 1 %Do interpolation to increase resolution of peak
shifts
    %Trim x to match diff data
    len = (length(nodedata)-1)*mmPerStep;
    x = linspace(0, len, length(nodedata));
    xi = linspace(0, len, length(nodedata)*interpFactor);
    ali = interp1(x, nodedata, xi');
else
    ali = nodedata;
end

i=1;
numSteps = size(ali,2);
rawRange=zeros(numSteps,1);
NANSfound = 0;
for intTimeStep = 1 : numSteps

    %Store the range of temperature across the profile
    rawRange(intTimeStep,1) = range(ali(:, intTimeStep));

    %Gradient of raw data
    d1 = diff(ali(:, intTimeStep));

    %Filter the data to avoid quantisation issue (Less of an issue with
real
    %thermal imaging perhaps)

    f1 = filtdata(d1,[2,0.085,interpFactor],0);

    delta = range(f1)/5;
    if delta < 0.04
        delta = 0.04; %This may need adjusting
    end
    %xlength=(0:1:length(Fdifffilt)-1);
    [maxtab1, mintab1]=peakdet(f1, delta);
    if size(maxtab1,1) < 1
        sprintf('No max peak on time step %d', intTimeStep);
        maxtab1=[NaN, NaN];
        NANSfound = NANSfound+1;
    end
    if size(mintab1,1) < 1
        sprintf('No min peak on time step %d', intTimeStep);
        mintab1=[NaN, NaN];
        NANSfound = NANSfound+1;
    end
end
end
```

```

end
if doPlots      %Plotting
    close all
    plot(f1)
    hold on

plot(maxtab1(:,1),maxtab1(:,2),'b*',mintab1(:,1),mintab1(:,2),'r*');
    plot([maxtab1(:,1), mintab1(:,1)], [delta,delta]);
    title(sprintf('Raw range: %1.1f, Gradient range:
%1.2f',rawRange(intTimeStep),range(f1)))
    hold off
    pause
end

try
    peakPos1(i,:) = [maxtab1(1), mintab1(1)];
    t(i,1) = intTimeStep * timePerStep;
    i=i+1;
catch ME
    disp('Calc error')
    intTimeStep
end

end

%
peakPos1 = peakPos1 * mmPerStep;

figure;
plot(t,peakPos1/interpFactor, '-*')
xlabel('Time (s)')
ylabel('Peak shift (mm)')
legend('Peak 1','Peak 2')

figure;
plot(t,range(peakPos1,2)/interpFactor, '-*')
xlabel('Time (s)')
ylabel('Distance (mm)')
legend('Distance 1')
title('Distance between peaks')
pmax = peakPos1(:,1);
pmin = peakPos1(:,2);

NANSfound

```

c. *manySW* – Loading multiple solidworks file program

```

function [pmax, pmin, alldata] = manySW(fileFolder)

% MANYSW: Loads selected group of SW results CSV files

%---- OPTIONS: ----%
rawPlot = 1;
doFit = 1;
mmPerNode = 0.5;

if nargin < 1
    fileFolder = pwd;

```

```

end

currentFolder = pwd;
try
    cd(fileFolder)

    ver=version;
    if ver(1)>='7' %uigetfiles does not work on Matlab 2007 version or
later
        [fnames,pathName] = uigetfile({'*.csv','CSV-files (*.csv)'; ...
            '*.*', 'All Files (*.*)'}, ...
            string,...
            'MultiSelect','on');
    else
        [fnames,pathName] = uigetfiles(ftypes, string);
    end
    cd(currentFolder)
    if iscellstr(fnames)
        numfiles=size(fnames,2);
    else
        fnames=cellstr(fnames);
        numfiles=1;
    end

    legendText={};
    alldata(numfiles).t = [];
    alldata(numfiles).data = [];
    alldata(numfiles).filename='';
    %%
    for i=1:numfiles
        fname=char(fnames(1,i));
        [data,t, ~]=floadcsv('Point', fullfile(pathName, fname));

        t = data(:,1); %Extract time data from first column
        a = data(:,2:end-1); %Trim
        alldata(i).t = t;
        alldata(i).data = a;
        alldata(i).filename = fullfile(pathName, fname);
        %a5_05 = a'; %Transpose to get nodes as columns
        %t5_05 = t;

        % am = a - mean(a,2); %Removing the mean seemed to have no effect.

        [pmax(:,i),pmin(:,i)]=feapeaks(a', t(2)-t(1), mmPerNode, 1, 0);
        % [pmax1m,pmin1m]=feapeaks(a', t(2)-t(1), 0.5, 0);
        % [pmax_5_150,pmin_5_150]=feapeaks(a5_150, x(2)-x(1), 0.5, 0);
        pause
        legendText{i} = strcat('file',num2str(i));
    end
    pmax = pmax;
    pmin = pmin;

    plot(t,pmax,t,pmin,t,[pmin-pmax])
    title('MAX/MIN/DIFFERENCE')
    figure
    plot(t,[pmin-pmax])
    legend(legendText)
    title('DIFFERENCES')
catch ME
    cd(currentFolder)

```

```

        rethrow(ME)
    end
    cd(currentFolder)
end

%%-----
function [data,t, fnames]=floadcsv(headerString, fnames)
% FLOADASC: Loads ascii CSV files into variable
%
% Use: [data,fnames]=floadcsv
%
% Modified: November 2018 - New version for CSV and appending
% By: Simon Fletcher
% Description: filenames outputted & file dialog string input

if nargin == 0; headerString='sec'; end;

string='Select files';

ftypes={'*.csv'};

if nargin < 2
    ver=version;
    if ver(1)>='7' %uigetfiles does not work on Matlab 2007 version or
later
        [fnames,pathName] = uigetfile({'*.csv','CSV-files (*.csv)'; ...
            '*.*', 'All Files (*.*)'}, ...
            string,...
            'MultiSelect','on');
    else
        [fnames,pathName] = uigetfiles(ftypes, string);
    end
else
    pathName = '';
end

if iscellstr(fnames)
    numfiles=size(fnames,2);
else
    fnames=cellstr(fnames);
    numfiles=1;
end
if numfiles==1;
    fname=char(fnames(1,1));
    fname=fullfile(pathName,fname);
    [t, data]=getData(fname,headerString); %data=load(fname);
    if nargin == 0
        varName=char(fname(1:size(fname,2)-4));
        assignin('base',varName,data);
    end
else
    data=[];
    t=[];
    for i=1:numfiles
        fname=char(fnames(1,i));
        fname=fullfile(pathName,fname);
        [newt, newdata]=getData(fname,headerString); %load(fname);
        data=[data;newdata];
        if i>1

```

```

        maxt=max(t);
    else
        maxt=0;
    end
    t=[t;newt+maxt];
end
end

% if nargout > 1
%     t=data(:,1); data=data(:,2:end);
% end
end

function [X_Value,data] = getData(filename,headerString)

delimiter = ','; %comma

fileID = fopen(filename,'r');

%Need to auto determine number of columns to define correct format string
%Assume time column is there
frewind(fileID);
[lineFound,scratch,lineCount]=gotoLine(fileID,headerString);
dataString = fgetl(fileID);
cols=0;
while ~isempty(dataString)
    [val,dataString]=strtok(dataString,delimiter);
    cols=cols+1;
end

formatSpec_f='%f'; %Time col
formatSpec_s='%s'; %Time col
for i=1:cols-1
    formatSpec_f = strcat(formatSpec_f,'%f');
    formatSpec_s = strcat(formatSpec_s,'%s');
end
formatSpec_f = strcat(formatSpec_f,'%s%[\n\r]');
formatSpec_s = strcat(formatSpec_s,'%s%[\n\r]');

frewind(fileID);
startRow = lineCount+1; %23;
if startRow~=11;
    warning(sprintf('Expected start row for data to be 11. Check file.
Using: %d',startRow))
end
endRow = inf;
% delimiter='\t'
%% Read columns of data according to format string.
% This call is based on the structure of the file used to generate this
% code. If an error occurs for a different file, try regenerating the code
% from the Import Tool.
try
    formatSpec=formatSpec_f;
    dataArray = textscan(fileID, formatSpec, endRow(1)-startRow(1)+1,
'Delimiter', delimiter, 'EmptyValue' ,NaN,'HeaderLines', startRow(1)-1,
'ReturnOnError', false);
catch
    formatSpec=formatSpec_s;

```

```

        dataArray = textscan(fileID, formatSpec, endRow(1)-startRow(1)+1,
'Delimiter', delimiter, 'EmptyValue' ,NaN, 'HeaderLines', startRow(1)-1,
'ReturnOnError', false);
end

for block=2:length(startRow)
    frewind(fileID);
    dataArrayBlock = textscan(fileID, formatSpec, endRow(block)-
startRow(block)+1, 'Delimiter', delimiter, 'EmptyValue' ,NaN, 'HeaderLines',
startRow(block)-1, 'ReturnOnError', false);
    for col=1:length(dataArray)
        dataArray{col} = [dataArray{col};dataArrayBlock{col}];
    end
end

%% Close the text file.
fclose(fileID);

%% Post processing for unimportable data.
% No unimportable data rules were applied during the import, so no post
% processing code is included. To generate code which works for
% unimportable data, select unimportable cells in a file and regenerate the
% script.

%% Allocate imported array to column variable names
X_Value = dataArray{:, 1};
convert=0;
%s=size(dataArray);
if iscellstr(X_Value(1,1));
    convert=1;
end
k=1;

for j=2:cols
    data(:,k) = dataArray{:, j};
    k=k+1;
end
h = waitbar(0, 'Please wait...');
if convert
    try
        rI=1;
        for i=1:length(data)
            rowval=str2num(char(X_Value(i,1)));
            if ~isempty(rowval) & isnumeric(rowval)
                newX(rI,1)=rowval;
                for j=1:size(data,2)
                    newdata(rI,j)=str2num(char(data(i,j)));
                end
                rI=rI+1;
            end
            waitbar(i/length(data),h)
        end
        X_Value=newX;
        data=newdata;
    catch ME
        error;
    end
end
close(h)
end

```

```

%-----
function [lineFound,line,linecount]=gotoLine(fid,lineString)

frewind(fid)
lineFound=0;
linecount=0;
while ~lineFound & ~feof(fid)
    line = fgetl(fid);
    lineFound1 = instring(lineString, line);
    lineFound2 = strfind(line, lineString);
    if any([lineFound1, lineFound2]); lineFound = 1; end;
    linecount = linecount+1;
end
end

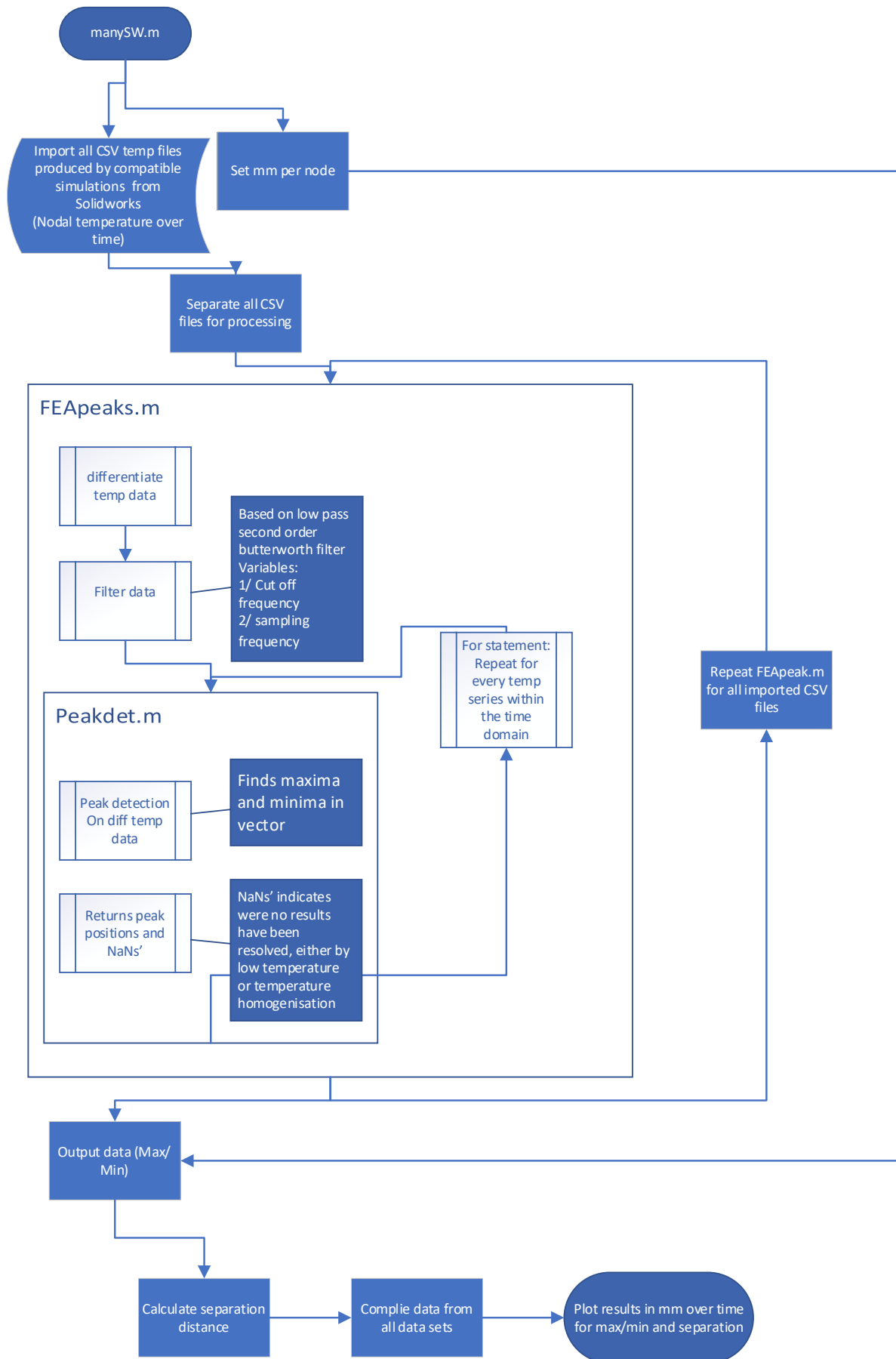
function [f,startIndex]=instring(stringBit,string,onlyFirst)

% INSTRING: checks string exists in another string.
%
% [f,startIndex]=instring(stringBit,string,onlyFirst)
% returns '1' if 'stringBit' exists in 'string'

if nargin < 3
    onlyFirst=0;
end

there=ismember(stringBit,string);
f=0; startIndex=[]; j=1;
if all(there)
    %worth looking at
    extra=length(string)-length(stringBit);
    if extra==0; extra=1; end;
    endI=length(stringBit);
    startI=endI-length(stringBit)+1;
    while endI<=length(string)
        if strcmp(stringBit,string(startI:endI))
            f=1;
            startIndex(j)=startI;
            if onlyFirst
                continue
            end
            j=j+1;
        end
        endI=endI+1;
        startI=startI+1;
    end
end
end
end

```



d. *Extract* - Feature extraction code

```
function [ faceoneav,complied,startpoint,startpoint2] = extract( input_args
);

%UNTITLED4 Summary of this function goes here
% Detailed explanation goes here
close all
clear
disp ('enter true length and height in mm');
realheight=input('height=');
reallength=input('length=');

image=uigetfile('*.jpg','image file name'),'select image'; % image file
name remember to have image export on actual size
tempData=load(uigetfile('*.mat','temp mat file name'))% mat temp data load
image=imread(image);
figure,imshow(image)
bw=rgb2gray(image); % colour to gray conversion
edgedec=edge(bw,'canny'); % edge detection
image_edge=edgedec;
figure,imshow(image_edge)
disp('pick X1, X2, Y1, Y2(return after each pick)') %pick XY edge
coordinates
[X1]=getpts;
[X2]=getpts;
[not,Y1]=getpts;
[not,Y2]=getpts;
Length=X2-X1;Height=Y2-Y1; % height and width of images
backcrop=imcrop(image,[X1,Y1,Length,Height]); %cropping function
cl=reallength/Length;
ch=realheight/Height;
conversion=(cl+ch)/2; % conversion factor from pix to mm
tempcrop=imcrop((tempData.Frame),[X1,Y1,Length,Height]); % temp cropping
figure,surf(tempcrop)
noise=wiener2(tempcrop,[5 5]); % wiener 2D noise filter
figure,surf(noise);
d1=designfilt('lowpassiir','FilterOrder',20,'HalfPowerFrequency',0.35,'Desi
gnMethod','butter');
delta=0.12
xlength=(0:1:Length-1);
peakNum=[];
%ginput command to get initial line location
figure,imshow(backcrop);
disp('choose ref point')
[x,y]=ginput(1);
rI = y; %selected row of image
numLines=10;
Fsection=noise(rI-numLines/2:rI+numLines/2,:); %averaging of selection
avsection=mean(Fsection);
figure,plot(avsection);
Fdiff=diff(avsection);
figure,plot(Fdiff);
Fdiffflit = filtfilt(d1,Fdiff); %No filter in iteration version.
missStart = 5;
missEnd = 5;
[maxtab1, mintab1]=peakdet(Fdiffflit, delta, xlength)
```

```

[maxtab1, mintab1]=peakdet(Fdiffflit(1,missStart:end-missEnd), delta,
xlength(1,missStart:end-missEnd));
%Number of peAKS FOR INITIAL SCAN
numPeaks =size(maxtab1,1);
tolBand = 10
maxtab=[];
rI=1;
figure

for i = 1: size(noise,1)
    Fsection=noise(i,:);
    if size(Fsection,1) > 1
        avsection=mean(Fsection);
    else
        avsection = Fsection;
    end
    Fdiff=diff(avsection);
    %Fdiffflit=filtfilt(d1,Fdiff);
    Fdiffflit = Fdiff; %No filter in iteration version.

    plot(Fdiffflit);
    hold on
    % delta=input('delta=');
    [maxtab, mintab]=peakdet(Fdiffflit(1,missStart:end-missEnd), delta,
xlength(1,missStart:end-missEnd));

    if isempty(maxtab) || isempty(mintab)
        continue
    end
    xmaxtab=maxtab(:,1);
    ymaxtab=maxtab(:,2);
    xmintab=mintab(:,1);
    ymintab=mintab(:,2);
    if length(xmaxtab) == numPeaks && length(xmintab) == numPeaks;
        checkGood=zeros(1,numPeaks);
        for pI = 1 : numPeaks
            if abs(xmaxtab(pI) - maxtab1(pI,1)) < tolBand
                checkGood(pI) = 1;
            end
        end
        if all(checkGood)
            maxpeakxfv(rI,:) = transpose(xmaxtab);
            maxpeakyfv(rI,:) = [i,i,i];
            maxpeakafv(rI,:) = transpose(ymaxtab);
            minpeakxfv(rI,:) = transpose(xmintab);
            minpeakyfv(rI,:) = [i,i,i];
            minpeakafv(rI,:) = transpose(ymintab);
            rI=rI+1;
        end
    end
end
end
yheight=[0:1:Height-1];
figure,imshow(backcrop);
disp('choose ref point')
[x,y]=ginput(1);
cI = x; %selected column of image
numLines=10;
Fsection=noise(:,cI-numLines/2:cI+numLines/2); %averaging of selection
avsection=mean(Fsection,2);
avsection=avsection';
figure,plot(avsection);

```

```

Fdiff=diff(avsection);
figure,plot(Fdiff);
Fdiffflit = filtfilt(d1,Fdiff); %No filter in iteration version.
missStart = 5;
missEnd = 3;
%[maxtab1, mintab1]=peakdet(Fdiffflit, delta, yheight)
[maxtab1, mintab1]=peakdet(Fdiffflit(1,missStart:end-missEnd), delta,
yheight(1,missStart:end-missEnd));
%Number of peAKS FOR INITIAL SCAN
numPeaks =size(maxtab1,1);
tolBand = 10;
maxtab=[];
rI=1;
figure
for i =1:size(noise,2);
    Fsection=noise(:,i);
    if size(Fsection,1) > 1
        avsection=mean(Fsection,2);
    else
        avsection = Fsection;
    end
    avsection=avsection';
    Fdiff=diff(avsection);
    %Fdiffflit=filtfilt(d1,Fdiff);
    Fdiffflit = Fdiff; %No filter in iteration version.

    plot(Fdiffflit);
    hold on
    % delta=input('delta=');
    %[maxtab1, mintab1]=peakdet(Fdiffflit, delta, yheight)
    [maxtab, mintab]=peakdet(Fdiffflit(1,missStart:end-missEnd), delta,
yheight(1,missStart:end-missEnd));

    if isempty(maxtab) || isempty(mintab)
        continue
    end
    xmaxtab=maxtab(:,1);
    ymaxtab=maxtab(:,2);
    xmintab=mintab(:,1);
    ymintab=mintab(:,2);
    numpeaks(i)=length(xmaxtab);
    if length(xmaxtab) == numPeaks && length(xmintab) == numPeaks;
        checkGood=zeros(1,numPeaks);

        for pI = 1 : numPeaks
            if abs(xmaxtab(pI) - maxtab1(pI,1)) < tolBand
                checkGood(pI) = 1;
            end
        end
        if all(checkGood)
            maxpeakxfh(rI,:) = transpose(xmaxtab);
            maxpeakyfh(rI,:) = [i,i,i];
            maxpeakafh(rI,:) = transpose(ymaxtab);
            minpeakxfh(rI,:) = transpose(xmintab);
            minpeakyfh(rI,:) = [i,i,i];
            minpeakafh(rI,:) = transpose(ymintab);
            rI=rI+1;
        end
    end
end
end
a=(1:1:realheight)';

```

```

b=size(a);
c=zeros(b);
LH=[c a];
e=(1:1:reallength)';
f=size(e);
g=zeros(f);
BOT=[e g];
TOP=[e (ones(length(e),1)*75)];
RH=[(ones(length(a),1)*50) a];
complied=[LH;BOT;TOP;RH];
figure,imshow(backcrop)
hold on
plot(maxpeakxfv, maxpeakyfv, '*g')
plot(minpeakxfv, minpeakyfv, '*g')
plot(maxpeakyfh, maxpeakxfh, '*')
plot(minpeakyfh, minpeakxfh, '*')
hold off
maxpeakxfh=maxpeakxfh*conversion;
maxpeakyfh=maxpeakyfh*conversion;
minpeakxfh=minpeakxfh*conversion;
minpeakyfh=minpeakyfh*conversion;
maxpeakyfv=maxpeakyfv*conversion;
maxpeakxfv=maxpeakxfv*conversion;
minpeakyfv=minpeakyfv*conversion;
minpeakxfv=minpeakxfv*conversion;
flh=[maxpeakxfv,maxpeakyfv(:,1)];
frh=[minpeakxfv, minpeakyfv(:,1)];
ft=[maxpeakyfh(:,1), maxpeakxfh];
fb=[minpeakyfh(:,1), minpeakxfh];
faceone=[flh;frh;ft;fb];
figure,plot(faceone(:,1),faceone(:,2),'*')
set(gca, 'YDir','reverse')
xlabel('x')
ylabel('y')
axis equal
flhav=[ones(length(maxpeakxfv),1)*mean(maxpeakxfv),maxpeakyfv(:,1)];
frhav=[ones(length(minpeakxfv),1)*mean(minpeakxfv), minpeakyfv(:,1)];
ftav=[maxpeakyfh(:,1),ones(length(maxpeakxfh),1)*mean(maxpeakxfh)];
fbav=[minpeakyfh(:,1),ones(length(minpeakxfh),1)*mean(minpeakxfh)];
faceoneav=[flhav;frhav;ftav;fbav];
hold on
plot(faceoneav(:,1),faceoneav(:,2),'g*')
plot(complied(:,1),complied(:,2),'o')
startpoint=flhav(:,1);
startpoint2=frhav(:,1);
%edge2=
end

```

e. *Peakdet* - Peak detection Code

```
function [maxtab, mintab]=peakdet(v, delta, x)
```

```

%PEAKDET Detect peaks in a vector
%
% [MAXTAB, MINTAB] = PEAKDET(V, DELTA) finds the local
% maxima and minima ("peaks") in the vector V.
% MAXTAB and MINTAB consists of two columns. Column 1
% contains indices in V, and column 2 the found values.
%
% With [MAXTAB, MINTAB] = PEAKDET(V, DELTA, X) the indices
% in MAXTAB and MINTAB are replaced with the corresponding
% X-values.
%

```

```

%       A point is considered a maximum peak if it has the maximal
%       value, and was preceded (to the left) by a value lower by
%       DELTA.

maxtab = [];
mintab = [];

v = v(:); % Just in case this wasn't a proper vector

if nargin < 3
    x = (1:length(v))';
else
    x = x(:);
    if length(v)~= length(x)
        error('Input vectors v and x must have same length');
    end
end

if (length(delta(:)))>1
    error('Input argument DELTA must be a scalar');
end

if delta <= 0
    error('Input argument DELTA must be positive');
end

mn = Inf; mx = -Inf;
mnpos = NaN; mxpos = NaN;

lookformax = 1;

for i=1:length(v)
    this = v(i);
    if this > mx, mx = this; mxpos = x(i); end
    if this < mn, mn = this; mnpos = x(i); end

    if lookformax
        if this < mx-delta
            maxtab = [maxtab ; mxpos mx];
            mn = this; mnpos = x(i);
            lookformax = 0;
        end
    else
        if this > mn+delta
            mintab = [mintab ; mnpos mn];
            mx = this; mxpos = x(i);
            lookformax = 1;
        end
    end
end
end

```

f. *Squareass* - Assembly Code

```

function [set] =

squareass(faceone, facetwo, surround1, surround2, start, start2, start3, start4 );

%squareass reassembles data

```

```

% Detailed explanation goes here
close all

disp ('enter true width in mm');
width=input('width=');
Length=input('length=');
profilef=[surround1(:,1) zeros(length(surround1),1) surround1(:,2)];
profilerh=[ones(length(surround2),1)*width surround2(:,1) surround2(:,2)];
profileb=[surround1(:,1) ones(length(surround1),1)*Length surround1(:,2)];
profilelh=[zeros(length(surround2),1)*0 surround2(:,1) surround2(:,2)];
frontface=[faceone(:,1) ones(length(faceone),1)*mean(start3) faceone(:,2)];
lefthand=[ones(length(facetwo),1)*mean(start) facetwo(:,1) facetwo(:,2)];
backface=[faceone(:,1) ones(length(faceone),1)*mean(start4) faceone(:,2)];
righthand=[ones(length(facetwo),1)*mean(start2) facetwo(:,1) facetwo(:,2)];
set=[profilef;profilerh;profileb;profilelh;frontface;lefthand;backface;righ
thand];
scatter3(set(:,1,:),set(:,2,:),set(:,3,:), '*');
set(gca,'zdir','reverse')
axis equal
end

```

Appendix I. REVETTI results

a. Curved feature line fitting results

i. Peak 1 curve fitting

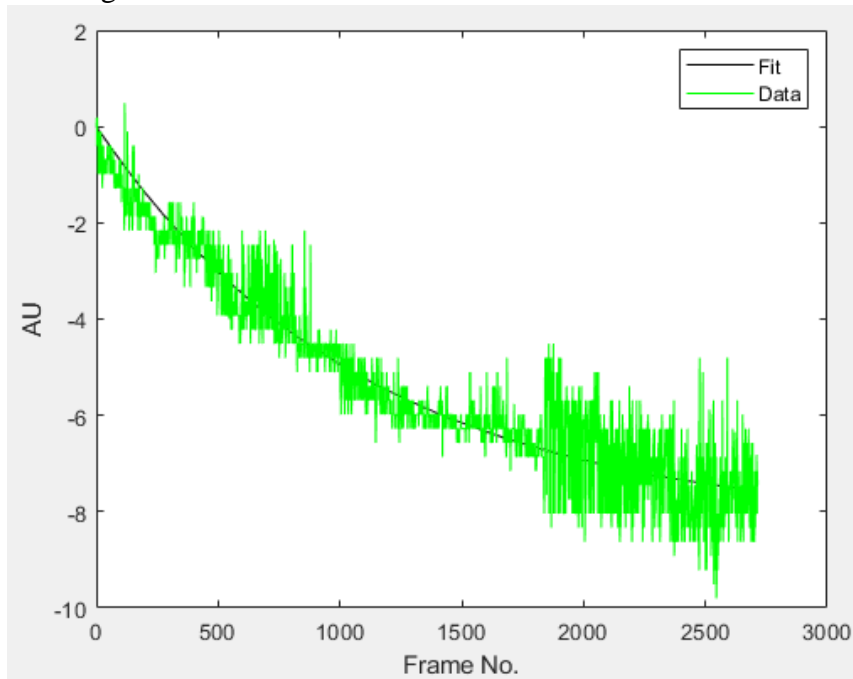


Figure I-1: Curve fitting for peak 1 of circulate profile

ii. Peak 2 curve fitting

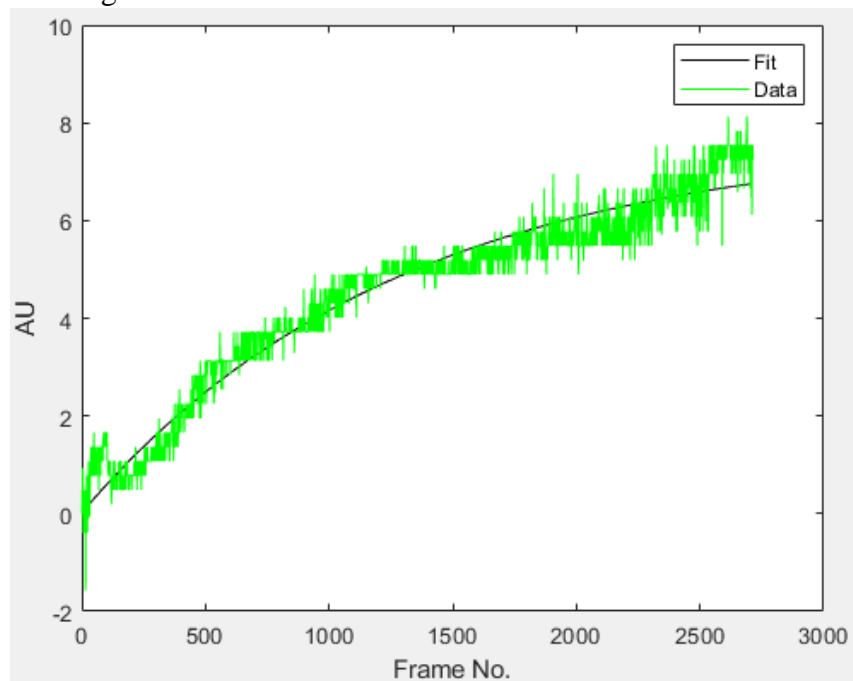


Figure I-2: Curve fitting for peak 2 of circulate profile

b. Angled feature line fitting results

i. Peak 1 curve fitting

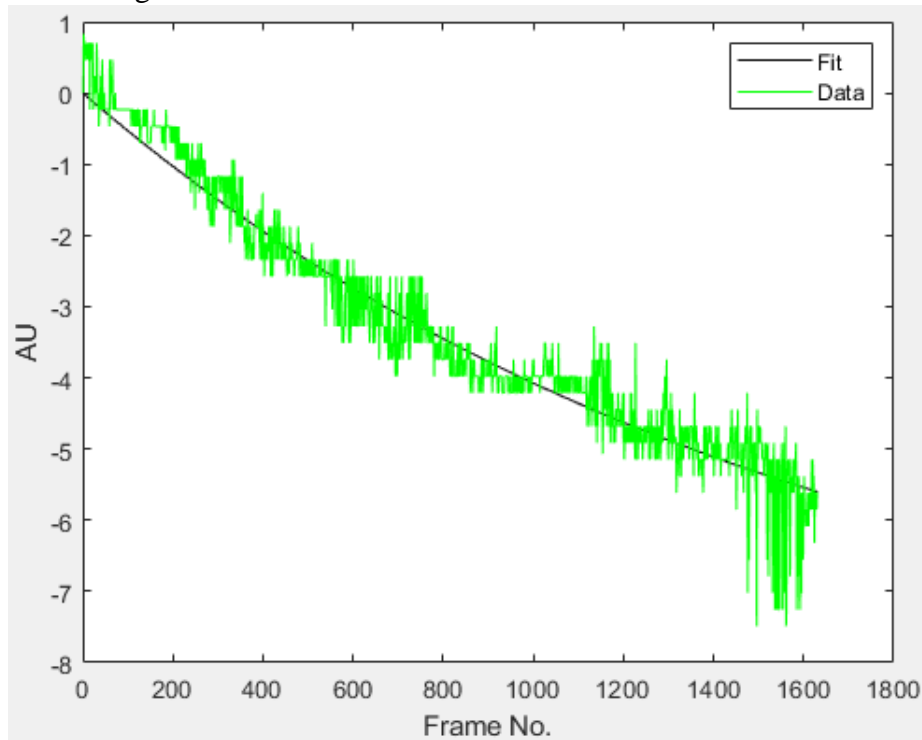


Figure I-3: Curve fitting for peak 1 of angled profile

ii. Peak 2 curve fitting

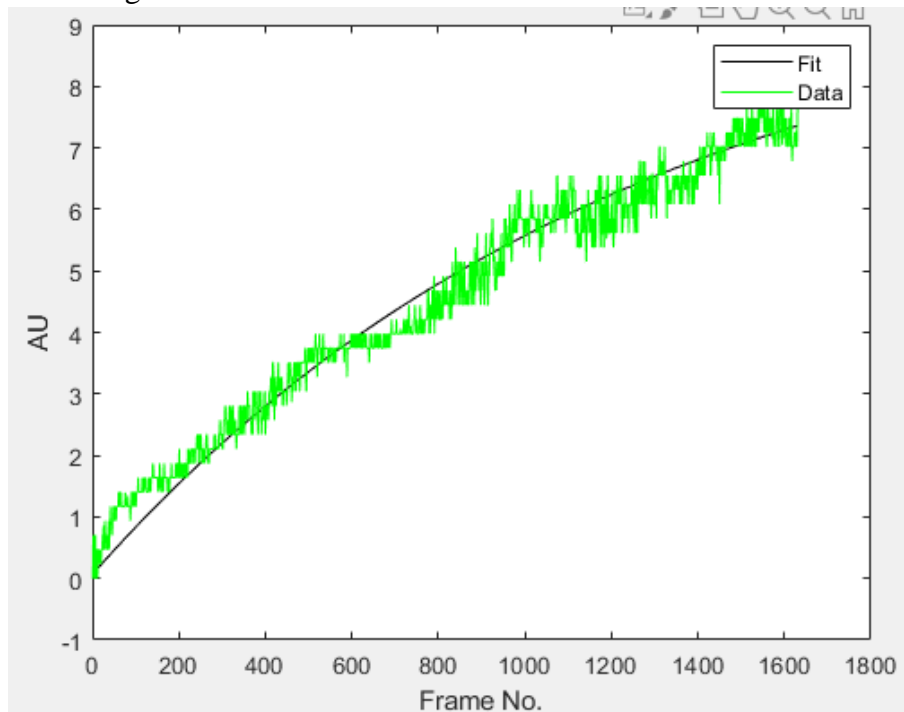


Figure I-4: Curve fitting for peak 1 of angled profile

iii. Exponential curve extension for peak 1

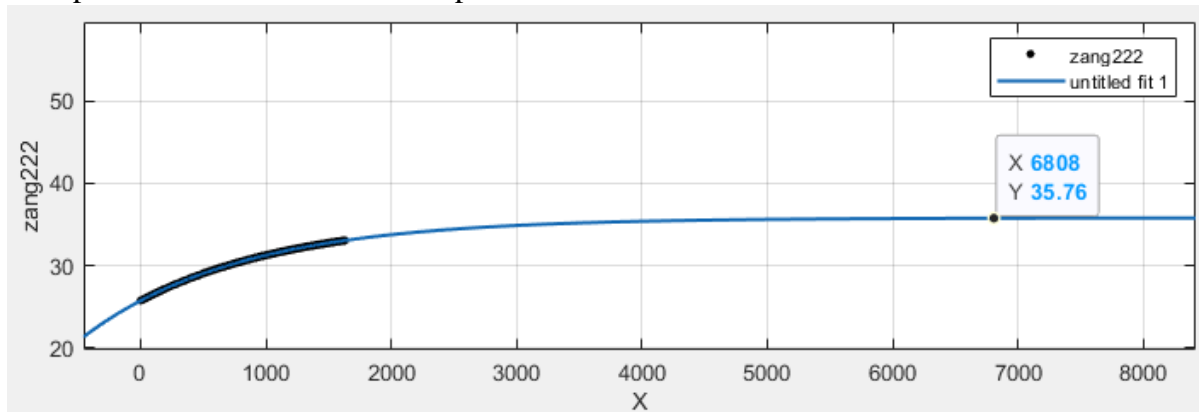


Figure I-5: Exponential curve extension from best-fit curve from peak 1

iv. Exponential curve extension for peak 2

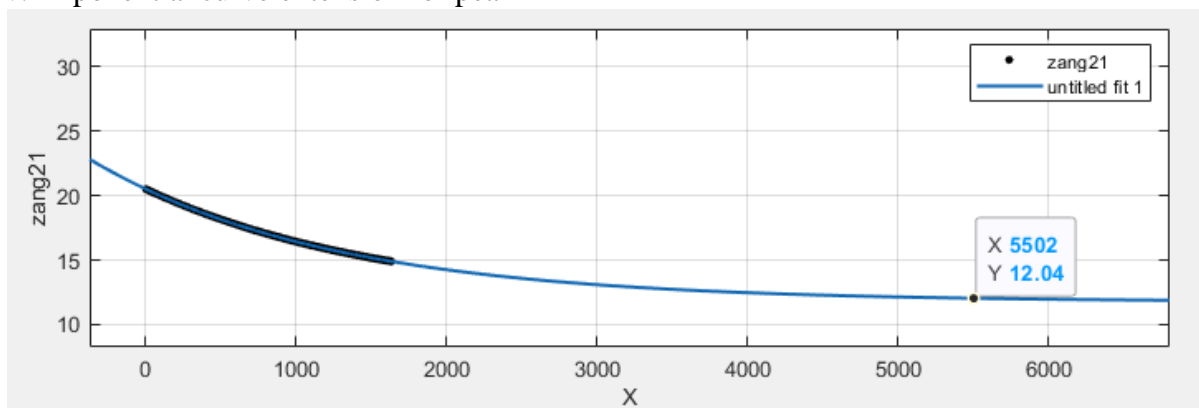


Figure I-6: Exponential curve extension from best-fit curve from peak 2

Appendix J. Thermograms used in accuracy and repeatability tests – square artifact

a. Run 1

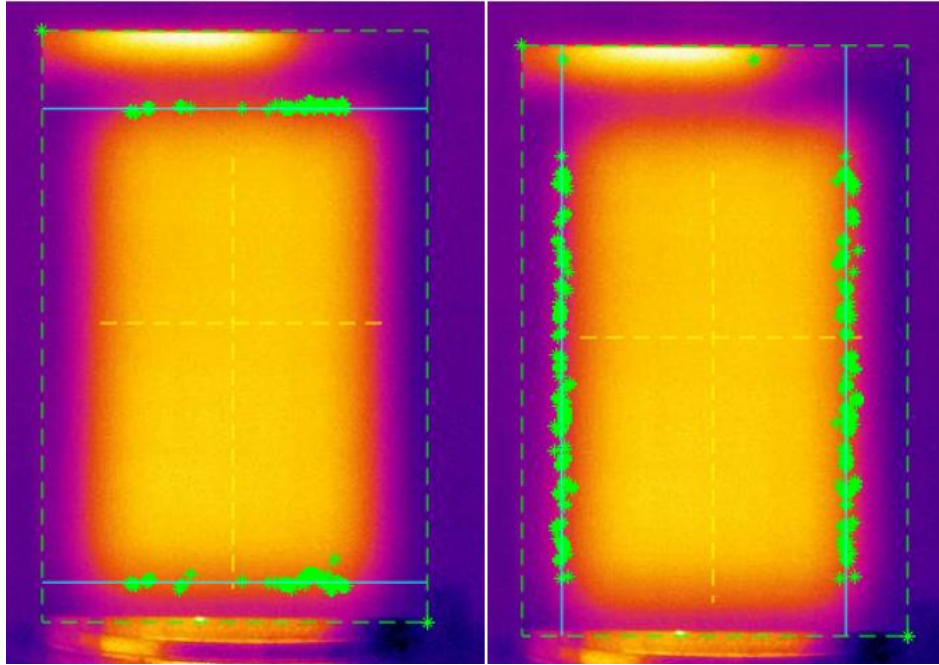


Figure J-1: L - Horizontal edges, R - vertical edges for run 1

b. Run 2

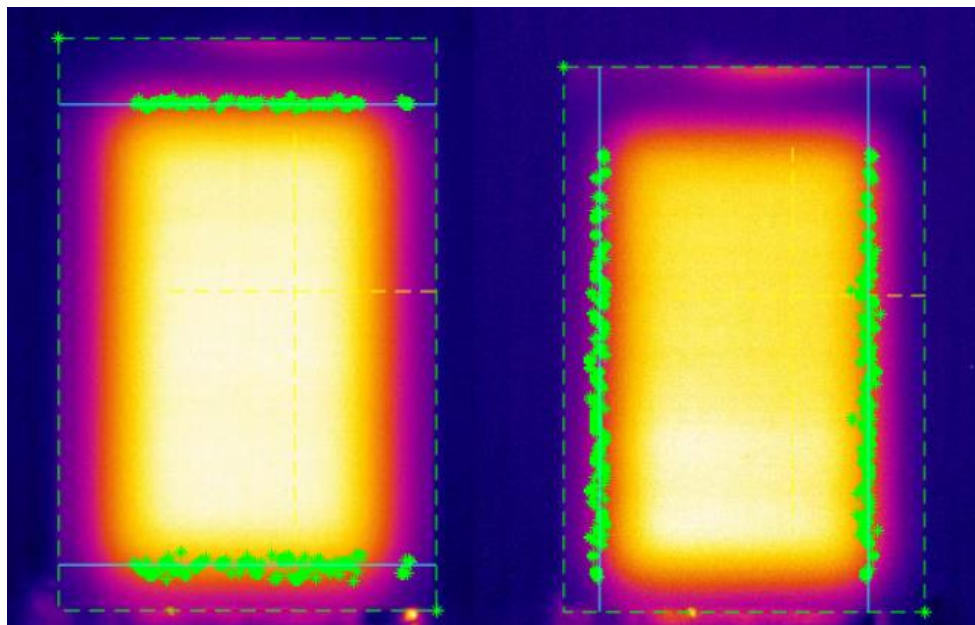


Figure J-2: L - Horizontal edges, R - vertical edges for run 2

c. Run 3

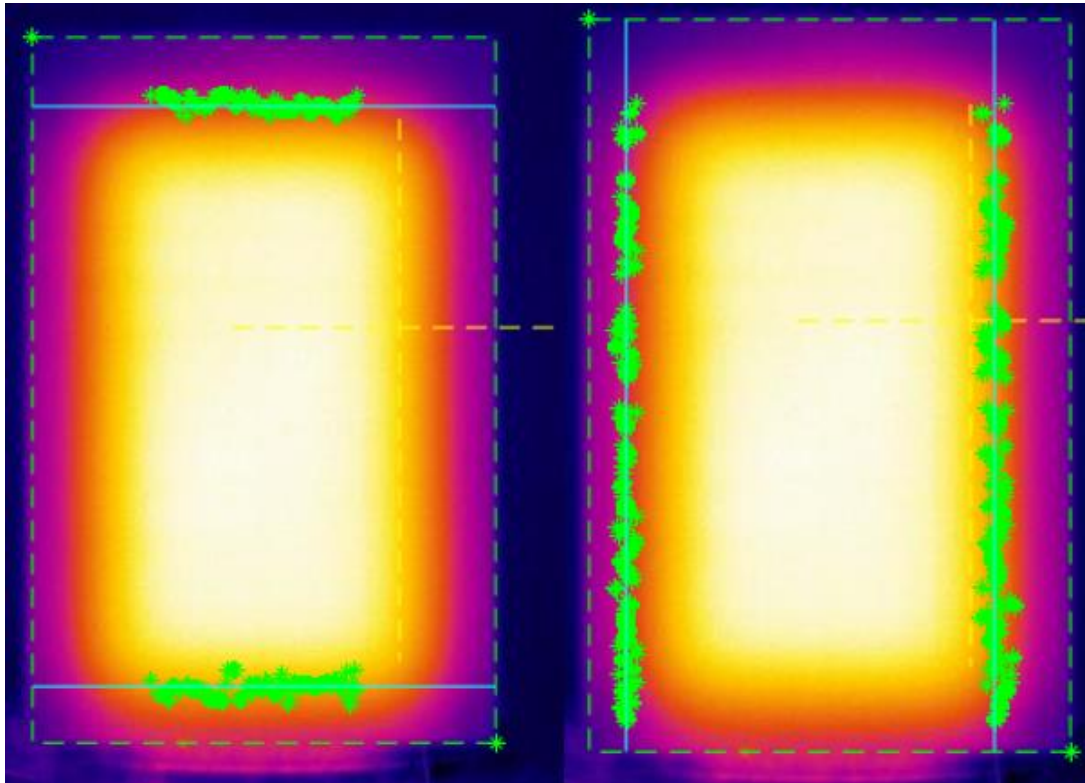


Figure J-3: L - Horizontal edges, R - vertical edges for run 3

d. Run 4

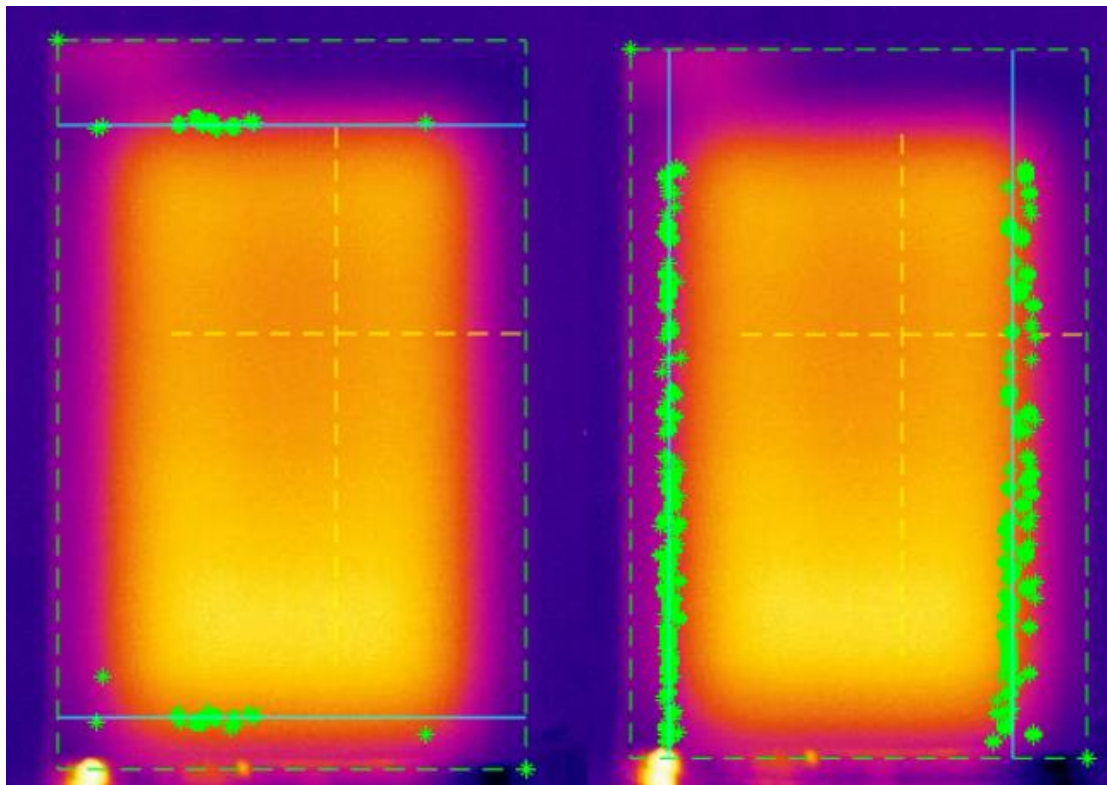


Figure J-4: L - Horizontal edges, R - vertical edges for run 4

e. Run 5

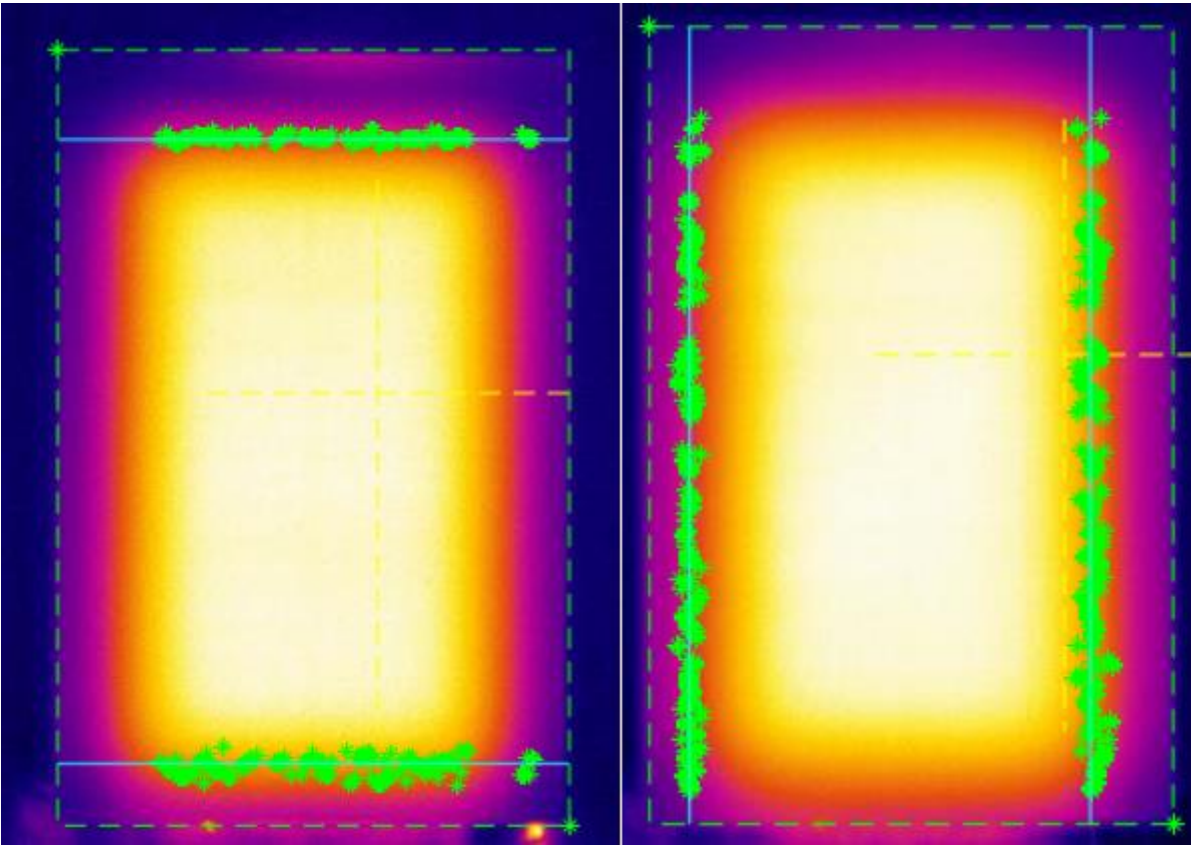


Figure J-5: L - Horizontal edges, R - vertical edges for run 5

Appendix K. Thermograms used in accuracy and repeatability tests – L-shaped artifact

a. Run 1

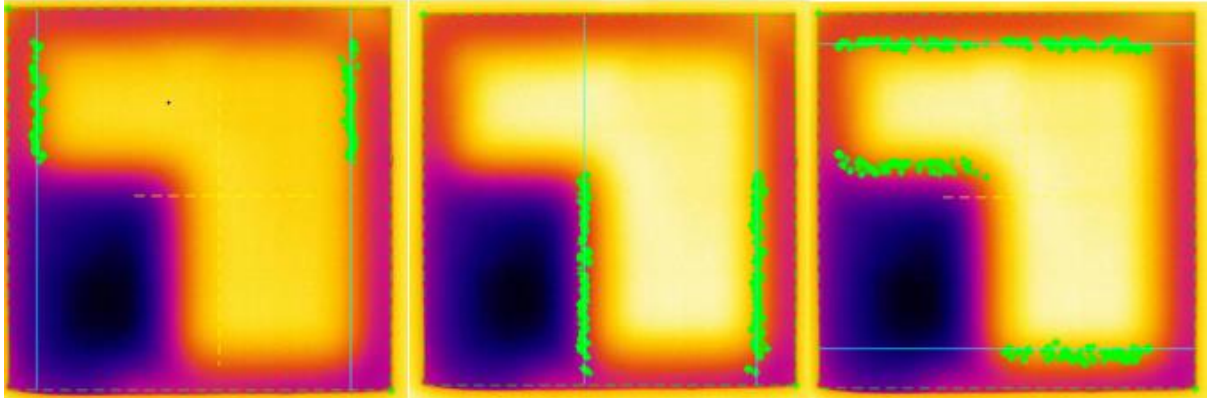


Figure K-1: L - Vertical edges 1, C - Vertical edges 2, R - Horizontal edges for run 1

b. Run 2

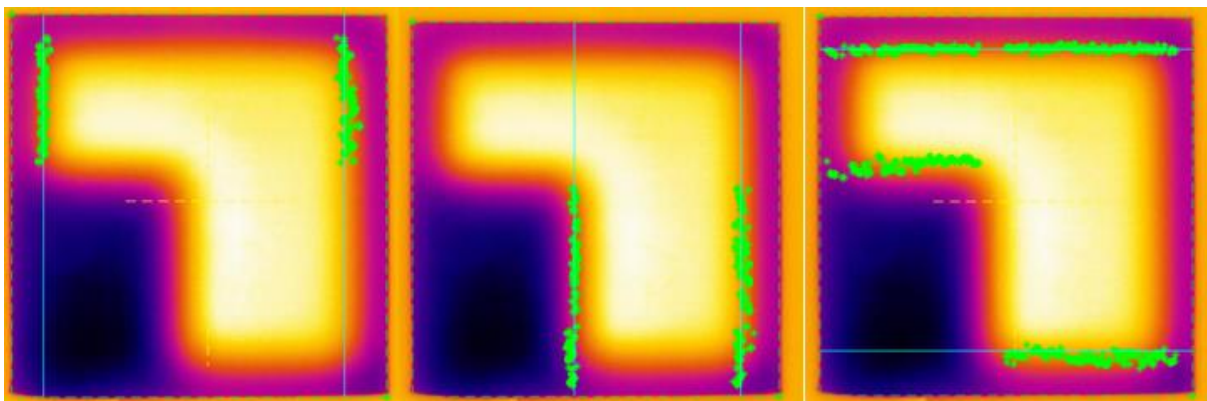


Figure K-2: Vertical edges 1, C - Vertical edges 2, R - Horizontal edges for run 2

c. Run 3

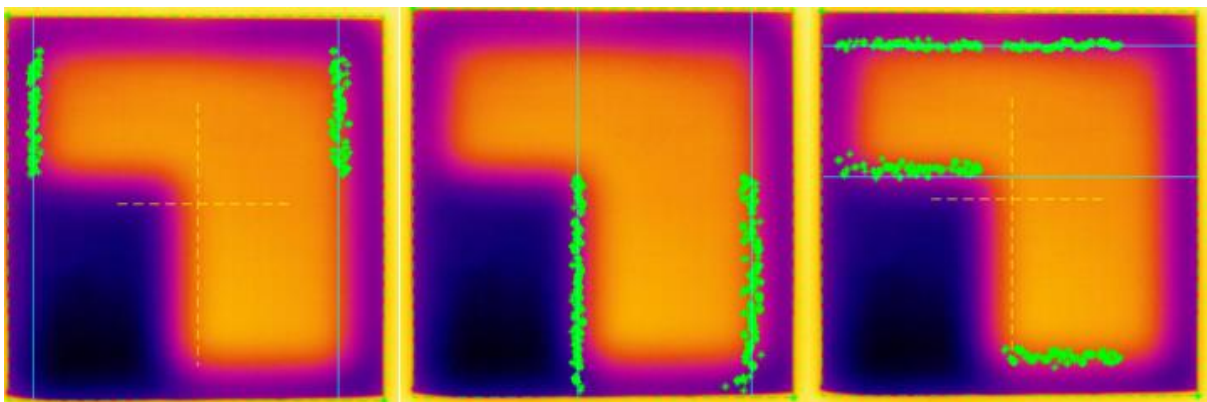


Figure K-3: Vertical edges 1, C - Vertical edges 2, R - Horizontal edges for run 3

d. Run 4

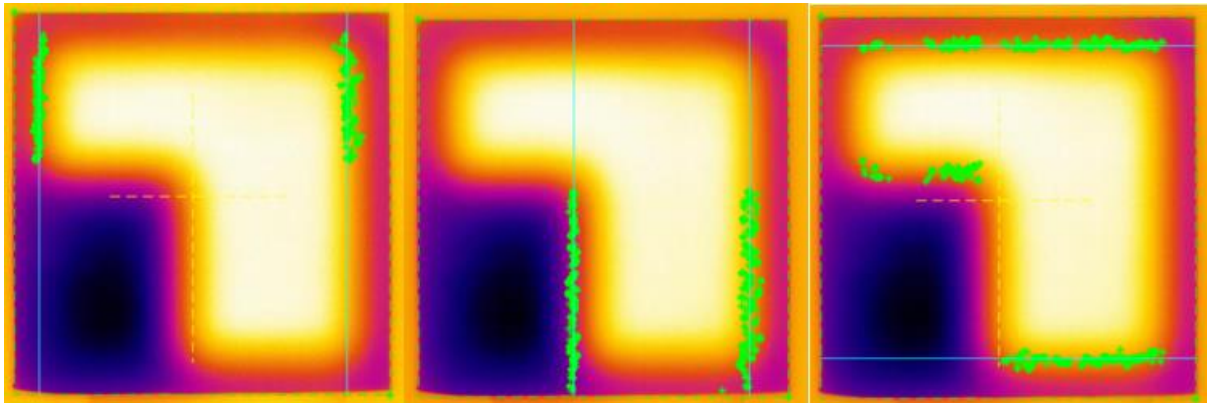


Figure K-4: Vertical edges 1, C - Vertical edges 2, R - Horizontal edges for run 4

e. Run 4

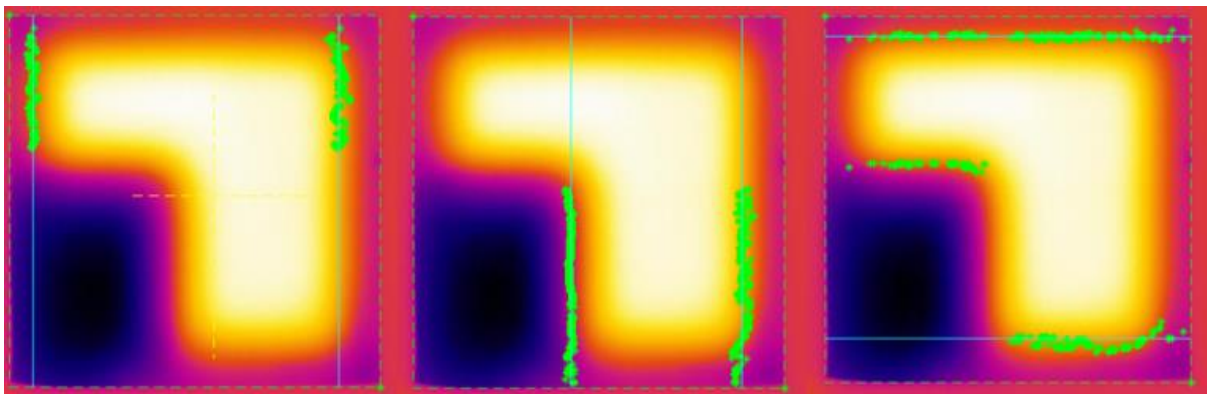


Figure K-5: Vertical edges 1, C - Vertical edges 2, R - Horizontal edges for run 5

Appendix L. Thermograms used in accuracy and repeatability tests – square artifact with A35

a. Run 1

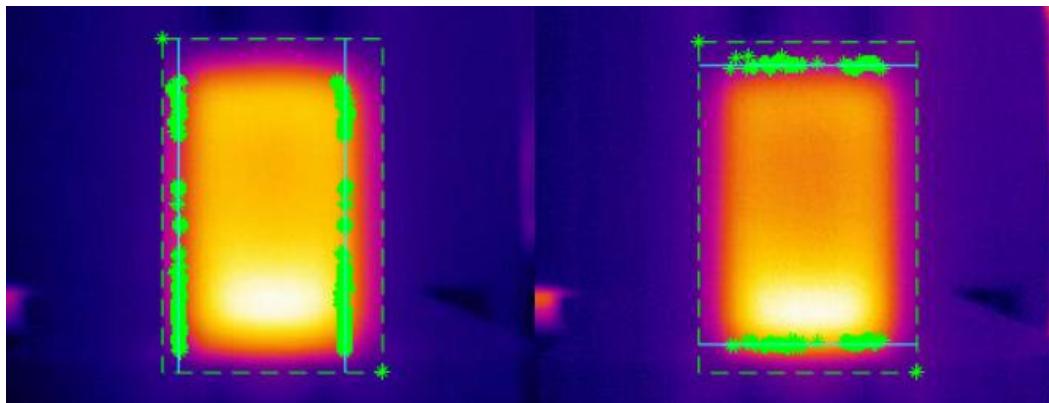


Figure L-1: Horizontal edges, R - vertical edges for run 1

b. Run 2

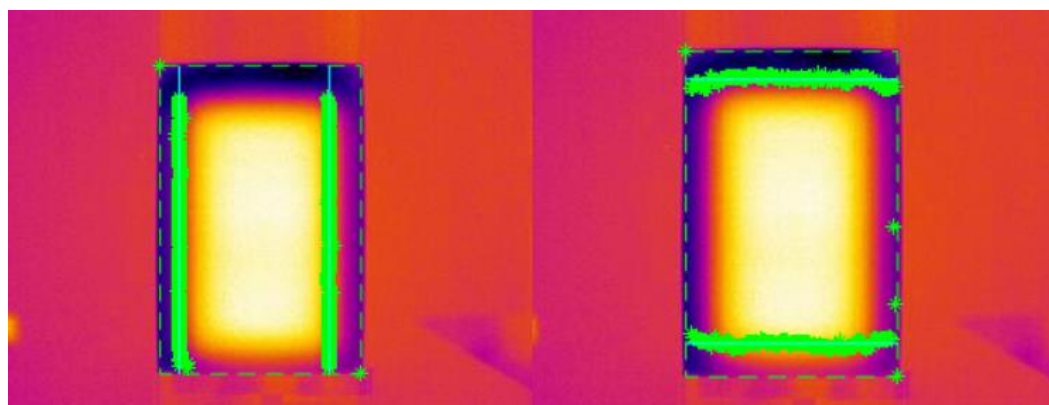


Figure L-2: Horizontal edges, R - vertical edges for run 2

c. Run 3

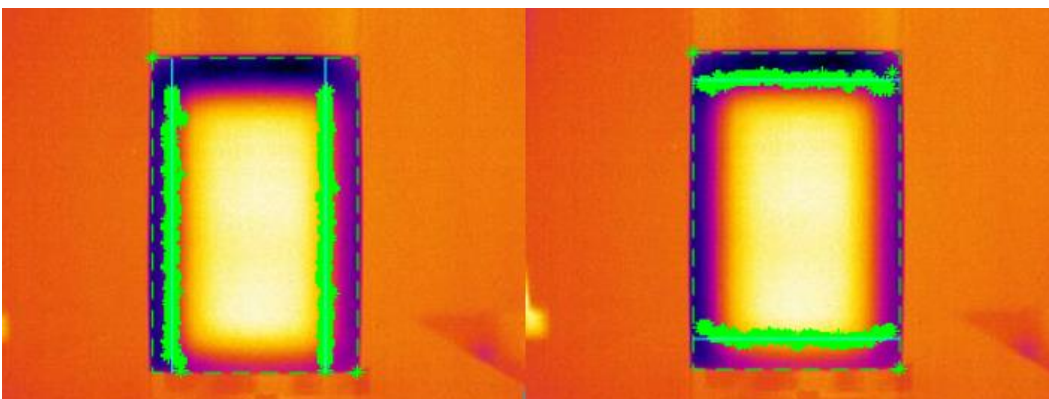


Figure L-3: Horizontal edges, R - vertical edges for run 3

d. Run 4

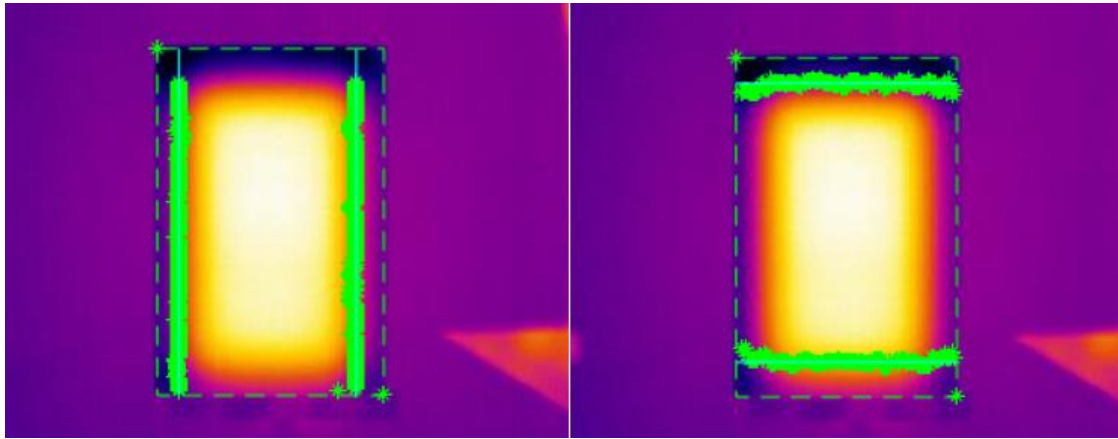


Figure L-4: Horizontal edges, R - vertical edges for run 4

e. Run 5

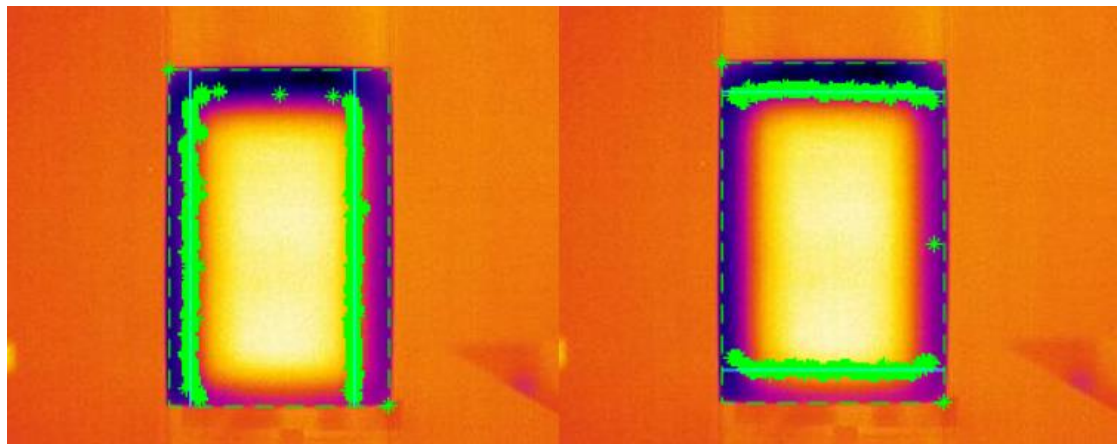


Figure L-5: Horizontal edges, R - vertical edges for run 5